This is to certify that the
dissertation entitled

INVESTIGATION OF A DEFORMABLE MIRROR MICROWAVE IMAGING AND THERAPY TECHNIQUE FOR BREAST CANCER

presented by

KAVITHA ARUNACHALAM

has been accepted towards fulfillment
of the requirements for the

DOCTORAL degree in Electrical & Computer Engineering

Kabita Udpa
Major Professor's Signature

Feb 21, 2007
Date

INVESTIGATION OF A DEFORMABLE MIRROR MICROWAVE IMAGING AND THERAPY TECHNIQUE FOR BREAST CANCER

VOLUME I

By

Kavitha Arunachalam

A DISSERTATION

Submitted to
Michigan State University
in partial fulfillment of the requirements
for the degree of

DOCTOR OF PHILOSOPHY

Department of Electrical and Computer Engineering

2007

ABSTRACT

INVESTIGATION OF A DEFORMABLE MIRROR MICROWAVE IMAGING AND THERAPY TECHNIQUE FOR BREAST CANCER

By

Kavitha Arunachalam

A novel deformable mirror microwave tomography technique for the nondestructive evaluation of non- or poorly conducting materials is investigated in this thesis. The proposed tomography technique utilizes a fixed transmitter antenna and a continuously deformable mirror with reflective coating to acquire multi-view measurements for permittivity reconstruction. The concept of using adaptive reflector antenna for medical imaging is introduced in this thesis with emphasis on breast cancer detection. Numerical simulations of the proposed imaging technique investigated using finite element boundary integral method and Tikhonov regularization technique for heterogeneous mathematical breast models indicate the feasibility of the new deformable mirror microwave tomography for breast imaging. Besides the computational study in the microwave regime, a simple experimental setup in the visible spectrum of electromagnetic radiation is also investigated to evaluate the merit in using mirror for multi-view measurements for material property inversion. One dimensional inversion results of material refractive index obtained using the proof-of-concept optical prototype employing single perfectly reflecting mirror emphasize the merit in using mirror for multi-view measurements and reinstates the feasibility of deformable mirror tomography technique.

In addition to its use for imaging, the system can be used for breast cancer therapy as well. A non-invasive thermal therapy technique employing dual deformable mirrors is investigated for the treatment of localized breast tumors. The proposed

technique uses the deformable mirror to focus the incident electromagnetic radiation at the target tumor for thermal therapy. The feasibility of the proposed technique is evaluated via numerical simulations on two-dimensional breast phantoms. The electric field maintained by the deformable mirror is modeled and estimated using the boundary integral method. The EM energy deposited by the mirror is used in the bio-heat transfer equation to quantify the steady state temperature distribution inside the breast phantom. Computational studies on mathematical and MRI derived patient models indicate preferential EM energy deposition and temperature elevation inside the tumor with minimum collateral damage to the neighboring benign tissues. Extended simulation studies for non-invasive tumor ablation appear promising and indicate the prospects of a new applicator design.

To my beloved parents

ACKNOWLEDGMENTS

This Thesis, my first scientific accomplishment has significantly shaped my philosophical and scientific perspective of life on this universe. Many individuals have helped me achieve this.

This Thesis would not have been possible without the able guidance of my advisors Dr. Lalita Udpa and Dr. Satish Udpa. Particularly, my very special thanks to Lalita Udpa, who gave me a break from my mundane life as a software engineer into the challenging and interesting world of science and engineering. I am grateful for her intellectual and financial support, inspiration, freedom of work, invaluable advice and above all trust that gave me the confidence and guided me to take the right decisions throughout my graduate studies. I also sincerely thank my coadvisor Satish Udpa for his intellectual guidance, discussions and encouragement in many aspects of my graduate studies. I am glad to work with him. My advisors, Lalita Udpa and Satish Udpa are not only great visionary scientists with renowned reputation but they are also very kind and gentle individuals I have known. I have learned science and many invaluable moral values working with them and I look forward to work with them in future.

I am also very grateful to Dr. Edward Rothwell for teaching me electromagnetics and its applications. His contribution has a huge influence on my Thesis and my knowledge of electromagnetics. I would like to thank Dr. Rothwell for giving me the opportunity as a Teaching Assistant in the Electromagnetics Laboratory at MSU. He taught and guided me with the Lab equipments and experiments. His trust, guidance

and inspiration helped me and my friend Vikram to conduct microwave experiments on concrete specimens and other dielectric samples in the EM Lab at MSU.

I also sincerely thank Dr. Shanker Balasubramaniam for his continued interest in my Thesis and career. He taught me computational electromagnetics and much more about electromagnetics, a key element in this Thesis. He is a passionate teacher and he was always there to help me with my computational models and clarify my questions. His guidance at the most important times of my Thesis helped me move forward. Besides electromagnetics, I am also thankful for his encouragement and invaluable advice that he provided over the years.

My sincere thanks to Dr. Gerald Aben, Department of Radiology at MSU. Evaluation of the computational algorithms on MR breast data would not have been possible without the help of Dr. Aben. His help and guidance has been instrumental in submitting and clearing the IRB application for the MR breast data. He completed the lengthy and complicated IRB application form on my behalf and was always willing to help me with my Thesis amidst his hectic schedule. I am grateful to him for introducing me to Ms. Lori Hoisington, radiologist at MSU. I thank her for all the de-identified MRI breast data I received with patient history. I also thank Ms. Lori for explaining me the MR data acquisition procedures and teaching me how to interpret the datasets.

I had the pleasure to work with many graduate students from all over the globe and I thank them for the memorable get-together, intellectual discussions, fruitful project meetings, team work and fun. My special thanks to my friend Vikram Melapudi for the intellectual discussions, moral support and dedicated team work on the microwave

experiments with concrete specimens. He introduced me to OpenGL and Latex. I would also like to thank Naveen Nair for his help with Latex Beamer. I am thankful to Bob Clifford for his help in building things for all my experimental work and I thank Linda Clifford, our Lab secretary who took care of all paper works and pay cheques in a timely manner.

I would like to thank my friends Praveena and Priya for their help with my application to graduate school. My sincere thanks to my brother Sridhar, for his help and guidance with my graduate school application. And to my sister, Geetha Arunachalam for her company as my roommate during her Master's studies which made my student life more interesting at MSU.

Finally, I would like to thank my parents S. Arunachalam and A. Amirthaveni for their unconditional support, love and caring which helped me with the journey of life and graduate studies with humility and honesty. To them, I dedicate this Thesis.

TABLE OF CONTENTS

LIST OF TABLES

LIST OF FIGURES

KEY TO SYMBOLS AND ABBREVIATIONS

EM: Electromagnetics

TE: Transverse Electric

TM: Transverse Magnetic

FEM: Finite Element Method

FEBI: Finite Element Boundary Integral

MOM: Method of Moments

MEMS: Micro-electro-mechanical Systems

CMOS: Complementary Metal Oxide Semiconductor

MDM: Membrane Deformable Mirror

SAR: Specific Absorption Rate

BHTE: Bio-heat Transfer Equation

MR: Magnetic Resonance

CCD: Charge Coupled Device

1D: One Dimensional

2D: Two Dimensional

CHAPTER 1

INTRODUCTION

1.1 Motivation & Objectives

Breast cancer is the second leading cause of cancer deaths amongst women in the United States. The five-year survival rate for breast cancers diagnosed prior to metastasis has been reported as 97%. Thus, regular health examinations at an early age could help detect cancer and increase the survival rate. The need for early stage cancer detection with high levels of specificity and sensitivity has led to the development of several diagnosis and treatment methods. Unfortunately, even in the case of well-established X-ray mammography techniques, about 5-15% of breast cancer cases are improperly diagnosed and biopsy outcome corroborating the findings of X-ray mammogram has been reported to range between 10-50%. X-ray mammography is poor in screening radiographically dense breast, involves the use of ionizing radiation and requires painful breast compression.

The limitations of X-ray mammography have led to an interest in alternate breast-imaging methods. Amongst the complementary methods, microwave breast imaging is very promising because of the very high contrast between the electrical properties of cancerous and benign breast tissues. Moreover, microwave breast imaging does not involve radiation exposure or breast compression and is a safer alternative non-invasive imaging method. Conventional microwave tomography for biological bodies involves illumination at different angles/positions for imaging and often require antenna switching mechanisms, antenna compensation algorithms and at times increase in the number of antennas for more multi-view field measurements.

This gives the impetus to explore alternate techniques for microwave imaging that can exploit the advantages of microwaves for breast imaging. A new active microwave

imaging system employing a continuously deformable mirror is proposed in this work as an alternative strategy. The membrane deformable mirror in the proposed system steers the incident field for multi-view illumination without the need for antenna switching and compensation. Besides imaging, the deformable mirror could also be used to deliver electromagnetic thermal therapy to treat localized breast tumors. The deformable mirror with reflective coating functions as an adaptive focusing mirror and preferentially deposit thermal energy at the tumor site inside the breast. The proposed hyperthermia technique is devoid of the complexities associated with conventional electromagnetic thermal treatments that require optimization of the amplitude and phase of multiple antenna elements for focusing.

1.2 Scope of the Thesis

This thesis aims to evaluate the feasibility of the deformable mirror microwave tomography and therapy technique using numerical models and proof of concept optical prototype. Electromagnetic wave interaction with biological objects and operational principles of adaptive mirrors essential to investigate system feasibility are explained in detail using numerical models. Systematic computational studies involving theory, system functionality and mathematical equations that govern data acquisition, imaging and therapy delivery are also explained.

The computational feasibility study also include devising and testing efficient techniques and algorithms to identify optimal mirror shapes for information rich multi-view data for tomographic reconstruction. The performance of proposed techniques are extensively evaluated using 2D breast models with varying permittivity distributions. Techniques developed for automated estimation of mirror shape for efficient delivery of thermal dose at the tumor site with minimal superficial skin heating and collateral tissue damage are evaluated using bio-heat transfer equation. The bio-heat transfer model uses the EM energy deposited within the tissue to calculate the steady

state temperature distribution inside breast phantoms. A quantitative analysis of the mirror based thermal therapy technique is evaluated using MRI data of patients with different histological and pathological history.

1.3 Organization of the Thesis

A brief introduction of breast cancer and current clinical diagnostic and treatment procedures available for symptomatic women are covered in chapter 2. In order to develop diagnostic techniques it is essential to understand the interaction of EM waves with biological tissues. Chapter 3 summarizes EM field interaction with tissues in the radio and microwave frequency spectrum. Chapter 4 briefly reviews the basics of time harmonic EM field necessary to understand EM radiation and scattering phenomenon in the deformable mirror based microwave tomography and therapy technique. Differential and integral solutions to EM wave scattering are derived in chapter 5 for TM and TE modes. A literature survey related to the evolution of microwave tomography and the underlying theory of different inverse scattering techniques are briefly covered in chapter 6. An overview of the development and role of active mirrors in adaptive optic systems and the different types of active mirrors, their design and applications are discussed in chapter 7. The design and mathematical theory that governs the mirror functionality, the key element of the thesis are also covered in chapter 7. Preliminary proof of the proposed mirror concept for breast cancer is investigated in chapter 8 via simulations neglecting diffraction and scattering.

The design and functionality of the proposed deformable mirror microwave tomography setup is presented in chapter 9 with detailed explanations on the choice of operating frequency and mirror deformations for microwave tomography. The mathematics and numerical implementation of breast permittivity reconstruction using deformable mirror setup are detailed in chapter 10 via numerical simulations on two

dimensional heterogeneous breast models. Other potential applications of the proposed mirror based tomography technique are also briefly covered in chapter 10. In addition to its use for imaging, the system can be used for therapy as well. Computational feasibility of an alternative mode of EM thermal therapy employing deformable mirrors for localized breast tumors is investigated in chapter 11. In chapter 11, bioheat transfer model is used to quantify the steady state temperature maintained by dual mirror therapy technique inside 2D breast phantoms with varying tumor size. Computational feasibility of dual mirror therapy technique is investigated in chapter 12 using high resolution MRI data of women reported to have breast malignancy. The optical prototype system discussed in chapter 13 serves as a proof of concept for the deformable mirror microwave tomography technique. Refractive index estimation of non-opaque objects using light measurements for different mirror rotations presented in chapter 13 sets the stage for potential use of deformable mirror in microwave regime for tomography. Thesis contributions, concluding remarks and future work are presented in chapter 14.

CHAPTER 2

BREAST CANCER

Introduction

Cancer is a disease caused due to malfunctioning of mutated genes that control cell growth and division. Cancer has been reported to be the second leading cause of deaths in the United States of America and it accounts for 1 in every 4 deaths [1]. Approximately 5% to 10% of cancers have been reported to be hereditary with the remaining due to mutations caused by internal factors such as hormones or external factors such as tobacco, alcohol, chemicals and sunlight [1]. The cause of cancer is not clearly understood and the uncontrolled growth of the cancerous cells leads to death. In the United States, the probability of an individual to succumb to or die from cancer is little less than 1 in 2 for men and little more than 1 in 3 for women [1]. Between 1990-2004, 18 million new cancer cases have been diagnosed and about 1,372,910 new cases were expected to be diagnosed by 2005 [1, 2].

The estimated incidence of new cancer cases and mortality due to all types of cancer in both sexes in the United States since 1997 is shown in Figure Figure 2.1 [1]-[10]. The 5-year survival rate for individuals treated for cancer reported during 1997-2005 is shown in Figure Figure 2.2. Figure Figure 2.2 indicates a steady increase in survival rate due to increased awareness and early stage screening [1]-[10]. Reports indicate that about 76% of all cancers are diagnosed only at age 55 or older. Regular health examinations will increase the survival rate by detecting most of the commonly occurring cancers at an early stage [1]. Early stage cancer is small in size, localized and is less likely to spread to the neighboring tissues and can be effectively treated. The need for early stage cancer detection with lower false alarm has led to the development of several diagnostic and treatment methods for cancer such as X-ray mammogram,

X-ray computed tomography (CT), nuclear medicine, magnetic resonance imaging and ultrasound imaging [11].

This chapter gives a brief introduction of breast cancer and covers the current clinical diagnostic and treatment procedures available for symptomatic women. The statistics compiled over the years for breast cancer is summarized in section 2.1. In section 2.2, the occurrence and types of breast cancer depending on the physical location and the tumor stage are explained with respect to the female breast anatomy. The early stage breast cancer screening guidelines advocated for asymptomatic women and limitations of the widely used X-ray mammography are discussed in section 2.3. The conventional and contemporary diagnostic procedures available to confirm the findings of breast screening are briefly covered in section 2.4. The clinical treatment options available for symptomatic women depending on the location, size and stage of the cancer and other complementary therapy techniques are covered in sections 2.5 and 2.6 respectively.

2.1 Breast Cancer - Epidemic

Amongst the different types of cancers, women in the United States and else where in the world are more prone to the breast cancer disease. In the United States, the most common cancer diseases diagnosed amongst women include the cancer of the lung and breast. The incidence of new cases of lung and breast cancer compared to the other 43 types of cancer cases reported since 1997 is summarized in Figure Figure 2.3 [1]-[10]. Figure Figure 2.4 shows the estimated number of the cancer deaths amongst the US women reported since 1997. On an average, Figures Figure 2.3-Figure 2.4 indicate that breast cancer accounts for one in every three cancer cases diagnosed and is the second leading cause of deaths amongst women in the United States next to lung cancer. Breast cancer is broadly classified into invasive and in-situ depending on the proliferation of malignant cells to the neighboring benign cells. Figure Figure

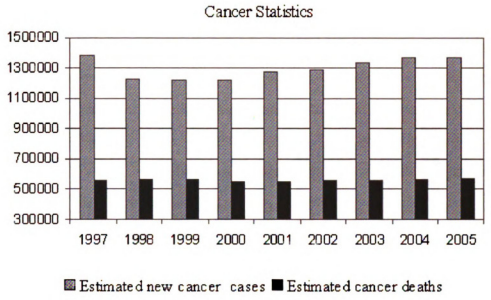

Figure 2.1. Estimated cancer statistics in the United States [1]-[10].

2.5 shows the 2005 statistics for breast cancer incidence and mortality reported by the American Cancer Society. In 2005, the number of new cases was estimated to be 211,240 for invasive and 58,490 for in-situ breast cancer with the total breast cancer mortality equal to 40,140 [10]. It is anticipated that one in every 8 women will succumb to breast cancer during their life time. The incidence and mortality rates reported for breast carcinoma is of utmost public health concern in the United States.

2.2 Breast Disease

Carcinoma or cancer of the breast is a disease caused by mutations in cell growth inside the breast tissue. A typical anatomy of a mature female breast is shown in Figure Figure 2.6. Typical female breast tissue comprises of milk producing glands also named as the lobules, ducts that carry the milk from the lobules to the nipple,

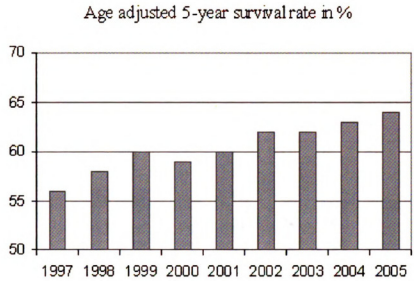

Figure 2.2. Overall five year survival rate for US individuals with cancer [1]-[10].

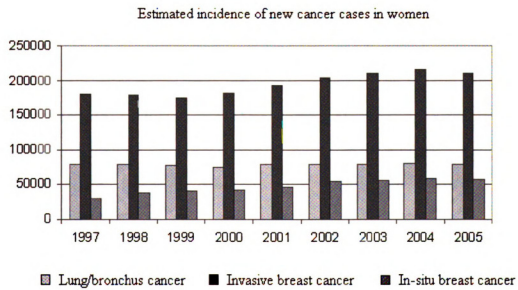

Figure 2.3. Estimated incidence of cancer cases amongst women in United States [1]-[10].

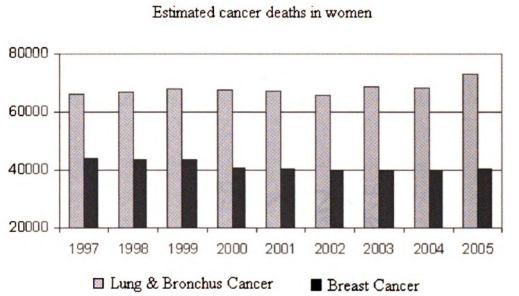

Figure 2.4. Estimated mortality caused by lung/bronchus and breast cancers amongst US women [1]-[10].

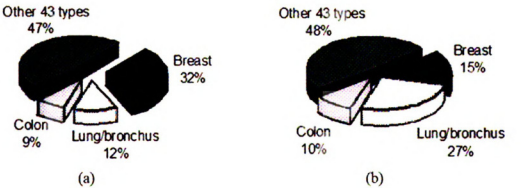

Figure 2.5. Distribution of cancer cases and deaths reported for 2005 [1].

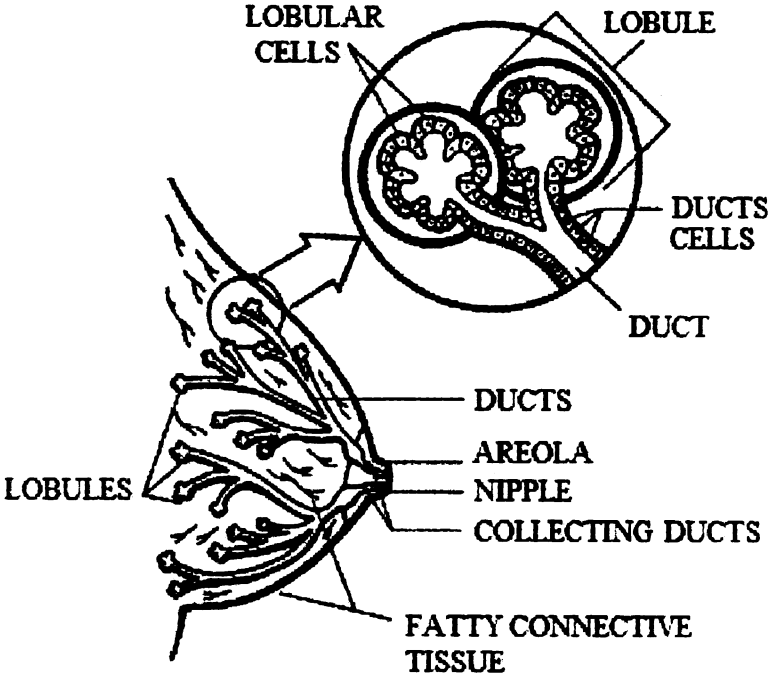

Figure 2.6. Breast Anatomy [12].

fatty connective tissue called the stroma, blood vessels and lymphatic tissues [13, 14]. The lobules are surrounded by fibrous and fatty/adipose tissue as shown in Figure Figure 2.6. The lobules composed of ductules and intra-lobular ducts is the smallest unit in the breast. The milk carrying ducts are the most common site for carcinoma. Early stage malignant cells in the breast are often small and localized and mostly occur inside the milk ducts. Early stage cancer if unattended ruptures the cell walls and begins to spread to the surrounding benign tissue. The invasive carcinogenic cells can potentially be transported to a distant site through the lymph nodes and can manifest as a meta-state cancer. The different types of breast cancer categorized depending on the location, size and growth of the lesion are discussed below.

2.2.1 Breast Cancer Types

Ductal Carcinoma In-situ (DCIS) refers to the local occurrence of cancer inside the milk duct of the breast tissue. DCIS is the most common type of non-invasive breast cancer that accounts for 25% - 30% of mammographically detected breast cancers [13]. With increased usage of X-ray mammography, the incidence of DCIS increased and it accounted for 85% of the in-situ breast cancer diagnosed from 1998-2002 [1]. The largest occurrence of DCIS was observed to be in women aged 50 and above [1, 14].

Lobular Carcinoma In-situ (LCIS) also called as lobular neoplasia is another type of early stage cancer that appears inside the milk glands and are contained inside the walls of the lobules. LCIS has been reported to occur exclusively in women older than 40 years [1, 15]. It is less likely to occur than DCIS and accounts for approximately 12% of the in-situ breast cancers in women [1].

Invasive Ductal Carcinoma (IDC) is the most common breast cancer that accounts for 80% of the invasive cancers. The malignant cells inside the duct penetrates the ductal walls to the surrounding fatty tissue and can metastasize through the lymphatic tissues and blood vessels at a distant site. Genetic similarity between

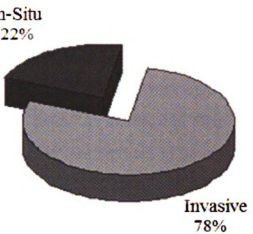

Figure 2.7. Broad distribution of breast cancer types.

the histology of DCIS and IDC in many cases indicates DCIS as a precursor to IDC [13].

Invasive Lobular Carcinoma (ILC) is infiltrating carcinoma that starts at the lobules and invades the surrounding fatty tissue and could eventually spread to a distant site via meta-stasis. Though it is infiltration of LCIS, most invasive breast malignancies that follow LCIS are often of ductal histology [15]. Thus, ILC is less common and accounts only for 5% of the invasive breast cancer. The other less common breast cancers include inflammatory, medullary, tubular and mucinous cancers, paget's disease and phyllodes tumor [13]. The different types of breast cancer discussed in this section are broadly classified as in-situ or invasive. The ratio of incidence of new cancer cases based on the lesion growth estimated for 2005 is shown in Figure Figure 2.7. Almost 80 % of the new cases diagnosed have been reported to be invasive which is an impeding factor to extend the patient survival rate.

2.3 Breast Cancer Screening

Cancer is commonly perceived as a group of malignant cells that begins to multiply and spread to the surrounding tissue thereby damaging the benign cells. The rampant growth of the malignant cells in the breast might result in meta-stasis spreading to the lungs thereby leading to death. As indicated in Figure Figure 2.7, only 20% of the breast cancer cases diagnosed are reported to be in-situ or localized. The five year survival rate for individuals with localized breast cancer is approximately equal to 98% [1]. Thus, early stage screening is key to detect and control the growth of localized tumor cells before they mature to regional or meta-stasis state. The most popular and commonly used breast screening methods include X-ray mammography, clinical breast examination (CBE) and breast self examination (BSE) [1, 13, 16]. Age dependent guidelines advocated by the American Cancer Society and health care professionals for early detection of breast cancer include:

- **Age 20-39**
    - Monthly Breast Self Examination (BSE)
    - Clinical Breast Examination (CBE) once in every three years
- **Age 40 and above**
    - Monthly BSE
    - Annual CBE
    - Annual Mammogram

2.3.1 Screening Procedures

X-ray Mammography is the well established and widely used screening tool for early stage breast cancer detection [1], [13]-[15]. In X-ray mammogram, radiographic projections of the compressed breast are obtained along different planes of view. On

an average, X-ray mammography is estimated to detect 80-90% of breast cancers in asymptomatic women with 10-15% incorrect diagnosis [1].

CBE is conducted by trained personnel for screening asymptomatic women and for diagnosing individuals with breast complaints. With the advent of X-ray mammography, the prevalence of CBE has diminished. CBE is recommended for women less than 30 years at least once in every three years as a part of the regular health examination [1]. In addition to X-ray mammography, annual CBE is recommended for women above 40 to detect smaller breast masses that could be missed by mammography.

BSE is widely promoted by hospitals and health care clinics to increase public awareness for early stage breast cancer detection. Regular practice of the BSE techniques taught by certified medical health professionals enable individuals to detect anamolies. Though subjective, BSE techniques are advantageous in that they are easy and simple to apply, non-intrusive and inexpensive.

2.3.2 Limitations - X-ray Mammography

The low-cost, well established and widely used X-ray mammography is fraught with limitations. It suffers from poor sensitivity, specificity and detects only 80-90% of breast cancer. About 5-15% of breast cancer cases are improperly diagnosed and require additional tests. Breast biopsy outcome corroborating the findings of X-ray mammogram has been reported to range between 10-50% [11, 17]. These limitations are mainly due to the poor density contrast between the benign and cancerous tissues of the breast in the X-ray regime. Figure Figure 2.8 shows X-ray attenuation coefficient in different breast tissues and the contrast between benign and malignant breast tissues over the clinical diagnostic X-ray energy range. In Figure Figure 2.8, it can be observed that the density contrast between tumor and normal tissue is higher at energy level near 15 keV and is poor above 35 keV. Even at lower energy levels, the tissue density contrast between benign and malignant tissue is less than 12% .

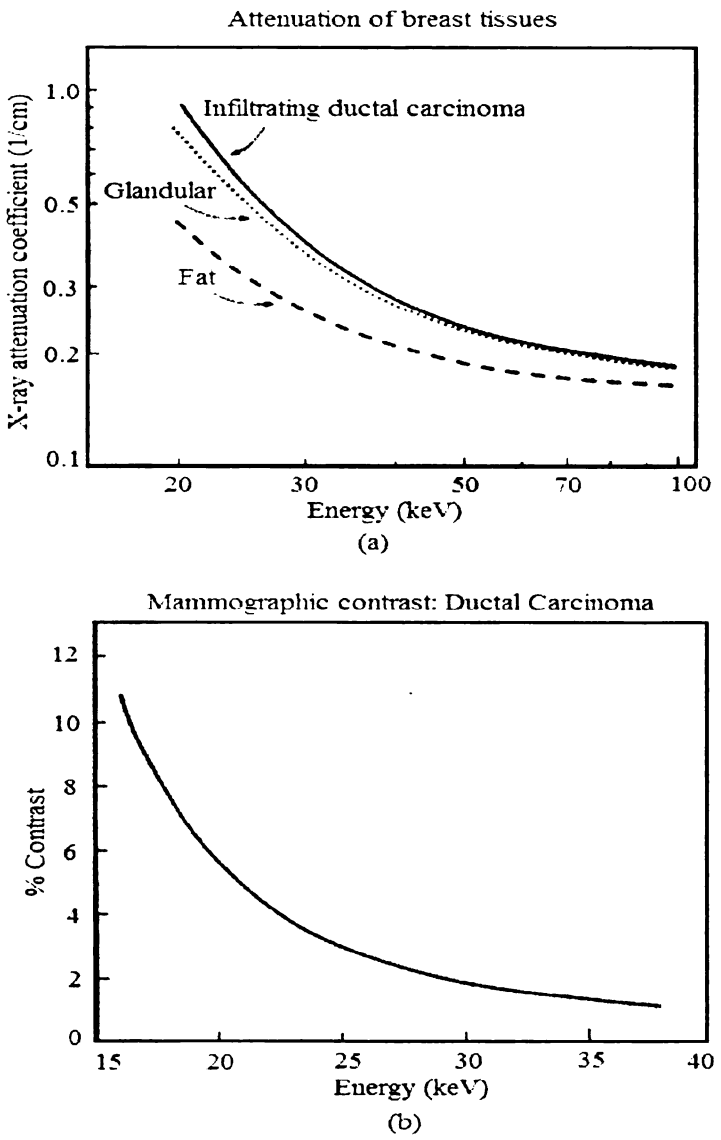

Figure 2.8. Property of breast tissue in X-ray regime (a) X-ray attenuation (b) Mammographic contrast.

Besides low contrast, the higher X-ray absorption at these energy levels require longer exposure of the breast to the ionizing X-ray radiation to obtain mammograms. In practice, the radiation dose and absorption at lower energy levels is minimized by a painful breast compression during screening.

Besides breast compression, the poor contrast in X-ray attenuation property between the fibro-glandular and cancerous tissue shown in Figure Figure 2.8 results in poor sensitivity and specificity in screening women with radiologically dense breast. Thus, X-ray mammogram has been reported to be less accurate in screening asymptomatic pre-menopausal women with dense breast tissue. The accuracy of X-ray mammogram is higher for screening post-menopausal women who tend to have more adipose tissue than fibrous tissue. X-ray mammography involves imaging of the compressed breast by illuminating the breast under ionizing radiation and high quality mammograms depend on optimal breast compression to reduce image blurring caused by scattering and higher absorption at lower energy levels. Hence, other limitations include patients tolerance to breast compression, variability in radiological interpretation and radiation dosimetry.

2.4 Breast Cancer Imaging

2.4.1 Clinical Diagnostic Procedures

The incidence and mortality rates of breast cancer necessitates the need for breast imaging techniques with high sensitivity and low false calls to diagnose asymptomatic women both pre and post menopause. Several non-invasive imaging techniques are used in practice to diagnose lesions detected by clinical findings. The imaging methods include diagnostic X-ray mammography, ultrasonography, magnetic resonance imaging, X-ray computed tomography, digital subtraction angiography, radionuclide imaging and diaphanography [11], [18]. All imaging methods exploit the physical, optical or electrical differences between the cancerous and normal breast tissues to the

penetrating energy source. The key requirement of these different imaging modalities is to provide early stage detection with high specificity, sensitivity and low negative calls for improved treatment and higher patient survival rate.

2.4.2 Complementary Diagnostic Methods

The limitations of X-ray mammography led to research in the development of complementary imaging techniques that are noninvasive and non-radioactive for breast cancer detection. Imaging methods that are currently being researched as a viable complementary clinical breast imaging techniques include optical tomography [19, 20], electrical impedance tomography [21, 22], elastography [23, 24] and microwave tomography [25].

The significant contrast in the electrical property between benign and malignant breast tissues reported in different regimes of the electromagnetic spectrum has motivated the use of electromagnetic waves as an alternative energy source for breast cancer detection [25]. Besides the high contrast ratio, microwaves are non-ionizing energy source that does not require breast compression for imaging. In the last decade there has been tremendous research in the development of microwave theory and techniques for imaging breast cancer. These noninvasive imaging techniques are yet to become certified clinical procedures for breast imaging.

2.5 Breast Cancer Treatment

Pathological staging of the disease is essential to provide systematic treatment to localized, regional and metastasized breast lesions [1], [13]-[15]. Depending on the cancer stage, age and health factors; one or a combination of the following treatments is prescribed.

- Surgery
- Radiation Therapy

- Hormone Therapy
- Chemotherapy
- Biological Therapy

Surgery is the most common treatment prescribed for localized breast lesions. The most commonly performed procedures are radical mastectomy and lumpectomy also known as the breast conservation surgery. Surgery is frequently performed with adjuvant treatment techniques such as radiation therapy, chemotherapy and hormone therapy to aid the surgical procedure.

Radiation Therapy is a non-interventional procedure that employs external high energy X-ray radiations to destroy tumor cells. The procedure lasts few minutes and is delivered on a regular basis as a primary treatment for breast cancer. It is also used as an adjuvant technique to shrink the tumor size prior surgery and to destroy remanent malignant cells bordering the lesion after surgery.

Hormone Therapy is given to individuals with breast cancer that is receptive to estrogen. It involves intake of drugs that inhibit the effects of estrogen on tumor cells. The drug inhibits production of estrogen and deprives estrogen supply to the tumor which is essential for its growth. It is often prescribed for a long period of time after breast surgery to prevent recurrence and is effective in both post and pre-menopausal patients with cancers that test positive to hormone receptors.

Chemotherapy involves drug intake administered either intravaneously or orally. A combination of drugs that slows down growth and kills cancerous cells are used to destroy tumors that have metastasized to the lymph nodes. It is the primary treatment for individuals not responsive to hormone therapy and who suffer from metastasis. It is also used as an adjuvant therapy to shrink tumor prior to surgery.

Biological Therapy also called *immunotherapy* aims to improve the capability of immune system to fight cancer with intake of drugs. The procedure is also combined

with chemo or hormone therapy to improve the effectiveness of the treatment for metastatic breast cancers.

2.6 Contemporary Treatment Procedures

Hyperthermia and RF ablation techniques are actively pursued as an alternative to the conventional treatments for breast carcinoma. The application of electromagnetic field in medicine for destruction and growth control of cancer cells dates back to 1800s [26]. Electromagnetic therapy techniques are broadly classified into hyperthermia and ablation procedures. Experimental studies indicate that hyperthermia induces transient physiological effects such as increase in blood circulation, tissue vascularization and metabolic activity that shrinks the tumor size. Hyperthermia involves prolonged exposure of the tissue to external EM radiation above 42°C combined with radiation or chemotherapy for effective treatment of the malignant cells. Ablation techniques leads to irreversible physiological effects such as vascular stasis, protein denaturation resulting in tumor cell death. In RF ablation, the temperature inside the tumor is elevated above 60°C for a few minutes for tumor tissue necrosis using invasive EM applicators.

CHAPTER 3

TISSUE PROPERTIES AT MICROWAVE FREQUENCIES

Introduction

The electromagnetic (EM) spectrum represents a wide range of frequencies ranging from DC to frequencies, such as gamma and cosmic rays. The EM spectrum includes X-rays, visible light, microwaves and radio frequencies. During the past 2 decades, bioelectromagnetics is gaining significance in human medicine. The physical and behavioral changes influenced by biological tissues in the presence of external EM fields has led to the development of several diagnostic and therapeutic techniques and systems employing RF and microwaves. In order to develop diagnostic tools it is essential to understand the interaction of EM waves with biological tissues.

The EM field interaction with tissues in the radio and microwave frequency spectrum is summarized in this chapter. Maxwell's equations that govern the behavior of EM field in materials is presented in section 3.1. The thermal and athermal effects induced in biological organs due to EM field interaction with tissue is covered in 3.2. The Penne's bio-heat transfer model that governs the tissue heating inside biological systems exposed to near field EM energy is presented in section 3.3. The electrical properties of various biological tissues and the parametric equations developed based on experimental findings are discussed in section 3.4. Section 3.5, presents the experimental results and analytical model for the dielectric property of benign and malignant breast tissues analyzed by several investigators.

3.1 Maxwell's Equations

Biological systems undergo physiological changes when exposed to radiofrequency and microwaves. The interaction of electromagnetic fields with biological tissues

has been investigated by several investigators in the past [26]. The study of EM wave interaction with tissues has enabled harnessing of diagnostic and therapeutic potentials of EM waves in medicine and has led to the development of standards for safe operation of EM devices. The EM field interaction with biological systems is given by the Maxwell's equations [27, 28],

$$\begin{aligned} \nabla \times \vec{E} &= -\frac{\partial \vec{B}}{\partial t} - \vec{J_m} \\ \nabla \times \vec{H} &= \frac{\partial \vec{D}}{\partial t} + \vec{J} \\ \nabla \cdot \vec{D} &= \rho \\ \nabla \cdot \vec{B} &= -\rho_m \end{aligned} \tag{3.1}$$

along with the continuity equations,

$$\begin{aligned} \nabla \cdot \vec{J} &= -\frac{\partial \rho_e}{\partial t} \\ \nabla \cdot \vec{J_m} &= -\frac{\partial \rho_m}{\partial t} \end{aligned} \tag{3.2}$$

where

$\vec{E}$ and $\vec{H}$: electric and magnetic fields measured in (V/m) and (A/m)

$\vec{D}$ and $\vec{B}$: electric and magnetic flux densities measured in (C/m ^{2}) and Tesla

$\vec{J}$ and $\vec{J_m}$: electric and magnetic current densities in (A/m ^{3})

$\vec{\rho_e}$ and $\vec{\rho_m}$: electric and magnetic charge densities (C/m ^{3})

Several numerical models using (3.1)-(3.2) and experiments on animal subjects and freshly excised tissue specimens were investigated in the past to understand the physiological effects induced by RF and microwave radiations in human and animal subjects.

3.2 EM Field Interaction with Tissues

Investigations indicate that electrical properties of biological tissues are dispersive in nature and vary between tissues. Variations in tissue electrical properties are often characterized in terms of the percentage of water content. Tissues with high water content exhibit higher constitutive parameters than those with lower water content [29, 30]. Variations in tissue property inside biological systems result in a nonuniform internal EM energy deposition when exposed to EM fields [31]-[33].

Investigations by Foster et. al. revealed the thermal and athermal effects, tissue dielectric property, depth of penetration and power deposition inside biological tissues exposed to RF and microwaves [29, 30]. The thermal and athermal effects induced by EM waves result in various biological effects. It is known that the depth of penetration of microwaves inside tissue decreases with increase in frequency. Besides frequency of operation, signal attenuation in biological tissue also depends on tissue water content. The attenuation of EM fields is relatively higher inside tissues with higher water content. Attenuation of microwaves over the frequency range 1.8-2.7 GHz inside human torso indicated the feasibility of employing microwave radiations for diagnostic medical applications [34]. These studies clearly indicate the potential use of EM waves in human medicine.

3.3 Tissue Thermal Properties

Irradiation of living tissues with microwaves or RF waves primarily results in tissue heating. With modernization, human exposure to near field radiations from EM devices and their potential hazards to living organisms gained importance to determine the safe operation of the devices [33], [36]-[38]. EM energy deposition in biological tissues is influenced by several factors such as tissue thermal conduction, thermal convection due to blood flow and surface cooling of the tissue [35]. Tissue heating inside biological systems exposed to EM field was studied using the Pennes's heat

transfer equation [31], [35],

$$\rho_p c_p \frac{\partial T(x,y,t)}{\partial t} = \kappa \nabla^2 T(x,y,t) + \omega_b c_b (T_b - T(x,y,t)) + Q(x,y,t) \tag{3.3}$$

In (3.3),

$T(x,y,t)$: temperature distribution in $^\circ$ C

ρ_p, ρ_b : tissue and blood density in (kg/cm ^{3})

c_p, c_b : specific heat of tissue and blood in (J/kg/ $^\circ$ C)

T_b : arterial blood temperature in $^\circ$ C

ω_b : volumetric blood perfusion rate (kg/s/ cm ^{3})

κ : tissue thermal conductivity in (W/cm/ $^\circ$ C)

$Q(x,y,t)$: EM energy deposition in (W/cm ^{3})

Temperature distribution inside tissues exposed to EM waves studied using (3.3) with mathematical human models and experimental results helped determine the power levels for safe device operation [39].

3.4 Tissue Dielectric Properties

A comprehensive literature survey on the electrical properties of different tissues reported by several investigators over five decades is compiled in [40]. The electrical properties of biological tissues over the frequency range 10 Hz-20 GHz in [41] consolidates the EM field interaction with various biological tissues. Parametric equations based on experimental measurements led to the development of a parametric Cole-Cole dispersion model of the form [28],

$$\epsilon(\omega) = \epsilon_\infty + \sum_n \frac{\Delta\epsilon_n}{1 + (j\omega\tau_n)^{(1-\alpha_n)}} + \frac{\sigma_i}{j\omega\epsilon_0} \tag{3.4}$$

for a variety of biological tissues [42]. In (3.4), τ is the time constant, α is the dispersion distribution parameter, σ_i is the static ionic conductivity, $\Delta\epsilon n = \epsilon_{\infty,n} - \epsilon_{s,n}$ where $\epsilon_{\infty,n}$ is the tissue permittivity at higher frequency and $\epsilon_{s,n}$ is the static tissue permittivity for $\omega \rightarrow 0$, $\epsilon(\omega) = \epsilon' - j\epsilon''$ where ϵ' is the dielectric constant and $\epsilon'' = \frac{\sigma}{\omega\epsilon_0}$ and ω is the angular frequency. Experimental data on different biological tissues confirm the dispersion regions in the tissue dielectric spectrum studied by the previous researchers [29, 30], [41]. Experimental and parametric model studies on the dielectric properties of pathological tissues indicate the potential of nonionizing microwave radiation in medical diagnosis and therapy. The beneficial biological effects induced by RF and microwaves has led to the development of several EM devices for cancer diagnosis and therapy [43, 44].

3.5 Dielectric Properties of Breast Tissue

Limited research work is available on the dielectric properties of human breast in the RF and microwave frequency spectrum. In 1984, Chaudhary et al reported the average dielectric property of ex-vivo human breast tissues from 15 patients between 3MHz to 3 GHz frequency range [45]. The dielectric property of malignant tissues was reported to be significantly larger than benign tissues indicating the potential use of microwaves for cancer detection and local hyperthermia. The dielectric properties of cancerous and surrounding tissues of human breast reported over 20 kHz-100 MHz also indicated a pronounced dielectric contrast between the benign and malignant tissues [46]. Dielectric property measurements of freshly excised breast tissue over 50-900 MHz reported by Joines et al support the ex-vivo experimental findings of other investigators [47]. Figure Figure 3.1 shows the dielectric spectrum of benign and malignant breast tissues available in literature over a wide frequency range. Despite the variations in tissue samples and experimental techniques, a significant difference exists between the dielectric property of cancerous and normal breast tissues

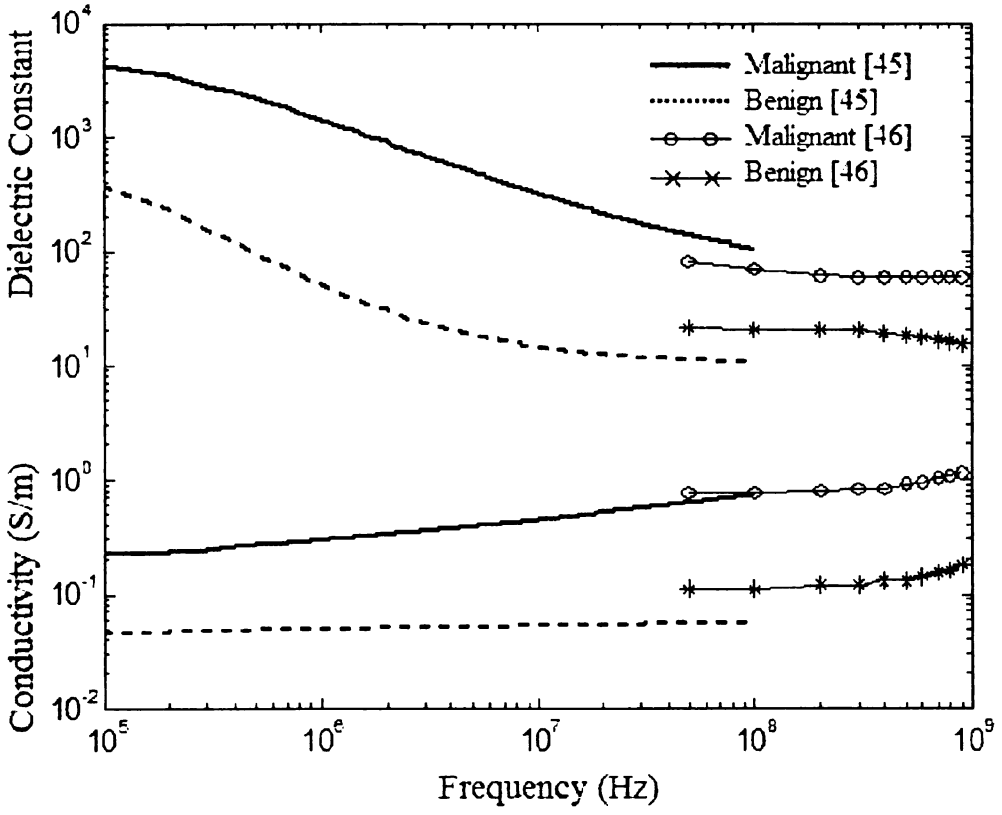

Figure 3.1. Dielectric spectrum of benign and malignant human breast tissue [46]-[47].

at microwave frequencies. The significant contrast between the dielectric spectrum of malignant and benign breast tissue in the RF and microwave frequency has instigated the development of several electromagnetic imaging and therapy techniques for breast cancer.

CHAPTER 4

TIME HARMONIC ELECTROMAGNETIC FIELDS

Introduction

Electromagnetics (EM) is a fundamental science essential to understand the basic concepts in physics and electrical engineering. EM theory deals with static, quasi static and moving charges that causes current flow and maintains electromagnetic fields. Unlike circuit theory, object dimensions are comparable to the operating wavelength in electromagnetic field theory and systems are analyzed using distributed parameters and coupling phenomenon. Electromagnetic field scattering, propagation, radiation, reception and generation are characterized with the aid of the Maxwell's equations and fundamental theorems.

This chapter briefly reviews the basics of time harmonic EM field necessary to understand EM radiation and scattering used in the proposed deformable mirror based microwave tomography for breast cancer. Maxwell's equations, fundamental for the EM phenomenon and the constitutive relations that characterize the EM field behavior inside different materials are briefly covered in sections 4.1 and 4.2 respectively. In section 4.3, the boundary conditions for the EM fields that takes into account the presence of dissimilar materials and discontinuities are explained. The power and energy carried by the time harmonic EM field are derived in section 4.4. The fundamental theorems useful to understand the radiation and scattering phenomenon for tomography are discussed in section 4.5. In section 4.6, vector wave equations are derived for the time harmonic EM field. The solution to wave equations in terms of the fictitious vector and scalar potentials for electric and magnetic sources are derived in 4.7.

4.1 Maxwell's Equations

Time harmonic electromagnetic fields are the most commonly used single frequency EM waves with cosine or sinusoidal time variations given by $e^{j\omega t}$ factor. The instantaneous EM fields for the time harmonic case are given by the relation,

$$\vec{\mathcal{E}}(x,y,z;t) = \Re\{\mathbf{E}(x,y,z)e^{j\omega t}\} \tag{4.1a}$$

$$\vec{\mathcal{H}}(x,y,z;t) = \Re\{\mathbf{H}(x,y,z)e^{j\omega t}\} \tag{4.1b}$$

$$\vec{\mathcal{D}}(x,y,z;t) = \Re\{\mathbf{D}(x,y,z)e^{j\omega t}\} \tag{4.1c}$$

$$\vec{\mathcal{B}}(x,y,z;t) = \Re\{\mathbf{B}(x,y,z)e^{j\omega t}\} \tag{4.1d}$$

$$\vec{\mathcal{J}}(x,y,z;t) = \Re\{\mathbf{J}(x,y,z)e^{j\omega t}\} \tag{4.1e}$$

$$\mathcal{Q}(x,y,z;t) = \Re\{q(x,y,z)e^{j\omega t}\} \tag{4.1f}$$

where $\vec{\mathcal{E}},\vec{\mathcal{H}},\vec{\mathcal{D}},\vec{\mathcal{B}},\vec{\mathcal{J}}$ and $\mathcal{Q}$ are the instantaneous quantities of the complex time harmonic fields $\mathbf{E}(x,y,z),\mathbf{H}(x,y,z),\mathbf{D}(x,y,z),\mathbf{B}(x,y,z),\mathbf{J}(x,y,z)$ and $q(x,y,z)$ respectively. Time variations, $\frac{\partial}{\partial t}$ in the field equations (3.1) for time harmonic case are simplified using time domain differentiation property of Fourier transform [48] to the form [27, 28, 49],

$$\nabla \times \mathbf{E} = -j\omega\mathbf{B} - \mathbf{M} \tag{4.2a}$$

$$\nabla \times \mathbf{H} = j\omega\mathbf{D} + \mathbf{J} \tag{4.2b}$$

$$\nabla \cdot \mathbf{D} = \rho \tag{4.2c}$$

$$\nabla \cdot \mathbf{B} = \rho_m \tag{4.2d}$$

where the virtual magnetic current $\mathbf{M}$ and charge ρ_m densities are introduced for mathematical ease. The continuity equations are given by,

$$\nabla \cdot \mathbf{M} = -j\omega\rho \tag{4.3a}$$

$$\nabla \cdot \mathbf{J} = -j\omega\rho_m \tag{4.3b}$$

where the EM field quantities in (1-3) are

$\mathbf{E}$ and $\mathbf{H}$: electric and magnetic fields measured in (V/m) and (A/m)

$\mathbf{D}$ and $\mathbf{B}$: electric and magnetic flux densities measured in (C/m ^{2}) and $(Tesla)$

$\mathbf{J}$ and $\mathbf{M}$: electric and magnetic current densities in (A/m ^{3})

ρ and ρ_m : electric and magnetic charge densities (C/m ^{3})

4.2 Constitutive Parameters

In the presence of electromagnetic fields, the stable state of the particles inside a material is altered. Alterations in the microscopic lattice structure of material determines the behavior of macroscopic EM fields supported inside the material. The relation between EM field quantities inside the material is captured by the constitutive parameters. The constitutive relations that characterize the electrical property of a material are

$$\mathbf{D} = \epsilon_0\mathbf{E} + \epsilon_0\chi_e\mathbf{E} \tag{4.4a}$$

$$\mathbf{B} = \mu_0\mathbf{H} + \mu_0\chi_m\mathbf{H} \tag{4.4b}$$

$$\mathbf{J} = \sigma\mathbf{E} \tag{4.4c}$$

where

ϵ_0 and μ_0 : free space permittivity (H/m) and permeability (F/m)

$\chi_e = (\epsilon_r - 1)$ and $\chi_m = (\mu_r - 1)$: dimensionless electric and magnetic susceptibilities

ϵ_r and μ_r : dimensionless material relative permittivity and permeability

σ : material electrical conductivity (Siemens/m).

The constitutive parameters are used to broadly classify materials into dielectric, magnetic, conductor or semi-conductor. They are also used to classify the materials as linear or nonlinear, homogeneous or inhomogeneous, isotropic or anisotropic and dispersive or nondispersive.

4.3 Boundary Conditions

Dissimilar material interfaces and sources along boundaries result in discontinuous field behavior. At such boundaries, the derivatives of field vectors in (3.1) are meaningless and cannot be used to define the field behavior. Instead, the field behavior is given by the boundary conditions that examine the field vectors themselves at discontinuous boundaries.

Consider an interface between two media with constitutive parameters $\epsilon_1, \mu_1, \sigma_1$ and $\epsilon_2, \mu_2, \sigma_2$ respectively as illustrated in Figure Figure 4.1. Let $\hat{n}$ be the normal vector at the material interface pointing into Media 2. The boundary conditions for time harmonic EM fields for different material interfaces are listed in Table Table 4.1. In Table Table 4.1, the quantities $\mathbf{J}_s, \mathbf{M}_s$ are the electric and magnetic surface current densities and ρ_s, ρ_{ms} are the electric and magnetic surface charge densities at the material discontinuity. The field quantities with subscripts "1" and "2" in Table Table 4.1 belong to Media 1 and 2 respectively.

4.4 Power and Energy

Power and energy associated with time harmonic electromagnetic fields are given by the energy conservation equation. Dot product of $\mathbf{H}^*$ with Faraday's law and $\mathbf{E}$ with

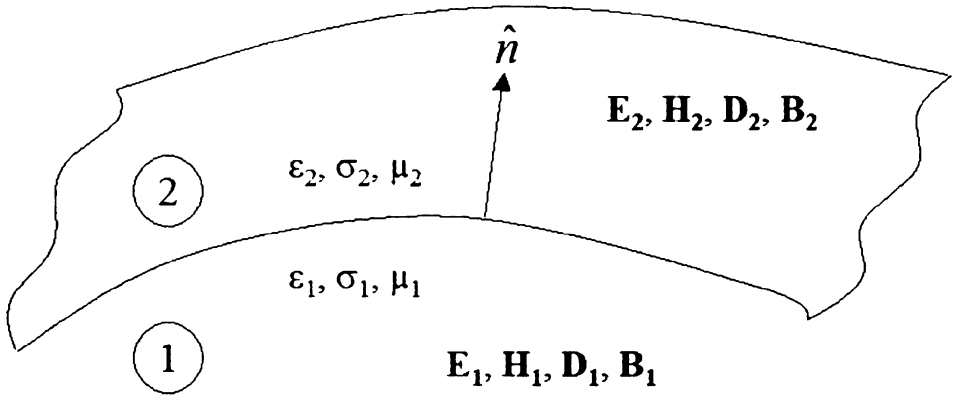

Figure 4.1. Geometry for boundary conditions at material interface.

Table 4.1. Boundary conditions [27]

Tangential electric field intensity	$\hat{n} \times (\mathbf{E}_2 - \mathbf{E}_1) = -\mathbf{M}_s$
Tangential magnetic field intensity	$\hat{n} \times (\mathbf{H}_2 - \mathbf{H}_1) = \mathbf{J}_s$
Normal electric flux density	$\hat{n} \cdot (\mathbf{D}_2 - \mathbf{D}_1) = \rho_s$
Normal magnetic flux density	$\hat{n} \cdot (\mathbf{B}_2 - \mathbf{B}_1) = \rho_{ms}$

conjugate of Ampere's law yield

$$\mathbf{H}^* \cdot (\nabla \times \mathbf{E}) = -\mathbf{H}^* \cdot \mathbf{M}_i - j\omega\mu\mathbf{H} \cdot \mathbf{H}^* \tag{4.5a}$$

$$\mathbf{E} \cdot (\nabla \times \mathbf{H}^*) = \mathbf{E} \cdot \mathbf{J}_i^* + \sigma\mathbf{E} \cdot \mathbf{E}^* - j\omega\epsilon\mathbf{E} \cdot \mathbf{E}^* \tag{4.5b}$$

Subtracting (4.5a) from (4.5b) and invoking vector identities yields the energy conservation equation,

$$-\nabla \cdot \left(\frac{1}{2}\mathbf{E} \times \mathbf{H}^*\right) = \frac{1}{2}\mathbf{H}^* \cdot \mathbf{M}_i + \frac{1}{2}\mathbf{E} \cdot \mathbf{J}_i^* + \frac{1}{2}\sigma|\mathbf{E}|^2 + 2j\omega\left(\frac{1}{4}\mu|\mathbf{H}|^2 - \frac{1}{4}\epsilon|\mathbf{E}|^2\right) \tag{4.6}$$

Integrating (4.5a) over a volume and applying divergence theorem yields the integral form of the energy conservation equation,

$$-\frac{1}{2}\iiint_V \left(\mathbf{E}\cdot\mathbf{J}_i^* + \mathbf{H}^*\cdot\mathbf{M}_i\right)dv = \iint_S \frac{1}{2}\left(\mathbf{E}\times\mathbf{H}^*\right)\cdot d\mathbf{s} + \frac{1}{2}\iiint_V \sigma|\mathbf{E}|^2 dv + 2j\omega\iiint_V \left(\frac{1}{4}\mu|\mathbf{H}|^2 - \frac{1}{4}\epsilon|\mathbf{E}|^2\right)dv \quad (4.7)$$

which is rewritten as

$$P_s = P_e + P_d + 2j\omega\left(\bar{W}_m + \bar{W}_e\right) \quad (4.8)$$

where

$P_s = -\frac{1}{2}\iiint_V \left(\mathbf{E}\cdot\mathbf{J}_i^* + \mathbf{H}^*\cdot\mathbf{M}_i\right)dv$ is complex input power (W)

$P_e = \iint_S \frac{1}{2}\left(\mathbf{E}\times\mathbf{H}^*\right)\cdot d\mathbf{s}$ is the exiting complex power (W)

$P_d = \frac{1}{2}\iiint_V \sigma|\mathbf{E}|^2 dv$ is the dissipated real power (W)

$\bar{W}_m = \iiint_V \frac{1}{4}\mu|\mathbf{H}|^2 dv$ is the time average magnetic energy (J)

$\bar{W}_e = \iiint_V \frac{1}{4}\epsilon|\mathbf{E}|^2 dv$ is the time average electric energy (J)

4.5 Fundamental Theorems

Fundamental theorems in electromagnetic theory are essential to understand different electromagnetic phenomena such as radiation, scattering, coupling, electromagnetic generation, wave propagation and reception. A subset of the fundamental theorems namely *duality*, *uniqueness*, *reciprocity*, *volume equivalence* and *surface equivalence* theorems are discussed in this section [27, 28, 49].

4.5.1 Duality

Duality theorem facilitate solutions to two system of equations with two different variables but with same mathematical form. The solution for one system of equation can

Table 4.2. Dual equations for electric and magnetic currents [27]

Electric sources ($\mathbf{J} \neq 0, \mathbf{M} = 0$)	Magnetic sources ($\mathbf{J} = 0, \mathbf{M} \neq 0$)
$\nabla \times \mathbf{E}_A = -j\omega\mu\mathbf{H}_A$	$\nabla \times \mathbf{H}_F = j\omega\epsilon\mathbf{E}_F$
$\nabla \times \mathbf{H}_A = \mathbf{J} + j\omega\epsilon\mathbf{E}_A$	$-\nabla \times \mathbf{E}_F = \mathbf{M} + j\omega\mu\mathbf{H}_F$

Table 4.3. Dual quantities for electric and magnetic currents [27]

Electric sources ($\mathbf{J} \neq 0, \mathbf{M} = 0$)	Magnetic sources ($\mathbf{J} = 0, \mathbf{M} \neq 0$)
$\mathbf{E}_A$	$\mathbf{H}_F$
$\mathbf{H}_A$	$-\mathbf{E}_F$
$\mathbf{J}$	$\mathbf{M}$
ϵ	μ
μ	ϵ

be used to obtain the solution for the other system of equations by appropriate interchange of the dual quantities. This is often used to obtain the solution to Maxwell's equations in the presence of electric ($\mathbf{J} \neq 0, \mathbf{M} = 0, \mathbf{E}_A, \mathbf{H}_A$) and magnetic current ($\mathbf{J} = 0, \mathbf{M} \neq 0, \mathbf{E}_F, \mathbf{H}_F$) sources. The dual equations and quantities for the electric and magnetic current sources are listed in Tables Table 4.2 - Table 4.3. In Tables Table 4.2 - Table 4.3, ($\mathbf{E}_A, \mathbf{H}_A$) and ($\mathbf{E}_F, \mathbf{H}_F$) are the dual field vectors maintained by electric and magnetic sources respectively.

4.5.2 Uniqueness

The uniqueness theorem yields conditions that guarantee uniqueness of the solution that satisfies Maxwell's equations. Consider V to be a lossy isotropic volume enclosed by a bounding surface S with constitutive parameters $\epsilon = \epsilon' - j\epsilon''$ and $\mu = \mu' - j\mu''$. Let ($\mathbf{E}_1, \mathbf{H}_1$) and ($\mathbf{E}_2, \mathbf{H}_2$) be two sets of solution inside V in the presence of sources,

$\mathbf{J}_i$ and $\mathbf{M}_i$. The two sets of fields satisfy the Maxwell's equations,

$$\nabla \times \mathbf{E}_1 = -\mathbf{M}_i - j\omega\mu\mathbf{H}_1 \qquad \nabla \times \mathbf{H}_1 = \mathbf{J}_i + j\omega\epsilon\mathbf{E}_1 \tag{4.9a}$$

$$\nabla \times \mathbf{E}_2 = -\mathbf{M}_i - j\omega\mu\mathbf{H}_2 \qquad \nabla \times \mathbf{H}_2 = \mathbf{J}_i + j\omega\epsilon\mathbf{E}_2 \tag{4.9b}$$

Subtracting (4.9a) from (4.9b) yields

$$\nabla \times \delta\mathbf{E} = -j\omega\mu\delta\mathbf{H} \qquad \nabla \times \delta\mathbf{H} = j\omega\epsilon\delta\mathbf{E} \tag{4.10}$$

where $\delta\mathbf{E} = \mathbf{E}_1 - \mathbf{E}_2$ and $\delta\mathbf{H} = \mathbf{H}_1 - \mathbf{H}_2$. The difference fields satisfy the Maxwell's source free equations. For uniqueness, the difference fields should be equal to 0 which, implies $\mathbf{E}_1 = \mathbf{E}_2$ and $\mathbf{H}_1 = \mathbf{H}_2$. The energy conservation equation for the time harmonic difference fields can be written as,

$$\iint_S \left(\delta\mathbf{E} \times \delta\mathbf{H}^*\right) \cdot d\mathbf{s}' + \iiint_V \left(\mathbf{E}.\mathbf{J}_t^* + \mathbf{H}^*.\mathbf{M}\right) dv' = 0 \tag{4.11}$$

where $J_t = (\sigma + j\omega\epsilon)\delta\mathbf{E}$. If the following is true

$$\iint_S \left(\delta\mathbf{E} \times \delta\mathbf{H}^*\right) \cdot d\mathbf{s}' = 0 \tag{4.12}$$

then, the volume integral in (4.11) equals to zero. Substituting for J_t, ϵ, μ the real and imaginary parts of the integral reduces to

$$\iiint_V \left[\left(\sigma + \omega\epsilon''\right)|\delta\mathbf{E}|^2 + \omega\mu''|\delta\mathbf{H}|^2\right] dv' = 0 \tag{4.13a}$$

$$\iiint_V \left[-\omega\epsilon'|\delta\mathbf{E}|^2 + \omega\mu'|\delta\mathbf{H}|^2\right] dv' = 0 \tag{4.13b}$$

For lossy isotropic media, the parameters $\left(\sigma + \omega\epsilon''\right)$ and $\omega\mu''$ in (4.13a) are positive which, implies that $|\delta\mathbf{E}|^2$ and $|\delta\mathbf{H}|^2$ are equal to zero or $\delta\mathbf{E} = \delta\mathbf{H} = 0$. This proof of

uniqueness is based on the assumption that (4.12) is valid in S. Equation (4.12) can be rewritten using vector identity as

$$\begin{aligned} \iint_S (\delta\mathbf{E} \times \delta\mathbf{H}^*) \cdot \hat{n} ds' &= \iint_S \delta\mathbf{H}^* . (\hat{n} \times \delta\mathbf{E}) \, ds' \\ &= \iint_S \delta\mathbf{E} . (\delta\mathbf{H}^* \times \hat{n}) \, ds' \end{aligned} \tag{4.14}$$

The conditions for uniqueness $\mathbf{E}_1 = \mathbf{E}_2$ and $\mathbf{H}_1 = \mathbf{H}_2$ require either $(\hat{n} \times \delta\mathbf{E}) = 0$ or $(\hat{n} \times \delta\mathbf{E}) = 0$ over S i.e., the tangential components of $\mathbf{E}_1$ and $\mathbf{E}_2$ and/or the tangential components of $\mathbf{H}_1$ and $\mathbf{H}_2$ are identical over S and are equal to some specified values. The condition for uniqueness of the fields maintained by sources $\mathbf{J}_i$ and $\mathbf{M}_i$ inside a lossy isotropic medium includes one of the following:

1. Tangential component of the electric field over the bounding surface S
2. Tangential component of the magnetic field over the bounding surface S
3. Tangential component of the electric field over a part and tangential component of magnetic field over the rest of the bounding surface S

4.5.3 Reciprocity

Reciprocity theorem is the most commonly used theorem to understand the transmission and reception properties of antennas. Consider a linear isotropic medium with two sets of sources $\mathbf{J}_1, \mathbf{M}_1$ and $\mathbf{J}_2, \mathbf{M}_2$ maintaining fields $\mathbf{E}_1, \mathbf{H}_1$ and $\mathbf{E}_2, \mathbf{H}_2$ respectively at the same frequency. The fields maintained by the sources satisfy the Maxwell's equations,

$$\begin{aligned} \nabla \times \mathbf{E}_1 &= -\mathbf{M}_1 - j\omega\mu\mathbf{H}_1 \\ \nabla \times \mathbf{H}_1 &= \mathbf{J}_1 + j\omega\epsilon\mathbf{E}_1 \end{aligned} \tag{4.15a}$$

$$\begin{aligned} \nabla \times \mathbf{E}_2 &= -\mathbf{M}_2 - j\omega\mu\mathbf{H}_2 \\ \nabla \times \mathbf{H}_2 &= \mathbf{J}_2 + j\omega\epsilon\mathbf{E}_2 \end{aligned} \tag{4.15b}$$

Taking dot products between $\mathbf{H}_2$ and (4.15a), $\mathbf{E}_1$ and (4.15b) and subtracting the dot products yields,

$$\mathbf{E}_1 \cdot (\nabla \times \mathbf{H}_2) - \mathbf{H}_2 \cdot (\nabla \times \mathbf{E}_1) = \mathbf{E}_1 \cdot \mathbf{J}_2 + \mathbf{H}_2 \cdot \mathbf{M}_1 + j\omega\epsilon\mathbf{E}_1 \cdot \mathbf{E}_2 + j\omega\mu\mathbf{H}_1 \cdot \mathbf{H}_2 \tag{4.16}$$

Using the vector identity,

$$\nabla \cdot (\mathbf{A} \times \mathbf{B}) = \mathbf{B}.(\nabla \times \mathbf{A}) - \mathbf{A}.(\nabla \times \mathbf{B}) \tag{4.17}$$

equation (4.16) can be rewritten as

$$-\nabla \cdot (\mathbf{E}_1 \times \mathbf{H}_2) = \mathbf{E}_1 \cdot \mathbf{J}_2 + \mathbf{H}_2 \cdot \mathbf{M}_1 + j\omega\epsilon\mathbf{E}_1 \cdot \mathbf{E}_2 + j\omega\mu\mathbf{H}_1 \cdot \mathbf{H}_2 \tag{4.18}$$

Similarly, the difference of the dot products between $\mathbf{E}_2$ and (4.15a) and $\mathbf{H}_1$ and (4.15b) yields

$$-\nabla \cdot (\mathbf{E}_2 \times \mathbf{H}_1) = \mathbf{E}_2 \cdot \mathbf{J}_1 + \mathbf{H}_1 \cdot \mathbf{M}_2 + j\omega\epsilon\mathbf{E}_2 \cdot \mathbf{E}_1 + j\omega\mu\mathbf{H}_2 \cdot \mathbf{H}_1 \tag{4.19}$$

Subtracting (4.19) from (4.18) yields the *Lorentz Reciprocity* theorem,

$$-\nabla \cdot (\mathbf{E}_1 \times \mathbf{H}_2 - \mathbf{E}_2 \times \mathbf{H}_1) = \mathbf{E}_1 \cdot \mathbf{J}_2 + \mathbf{H}_2 \cdot \mathbf{M}_1 - \mathbf{E}_2 \cdot \mathbf{J}_1 - \mathbf{H}_1 \cdot \mathbf{M}_2 \tag{4.20}$$

Using the divergence theorem, the integral form of (4.20) is written as

$$-\iint_S (\mathbf{E}_1 \times \mathbf{H}_2 - \mathbf{E}_2 \times \mathbf{H}_1).d\mathbf{s}' = \mathbf{E}_1 \cdot \mathbf{J}_2 + \mathbf{H}_2 \cdot \mathbf{M}_1 - \mathbf{E}_2 \cdot \mathbf{J}_1 - \mathbf{H}_1 \cdot \mathbf{M}_2 \tag{4.21}$$

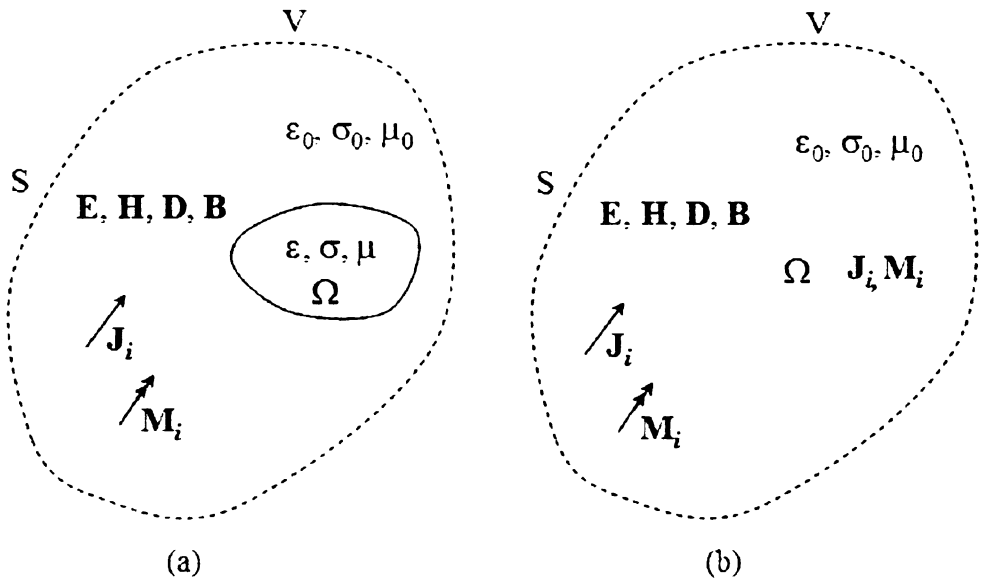

Figure 4.2. Illustration of volume equivalence theorem [27] (a) Actual (b) Equivalent model.

4.5.4 Volume Equivalence Theorem

Volume equivalence theorem facilitates the solution for the field scattered by a dielectric obstacle or scatterer. Let $\mathbf{E}_0, \mathbf{H}_0$ be the fields maintained by the sources $\mathbf{J}_i, \mathbf{M}_i$ as illustrated in Figure Figure 4.2(a). The sources and fields satisfy Maxwell's equations

$$\nabla \times \mathbf{E}_0 = -\mathbf{M}_i - j\omega\mu_0\mathbf{H}_0 \tag{4.22a}$$

$$\nabla \times \mathbf{H}_0 = \mathbf{J}_i + j\omega\epsilon_0\mathbf{E}_0 \tag{4.22b}$$

The fields $\mathbf{E}, \mathbf{H}$ maintained by the same sources inside a medium with constitutive parameters ϵ, μ satisfy Maxwell's equations

$$\nabla \times \mathbf{E} = -\mathbf{M}_i - j\omega\mu\mathbf{H} \tag{4.23a}$$

$$\nabla \times \mathbf{H} = \mathbf{J}_i + j\omega\epsilon\mathbf{E} \tag{4.23b}$$

Subtracting (4.22a) from (4.23a) and (4.22b) from (4.23b) leads to

$$\nabla \times \mathbf{E}^s = -j\omega(\mu\mathbf{H} - \mu_0\mathbf{H}_0) \tag{4.24a}$$

$$\nabla \times \mathbf{H}^s = j\omega(\epsilon\mathbf{E} - \epsilon_0\mathbf{E}_0) \tag{4.24b}$$

where $\mathbf{E}^s = \mathbf{E} - \mathbf{E}_0, \mathbf{H}^s = \mathbf{H} - \mathbf{H}_0$ are the scattered fields. Adding and subtracting $\mu_0\mathbf{H}$ to (4.24a) and $\epsilon_0\mathbf{E}$ to (4.24b) gives

$$\begin{aligned} \nabla \times \mathbf{E}^s &= -j\omega(\mu - \mu_0)\mathbf{H} - j\omega\mu_0\mathbf{H}^s) \\ &= -\mathbf{M}_{eq} - j\omega\mu_0\mathbf{H}^s \end{aligned} \tag{4.25a}$$

$$\begin{aligned} \nabla \times \mathbf{H}^s &= j\omega(\epsilon - \epsilon_0)\mathbf{E} + j\omega\epsilon_0\mathbf{E}^s) \\ &= j\omega\mathbf{J}_{eq} + j\omega\epsilon_0\mathbf{E}^s \end{aligned} \tag{4.25b}$$

The equivalent volume electric and magnetic current densities in (4.25a)-(4.25b) are given by the expression,

$$\mathbf{J}_{eq} = j\omega(\epsilon - \epsilon_0)\mathbf{E} \tag{4.26a}$$

$$\mathbf{M}_{eq} = j\omega(\mu - \mu_0)\mathbf{H} \tag{4.26b}$$

In (4.25a)-(4.25b), the equivalent volume electric and magnetic current densities $\mathbf{J}_{eq} = j\omega(\epsilon - \epsilon_0)\mathbf{E}$ and $\mathbf{M}_{eq} = j\omega(\mu - \mu_0)\mathbf{H}$ within S yield the same scattered fields $\mathbf{E}, \mathbf{H}$ outside S. The computational model for the equivalent problem is shown in Figure Figure 4.2(b).

4.5.5 Surface Equivalence Theorem

Fields scattered by conducting surfaces and radiated by sources are often determined using surface equivalence theorem. The theorem provides a means to replace the conducting body or actual sources with imaginary sources over a bounding surface

that maintain exactly the same field as the perfectly conducting obstacles and actual sources.

Consider the radiation problem in Figure Figure 4.3(a). The fields $\mathbf{E}_1, \mathbf{H}_1$ maintained by the current densities $\mathbf{J}, \mathbf{M}$ in V_1 can be obtained by solving the equivalent problem in Figure Figure 4.3(b). The equivalent surface currents $\mathbf{J}_s, \mathbf{M}_s$ in Figure Figure 4.3(b) replaces the actual radiating sources $\mathbf{J}, \mathbf{M}$ and establish fields $\mathbf{E}_1, \mathbf{H}_1$ outside S and $\mathbf{E}, \mathbf{H}$ inside S. The fictitious sources results in the boundary conditions

$$\mathbf{J}_s = \hat{n} \times (\mathbf{H}_1 - \mathbf{H})|_S \tag{4.27a}$$

$$\mathbf{M}_s = -\hat{n} \times (\mathbf{E}_1 - \mathbf{E})|_S \tag{4.27b}$$

The fields $\mathbf{E}, \mathbf{H}$ inside a virtual bounding surface S are not of interest for radiating sources and perfectly conducting bodies and can be set to zero. This reduces the equivalent current densities to the form

$$\mathbf{J}_s = \hat{n} \times \mathbf{H}_1|_S \tag{4.28a}$$

$$\mathbf{M}_s = -\hat{n} \times \mathbf{E}_1|_S \tag{4.28b}$$

Figure Figure 4.3(c) shows the equivalent problem for the actual scattering problem in Figure Figure 4.3(a).

4.6 Wave Equations

In electromagnetic theory, the electric and magnetic fields are solutions to the coupled first order partial differential Maxwell's equations. Instead of solving the coupled partial differential equations for the unknown electromagnetic fields, the de-coupled second order partial differential wave equations are often solved. Assuming a homo-

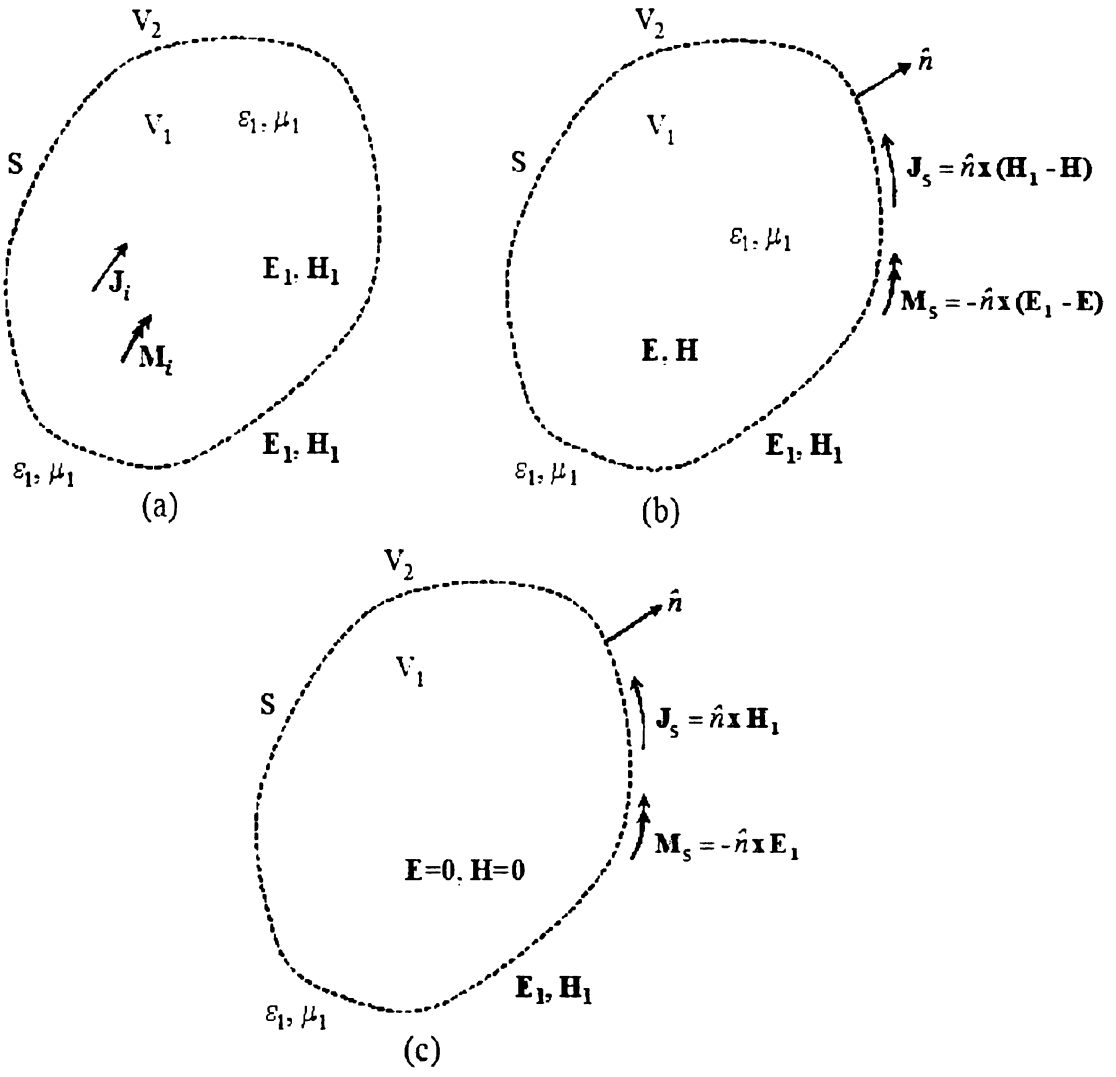

Figure 4.3. Illustration of surface equivalence theorem [27] (a) Actual (b) Equivalent model (c) Love's equivalent model.

geneous isotropic medium, the curl of Faraday's law can be written as

$$\nabla \times \nabla \times \mathbf{E} = -\nabla \times \mathbf{M}_i - j\omega\mu\nabla \times \mathbf{H} \tag{4.29}$$

Substituting Ampere's law for $\nabla \times \mathbf{H}$ and using vector identity leads to

$$\nabla\nabla \cdot \mathbf{E} - \nabla^2\mathbf{E} = -\nabla \times \mathbf{M}_i - j\omega\mu\nabla \times (\mathbf{J}_i + \mathbf{J}_c) + \omega^2\mu\epsilon\mathbf{E} \tag{4.30}$$

where $\mathbf{J}_c = \sigma\mathbf{E}$. Substituting $\nabla \cdot \mathbf{E}$ with Gauss's law and rearranging (4.30) leads to the electric field wave equation

$$\nabla^2\mathbf{E} + \omega^2\mu\epsilon\mathbf{E} = \nabla \times \mathbf{M}_i + j\omega\mu\nabla \times \mathbf{J}_i + \mathbf{J}_c) + \frac{1}{\epsilon}\nabla\rho \tag{4.31}$$

Following a similar procedure for the Ampere law yields the magnetic field vector wave equation

$$\nabla^2\mathbf{H} + \omega^2\mu\epsilon\mathbf{H} = -\nabla \times \mathbf{J}_i + j\omega\epsilon\mathbf{M}_i + \sigma\mathbf{M}_i + \frac{1}{\mu}\nabla\rho_m \tag{4.32}$$

4.7 Vector Potentials

Often in electromagnetics, boundary value problems are solved with the aid of the fictitious electric and magnetic vector potentials to facilitate solutions to the electromagnetic fields $(\mathbf{E}, \mathbf{H})$. The vector potentials are nonphysical quantities introduced for mathematical convenience. These imaginary quantities simplify the solution to electric and magnetic fields that satisfy the Maxwell's equations.

4.7.1 Magnetic Vector Potential (A)

Inside a source free region, the Gauss'law for magnetic field is divergence free which, implies that the magnetic flux density can be written as

$$\begin{aligned} \nabla \cdot \mathbf{B}_A &= 0 \\ &= \nabla \cdot (\nabla \times \mathbf{A}) \qquad [\nabla \cdot (\nabla \times \mathbf{A}) = 0] \end{aligned} \tag{4.33}$$

$$\therefore \qquad \mathbf{B}_A = \nabla \times \mathbf{A}, \qquad \mathbf{H}_A = \frac{1}{\mu} \nabla \times \mathbf{A} \tag{4.34}$$

where $\mathbf{A}$ is the auxiliary magnetic vector potential used to characterize the flux density $\mathbf{B}_A$. Substituting $\mathbf{H}_A$ with the vector potential $\mathbf{A}$ in Faraday's law leads to

$$\begin{aligned} \nabla \times \mathbf{E}_A &= -j\omega \nabla \times \mathbf{A} \\ \Rightarrow \nabla \times [\mathbf{E}_A + j\omega \mathbf{A}] &= 0 \end{aligned} \tag{4.35}$$

Invoking the vector identity, $\nabla \times (-\nabla \phi_e) = 0$ yields the final form for the electric field intensity as

$$\mathbf{E}_A + j\omega \mathbf{A} = -\nabla \phi_e \tag{4.36}$$

for an arbitrary ϕ_e referred as the scalar electric potential function. Taking curl of (4.34) and using vector identity gives

$$\mu \nabla \times \mathbf{H}_A = \nabla \nabla \cdot \mathbf{A} - \nabla^2 \mathbf{A} \tag{4.37}$$

Using Ampere's law for homogeneous medium and substituting $\mathbf{E}_A$ by (4.36) reduces (4.37) to,

$$\nabla^2 \mathbf{A} + \omega^2 \mu \epsilon \mathbf{A} = -\mu \mathbf{J} + \nabla \left(\nabla \cdot \mathbf{A} + j\omega \mu \epsilon \phi_e \right) \tag{4.38}$$

Both curl and divergence equations are required to uniquely define the vector potential $\mathbf{A}$. One choice that simplifies (4.38) is the *Lorentz condition*,

$$\nabla \cdot \mathbf{A} = -j\omega\mu\epsilon\phi_e \tag{4.39}$$

The gauge condition in (4.39) yields the wave equation,

$$\nabla^2\mathbf{A} + \omega^2\mu\epsilon\mathbf{A} = -\mu\mathbf{J} \tag{4.40}$$

for the vector potential and the expression,

$$\begin{aligned} \mathbf{E}_A &= -j\omega\mathbf{A} - \nabla\phi_e \\ &= -j\omega\mathbf{A} - \frac{j}{\omega\mu\epsilon}\nabla(\nabla \cdot \mathbf{A}) \end{aligned} \tag{4.41}$$

for the electric field. Taking divergence of (4.41) and using (4.39) yields the wave equation for the electric scalar potential,

$$\begin{aligned} \nabla \cdot \mathbf{E}_A &= -\omega^2\mu\epsilon\phi_e - \nabla^2\phi_e \\ \Rightarrow \quad \nabla^2\phi_e + \omega^2\mu\epsilon\phi_e &= -\frac{\rho}{\epsilon} \quad [\because \quad \epsilon\nabla \cdot \mathbf{E} = \rho] \end{aligned} \tag{4.42}$$

4.7.2 Electric Vector Potential (F)

The fictitious electric vector potential $\mathbf{F}$ is obtained along the same lines using the dual equations and quantities for the electric field. The auxiliary vector $\mathbf{F}$ is defined starting with the electric Gauss's law for source-free medium, $\nabla \cdot \mathbf{D}_F = 0$ to yield the equations for the electric and magnetic fields,

$$\mathbf{E}_F = -\frac{1}{\epsilon}\nabla \times \mathbf{F} \tag{4.43a}$$

$$\mathbf{H}_F = -j\omega\epsilon\mathbf{F} - \nabla\phi_m \tag{4.43b}$$

where ϕ_m is the arbitrary magnetic scalar potential. Substituting (4.43a) in Ampere's law and using vector identities gives

$$\nabla^2\mathbf{F} + \omega^2\mu\epsilon\mathbf{F} = -\epsilon\mathbf{M} + \nabla\left(\nabla\cdot\mathbf{F} + j\omega\mu\epsilon\right) \tag{4.44}$$

For uniqueness of $\mathbf{F}$, $\nabla\cdot\mathbf{F}$ is defined as

$$\nabla\cdot\mathbf{F} = -j\omega\mu\epsilon\phi_m \tag{4.45}$$

Substituting the *Lorentz condition* in (4.45) into (4.44) yields the vector wave equation,

$$\nabla^2\mathbf{F} + \omega^2\mu\epsilon\mathbf{F} = -\epsilon\mathbf{M} \tag{4.46}$$

and the magnetic field

$$\mathbf{H}_F = -j\omega\epsilon\mathbf{F} - \frac{j}{\omega\mu\epsilon}\nabla(\nabla\cdot\mathbf{F}) \tag{4.47}$$

Taking divergence of (4.43bb) and substituting (4.45) and $\mu\nabla\cdot\mathbf{H}_F = \rho_m$ gives the wave equation for the magnetic scalar potential

$$\nabla^2\phi_m + \omega^2\mu\epsilon\phi_m = -\frac{\rho_m}{\mu} \tag{4.48}$$

The total field due to the electric and magnetic vector potentials are expressed as a superposition of the electromagnetic fields $(\mathbf{E}_A, \mathbf{H}_A)$ and $(\mathbf{E}_F, \mathbf{H}_F)$. The total fields take the form

$$\begin{aligned}\mathbf{E} &= \mathbf{E}_A + \mathbf{E}_F \\ &= -j\omega\mathbf{A} - \frac{j}{\omega\mu\epsilon}\nabla(\nabla\cdot\mathbf{A}) - \frac{1}{\epsilon}\nabla\times\mathbf{F}\end{aligned} \tag{4.49}$$

$$\begin{aligned}\mathbf{H} &= \mathbf{H}_A + \mathbf{H}_F \\ &= \frac{1}{\mu}\nabla \times \mathbf{A} - j\omega\epsilon\mathbf{F} - \frac{j}{\omega\mu\epsilon}\nabla(\nabla \cdot \mathbf{F}) \end{aligned} \tag{4.50}$$

4.7.3 Solutions to Inhomogeneous Potential Wave Equations

The wave equation satisfied by the scalar Greens function in a homogeneous medium with ϵ and μ given by

$$\left(\nabla^2 + \omega^2\mu\epsilon\right) g(\mathbf{r}, \omega; \mathbf{r}') = -\delta(\mathbf{r}; \mathbf{r}') \tag{4.51}$$

facilitates the solution to the magnetic and vector potentials in (4.38) and (4.44) respectively. The source terms in (4.40), (4.42), (4.46) and (4.48) can be expressed as a convolution integral of the source with the Dirac delta function in (4.51). This representation results in the integral equation solution of the potentials

$$\mathbf{A}(\mathbf{r}) = \mu \iiint_V \mathbf{J}(\mathbf{r}')g(\mathbf{r}, \beta; \mathbf{r}')dv' \tag{4.52}$$

$$\mathbf{F}(\mathbf{r}) = \epsilon \iiint_V \mathbf{M}(\mathbf{r}')g(\mathbf{r}, \beta; \mathbf{r}')dv' \tag{4.53}$$

$$\phi_e(\mathbf{r}) = \frac{1}{\epsilon} \iiint_V \rho(\mathbf{r}')g(\mathbf{r}, \beta; \mathbf{r}')dv' \tag{4.54}$$

$$\phi_m(\mathbf{r}) = \frac{1}{\mu} \iiint_V \rho_m(\mathbf{r}')g(\mathbf{r}, \beta; \mathbf{r}')dv' \tag{4.55}$$

where the 3D scalar Greens function is given by the expression,

$$g(\mathbf{r}, \beta; \mathbf{r}') = \frac{e^{-j\beta r}}{4\pi r} \tag{4.56}$$

with $beta = \omega\sqrt{\mu\epsilon}$ being the wave number in the homogeneous medium and $r = |\mathbf{r} - \mathbf{r}'|$. The integral equation solution to the vector potentials in (4.52)-(4.55) is the

widely used form to study wave propagation in scattering and radiation problems. For two dimensional problems, the scalar Greens function takes the form,

$$g(x, y, \beta; x', y') = \frac{j}{4} H_0^{(2)}(\beta\rho) \tag{4.57}$$

where $\rho = \sqrt{(x - x')^2 + (y - y')^2}$ and $H_0^{(2)}$ is the zeroth order Hankel function of the second kind.

CHAPTER 5

TIME HARMONIC ELECTROMAGNETIC WAVE SCATTERING

Introduction

The solution to EM wave scattering is derived in this chapter in terms of the two commonly used modes namely TM and TE. The EM field quantities for the TE and TM modes are derived in section 5.1 using the vector potentials. The differential and integral forms of the solution to TM^z scattering from two-dimensional arbitrarily shaped perfectly conducting and penetrable dielectric scatterers are derived in sections 5.2 and 5.3 respectively. The EM field maintained by two-dimensional dielectric and perfectly conducting obstacles for TM^z polarization is derived in section 5.4 using fictitious vector potentials.

5.1 Electromagnetic Modes

In electromagnetics, most often more than one field configuration or mode exists to the boundary value problem. The field configurations that are solutions to the electromagnetic boundary value problem satisfy Maxwell's equations. The widely known modes are Transverse Electromagnetic (TEM), Transverse Electric (TE) and Transverse Magnetic (TM). Amongst the three commonly used modes, TEM is the simplest and lowest order mode. The remaining two field configurations namely, TE and TM are constructed using the vector potentials described in section 4.7.

5.1.1 Transverse Electric Wave

TE modes are higher order field configurations that are frequently used to solve boundary value problems in EM scattering theory. Here, all non-zero electric field components lie in a plane transverse to the direction of wave propagation. For example in TE^z mode, the wave propagates in z-direction with ($E_z = 0$) and the remaining

electric (E_x, E_y) and magnetic (H_x, H_y, H_z) field components may or may not exist depending on the electrical property and boundary conditions in the medium of interest.

TE^z Fields

Let z be the direction of wave propagation for the TE mode. Then from (4.49) and (4.50), the solution to TE^z field configuration can be obtained using the electric vector potential, **F**. Let,

$$\mathbf{F} = \hat{z}F_z(\mathbf{r}) \tag{5.1a}$$

$$\mathbf{A} = 0 \tag{5.1b}$$

For TE^z mode inside a source free region (**M**=0), equation (4.46) for **F** reduces to the scalar form

$$\nabla^2 F_z(x,y,z) + \beta^2 F_z(x,y,z) = 0 \tag{5.2}$$

Substituting the solution of (5.2) in (4.49)-(4.50) yields the TE^z fields,

$$\begin{aligned} E_z(x,y,z) &= 0 & H_z(x,y,z) &= \frac{-j}{\omega\mu\epsilon}\left(\frac{\partial^2}{\partial z^2} + \beta^2\right)F_z \\ E_x(x,y,z) &= \frac{-1}{\epsilon}\frac{\partial F_z}{\partial y} & H_x &= \frac{-j}{\omega\mu\epsilon}\frac{\partial^2 F_z}{\partial x \partial z} \\ E_y(x,y,z) &= \frac{1}{\epsilon}\frac{\partial F_z}{\partial x} & H_y &= \frac{-j}{\omega\mu\epsilon}\frac{\partial^2 F_z}{\partial y \partial z} \end{aligned} \tag{5.3}$$

In a similar manner, TE field configurations for waves propagating along x or y direction can be obtained using the respective components of the vector potential **F**.

5.1.2 Transverse Magnetic Wave

Similar to TE modes, TM modes are also higher order field configurations that are frequently used to solve boundary value problems. In TM modes, the magnetic field components lie in a plane transverse to a given direction. The direction transverse to the plane containing the magnetic field components is often chosen to be the

propagation path of the EM field. Thus, for TM to z mode (TM^z), the z-component of the magnetic field is zero (H_z=0). Depending on the boundary value problem, the remaining magnetic field components (H_x, H_y) and all electric field components (E_x, E_y, E_z) may or may not exist.

TM^z Fields

Let z be the direction of wave propagation for TM field configuration. Then from (4.49) and (4.50), the solution to TM^z field configuration can be obtained using the electric vector potential, **A**. Let,

$$\mathbf{A} = \hat{z} A_z(\mathbf{r}) \tag{5.4a}$$

$$\mathbf{F} = 0 \tag{5.4b}$$

For TM^z mode inside a source free region (**J**=0), (4.40) satisfied by the vector potential **A** reduces to the scalar wave equation

$$\nabla^2 A_z(x,y,z) + \beta^2 A_z(x,y,z) = 0 \tag{5.5}$$

where $\beta = \omega\sqrt{\mu\epsilon}$ is the wavenumber in the source free region. The TM^z fields can be obtained by substituting the solution to (5.5) in (4.49)-(4.50) for the source free case. The resulting TM^z fields are given by

$$\begin{aligned} E_z(x,y,z) &= \frac{-j}{\omega\mu\epsilon}\left(\frac{\partial^2}{\partial z^2} + \beta^2\right) A_z & H_z &= 0 \\ E_x(x,y,z) &= \frac{-j}{\omega\mu\epsilon}\frac{\partial^2 A_z}{\partial x \partial z} & H_x &= \frac{1}{\mu}\frac{\partial A_z}{\partial y} \\ E_y(x,y,z) &= \frac{-j}{\omega\mu\epsilon}\frac{\partial^2 A_z}{\partial y \partial z} & H_y &= -\frac{1}{\mu}\frac{\partial A_z}{\partial x} \end{aligned} \tag{5.6}$$

Similarly, EM fields for TM wave propagating along x or y direction can be derived using A_x and A_y components of the electric vector potential **A**.

Scattering from perfectly conducting and penetrable obstacles are dealt in this

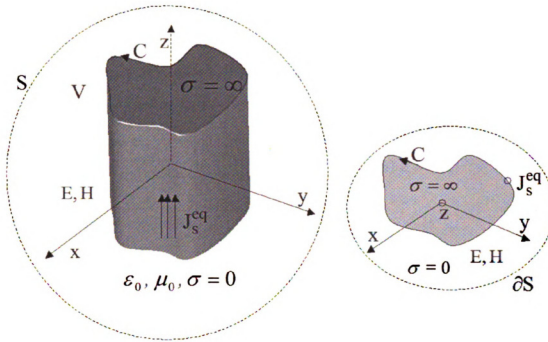

Figure 5.1. TM^z scattering from a two dimensional perfectly conducting cylinder (a) 3D (b) 2D computational Model.

chapter. Solution to the scattered field can be obtained in several ways. In this section, differential and integral solutions of the TM^z scattering problems are derived for the two dimensional case.

5.2 TM^z Scattering from Conducting Cylinders

Consider an arbitrary shaped perfectly conducting cylinder with its principal axis parallel to the z axis. Let the cylinder be invariant along the z-axis as shown in Figure Figure 5.1. The conducting cylinder positioned in a linear homogeneous isotropic medium irradiated by a TM^z polarized time harmonic electromagnetic field supports z-directed current density on the conductor surface.

5.2.1 Differential Equation Solution - PEC Cylinder

From (5.4), (5.6) for the two-dimensional case, $E_z \neq 0, H_z = 0, \frac{\partial}{\partial z} = 0$ holds good. For TM^z case, the field maintained by the conducting cylinder in the presence $\mathbf{E}^{inc}$ satisfies the scalar wave equation,

$$\nabla^2 E_z(x,y) + \beta^2 E_z(x,y) = 0 \qquad (x,y) \in S \tag{5.7}$$

with the boundary conditions,

$$E_z(x,y) = 0, \quad (x,y) \in C \tag{5.8a}$$

$$\alpha \frac{\partial E_z(x,y)}{\partial n} + \gamma E_z(x,y) = q, \quad (x,y) \in S \tag{5.8b}$$

Equation (5.8a), implies that the tangential component of the electric field is zero on the conducting cylinder. Equation (5.8b) is the radiation or absorbing boundary condition that emulates free space. In (5.8b), the quantities α, γ and q are given by

$$\alpha = \frac{1}{\mu_r} \tag{5.9a}$$

$$\gamma = j\beta + \frac{\kappa(s)}{2} \tag{5.9b}$$

$$q = \alpha \left[\frac{\partial}{\partial n} + j\beta + \frac{\kappa(s)}{2} \right] E_z^{inc} \tag{5.9c}$$

where E_z^{inc} is the TM^z polarized incident time harmonic field, $\kappa(s)$ is the curvature of the of arbitrarily shaped conducting cylinder and n is the outward normal vector along ∂S.

The solution to the boundary value problem in (5.7)-(5.8b) yields the total field $E_z(x,y)$ maintained by an infinitely long arbitrarily shaped perfectly conducting cylinder for TM^z polarization. Solution to time harmonic boundary value problem can be obtained using the finite element method [50, 51]. The differential equation

solution to (5.7)-(5.8a) yields the total field inside the computational domain, S that also includes the observation point, (x_f, y_f).

5.2.2 Electric Field Integral Equation - PEC Cylinder

The integral equation solution to scattering from perfectly conducting cylinder is obtained using the electric vector potential $\mathbf{A}$. For two-dimensional TM^z case $\left(\frac{\partial}{\partial z} = 0\right)$, the vector wave equation (4.40) reduces to the form

$$\nabla^2 A_z(x,y) + \beta^2 A_z(x,y) = -\mu J_s^{eq}(x,y), \qquad (x,y) \in C \tag{5.10}$$

where $J_s^{eq}(x,y) = \hat{n} \times \mathbf{H}$ is the current density induced by the TM^z incident field on the conducting cylinder. From the surface equivalence theorem (4.28a), $J_s^{eq}(x,y)$ is the equivalent surface current source that maintains the same fields in media 1 as the perfectly conducting cylinder. From (4.52) and (5.6) the scattered field maintained by the conducting cylinder is given by the electric field integral equation,

$$\begin{aligned} E_z^{sc}(x,y) &= -j\omega\mu \iint_C J_s^{eq}(x',y') g_{2D}(x,y,\beta;x',y') dx'dy' \\ &= -\frac{\omega\mu}{4} \iint_C J_s^{eq}(x',y') H_0^{(2)}(x,y,\beta;x',y') dx'dy' \end{aligned} \tag{5.11}$$

The expression for the 2D scalar Greens function in (4.57) is substituted into (5.11). The boundary condition in (5.8a) implies

$$\begin{aligned} E_z^{sc}(x,y) + E_z^{in}(x,y) &= 0, \qquad (x,y) \in C \\ \Rightarrow E_z^{sc}(x,y) &= -E_z^{in}, \quad (x,y) \in C \end{aligned} \tag{5.12}$$

From (5.12) and (5.11), the unknown current density $J_s^{eq}(x,y)$ is obtained by solving the boundary integral equation

$$\frac{\omega\mu}{4}\iint\limits_C J_s^{eq}(x',y')H_0^{(2)}(x,y,\beta;x',y')dx'dy' = E_z^{in}(x,y), \qquad (x,y)\in C \qquad (5.13)$$

In electromagnetics, solution to integral equations are facilitated by the method of moments [51, 52]. Substituting the solution to (5.13) in (5.11) yields the TM^z field maintained by the perfectly conducting cylinder. In integral formulation, scattering from a perfectly conducting cylinder can be treated as radiation by an equivalent surface current, J_s^{eq} maintained by the conducting object. Unlike differential formulation, integral equation often solves the unknown current density on the conducting surface which, can be used to determine the field anywhere in medium 1 shown in Figure Figure 5.1.

5.3 TM^z Scattering from Dielectric Cylinder

Unlike the impenetrable perfectly conducting objects, dielectric scatterers are penetrable obstacles. The integral and differential solutions for TM^z scattering from penetrable objects is considered in this section. Consider a two dimensional, arbitrarily shaped dielectric object with the principal axis parallel to the z-axis. Let the dielectric scatterer be present in a source free, linear, isotropic and homogeneous medium with constitutive parameters ϵ and μ. Figure Figure 5.2 illustrates the linear, inhomogeneous and isotropic dielectric cylinder characterized by (ϵ_d,μ) irradiated by a time harmonic TM^z wave $\mathbf{E}_z^{inc}$.

5.3.1 Differential Equation Solution - Dielectric Cylinder

Similar to scattering from conducting cylinder, TM^z scattering from two dimensional dielectric object is obtained by solving the boundary value problem for the

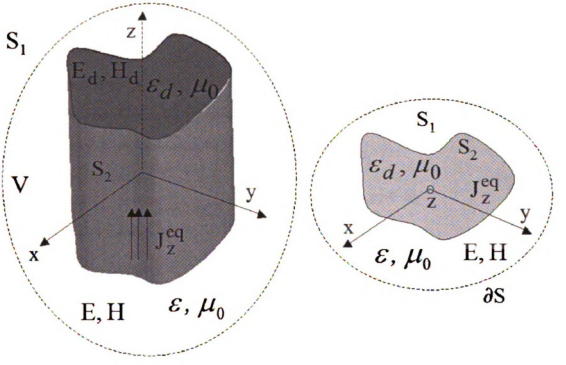

Figure 5.2. TM^z scattering from a two dimensional dielectric cylinder (a) 3D (b) 2D computational Model.

z-component of the total field,

$$\nabla^2 E_z(x,y) + \beta^2 E_z(x,y) = 0, \quad (x,y) \in S \tag{5.14}$$

with boundary condition,

$$\alpha \frac{\partial E_z(x,y)}{\partial n} + \gamma E_z(x,y) = q, \quad (x,y) \in \partial S \tag{5.15}$$

The boundary condition (5.15) emulates radiation boundary condition in the infinite space with constitutive parameters (ϵ, μ_0). In (5.14),

$$\begin{aligned} S &= S_1 \cup S_2 \\ \beta &= \begin{cases} \omega\sqrt{\mu_0\epsilon}, & \forall (x,y) \in S_1 \\ \omega\sqrt{\mu_0\epsilon_d(x,y)}, & \forall (x,y) \in S_2 \end{cases} \\ E_z(x,y) &= E_z^{in}(x,y) + E_z^{sc}(x,y) \end{aligned}$$

Solution to the boundary value problem, (5.14)-(5.14) yields the total field maintained by the inhomogeneous penetrable dielectric cylinder. The remaining electric components and all magnetic components for the 2D TM^z field configuration can be obtained using (5.6) under the condition $\left(\frac{\partial}{\partial z} = 0\right)$.

5.3.2 Electric Field Integral Equation - Dielectric Cylinder

The electric field integral equation for the scattered field maintained by the dielectric cylinder shown in Figure Figure 5.2 for the TM^z mode is derived using the volume equivalence principle discussed in section (3.5.4). From (4.26a), the volume equivalent current density for TM^z mode takes the form

$$J_z^{eq} = j\omega\epsilon_0 \left(\epsilon_d - \epsilon\right) E_{dz}(x,y)$$

$$= j\omega\epsilon_0\epsilon\left(\frac{\epsilon_d}{\epsilon}-1\right)E_{dz}(x,y) \tag{5.16a}$$

where $E_{dz}(x,y)$ is the z-component of the total field inside the dielectric scatterer. For 2D object, the vector potential in (4.52) reduces to

$$A_z(x,y) = \mu \iint_{S_2} J_z^{eq}(x',y')\frac{1}{4j}H_0^{(2)}(\beta\rho)dx'dy' \tag{5.17}$$

where $\rho = \sqrt{(x-x')^2+(y-y')^2}$. Equations (5.16) and (4.41) yield the electric field component,

$$\begin{aligned} E_{dz}(x,y) &= \frac{J_z^{eq}(x,y)}{j\omega\epsilon_0(\epsilon_d(x,y)-\epsilon)} \\ &= E_z^{in}+E_z^{sc} \\ &= E_z^{in}-j\omega A_z, \quad (x,y)\in S_2 \end{aligned} \tag{5.18a}$$

Substituting (5.17) in (5.16) yields the electric field integral equation

$$E_z^{in} = \frac{J_z^{eq}(x,y)}{j\omega\epsilon_0(\epsilon_d(x,y)-\epsilon)} + j\omega\mu \iint_{S_2} J_z^{eq}(x',y')\frac{1}{4j}H_0^{(2)}(\beta\rho)dx'dy', \quad (x,y)\in S_2 \tag{5.19}$$

for the unknown volume current density inside the dielectric scatterer.

The unknown volume current density, J_z^{eq} in (5.19) can be solved using the moment method [51, 52]. From the knowledge of volume current density, total field anywhere inside S_1 can be computed using (5.18). Substituting (5.19) in (5.6) yields the remaining 2D TM^z field components maintained by the dielectric cylinder.

5.4 TM^z Scattering from Dielectric and Conducting Cylinders

Let a time harmonic TM^z field be present in a linear, homogeneous, isotropic medium with arbitrary shaped two dimensional dielectric and perfectly conducting cylinders

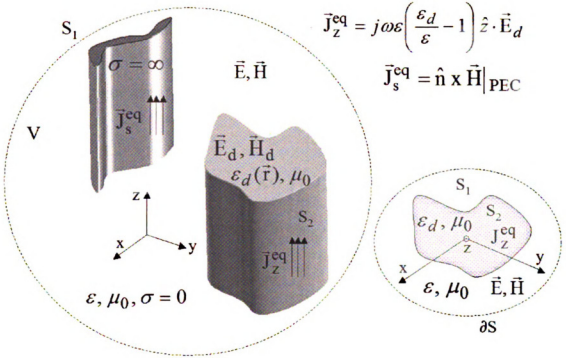

Figure 5.3. TM^z scattering from a two dimensional dielectric and perfectly conducting cylinders.

as illustrated in Figure Figure 5.3. The total field maintained by the penetrable and impenetrable scatterers can be obtained invoking the linear superposition theorem [27, 28].

5.4.1 Differential Equation Solution

In the presence of dielectric and perfectly conducting cylindrical scatterers, the total field in S_1 is obtained by solving the scalar wave equation (5.14) with the boundary conditions (5.15) and (5.8a). The unknown total field $E_z(x, y)$ maintained by the dielectric and conducting cylinders for 2D TM^z case is obtained using linear superposition of the contributions from both scatterers. The remaining TM^z field components are obtained from (5.6).

5.4.2 Integral Equation Solution

Similar to the differential form, the integral equation solution for the unknown electric field $E_z(x,y)$ is obtained by a linear superposition of the surface and volume equivalent current densities. The $E_z(x,y)$ field is obtained by solving the integral equation,

$$\frac{J_z^{eq}(x,y)}{j\omega\epsilon_0(\epsilon_d(x,y)-\epsilon)} + j\omega\mu \iint_{S_2} J_z^{eq}(x',y')\frac{1}{4j}H_0^{(2)}(\beta\rho)dx'dy'$$
$$+\frac{\omega\mu}{4}\int_C J_s^{eq}(x',y')H_0^{(2)}(x,y,\beta;x',y')dx'dy' = E_z^{in}(x,y), \quad (x,y)\in S_2 \qquad (5.20)$$

with the boundary condition,

$$\hat{n}\times\mathbf{E} = 0, \quad (x,y)\in\partial S_2 \qquad (5.21)$$

for the unknown equivalent current densities. As explained before, the remaining TM^z field components are obtained from (5.6).

CHAPTER 6

MICROWAVE TOMOGRAPHY

Introduction

Several microwave breast imaging modalities have been proposed for noninvasive characterization of the breast for cancer detection. The microwave breast imaging methods can be broadly classified into passive, hybrid and active methods. In passive microwave imaging method, microwave radiometers surrounding the breast measure the temperature distribution inside the breast [53, 54]. Microwave radiometry has long been explored as an adjuvant for X-ray mammogram due to lack of radiation risk. The passive method exploits the fact that the temperature of malignant tissues is relatively higher than that of the benign breast tissue [16]. The hybrid microwave imaging methods employs both acoustic and microwaves for breast health assessment [55]. In the hybrid methods, the EM source illuminating the breast deposits more energy inside the tumor due to the higher conductivity of the malignant cells than the benign cells. The deposited energy heats the tumor tissue resulting in tumor tissue expansion. The pressure waves generated by the cancerous tissue are recorded by ultrasound transducers to obtain an acoustic image of the breast. The active microwave imaging methods belong to the class of an inverse scattering problem in which, the microwave illuminates the breast and the scattered field measured at different locations surrounding the breast is used to detect and locate the presence of the tumor [102]. The electromagnetic basics necessary to understand the inverse scattering problem are briefly covered in this chapter.

The Maxwell's equations, fundamental theorems and scattering theory for the EM fields covered in the previous sections facilitate the solution to the inverse scattering problem. Microwave tomography is a classical ill-posed inverse problem studied by

several investigators. The theory underlying different techniques proposed for inverse scattering are briefly covered in this section. The earliest form of tomography developed for penetrating ionizing X-ray radiations is discussed in section 6.1. Section 6.2 covers the requisite mathematical theory to understand the inverse scattering technique that aims to recover the unknown electrical property of an obstacle or a penetrable scatterer from scattered field measurements. The linearized diffraction tomography techniques developed for imaging weak scatterers and their limitations are discussed in section 6.3. The different nonlinear inverse scattering techniques proposed to image the unknown penetrable scaterrer using back and forward scattered waves are discussed in sections 6.4 and 6.5 respectively.

6.1 Tomography Evolution

"Tomography" is a method of sectional imaging that uses "projections" or measurements acquired by illuminating the object from different angles using a penetrating energy source. The earliest tomography technique employed ionizing X-rays for medical imaging applications. In the X-ray regime, waves travel along a straight line and penetrates objects or obstacles in the path. The intensity of the incident X-rays emerging from an object is given by the X-ray attenuation property of the object as [56],

$$I = I_0 \exp^{-\int_L \mu(x,y)dL} \tag{6.1}$$

where I_0 and I are the X-ray intensities before and after traversing the object and $\mu(x,y)$ is the X-ray attenuation coefficient of the object along the line L shown in Figure Figure 6.1. The mathematical foundations for image reconstruction from projections dates back to Radon's contribution in 1917 [57]. The X-ray tomography system invented by Hounsfield [58, 59] and the reconstruction algorithms developed by Allen Cormack [60] are the foundations of the modern X-ray computed tomogra-

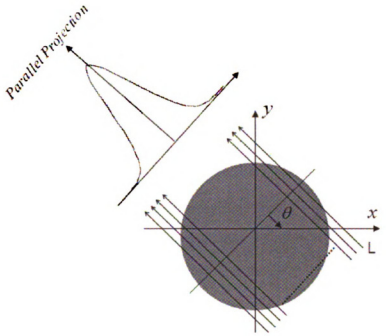

Figure 6.1. X-ray projections.

phy (CT) systems. Since its conception, X-ray CT has become a key screening tool for medical diagnosis and nonintrusive inspection in science and engineering [61, 62]. The earliest CT reconstruction algorithms utilized the iterative Algebraic Reconstruction Techniques (ART) [63, 64]. The filtered backprojection algorithms proposed by Bracwell which was later independently investigated by Ramachandran and Lakshmanan outperformed the slow and iterative ART [56, 65, 66]. Development of fast and efficient data collection and reconstruction techniques led to the realization of new CT generations [67], [56], [68]-[72]. Over the past three decades, CT has evolved into a key diagnostic tool with myriad applications in varied disciplines such as medicine, geology, anthropology and engineering science for visualizing the interior structure of solid objects.

Over the years, the underlying concept of X-ray tomography has been successfully extended to radio isotopes, magnetic resonance, ultrasound, radiofrequency (RF), microwaves, optical and other forms of penetrating energy sources. Depending on the

energy source and data acquisition procedures, tomography techniques are broadly classified into one of the following:

- Transmission tomography : X-ray CT, microwaves, optics
- Reflection tomography : Ultrasound, RF, microwaves
- Emission tomography : Positron emission tomography, radio-nuclide imaging

Several tomography techniques developed for the non-ionizing microwaves are discussed in the following sections of this chapter.

6.2 Inverse Scattering

Microwaves are electromagnetic radiation that falls in the range of 30MHz-300GHz. In the microwave regime, waves no longer travel in a straight path as the size of the objects are comparable to the wavelength. At these frequencies, the waves undergo diffraction and the straight ray tomography as in X-rays is no longer valid. The wave object interaction at microwave frequencies are governed by wave propagation and diffraction phenomenon. The EM waves satisfy the Maxwell's and continuity equations and the fields are related to the material property by the constitutive equations [27, 28]. An EM wave impinging on a penetrable object undergoes diffraction and multiple scattering within the object resulting in a nonlinear relationship between the measured field and electrical property of the object at the incident frequency [73]. Inverse scattering problems aims to reconstruct or estimate the spatial distribution of the scatterer's electrical property or the scattering potential of the obstacle from scattered field measurements. Figure Figure 6.2 shows the schematic illustration of different microwave tomography techniques.

6.2.1 Inhomogeneous Scalar Wave Equation

Consider a time harmonic EM wave incident on an isotropic and arbitrarily shaped penetrable object with $\mu_r(\vec{r},\omega) = 1.0$ and $\epsilon(\vec{r},\omega) = \epsilon_0\epsilon_r(\vec{r},\omega)$. Substituting Ampere's

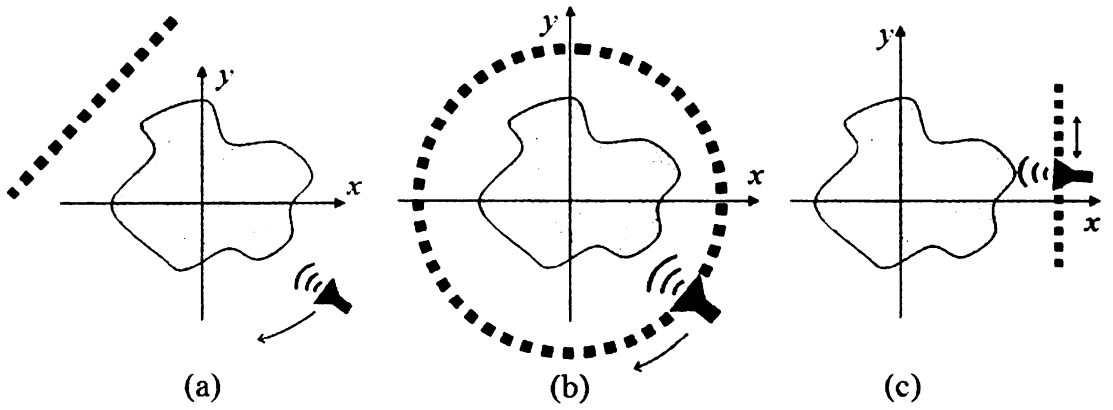

Figure 6.2. Commonly used Diffraction tomography setup (a)-(b) Transmission or forward scattered (c) Reflection or back-scattered.

law in Faraday's law and invoking the vector identities and Gauss's law, the free space vector wave equation is obtained as [27],

$$\nabla^2 \vec{E} + \omega^2 \mu_0 \epsilon(\vec{r}, \omega) \vec{E} = 0 \tag{6.2}$$

where $\epsilon(\vec{r}, \omega)$ is the electrical permittivity of the penetrable scatterer. The scalar wave equation which solves for one component of the vector electric field takes the generic form,

$$\nabla^2 \phi(\vec{r}) + \omega^2 \mu_0 \epsilon(\vec{r}, \omega) \phi(\vec{r}) = 0 \tag{6.3}$$

where $\phi(\vec{r})$ could be one of $E_x(\vec{r})$, $E_y(\vec{r})$ or $E_z(\vec{r})$ components of $\vec{E}(\vec{r})$. Adding and subtracting $\omega^2 \mu_0 \epsilon(\vec{r}, \omega)$ in (6.3) yields [56], [51],

$$\begin{aligned} \left(\nabla^2 + \omega^2 \mu_0 \epsilon(\vec{r}, \omega) + \omega^2 \mu_0 \epsilon_0 - \omega^2 \mu_0 \epsilon_0\right) \phi(\vec{r}) &= 0 \\ \left(\nabla^2 + \omega^2 \mu_0 \epsilon_0\right) \phi(\vec{r}) &= -\omega^2 \mu_0 \left(\epsilon(\vec{r}, \omega) - 1\right) \phi(\vec{r}) \\ \left(\nabla^2 + k_0^2\right) \phi(\vec{r}) &= -O(\vec{r}, \omega) \phi(\vec{r}) \end{aligned} \tag{6.4}$$

where $k_0 = \frac{2\pi}{\lambda}$ and λ is the wavelength of the time harmonic field. In the absence of the dielectric scatterer, incident $\phi^{inc}(\vec{r})$ exists everywhere and (6.4) reduces to the form,

$$\left(\nabla^2 + k_0^2\right) \phi^{inc}(\vec{r}) = 0 \tag{6.5}$$

Substituting $\phi(\vec{r}) = \phi^{inc}(\vec{r}) + \phi^{sc}(\vec{r})$ in (6.4) yields the wave equation,

$$\left(\nabla^2 + k_0^2\right) \phi^{sc}(\vec{r}) = -O(\vec{r},\omega)\phi(\vec{r}) \tag{6.6}$$

for the field scattered by the penetrable dielectric object. Equation (6.6) is the free space inhomogeneous scalar Helmholtz wave equation with the forcing function, $O(\vec{r},\omega)\phi(\vec{r})$.

6.2.2 Integral Equation Solution

The solution to an inhomogeneous wave equation in free space or a homogeneous linear isotropic medium can be obtained using the scalar Greens function. The unknown scattered field in (6.6) can be expressed in terms of the free space scalar Greens function, $g(\vec{r}|\vec{r}')$ which satisfies [51],

$$\left(\nabla^2 + k_0^2\right) g(\vec{r}|\vec{r}') = -\delta(\vec{r} - \vec{r}') \tag{6.7}$$

In (6.7), the Greens function is the response of the differential equation to an impulse function $\delta(\vec{r} - \vec{r}')$ and hence is the impulse response of the scalar wave equation. Then, from linear system theory, solution to (6.6) is the convolution of the forcing function $O(\vec{r},\omega)\phi(\vec{r})$ with the system impulse response, $g(\vec{r}|\vec{r}')$. Thus, the scattered field maintained by the dielectric scatterer is expressed as [51, 52],

$$\phi^{sc}(\vec{r}) = \int_{V'} O(\vec{r}',\omega)\phi(\vec{r}')g(\vec{r}|\vec{r}')d\vec{r}'. \tag{6.8}$$

Equation (6.8) is the well known Freedholm integral equation of the second kind. The integral equation solution of the scattered field in (6.8) is nonlinear as it is related to the unknown total field inside the scatterer due to multiple scattering.

In inverse scattering applications, either the differential form (6.3) or the integral form (6.8) is solved for the unknown spatial distribution of the dielectric scatterer. Inverse scattering problems are nonlinear and ill-posed and pose difficulties in recovering the true profile $O(\vec{r}, \omega)$ of the scatterer [74]-[76]. Several investigators have proposed solutions to the nonlinear inverse scattering problem [56, 73, 76]. The solution is achieved either by solving (6.8) using numerical techniques [51] or by linearizing the scattering problem using approximations [56]. For weakly scattering objects, the mathematical and computational complexities involved in permittivity reconstruction are reduced by linearizing the nonlinear problem. Such approximations are also referred to as the *physical-optics approximations.* The linear and nonlinear inverse scattering techniques of microwave tomography are discussed in sections 6.3-6.5.

6.3 Diffraction Tomography - Linearized inverse scattering

Early stage tomography techniques developed for diffracting sources such as microwaves are extensions of the straight ray tomography and are applicable only to weakly scattering objects. Diffraction tomography is a linearized inverse scattering method that involves reconstructing the spatial distribution of unknown permittivity of the dielectric object from scattered field measurements [56], [77]. The first and foremost techniques developed for inverse scattering employed the Born or Rytov approximations for permittivity estimation [56], [78].

6.3.1 Born Approximation

The Born approximation linearizes (6.8) for imaging weakly scattering dielectric objects. The first order Born approximation states [56], [79]

$$\begin{aligned} \phi(\vec{r}) &= \phi(\vec{r}^{inc}) + \phi(\vec{r}^{sc}) \\ &\backsimeq \phi(\vec{r}^{inc}) \end{aligned} \tag{6.9}$$

This condition is satisfied only if, $0 < O(\vec{r}, \omega) << 1$. Under such conditions, (6.8) simplifies to a linear equation of the form [80],

$$\phi^{sc}(\vec{r}) = \phi^{b}(\vec{r}) = \int_{V'} O(\vec{r}', \omega)\phi^{inc}(\vec{r}')g(\vec{r}|\vec{r}')d\vec{r}'. \tag{6.10}$$

Equation (6.10) can be solved for the unknown permittivity distribution due to known incident field and recorded field measurements. Better approximations to the scattered field is obtained by substituting (6.9) into (6.10). The resulting higher order Born approximation is given by the expression [56],

$$\phi_1^{sc}(\vec{r}) = \int_{V'} O(\vec{r}', \omega)\left[\phi^{inc}(\vec{r}') + \phi^{b}(\vec{r}')\right] g(\vec{r}|\vec{r}')d\vec{r}'. \tag{6.11}$$

Including more higher order terms inside the integrand yields better estimate for the scattered field. Several variations to the simple first order Born approximation have been proposed to provide better permittivity estimates of relatively strong scatterers [56], [81]-[84].

6.3.2 Rytov Approximation

An alternate approximation that linearizes the scattered field is the Rytov approximation. In the Rytov method, the complex phase of the scattered field is approximated to simplify the nonlinear scatter field equation. The total field is represented in

Euler's form as [85],

$$\phi(\vec{r}) = e^{\theta(\vec{r})}, \qquad \theta(\vec{r}) = \theta^{inc}(\vec{r}) + \theta^{sc}(\vec{r}) \tag{6.12}$$

Substituting (6.12) into (6.3) yields,

$$\left(\nabla^2 + k_0^2\right) \phi^{inc}(\vec{r})\theta^{sc}(\vec{r}) = -\phi^{inc}(\vec{r}) \left[\left(\nabla\theta^{sc}(\vec{r})\right)^2 + O(\vec{r},\omega)\right] \tag{6.13}$$

The solution to (6.13) in terms of the free space Greens function takes the form,

$$\phi^{in}(\vec{r})\theta^{sc}(\vec{r}) = \int_{V'} \phi^{inc}(\vec{r'})g(\vec{r}|\vec{r'}) \left[\left(\nabla\theta^{sc}(\vec{r'})\right)^2 + O(\vec{r'},\omega)\right] d\vec{r'}. \tag{6.14}$$

The approximation of the complex phase,

$$\left(\nabla\theta^{sc}(\vec{r})\right)^2 + O(\vec{r}) \backsimeq O(\vec{r}) \tag{6.15}$$

simplifies (6.14) to,

$$\begin{aligned} \phi^{in}(\vec{r})\theta^{sc}(\vec{r}) &= \int_{V'} O(\vec{r'},\omega)\phi^{inc}(\vec{r'})g(\vec{r}|\vec{r'})d\vec{r'} \\ \theta^{sc}(\vec{r}) &= \frac{\phi^b(\vec{r})}{\phi^{in}(\vec{r})} \end{aligned} \tag{6.16}$$

Numerical simulations demonstrating the feasibility of diffraction tomography for two-dimensional objects under order Rytov approximation are reported in [86].

6.3.3 Limitations

Linearization using the Born and Rytov approximations are applicable only to weakly scattering objects. In Born approximation, the assumption (6.9) implies that the scaterred field is smaller than the incident field and the formulation can be used

only if $(\epsilon_r - 1) << 1$ is true. Real life inverse scattering problems involve strong scatterers with wide variations in the spatial permittivity distribution for which the Born approximation fails [87]-[89]. For a weak homogeneous cylinder of radius a with dielectric contrast, $n_\delta = \sqrt{\epsilon_r \mu_r - 1}$ Born approximation is valid only if [56]

$$an_\delta < \frac{\lambda}{4} \tag{6.17}$$

is satisfied where λ is the wavelength of the incident field. Condition (6.17) imposes the constraint that phase change between the wave propagating inside the scatterer and the incident wave should be less than π. Likewise, the Rytov approximation on the complex phase of the total field limits the applicability of the linearized scattering equation to image strong scatterers. The Rytov approximation in (6.15) yields the condition [56],

$$n_\delta >> \frac{(\nabla \theta_{sc})^2}{k_0^2} \tag{6.18}$$

to be satisfied for reliable permittivity estimation for the scatterer. Unlike (6.17), condition (6.18) on the refractive index of the dielectric object is relatively weak as there is no constraint imposed on the object size. Thus, Rytov approximation is a relatively weaker condition than Born approximation and is valid as long as the phase change over a λ inside the scatterer is less than π.

6.3.4 Fourier Diffraction Theorem

The permittivity reconstruction algorithms developed for linearized inverse scattering problems are based on the *Fourier Diffraction* theorem. The Fourier Diffraction theorem is the basis for diffraction tomography and hence is valid only for weakly scattering objects. The theorem relates the spatial Fourier transform of the scattered time harmonic field measurements recorded along an angle in the image space to the 2D electrical property of the scatterer along a semicircular arc in the Fourier

space $O(k_x, k_y; \omega)$ [56], [73], [76], [87]. Scattered fields measured for different angles of illumination around the object are used to fill the Fourier space as illustrated in Figure Figure 6.3, to recover the unknown function $O(\vec{r}, \omega)$ via Fourier inversion. The scattered field $\phi_b(\vec{r})$ used in the Fourier Diffraction theorem could either be the field amplitude as in Born approximation [80], [86], [90],

$$\phi^b(\vec{r}) = \int_{V'} O(\vec{r}', \omega)\phi^{inc}(\vec{r}')g(\vec{r}|\vec{r}')d\vec{r}' \tag{6.19}$$

or the phase relation [88]-[90],

$$\phi^b(\vec{r}) = \phi^{in}(\vec{r})\theta^{sc}(\vec{r}) \tag{6.20}$$

assumed in Rytov approximation. Both spatial and frequency domain approaches have been adopted to solve the linearized inverse scattering problems on the basis of the Fourier Diffraction theorem [56]. The inherent mathematical limitations in the Fourier Diffraction Theorem severely limits the reconstruction accuracy and the range of objects for noninvasive imaging. The fundamental mathematical limitations are due to Born and Rytov approximations applied on the field measurements [88], [91]. Other mathematical limitations are due to finite number of experimental measurements that can be used to fill the Fourier space for inversion. Interpolation techniques for limited measurements in the Fourier and spatial domains and the presence of evanescent waves also affect the accuracy of the reconstruction. Higher order Born and Rytov approximations, iterative and distorted iterative Born approximation methods, vector born approximation and other variants have been proposed to overcome the shortcomings of the first order approximations and to account for multiple scattering to some extent [81]-[84], [92]-[94]. These modified approximations could only extend the contrast range of the objects for imaging indicating the need to solve the nonlinear

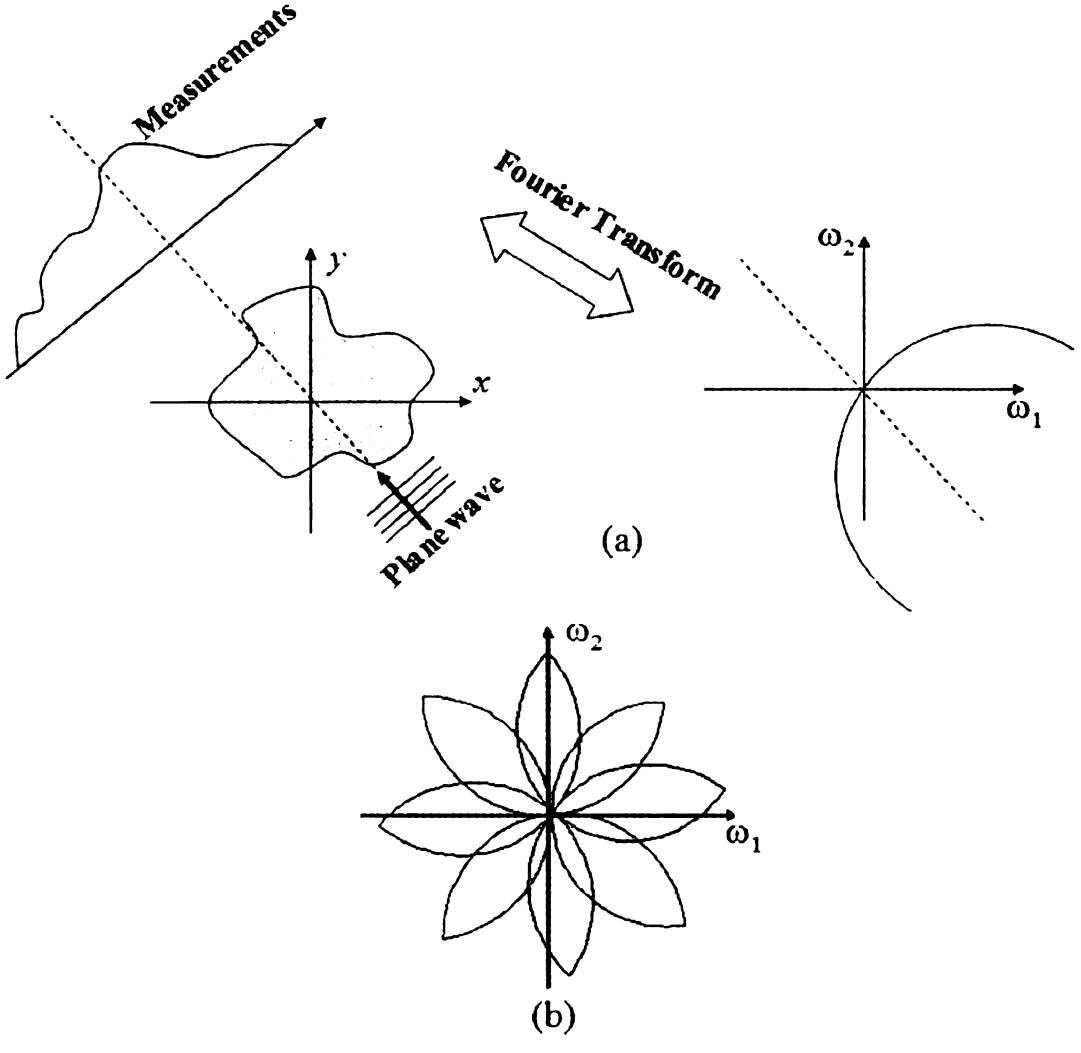

Figure 6.3. Fourier Diffraction Theorem (a)Schematic illustration (b)Fourier space filling.

inverse scattering problem for accurate permittivity reconstruction.

6.4 Reflection Tomography

Reflection microwave tomography widely known as *synthetic aperture radar* provides the spatial locations of the potential scatterers inside the imaging region. Reflection tomography employs an array of transceiver antennas or a bi-static antenna pair excited by wide band(short pulse) signals for enhanced spatial resolution. The field emitted by an antenna gets back scattered from the scatterer and are measured at the transceiver locations. The field measured at the receivers for each transmitting antenna are used to locate the potential scatterers inside the penetrable object. Figure Figure 6.4 illustrates a simple reflection tomography setup with an array of transceivers. The scattering potential at a position $\vec{r}$ inside the dielectric object in terms of the N antenna measurements is given by,

$$B(\vec{r}) = \sum_{n=1}^{N} v_n(\vec{r}, t_n) h_n(\vec{r}) \tag{6.21}$$

where $h_n(\vec{r})$ and $v_n(\vec{r}, t_n)$ are the apodizing function and the time domain diffracted field measurement for the n^{th} transceiver antenna. The distance between $\vec{r}$ and the n^{th} receiver is given by the expression, $d_n = 2\frac{|\vec{r}-\vec{r}_n|}{\nu t_n}$ for the assumed velocity of propagation ν inside the scatterer. Reflection tomography utilizes the *time of flight* information to identify the signal arrival time after scattering within the dielectric object [95]. Reflection tomography is widely used in *Ground Penetrating Radar*(GPR) to image the ground surface for land mines and buried dielectric and metallic objects [96, 97] and to inspect roads and civil structures for delaminations, voids and cracks [98]-[101]. This is also the basis for B-scan imaging in ultrasound medical diagnosis and nondestructive evaluation of materials in engineering science [56], [62]. During the past decade, the underlying principles of synthetic aperture radar imaging has

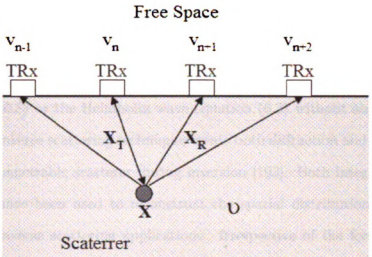

Figure 6.4. Reflection tomography setup using linear antenna array.

been extended to image biological objects for noninvasive tumor detection in the breast[102]. These reconstruction algorithms employ simple post processing routines on the received signals to detect the scattering potential inside the imaging region. Thus, the computationally faster back-scattering techniques do not yield the material property of the dielectric object which, is essential to understand the physics of wave interaction inside unknown penetrable objects.

6.5 Nonlinear Inverse Scattering

Microwave noninvasive imaging has been a topic of interest to many investigators. The nonradioactive microwaves is sought as a promising diagnostic tool in medical applications. Over the past three decades, several tomography techniques have been proposed to noninvasively characterize penetrable scatterers. Of the different tomography methods, iterative inversion techniques that solve the nonlinear inverse scattering problem are advantageous as they yield the physical location, size and the spatial distribution of the scatterer electrical property. Unlike the high-end radioactive X-ray CT systems, microwaves are penetrating, nonionizing radiation that can

be used to image both animate and inanimate penetrable objects using a relatively low cost tomography system.

Nonlinear inverse scattering applications solves the Freedholm integral equation (6.8) or the Helmholtz wave equation (6.3) without any approximations. Nonlinear inverse scattering techniques treats both diffraction and multiple scattering inside the penetrable scatterer during inversion [103]. Both integral and differential equations have been used to reconstruct the spatial distribution of the material property in inverse scattering applications. Irrespective of the form of the wave equation, the objective of an nonlinear inverse scattering problem involving dielectric scatterer is to seek the minimizer $\epsilon^{est}(\vec{r},\omega)$ of the cost function,

$$C(\epsilon) = \frac{1}{2}\sum_{k=1}^{M} \left|\phi_k^m(\vec{r}_m) - \phi_k^c(\vec{r}_m)\right|^2 \tag{6.22}$$

where $\phi^m(\vec{r}_m)$ represents the field measured at the receivers for the true permittivity distribution and $\phi^c(\vec{r}_m)$ represents the field computed for the estimated permittivity profile $\epsilon^{est}(\vec{r},\omega)$. Solution to the nonlinear inverse scattering problems iteratively estimates the spatial permittivity distribution inside the scatterer until the error between the measured and calculated fields at the receiver locations is below a predetermined threshold. The ill-posed nature of the nonlinear inverse scattering problem requires multi-view field measurements and prior information to guarantee a stable solution for the unknown object function $O(\vec{r},\omega)$.

The iterative reconstruction technique proposed by Pichot et. al. solves the integral equation and employs Newton Katororvich's method for permittivity reconstruction [104]. Mathematical formulation and experimental results using TM wave illumination were reported for imaging two-dimensional penetrable inanimate and biological objects [105, 106]. In 1995, the first prototype microwave imaging system employing monopole transceiver antennas developed for imaging biological objects

over 300-1100MHz for hyperthermia treatment monitoring was reported [107]. The iterative inversion procedure proposed by Meaney et al in the prototype system utilized the finite element boundary integral method for 2D TM^z polarization to recover the location, size and spatial permittivity distribution of the dielectric scatterer [107]-[110]. Imaging results of a canine heart at 2.45 GHz obtained using a two-dimensional microwave tomography system employing 32 transceivers was presented in [111]. Fast algorithms and robust regularization techniques were proposed for iterative permittivity inversion [94], [112]. Alternate inversion methods that utilize Polak-Ribiere nonlinear conjugate gradient optimization algorithm were proposed for 2D permittivity reconstruction under TM illumination [113]. Pre-clinical results on microwave imaging for biomedical applications demonstrated the feasibility of nonlinear inverse scattering techniques [114], [115].

CHAPTER 7

ACTIVE MIRROR TECHNOLOGY

Introduction

Active mirror is an optical element used in adaptive optic systems (AOS) whose functionality can be modified in real time to control the incident optical wavefront for desired performance [116] - [118]. A simple and common application of active optic element include real time tilt and focus corrections. The earliest use of active mirrors dates back to the "burning glass" built by Archimedes in 215 BC. It is widely presumed that the burning glass might have been an array of large array of metal coated mirrors maneuvered by humans to focus the sunlight to set the Roman fleet on fire [119]. The solar furnace located at Odeillo in the Pyrnes Orientales in France employs 63 flat mirrors is another example where mirrors are used to reflect the sunlight on to a parabolic reflector for power generation. Efforts to harness solar energy for power generation using mirrors was attempted in the United States in 1974 to direct the sunlight to a central boiler in a steam generating unit [116]. The early active multimirror systems built for harnessing solar power dealt only with intensity without consideration of the phase of the optical wavefront. In later stages, coherent multimirror adaptive systems were built for use in astronomy. In the early 80s, high cost and bulk coherent AOS were used to build high-end telescopes to study distant astronomical objects.

The organization of this chapter is as follows. Section 7.1 contains a brief overview of the development and role of active mirrors in adaptive optic systems during the past three decades. The different types of active mirrors, their design and applications are also covered in section 7.1. The design and mathematical theory that governs the mirror functionality and applications of membrane mirror, the key element in the

proposed microwave tomography technique for breast imaging, are covered in section 7.2. The use of the membrane mirror optical device in inverse scattering applications is introduced in section 7.3.

7.1 Adaptive Optics

Adaptive Optics systems employing active mirrors have been developed for both simple open loop systems and complex high precision systems functioning in closed feedback mode. System operating in open loop are widely used as simple wavefront tilt and focus correctors. The need for adaptive optics systems with wide operational and dimensional variations led to the invention of different types of active mirrors with complex functionalities [116]. Depending on the actuator and substrate design, active mirrors are grouped into one of the following categories:

- Segmented mirrors
- Continuous thin-plate mirrors
- Monolithic mirrors
- Membrane mirrors

The design and functionality of each mirror type is briefly presented in this section.

7.1.1 Segmented Mirrors

Segmented mirrors as the name implies comprises of an array of mirror segments for tilt and focus corrections. Each mirror segment in the array has rigid shape and are supported at three points by a piston type actuator. Figure Figure 7.1 shows the schematic of the two widely used segment mirror designs. Large arrays of segmented mirrors are used in astronomy to compensate for aberration due to atmospheric turbulence and to increase light gathering capacity of land-based telescopes

[116], [120, 121]. The deflection of a uniform plate of segmented mirrors under the influence of a uniform load is given by the equation [116],

$$W = \frac{\alpha_s}{qb^4} D \tag{7.1}$$

In (7.1), the mirror stiffness D takes the form [122],

$$D = \frac{Eh^3}{12(1-\nu^2)} \tag{7.2}$$

where

α_s: support configuration factor

b: space between supports

q: load per unit area

E: Young's modulus,

ν: Poisson's ratio and

h: Thickness of the mirror material.

Segmented mirrors offer scalability, assembly and possess no coupling between actuators. However, the gaps between the segmented rigid mirrors diffract the incident light and yields discontinuous phase and intensity variation across the mirror surface.

7.1.1.1 Digital Micromirror Device

With advance in micro-electro-mechanical systems (MEMS) and bulk semiconductor fabrication technology, the use of segmented mirrors for projection display has gained significant research interest. An array of segmented mirrors assembled using MEMS technology was developed by Texas Instruments for high quality digital video and

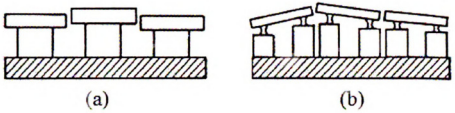

Figure 7.1. Segmented Mirrors [116] (a)Piston only (b)Piston and tilt.

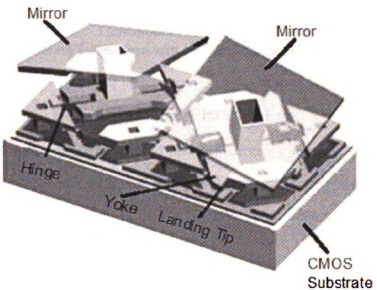

Figure 7.2. Schematic of Texas Instruments two DMD mirrors [126].

projection displays [123], [124]. The Digital Micromirror Device (DMD) developed by Texas Instruments is an array of closely spaced digital micromirrors monolithically integrated and controlled on a single silicon chip. An illustration of two DMD mirrors belonging to a large array is shown in Figure Figure 7.2. Besides projection display, DMDs are used as coherent optical correlators and spatial light modulators in adaptive optics [123]-[127].

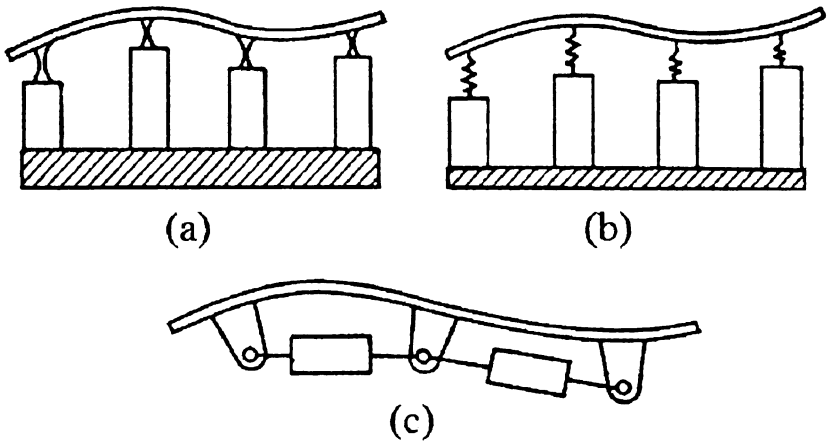

Figure 7.3. Continuous thin-plate mirrors [116](a)Discrete position actuators (b)Discrete force actuators (c)Bending moment force actuators.

7.1.2 Deformable Thin-Plate Mirrors

These are medium sized active mirrors ranging between 10 cm to 3 m in diameter that consists of a continuously deformable thin plate mounted on an discrete array of actuators [128, 129]. The actuators that deflects the thin plate could be one of the following design:

- Discrete position actuators
- Discrete force actuators
- Bending moment force actuators

Schematic illustrations of different types of thin-plate deformable mirror are shown in Figure Figure 7.3. The spatial frequency of the deformation caused by the actuator array depends on the spatial distribution of the underlying actuator elements. Unlike segmented mirror, thin-plate deformable mirrors do not diffract the incident light except at the corners and provide continuous intensity and phase variations across the mirror surface. The deflection d of an isotropic thin plate mirror with linear

stress-strain relationship is related to the actuator array force P by [116],

$$d = FP \tag{7.3}$$

where F is the *flexibility* matrix that defines the static behavior of the thin plate deflection at each point for a unit force applied at that point. The array of forces P required to achieve the desired deflection d is obtained using the inverse relationship,

$$P = F^{-1}d \tag{7.4}$$

7.1.3 Monolithic Active Mirrors

Monolithic active mirrors use a single block of homogeneous material for the mirror substrate and the piezoelectric elements of the actuator array. The functionality of the mirror, actuators and backplate are combined inside one monolithic substrate thereby reducing the operational variations caused by the use of multiple parts. Figure Figure 7.4 shows a typical monolithic mirror schema. Deformation created under the influence of an applied electrode voltage is local to the active electrode with minimal coupling between the neighboring electrodes. Monolithic piezoelectric mirrors are widely used for real time turbulence correction [116], [130].

7.1.4 Membrane Mirrors

A membrane mirror consists of a reflective and flexible thin membrane with no inherent stiffness mounted on an actuator array [116], [131, 132]. Unlike thin plate mirrors, membrane mirrors require tension to maintain surface flatness and hence are capable of providing deflections for relatively small electrostatic force. The MEMS based deformable membrane mirror offers advantages over monolithic piezoelectric mirrors in terms of bulk, low cost semiconductor fabrication technology, low actuator force and hence low operating voltages and the absence of hysteresis.

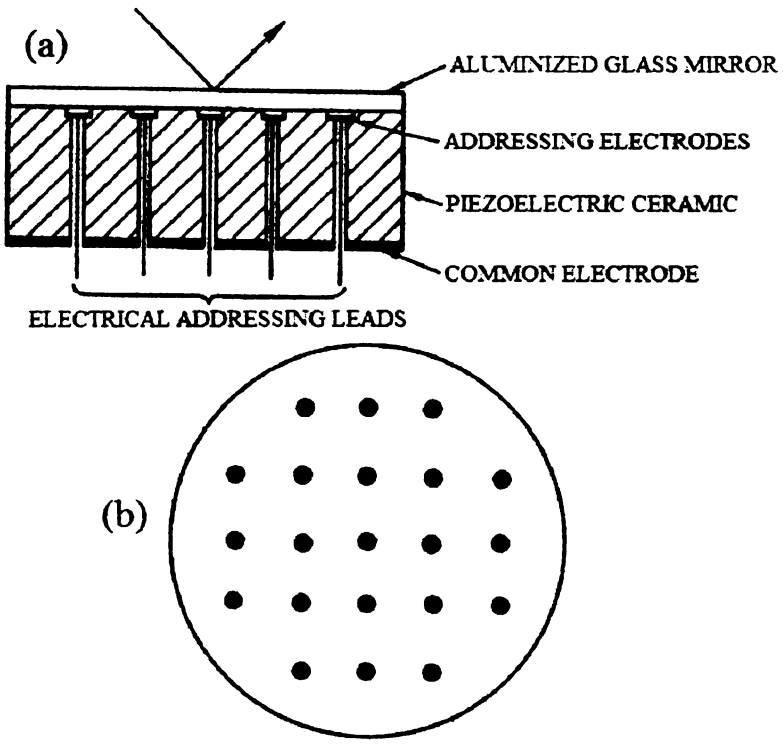

Figure 7.4. Monolithic mirror with piezoelectric actuator [116](a)Side view (b)Top view.

7.2 Membrane Deformable Mirror

The design, construction and working principles of the membrane deformable mirror is discussed in this section. The mathematical equations that govern the mirror deformation under the influence of an external load for a given set of boundary conditions is discussed using theory of plates and shells.

7.2.1 Mirror Design

A membrane mirror is a semiconductor MEMS device in which the flexible membrane is controlled by underlying CMOS circuits [133]-[135]. Figure Figure 7.5 shows schematic illustrations of different membrane mirror designs [133], [135]. The flexible membrane with reflective coating supported by an array of actuator posts acts as an thin film of reflecting mirror. The electrostatic actuators at discrete points are connected to the ground substrate and enable a smooth deformation of the mirror

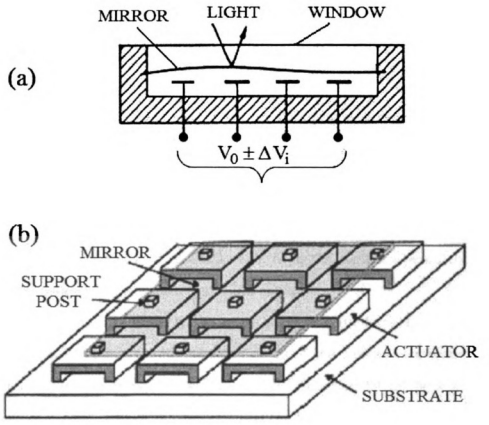

Figure 7.5. Membrane mirror schematics (a)[133] (b)[135].

surface governed by the basics of vibration theory [122]. When a potential distribution $V(x, y)$ is applied between an actuator and substrate, an electrostatic force is generated normal to the mirror surface. The electrostatic force deflects the mirror sheet mounted on the attachment post, creating a local deformation $w(x, y)$ of the membrane mirror sparing the rest of the mirror. Depending on the application, circular, rectangular and honey comb actuator array designs are available for fabrication.

7.2.2 Mirror Deformation

The deformation of flexible membrane mirror can be explained by the theory of thin plates and shells. The deformation $w(x, y)$ of a membrane mirror subjected to a load

q is characterized by the partial differential equation [122],

$$\frac{\partial^4 w}{\partial x^4} + 2\frac{\partial^4 w}{\partial x^2 \partial y^2} + \frac{\partial^4 w}{\partial y^4} = \frac{q}{D} \tag{7.5}$$

where q is the load maintained by the actuator potential distribution $V(x,y)$ normal to the membrane mirror. The electrostatic actuation acting on the mirror is given by the equation [122],

$$q(x,y) = \frac{k^2 \epsilon\epsilon_0 V^2(x,y)}{2g^2(x,y)} \tag{7.6}$$

In (7.6), k is the dielectric constant of air, $\epsilon\epsilon_0$ is the free space permittivity and $g(x,y)$ is the distance between membrane and actuator.

Mirror deflection under the influence of electrostatic force can be determined using (7.5) and boundary conditions along edges of the flexible membrane. Assuming a rectangular membrane mirror with mirror edges parallel to the x and y axes, the boundary conditions on mirror deflection can be one or a combination of the following types [122].

(i) Built-in Edge: Built-in edge implies zero deflection at the edge with no change in mirror deflection along the plane tangent to the mirror edge. The boundary conditions for a built-in edge along x=a are,

$$(w)_{x=a} = 0 \tag{7.7a}$$

$$\left(\frac{\partial w}{\partial x}\right)_{x=a} = 0 \tag{7.7b}$$

(ii) Simply Supported Edge: This boundary condition is applicable for mirrors with zero deflection and bending moment along the edge which, enables the mirror to rotate freely with respect to the edge. Membrane mirror with a simply supported

edge along $x = a$ satisfies the boundary conditions,

$$(w)_{x=a} = 0 \tag{7.8a}$$

$$\left(\frac{\partial w^2}{\partial x^2} + \nu\frac{\partial w^2}{\partial y^2}\right)_{x=a} = 0 \tag{7.8b}$$

(iii) Free Edge: A membrane mirror with free edge does not experience bending and twisting moments and vertical shear forces. In terms of analytical expressions, this implies

$$\left(\frac{\partial^3 w}{\partial x^3} + (2-\nu)\frac{\partial^3 w}{\partial x \partial y^2}\right)_{x=a} = 0 \tag{7.9a}$$

$$\left(\frac{\partial w^2}{\partial x^2} + \nu\frac{\partial w^2}{\partial y^2}\right)_{x=a} = 0 \tag{7.9b}$$

along the free edge. Equations (7.5) and (7.7) - (7.9) characterizes the deformation of the membrane mirror under the influence of electrostatic force. The inverse relation between the electrostatic force and mirror-substrate distance in (7.6) limits the mirror deflection. The dynamic range of mirror deflection is often stretched by using high bias voltage in the actuator design.

7.2.3 Mirror Applications

In the last decade, electro-statically actuated membrane mirror arrays have received tremendous attention [136]. The surge in bulk semiconductor fabrication of large arrays of inexpensive micromechanical structures has led to the successful development of continuously flexible and mechanically stable micro-machined membrane mirrors. Developments in micro-optics and MEMS enabled batch production of low energy consuming, miniature-sized, membrane deformable mirrors. Variations of the basic design and working principles of the membrane deformable mirror were proposed for

use in several applications such as optical switches [137], phase modulators [138], scanners [139, 140], imaging devices [141, 142], aberration correctors [143] and so on [144].

7.3 Adaptive Mirrors in Microwave Regime

The ability of active membrane mirrors to control surface deflection in closed feedback mode led to the application of adaptive optics device in optical imaging. The functionality of deformable active mirror can be extended to reflect and redirect the incident electromagnetic waves with the aid of a thin metallic coating on the membrane mirror surface. The concept of adaptive mirrors for nonintrusive microwave imaging is introduced in this thesis with a specific application for breast cancer detection and therapy. The use of deformable mirrors for macro level imaging applications in the EM spectrum is introduced for the first time via computational feasibility studies on mathematical breast models. The mathematical theory, problem formulation and tomographic technique essential for the computational study are explained in detail in the following chapters.

CHAPTER 8

PROOF OF CONCEPT WITH NONDIFFRACTING SOURCES

Introduction

Prior to modeling in the microwave regime, a simple numerical model employing straight ray theory applicable for X-rays was implemented to check the feasibility of the thesis proposal. The X-ray model is a simple and easy feasibility study that serves as a proof of the proposed mirror based tomography concept in the absence of diffraction and scattering effects. The numerical simulations for the X-ray model assumes the existence of a reflective coating for the deformable mirror capable of reflecting X-rays incident at angles greater than the grazing angle of incidence.

The organization of this chapter is as follows. A brief introduction of X-ray tomography and underlying theory of X-ray projections are presented in section 8.1. Evolution of contemporary X-ray computed tomography (CT), CT imaging techniques and simulations results are in section 8.2. In section 8.3, the proposed deformable mirror X-ray CT imaging technique and iterative reconstruction method are explained using computer simulations. Comparison and advantages of the proposed mirror based CT with conventional CT are covered in section 8.4 using additional numerical simulations. In section 8.5, the feasibility of extending the deformable mirror CT setup to focus high-energy X-ray radiations at tumor site for therapy is demonstrated via numerical simulations. Limitations with the realization of deformable mirror imaging cum therapy system in X-ray regime are discussed in section 8.6. Finally, the outcome of the proof of concept model using X-rays are summarized in the "Conclusions" section.

8.1 X-ray Tomography

Computed tomography(CT) is a mature imaging technique that involves reconstruction of 2D-cross sectional images of a 3D object using projection data. Several CT techniques employing different types of penetrating energy sources have been developed for non-intrusive inspection of which the foremost technology employs X-rays. X-rays are ionizing radiations capable of traversing through most objects in straight path. X-ray CT has a wide range of application as a diagnostic tool in varied disciplines of medicine, geology, anthropology and engineering science for visualizing interior structures of solid opaque objects. X-ray computed tomography is the first tool that revolutionized diagnostic medicine, followed by several variations including emission tomography (radioactive isotopes), magnetic resonance and ultrasound imaging.

8.1.1 X-ray Projections

The objective of CT is to reconstruct the 2D cross section of a 3D object from the ray-sums of the projections measured around the object. In X-ray CT, the projection along a direction θ in the image plane is given by a set of line integrals of linear attenuation function $\mu(x, y)$ of the object. Figure Figure 8.1 shows the simplest parallel beam projection of a 2D image at an angle θ from a collimated source emitting a pencil beam. For X-rays with monochromatic photons traveling along a line L, the intensity of beam at the detector, I is related to the incident beam intensity, I_0 by the line integral [56],

$$I = I_0 e^{-\int_L \mu(x,y)dl} \tag{8.1}$$

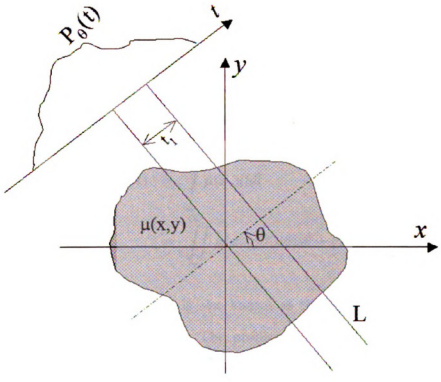

Figure 8.1. X-ray projection along a a direction θ.

where $\mu(x,y)$ is the linear X-ray attenuation function of the object. From (8.1), the X-ray projection is given by the logarithm of ratio of beam intensities along L as

$$\ln\left(\frac{I_0}{I}\right) = \int_L \mu(x,y)dl \tag{8.2}$$

Measurement of the ratio $\ln\left(\frac{I_0}{I}\right)$ for X-rays incident at different angles yields the projection data, $P_\theta(t)$ for 2D slice reconstruction.

8.1.2 X-ray CT

The mathematical foundation for reconstruction of unknown spatial function from projections $P_\theta(t)$ was first conceived by Johann Radon in 1917 [57]. The parametric form of the line integral in (8.2) takes the form,

$$\begin{aligned} P_\theta(t) &= \int_L \mu(x,y)dl \\ &= \int_{\infty}^{\infty}\int \mu(x,y)\partial(xcos\theta + ysin\theta - t)dxdy \end{aligned} \tag{8.3}$$

where the projection, $P_\theta(t)$ is also known as the Radon transform of spatial X-ray attenuation function $\mu(x,y)$. The problem of recovery of $\mu(x,y)$ from $P_\theta(t)$ is a linear inverse problem called *image reconstruction from projections* or inverse Radon transform [146], [76].

In discrete form, the projection operation in (8.3) is modeled as a linear system of the form [56],

$$\begin{aligned} \sum_{j=1}^{N^2} a_{ij}\mu_j &= g_i, \quad i = 1,2,..,M \\ A\mu &= g \end{aligned}$$

In (8.4), μ_j is the discretized unknown X-ray attenuation function of the object of

dimension N^2, g_i is the i^{th} X-ray projection or ray sum, a_{ij} is the contribution of the j^{th} image cell to the i^{th} X-ray, M is the total number of projections for all mirror shapes and A is a mapping from the image to projection space. For each unique mirror deformations, equations (8.1)-(8.3) were used to assemble the linear system of equation (8.4). Using ray tracing technique, contribution of all pencil beam X-rays comprising the fan beam are considered in the numerical simulations.

8.1.3 X-ray CT Imaging

With advances in technology, several fast and efficient implementations of reconstruction algorithms have emerged [56]. Fourier based approach for image reconstruction using projections put forth by Bracewell [145] and later independently introduced by Ramachandran and Laximnarayan [65] as Fourier weighted backprojection algorithm is one of the most commonly used reconstruction technique. The computationally fast Fourier weighted backprojection algorithms require a large number of equally spaced projections over [0-180) or [0-360) to reconstruct images with the desired level of accuracy for medical applications [56], [66].

Another commonly used CT imaging technique include the iterative reconstruction methods. Some of the early discussions on iterative reconstruction algorithms can be found in [63, 64, 68], [146] - [147]. The Algebraic Reconstruction Technique (ART), a series expansion approach for imaging three-dimensional biomedical objects [63], is a variation of the iterative method introduced by S. Kaczmarz in 1937 for solving a system of simultaneous equations [148]. Unlike search algorithms, iterative reconstruction require fewer projections and are well suited for limited-angle and missing-view tomography scenarios commonly found in many nondestructive imaging applications [56, 69]. The shortcoming of the iterative reconstruction algorithms is their computational cost, for which several efficient implementations have been proposed [77], [149]-[150].

8.2 Conventional X-ray CT

Over the past three decades, CT has evolved into a key diagnostic tool with myriad applications. Based on the scanning configuration, motion, beam geometry and detector arrangement; several generations of CT scanners have evolved. Current CT scanners are often referred to as 3rd, 4th or 5th generation systems. The CT scanners to date have used parallel, fan or cone beam source with translate/rotate, rotate/rotate, rotate-stationary and stationary-stationary (source and detectors are fixed on a circular array) scan configurations for projection measurements as illustrated in Figure Figure 8.2[151]-[152]. All these scan geometries require precise positioning and alignment of source-detector pairs. Commercial CT systems often employ Fourier based methods for reconstruction which, require equi-spaced X-ray projections over [0, 360] degrees.

8.2.1 Numerical Simulations

X-ray CT reconstructions for the scan geometry illustrated in Figure Figure 8.2(c) with 1° spacing between rotations were obtained for the modified Shepp-Logan head phantom in Figure Figure 8.3(a). In the numerical simulations, projections were collected for L projection angles with P pencil beam X-rays per projection angle. Iterative and Filtered Back Projection (FBP) algorithms were implemented for $L = 180$ and $P = 117$. Figures Figure 8.3(b)-(c) show CT reconstructions of Kaczmarz algorithm at 60^{th} and 300^{th} iterations respectively and Figures Figure 8.3(d)-(f) show reconstructions obtained using FBP for different filtering and interpolation choices. The FBP method smears the projections back into image space and yields reconstructions that lack in details and require post processing for image enhancement.

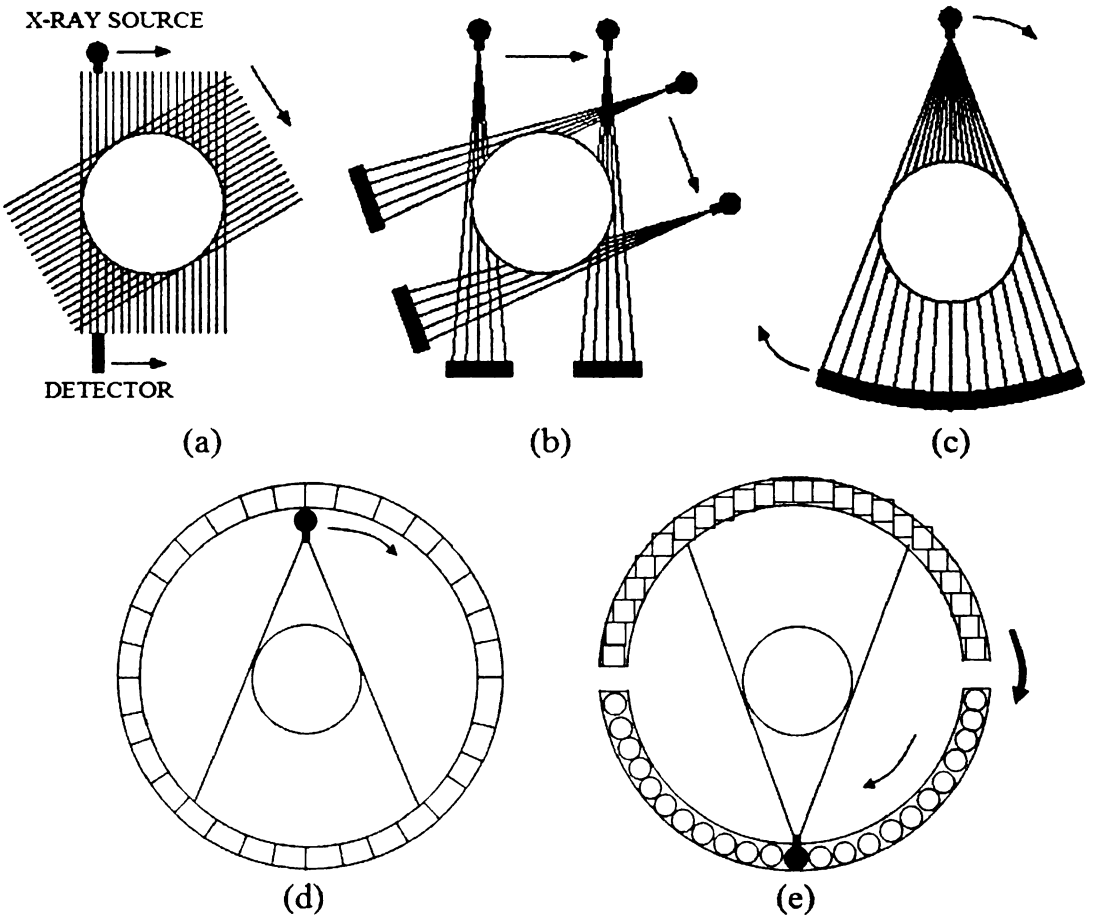

Figure 8.2. Schematic illustration of different generations of X-ray CT scan geometries. (a) First generation, translate-rotate pencil beam geometry. (b) Second generation, translate-rotate fan beam geometry (c)Third generation, rotate-only geometry [151] (d) Fourth generation rotate/stationary fan beam geometry (e) Fifth generation cone beam cylindrical geometry [152].

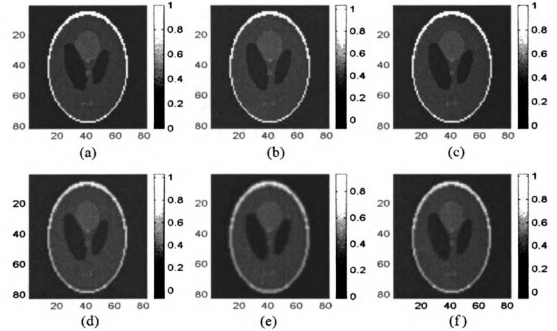

Figure 8.3. CT reconstruction results of conventional methods. (a) 81x81 Modified Shepp-Logan head phantom image. (b) Kaczmarz reconstruction at 60^{th} iteration. (c) Kaczmarz reconstruction at 300^{th} iteration. (d) FBP with Ram-Lak filter and spline interpolation. (e) FBP with Hamming filter and spline interpolation. (f) FBP with Shepp-Log filter and spline interpolation.

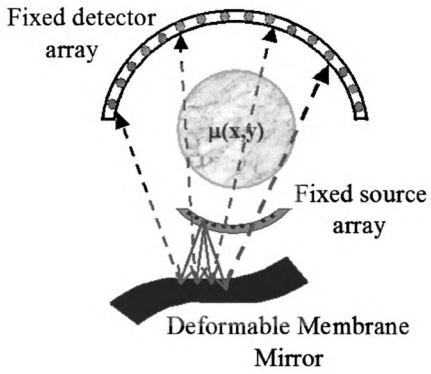

Figure 8.4. Schematic diagram of mirror based X-ray CT.

8.3 Mirror based X-ray CT

8.3.1 System Model

The schematic diagram of deformable mirror based X-ray CT technique is illustrated in Figure Figure 8.4. The numerical model for tomographic imaging consists of a fan beam X-ray source, detector array and deformable mirror arranged along an annular ring. The image plane containing the X-ray source, detectors and deformable mirror is transverse to the axis of the object as shown in Figure Figure 8.4. During data acquisition, for each fan beam source position, X-ray projections are collected for different unique mirror deformations $w(x, y)$ by adaptively changing the actuator potential distribution, $V(x, y)$. Depending on the mirror deformation, the incident X-ray gets diverted along a path governed by the Bragg's law of reflection [153] and

is measured at the detector after traversing the object under examination. From the knowledge of the reflective coating on the deformable X-ray mirror, the energy of the reflected X-ray can be determined. Using Bragg angle of the reflective coating and ray tracing technique [154], the path traversed by each X-ray from the source to detector array via the object is determined. The path traversed and the intensity of the individual X-rays at the detector are used to obtain the X-ray attenuation image of the object. The projection data collected for all unique mirror shapes aid in reconstructing the 2D slice of the 3D object using iterative algorithms.

The quasi-stationary imaging setup in Figure Figure 8.4 offers limited field-of-view (LFOV) of the object. A major concern with LFOV imaging in contemporary CT systems is limited angle projection data that leads to poor resolution and partial image reconstruction [56]. Unlike contemporary CT systems, in the mirror based CT system, even with LFOV, voluminous projection data can be acquired using a multitude of mirror shapes. For unique and information-rich projection data, several mirror shapes with smooth shapes that deflect the X-rays towards the object were used in the numerical simulations.

8.3.2 Kaczmarz Reconstruction

Tomographic image reconstruction involves the estimation of the unknown attenuation vector μ from the known projections g and mapping function A in 8.4. Since each X-ray traverses through few pixels in the discretized object, the resulting projection matrix, A is large and sparse. The sparsity of the huge projection matrix prohibits the use of conventional matrix theory methods. Thus, for solving (8.4) several iterative reconstruction techniques based on projection methods were proposed of which, the algorithm proposed by Kaczmarz [148] is the foremost. If a unique solution existed, the iterative method proposed by Kaczmarz was proved to solve non-singular, singular and inconsistent systems of equations [156].

The classical Kaczmarz algorithm starts with an initial estimate μ^{est} and projects

the estimate on the set of N^2 dimensional hyper planes in (8.4) to obtain g^{est}. The normalized projection estimate for the i^{th} ray is given by the expression,

$$g_i^{est} = \frac{a_i^T \mu^{est}}{a_i^T a_i}, \quad i = 1, 2, .., M \tag{8.5}$$

where $a_i = \left(a_{i1}, a_{i2}, ..., a_{iN2}\right)$ is the i^{th} row vector in the projection matrix A. The projection error $g_i - g_i^{est}$ for μ^{est} is used to compute the correction factor in the update equation. The correction factor,

$$\delta\mu^{est} = \frac{g_i - a_i^T \mu^{est}}{a_i^T a_i} a_i \tag{8.6}$$

that yields the new estimate,

$$\mu_{new}^{est} = \mu^{est} + \delta\mu^{est} \tag{8.7}$$

reduces the error $\|A\mu_{new}^{est} - g\|$. In iterative form, the estimate at the k^{th} successive projection is given by,

$$\mu^k = \mu^{k-1} + \frac{\left(g_i - a_i^T \mu^{k-1}\right)}{a_i^T a_i} a_i, \quad i = 1, 2, .., M \tag{8.8}$$

where μ^k is the k^{th} estimate of the solution μ^{soln}. If μ^{soln} exists and is unique, a successive projection of the estimate (8.8) onto the hyperplanes in (8.4) will converge to the true solution in the limit [156]. In the next section, simulations results obtained using the Kaczmarz algorithm for the limited-view X-ray CT technique is presented.

8.3.3 Numerical Simulations

For comparison with conventional CT, the commonly used *Shepp-Logan* head phantom was used in the numerical simulations [66]. In the simulations, X-ray scattering

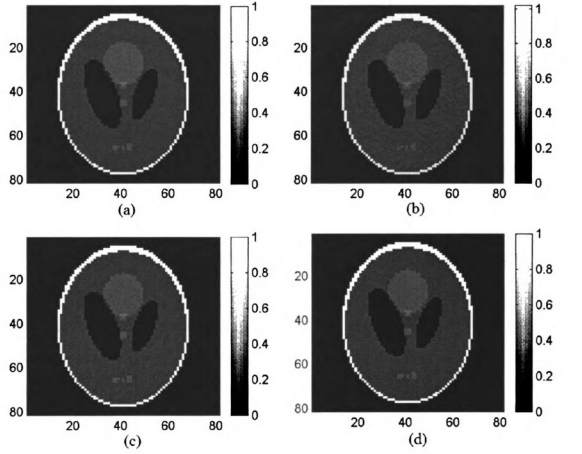

Figure 8.5. Kaczmarz reconstruction results for the deformable mirror based X-ray CT technique (a) 81x81 Modified Shepp-Logan head phantom image (b) Reconstruction at 100^{th} iteration (c) Reconstruction at 300^{th} iteration.

effects were neglected and only the primary X-ray path was considered for projection measurement. Due to lack of information on the physical properties of the X-ray reflective coating for the deformable mirror, Snells law of reflection was used instead of the Braggs law.

8.3.3.1 LFOV Mirror CT for 14 Source Locations

During data collection, a fan beam X-ray source with 45 pencil beams was positioned at 14 locations along an arc and unique mirror shapes (flat, quadratic and cubic) were used for X-ray projections. For each mirror shape, projection matrix A was

assembled and unique set of projection data were collected for all 14 positions of the fan beam X-ray source as illustrated in Figure Figure 8.4. X-ray projections acquired for the deformable mirror CT arrangement were used to iteratively reconstruct the X-ray attenuation property of the phantom using Kaczmarz algorithm. Using 61 mirror shapes, 7039 unique projections were collected. In the simulations, a single iteration of the Kaczmarz algorithm corresponds to obtaining projections on all the M projection planes, where M is the total number of unique projections.

Figures Figure 8.5(b)-(c) show the image reconstructions obtained using Kaczmarz algorithm at 100^{th} and 300^{th} iteration. At the 100^{th} iteration, even though the reconstructed image has speckle noise, all the ellipses in the head phantom are successfully recovered. With repeated projections, the quality of the reconstructed image improved with almost perfect reconstruction at the 300^{th} iteration. Figures Figure 8.7 (a)-(f) show image reconstructions and reconstruction errors for different iterations of Kaczmarz algorithm. Figure Figure 8.6 shows the horizontal and vertical line scans taken along the center of the head phantom after 100^{th} iteration. A successive projection yielded a solution close to the true solution for the over-determined consistent system (M=7039, N=6561), a characteristic of the Kaczmarz algorithm [148]. The convergence of the reconstructed CT image can be accelerated using modified iterative reconstruction algorithms [56]. Prior knowledge of the non-negative property of the spatial attenuation function $\mu(x, y)$ and the boundary of the object being imaged were used to constrain the estimate during each projection. The computation time for a single iteration was approximately 1.03 sec on a shared Sun Fire v880 server with 4x750 MHz UltraSPARC III processors.

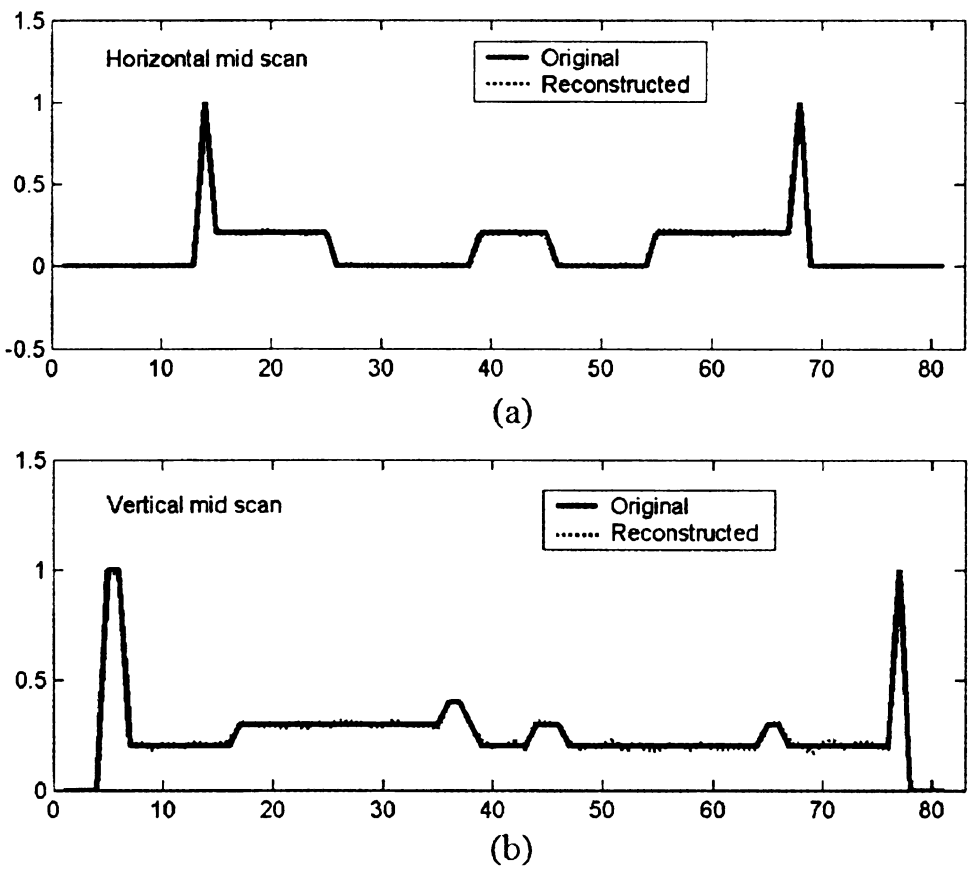

Figure 8.6. Central transects of the reconstructed phantom at 100^{th} iteration of Kaczmarz algorithm. (a) Horizontal line scan. (b) Vertical line scan.

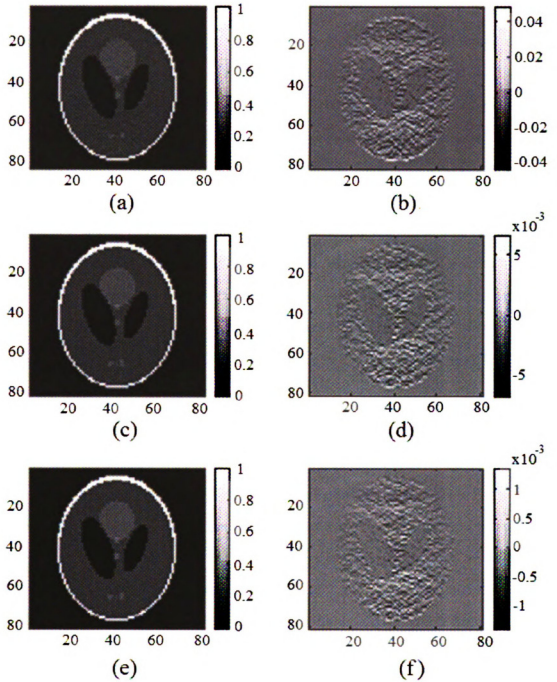

Figure 8.7. Convergence of the iterative reconstruction for X-ray mirror CT (a) reconstruction and (b) error at 100^{th} iteration; (c) reconstruction and (d) error at 300^{th} iteration; (e) reconstruction and (f) error at 500^{th} iteration.

8.4 Deformable Mirror Vs Conventional CT

8.4.1 System Advantages

In the mirror based tomography technique, the detector array remains stationary while the fan beam source is moved to a few predetermined positions for projection measurements. The quasi-static system configuration has minimal alignment and positioning errors associated with rotation or translation of the scanner unlike the contemporary CT setups shown in Figure Figure 8.2. Even with LFOV, more projection data can be acquired by varying the mirror deformations. Unlike contemporary CT systems, image reconstruction is not constrained by the number of available projections as enormous amount of projection data can be measured with appropriate choice of mirror shapes. Thus, with this scan arrangement good imaging results can be obtained for objects/scenarios that restrict full view or equal distribution of projection angle. The LFOV CT scan arrangement precludes the need for a closed chamber and hence is patient friendly.

8.4.2 Comparison - CT Reconstructions

To evaluate the performance of mirror based system with that of conventional CT, projections were calculated for different scan configurations for fan beam X-ray source. Projections were computed for the conventional CT configuration in Figure Figure 8.2(c) for source positioned at the same 14 predetermined locations as used in the deformable mirror X-ray CT discussed in section 8.3. X-ray projections collected for 14 source positions in the absence of deformable mirror yields limited data for image reconstruction. The projection data computed with conventional CT for 14 source positions was insufficient to reconstruct $\mu(x, y)$ and hence the reconstruction result is not presented here. Due to the sensitivity of conventional CT to limited view, subsequent simulations were conducted for 90° scan coverage for different equiangular spacing between individual rotations.

8.4.2.1 LFOV CT with 90° Coverage and 1° Spacing

Limited angle simulations were carried with conventional X-ray CT technique for equally distributed projection angles within [45°, 135°] interval for X-ray source with 117 pencil beams for the CT configuration in Figure Figure 8.2 (a). Figures Figure 8.8(b)-(c) show reconstruction results obtained using Kaczmarz algorithm at 60^{th} and 250^{th} iterations. As expected, iterative method results for limited-view X-ray CT are acceptable since the iterative method does not require full view projections for reconstruction[56], [69]. Figures Figure 8.8(d)-(f) show the reconstruction results of the FBP algorithm for Ram-Lak, Hamming and Shepp-Logan filters with spline interpolation. As FBP involves back projecting the filtered projections collected at equally distributed angles over 180° or 360° into image space, the reconstructions suffer severely for limited-view projections and lack the accuracy required in medical applications. During data acquisition with conventional X-ray CT, projections were measured with 1° rotational separation for 91 source-detector positions. In contrast, in the mirror based CT system, projections were collected only for 14 pre-determined source locations of the fan beam X-ray. In the limited view and fixed detector scan configuration, the deformable mirror enabled acquisition of multi-view data for reliable image reconstruction.

8.4.2.2 LFOV CT with 90° Coverage and 6° Spacing

Next, simulations with conventional CT shown in Figure Figure 8.2 (a) were conducted for 15 equi-spaced projection angles within the 90° scan coverage; similar to the scanning configuration in mirror based CT. Figure Figure 8.9(b) shows the reconstructed image at 200^{th} iteration obtained using Kaczmarz algorithm. The reconstruction result is apparently poor and did not improve with iterations. Even though the scan configuration was almost the same, with the mirror based approach more projections were easily obtained using a wise choice of mirror shapes. The mirror

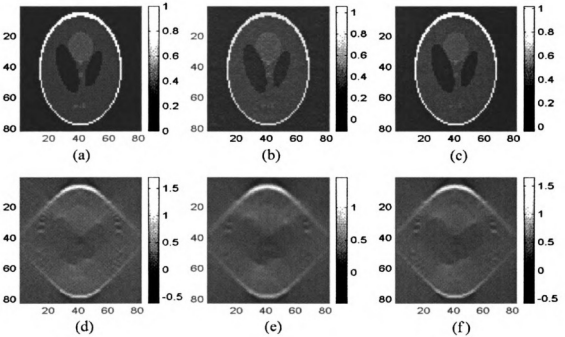

Figure 8.8. LFOV reconstruction results of conventional methods. (a) 81x81 Modified Shepp-Logan head phantom image (b) Kaczmarz reconstruction at 60^{th} iteration (c) Kaczmarz reconstruction at 250^{th} iteration (d) FBP with Ram-Lak filter and spline interpolation (e) FBP with Hamming filter and spline interpolation (f) FBP with Shepp-Log filter and spline interpolation.

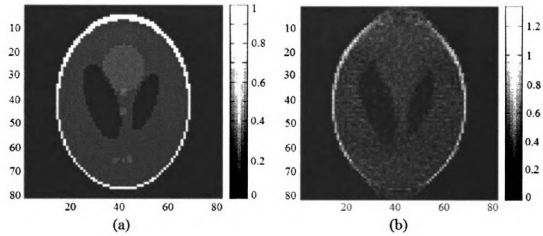

Figure 8.9. Kaczmarz reconstruction for conventional CT with LFOV scan configuration similar to the MMDM based CT technique. (a) 81x81 Modified Shepp-Logan head phantom image. (b) Kaczmarz reconstruction at 200th iteration for parallel beam X-ray source.

compensated the limited source movement and yielded superior image reconstruction. The detailed comparison of the simulation results obtained for the conventional and mirror based CT systems reveal the advantages of the deformable mirror based CT technique for noninvasive imaging.

A quantitative comparison of image reconstructions for the Shepp-Logan head phantom obtained with conventional X-ray CT for full and limited view scan configurations are tabulated in Table Table 8.1. Irrespective of the reconstruction method, the error in reconstruction is higher for limited-view CT. Particularly, the error is higher for FBP method than that for iterative image reconstruction. Table Table 8.2 lists the reconstruction error obtained with mirror based CT at different iterations. As expected, the error decreases with increase in iteration and is significantly better than the reconstruction errors obtained with conventional CT listed in Table Table 8.1. Image reconstructions in the numerical simulations demonstrate the advantages of the proposed deformable mirror CT compared to conventional CT. The proof of concept simulations of the deformable mirror CT in the X-ray regime gives the impe-

Table 8.1. Summary of the reconstruction error for conventional X-ray CT with 1° rotational spacing.

CT view	Kaczmarz 100^{th} iteration	Kaczmarz 300^{th} iteration	Shepp-Logan	Ram-Lak	Hamming
Full	0.5087	0.1949	4.0257	4.1066	4.0517
Limited	0.6503	0.4184	9.1527	19.2350	18.8240

Table 8.2. Image reconstruction error of Kaczmarz algorithm for X-ray Mirror CT.

CT	100^{th} iteration	300^{th} iteration	500^{th} iteration	1000^{th} iteration
Mirror CT	0.2090	0.0287	0.0060	0.0002

tus to investigate the feasibility of the proposed tomography system in the microwave regime. In the next section, feasibility of extending the imaging setup for cancer therapy is studied via numerical simulations using X-rays.

8.5 Mirror based Radiation Therapy

Besides CT imaging, the deformable mirror system configuration could also be used for radiation therapy. The feasibility of system configuration for radiation therapy is evaluated using the modified Shepp-Logan head phantom. Using the reconstructed CT image and a proper choice of mirror deformation, the tumor can be effectively destroyed by delivering focused high energy X-ray radiation at the tumor site with minimal damage to the surrounding normal tissue.

8.5.1 Focusing for Therapy

Figure Figure 8.10 shows the schematic diagram of adaptive mirror CT system for cancer radiation therapy. In Figure Figure 8.10, the high energy X-ray source and deformable X-ray mirror are positioned in Rowland circle geometry for radiation

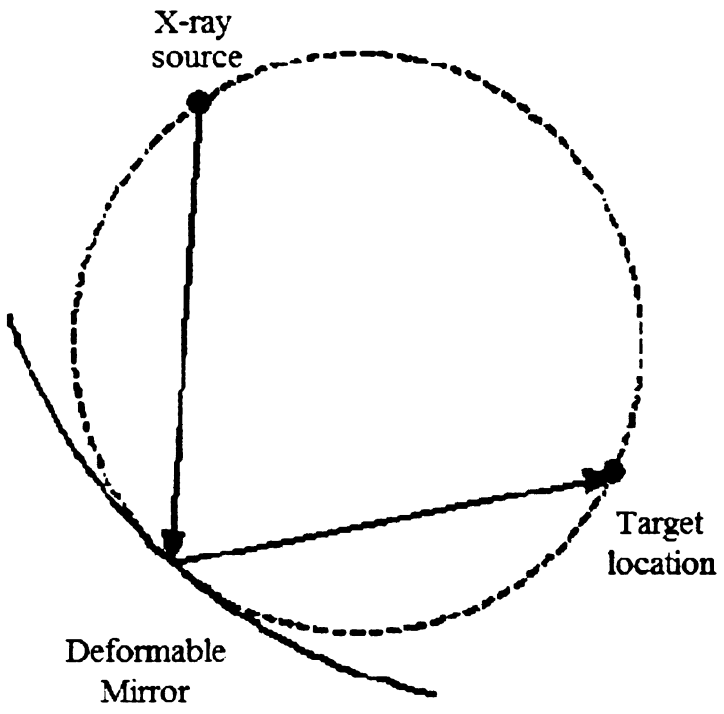

Figure 8.10. Rowland circle geometry for localized radiation therapy.

therapy. In the Rowland circle geometry, each pencil beam X-ray photons emanating from the source impinges on the mirror at the same angle and is focused back to an image point of the point source located on the same circle. In therapy setup shown in Figure Figure 8.10, the source and deformable X-ray mirror lie on a circle with diameter equal to the radius of curvature of the X-ray mirror. During therapy, the object is immobilized and remains in the same position as it was during imaging. Using the reconstructed CT image, the source, detector and mirror positions are aligned to lie on an appropriate Rowland circle and by applying a suitable potential distribution , a parabolic mirror deflection $w(x, y)$ with radius of curvature equal to the diameter of the Rowland circle is achieved. With the source and mirror aligned at Bragg angle, the incident X-ray photons are reflected and effectively focused at the tumor site with minimal collateral damage to adjacent healthy tissue.

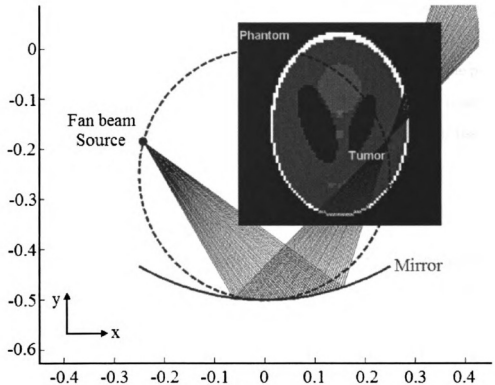

Figure 8.11. Adaptive focusing of high energy X-ray photons for radiation therapy using deformable X-ray mirror.

8.5.2 Numerical Simulations

The X-ray reflective mirror device in the Rowland circle configuration acts as a deformable lens and steers the high energy X-rays photons to focus to the desired depth and location and selectively kill the malignant tissue. The X-ray beam focused inside the head phantom in Figure Figure 8.11 demonstrates the therapeutic capability of the proposed radiation therapy technique. The proof of concept simulation using simple ray theory indicate the potential advantage of the proposed deformable mirror tomography for noninvasive imaging and cancer therapy. In the proposed system, radiation therapy can be performed using the same setup without the patient leaving the table and hence without the need for any re-calibration. This imaging cum therapy system also minimizes organ motion of both normal and tumor tissues caused by patient mobilization from imaging to radiation therapy facility.

8.6 Implementation Issues

X-ray reflecting mirrors using layers of high atomic elements were attempted as early as 1935 [157]. In 1970s high-reflective multi-layered mirror was successfully designed using alternate layers of absorbing and non-absorbing elements [158]. With advance in micro-lithography, multi-layered mirrors were designed for X-rays for applications over a wide energy range 8-180 keV [159]-[161]. Though the deformable mirror X-ray CT system in the simulation assumed a deformable X-ray mirror capable of reflecting X-rays incident at all angles of incidence, in practice X-ray mirrors exists only for grazing angle of incidence. In the proof of concept model, scattering and diffraction effects were ignored for simplicity. Also, the simulations were carried out for Snell's law of reflection instead of the Bragg's law due to the absence of multi-layered X-rays mirror for wide angles of incidence. The outcome of the proof of concept X-ray simulations for the mirror based tomography cum therapy setup appear promising. The simulated CT reconstructions are comparable to the full view classical X-ray CT

reconstructions and are superior those obtained with limited-view CT.

8.7 Conclusions

Numerical simulations in the X-ray regime simplifies wave propagation to a simple straight ray model without scatterring and diffraction effects. The outcome of the numerical simulations for the deformable mirror tomography in X-ray regime assuming the existence of multi-layer X-ray mirror appear promising. The simulations results of the proposed CT are comparable with full-view conventional CT. In the limited-view numerical simulations, the proposed CT technique out performs conventional CT and yields good reconstructions. The imaging setup also serves as a high energy radiation therapy device which, can be used to selectively kill the tumor by focusing the high energy radiations at the tumor site sparing the neighboring benign tissue. Image reconstruction obtained for deformable mirror X-ray CT paves the way for further investigation of the proposed tomography system in the microwave regime.

CHAPTER 9

OPTIMAL MIRROR DEFORMATIONS FOR MICROWAVE TOMOGRAPHY

Introduction

For any tomography system, it is essential to use unique measurements for reliable reconstruction. In the deformable mirror based tomography technique proposed in this thesis, the flexible mirror ensures unique and information rich measurements for breast imaging. Thus, it is paramount to determine the optimal mirror deformations for tomography. The strategies followed to obtain the optimal set of mirror deformations for permittivity inversion are discussed in detail in this chapter. The design and functionality of the proposed deformable mirror tomography setup is presented in section 9.1. The choice of the operating frequency for breast imaging is discussed in section 9.2. The need for optimal mirror deformations and the mathematical formulation for field equations are presented in section 9.3. The selection of useful and unique mirror deformations for tomography are explained in sections 9.4 and 9.5 respectively. Section 9.6 discussed the realization of the mirror deformations during data acquisition. The feasibility of the procedures described in this chapter are evaluated via 2D computational model. The step by step procedure followed to determine the optimal mirror shapes for multi-view field measurements are summarized in section 9.7.

9.1 Deformable Mirror Tomography Setup

The proposed microwave tomography technique for breast imaging employs a continuously deformable mirror with a metallic coating as shown in Figure Figure 9.1. The imaging setup consists of a fixed electromagnetic source illuminating the membrane deformable mirror and a circular array of receivers surrounding the breast

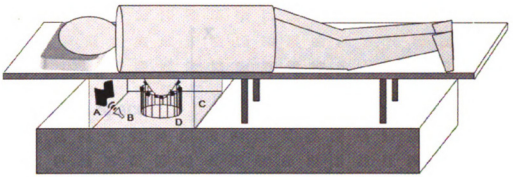

Figure 9.1. Schematic diagram of deformable mirror microwave tomography setup.

[166]. During data acquisition, the field emanating from an electromagnetic source which is incident on the deformable mirror is re-directed towards the imaging region containing breast for multi-view field measurements. By continuously deforming the mirror shape, the secondary field incident on the breast is steered for multi-view field measurements. The measurements obtained for each mirror shape are used in the permittivity inversion algorithm. Unlike conventional tomography system, a multitude of measurements can be acquired by changing the mirror deformation without the need to increase the number of transceiver antennas. The mirror setup with a single transmitter far away from the receivers eliminates the need for antenna compensation algorithms to minimize cross talk between the active and the neighboring in-active antennas.

9.2 Frequency Selection For Breast Imaging

In inverse scattering applications, it is of paramount importance to determine the optimal frequency range. The frequency of operation is often determined based on the average physical dimension of the scatterer which in this case is the average dimension of the coronal slice of mature female breast. The dielectric property of the

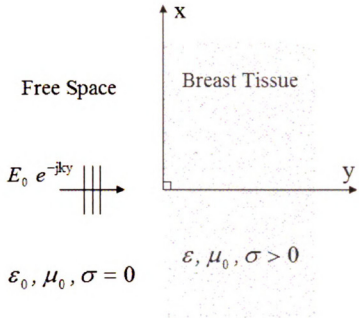

Figure 9.2. Planar Breast Tissue Model.

breast tissue at microwave frequencies is also one of the key factors that determines the operating frequency. The factors that were considered to determine the microwave frequency range for breast tomography is discussed in this section.

9.2.1 Plane Wave Penetration Inside Breast Tissue

The penetration depth of microwaves inside the breast limits the useful frequencies for tomography. An estimate of the operating frequency is determined with the aid of the tissue dielectric properties in the EM spectrum [47]. The penetration depth of a plane wave inside the benign and malignant breast tissues was calculated over 50MHz-10GHz using the experimental dielectric property reported by Joines et al [47] and the first order Debye dispersion model in [163]. Consider a plane wave of the

form,

$$\begin{aligned} E_z(x,y,\omega) &= E_0 e^{-jk\left(x\cos\theta^i + y\sin\theta^i\right)} \\ &= E_0 e^{-jky}, \quad [\because \theta^i = \frac{\pi}{2}] \end{aligned} \tag{9.1}$$

incident normally on a planar breast model as shown in Figure Figure 9.2. The plane wave inside the lossy breast given by (9.1) can be rewritten as,

$$\begin{aligned} E_z(x,y,\omega) &= E_0 e^{-(\alpha + j\gamma)} \\ &= E_0 e^{-\alpha y} e^{-j\gamma y}, \quad (\alpha > 0, \gamma > 0) \end{aligned} \tag{9.2}$$

In (9.2), α and γ are the attenuation and propagation constants of the plane wave inside the breast. Substituting $k = \omega\sqrt{\mu_0\left(\epsilon' - j\epsilon''\right)}$ into (9.2), yields the attenuation and propagation constants [27],

$$\alpha = \omega\sqrt{\frac{\mu\epsilon'}{2}}\left\{\left[\left(\frac{\epsilon''}{\epsilon'}\right)^2 + 1\right]^{\frac{1}{2}}\right\}^{\frac{1}{2}} \tag{9.3a}$$

$$\gamma = \omega\sqrt{\frac{\mu\epsilon'}{2}}\left\{\left[\left(\frac{\epsilon''}{\epsilon'}\right)^2 - 1\right]^{\frac{1}{2}}\right\}^{\frac{1}{2}} \tag{9.3b}$$

In (9.3a) - (9.3b), $\omega = 2\pi f, \mu = \mu_0, \epsilon' = \epsilon_0\epsilon_r(x,y)$ and $\epsilon'' = \frac{\sigma(x,y)}{\omega}$. The field strength inside the breast tissue is given by the equation,

$$|E_z(x,y,\omega)| = E_0 e^{-\alpha y} \tag{9.4}$$

The distance at which the field strength $|E_z(x,y,\omega)|$ drops to e^{-1} times the initial value $|E_z(x,y=0,\omega)|$ is defined as the *skin depth* of the incident time harmonic EM

wave. The skin depth distance,

$$\delta = \frac{1}{\alpha} \tag{9.5}$$

was calculated for the benign and malignant breast tissues over 50 MHz-10 GHz. Experimental data reported in [47] was used for 50-900 MHz frequency range and the first order Debye dispersion model [163],

$$\epsilon(\omega) = \epsilon_{\infty} + \frac{\epsilon_s - \epsilon_{\infty}}{1 + j\omega\tau} \tag{9.6}$$

was used for frequencies in 1-10 GHz range. In (9.6), the Debye parameters ($\epsilon_{\infty} = 7, \epsilon_s = 15, \sigma = 0.15 Sm^{-1}$) and ($\epsilon_{\infty} = 50, \epsilon_s = 4, \sigma = 0.7 Sm^{-1}$) were used for benign and malignant breast tissues respectively with $\tau = 6.4x10^{-12} ps$. Figure Figure 9.3 shows the skin depth calculated for the benign and malignant breast tissues. In Figure Figure 9.3, it can be observed that the signal attenuation is significantly higher at frequencies above 1000 MHz.

9.2.2 Excitation Frequency

In the mid frequency range of 50-900 MHz, the dielectric spectrum of breast tissues in Figure Figure 3.1 shows almost a flat response for both malignant and benign breast tissues and a very nonlinear behavior above 1 GHz. Due to the significantly large increase in tissue conductivity above 1 GHz the penetration depth deteriorates drastically in the higher end of frequency spectrum as seen in Figure Figure 9.3. Assuming the average coronal section of breast to vary between 9-12 cm in diameter, the operating frequency is chosen so that $\lambda_{breast} \backsimeq a$ for reliable permittivity reconstruction. Considering the depth of penetration and average tissue dielectric constant available in literature, the operating frequency range for breast imaging was chosen to vary between 700-900 MHz.,

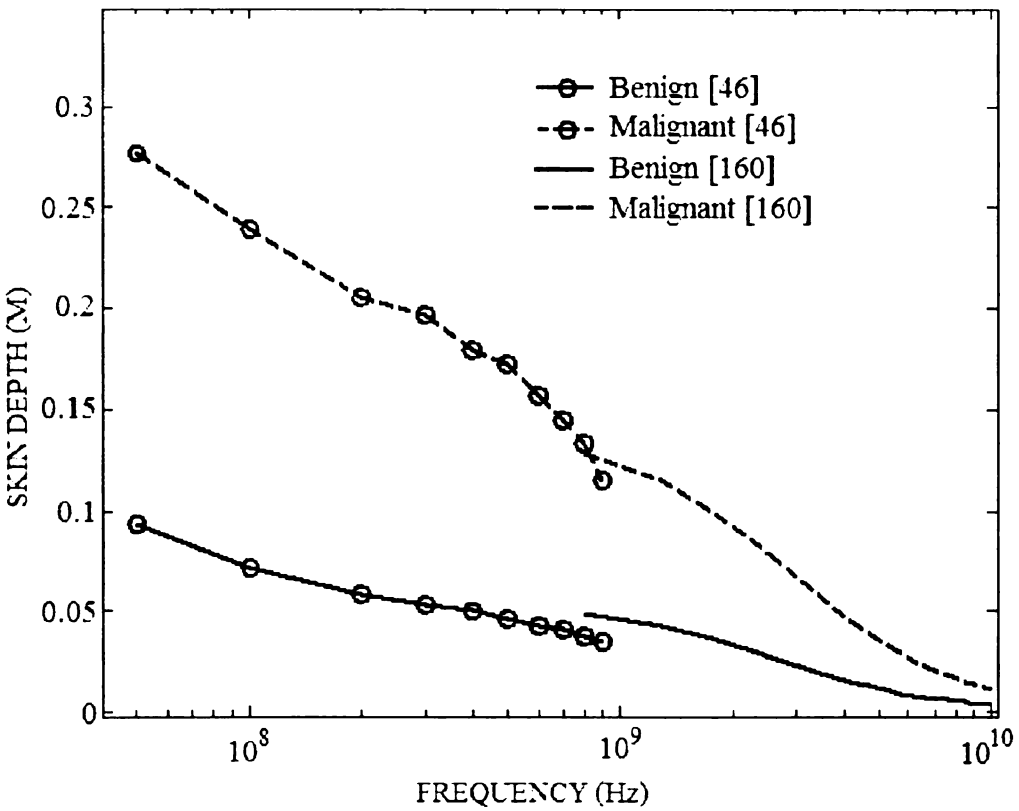

Figure 9.3. Skin depth of normally incident plane wave inside breast tissue

9.3 Need for Optimal Mirror Deformations

Microwave tomography for permittivity reconstruction is a classical inverse medium problem studied by several investigators. Microwave inverse scattering problems are ill-posed and often yield unstable and non-physical solutions [76, 162]. In order to obtain unique and stable solution to inverse scattering problem, diverse field measurements from infinitely many angles and multiple frequency measurements are required [75, 74]. The deformable mirror tomography technique proposed in this dissertation employs a single fixed EM source which essentially limits the field of view. Thus, it is essential to ensure that optimal mirror deformations are chosen to steer the incident field for information rich unique field measurements for stable permittivity inversion. This chapter presents the underlying mathematical theory, computational model and numerical techniques that yield optimal mirror deformations for breast imaging.

In two dimensions, the objective is to find useful mirror shapes such that,

$$f(x,y) \in \mathcal{R}^2 \tag{9.7a}$$

$$f \in C^2 \tag{9.7b}$$

$$Df \in C^2 \tag{9.7c}$$

The continuity and differentiability constraints in (9.7) ensure smooth mirror shapes without any undesired scattering from sharp corners [167, 168].

9.3.1 Bezier Curve Representation

There are numerous techniques to define curved objects with smooth surface [164, 165]. The Bezier parametric curve widely used in typesetting and computer graphics industry to represent smooth two dimensional curves is adapted to define the surface of the deformable mirror. The Bezier parametric curve function defined by a set of control points is obtained by fitting a curve inside the Bezier polygon with the

control points as vertices. The generalized Bezier or Bezier-Bernstein parametric curve function with N+1 control points is expressed as [165]

$$f(u) = \sum_{j=0}^{N} p_k b_{k,N}(u) \tag{9.8}$$

where $b_{k,N}$ are the Bernstein basis polynomials, p_k are the $N+1$ control points of the N^{th} order Bezier curve and $u \in [0,1]$. The Bernstein basis polynomials given by,

$$b_{k,N}(u) = \begin{pmatrix} N \\ k \end{pmatrix} u^k (1-u)^{N-k} \tag{9.9}$$

blends the control points to form the Bezier curve as illustrated in Figure Figure 9.4. The Bezier curve always passes through the first and last control points also known as the anchor points and lies within the convex hull of the control points. The blending function in (9.9) is a polynomial of degree one less than the number of control points. Bezier curves have wide applications as they are very stable and are easy to compute. Smooth mirror shapes were constructed using cubic Bezier curves inside the region of interest that contains the deformable mirror assembly. To minimize scattering from sharp end points, mirror surface with a rounded corners were modeled by joining lower order Bezier curves. Figure Figure 9.5 shows an example of a higher order mirror surface constructed using two lower order Bezier curves, $f_1(u)$ and $f_2(u)$. The basic set of mirror shapes constructed using cubic Bezier curves were used to generate a multitude of smooth shapes by sliding the control points between the anchor points and by rotating the Bezier curve about a pivot point. All mirror shapes thus generated could be used to steer the incident field for multi-view field measurements from the breast. Examples of different mirror shapes generated using Bezier polynomials for microwave tomography are shown in Figure Figure 9.6.

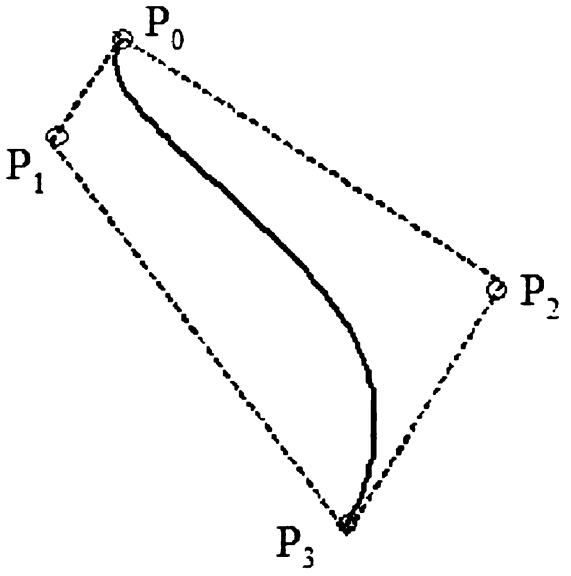

Figure 9.4. Bezier curve example.

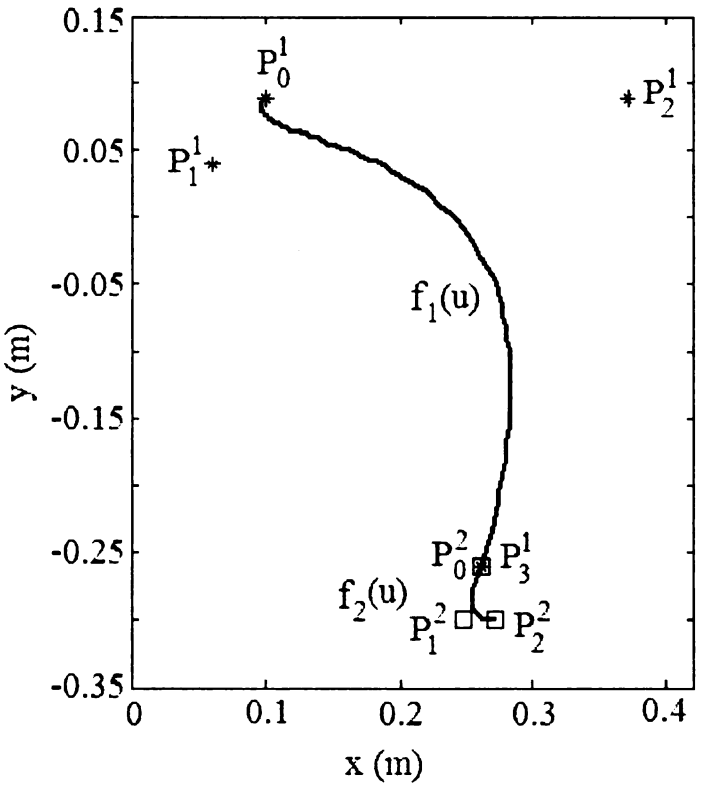

Figure 9.5. Representation of higher order curve using two lower order Bezier curves.

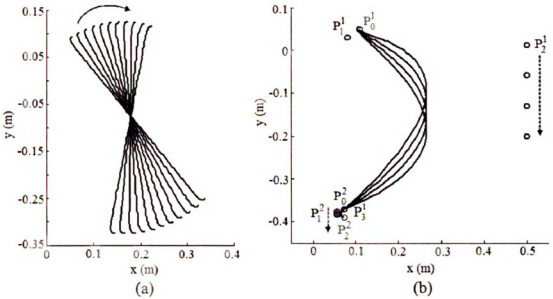

Figure 9.6. Bezier curve examples (a) Mirror shapes generated by sliding control points, p_2^1 and p_1^2 (b) Mirror shapes generated by simple rotation.

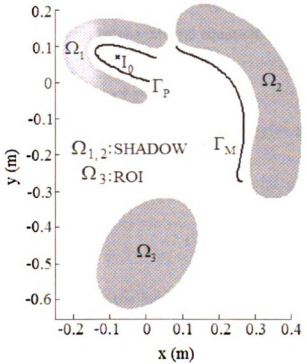

Figure 9.7. Two dimensional computational model for deformable mirror tomography.

9.3.2 TM^z Scattering from Mirror

Of the multitude of possible smooth mirror shapes, a predetermined set of curve functions are selected for breast imaging that meet the optimality conditions namely,

1. Maximum energy coupling towards scatterer with

2. Minimum energy leakage due to creeping waves.

Hence, all field simulations for this study are carried out in the absence of breast. The computational geometry for the two-dimensional case is shown in Figure Figure 9.7. In Figure Figure 9.7, the thin membrane mirror is modeled as a perfectly conducting smooth thin strip defined by the contour Γ_M and the directional EM source is approximated by a line current source I_0 with a metal backing defined by Γ_P to direct the emanating EM field towards the flexible mirror with thin metallic coating. Assuming TM^z polarization, the total field $E_z(x,y)$ maintained by the mirror, the source metal backing and the impressed line current inside Ω_3 in the absence of the breast is given by the integral equation,

$$\begin{aligned}
\hat{z}\mathbf{E}(x,y,\omega) = & - j\omega A_z \\
\hat{z}\mathbf{E}(x,y,\omega) = & - \hat{z}\frac{\omega\mu}{4}\int_{\Gamma_M} \mathbf{J}_M(x',y',\omega)H_0^{(2)}(x,y,k_b;x',y')dx'dy' \\
& - \hat{z}\frac{\omega\mu}{4}\int_{\Gamma_P} \mathbf{J}_P(x',y',\omega)H_0^{(2)}(x,y,k_b;x',y')dx'dy' \qquad (9.10) \\
& - \hat{z}\frac{\omega\mu}{4}I_0 H_0^{(2)}(k_b|x-x_s,y-y_s|)
\end{aligned}$$

where (x_s,y_s) is the location of the line current source and k_b is the wave number of the background medium. Equation (9.10), follows from the surface equivalence theorem and the EFIE derived in sections 4.5.5 and 5.2 respectively. The unknown induced current densities $\mathbf{J}_m$ and $\mathbf{J}_p$ are obtained by solving (9.10) with the boundary

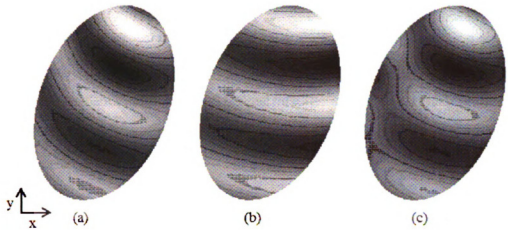

Figure 9.8. Field pattern, $\hat{z} \cdot \vec{\mathcal{E}}(x, y, z; t = 0)$ maintained by different mirror shapes in Ω_3.

conditions,

$$E_z(x, y, \omega) = 0, \quad (x, y) \in \Gamma_P, \Gamma_M \tag{9.11}$$

using method of moments [51, 52]. With the knowledge of induced current densities, the total field maintained by the mirror model inside Ω_3 that defines the imaging region is obtained using (9.10). In the 2D model illustrated in Figure Figure 9.7, the location of near field imaging region Ω_3 is chosen such that the direct interaction between the source and breast is minimized and that spurious scattering from the mirror corners are attenuated before they reach the breast. In the simulations, the optimal location of the breast inside Ω_3 was found to be approximately $2\lambda_{couplant}$ away from the nearest edge of the deformable mirror.

9.3.3 E-field Inside Imaging Region

For each mirror deformation $f(u)$, induced current densities computed using (9.10)-(9.11) were used to determine the total field $E_z(x, y, \omega)$ in Ω_1, Ω_2 and Ω_3 shown in Figure Figure 9.7. Of the multitude mirror shapes that satisfied (9.7) and the conditions in section 9.3.2, it was observed that fields generated by many mirror shapes

yield similar field patterns inside the imaging region Ω_3. Such mirror deformations yield redundant information in field measurements. Figure Figure 9.8 shows the z-component of the instantaneous field inside Ω_3 for unique mirror deformations. The field patterns in Figure Figure 9.8 illustrate the ability of the membrane mirror to maintain different angles of incidence in Ω_3 for multi-view field measurements from the breast.

9.4 Admissible Mirror Deformations

For tomography, redundancy in the field measurements has to be eliminated for stable reconstruction of spatial permittivity distribution of the breast. Thus, it is essential to eliminate mirror deformations that yield similar field measurements. In addition to the elimination of redundant mirror shapes, deformations that do not direct the EM waves towards the breast should also be disregarded. Strategies followed to identify **admissible** mirror shapes are discussed in this section.

9.4.1 Selection Criteria

Of the multitude mirror deformations, the surfaces Γ_M that yield useful measurements of the breast should be identified. A subset of the mirror deformations, $\{\Gamma_M\}_{i=1}^{K}$ generated using (9.8), that satisfy the criteria,

$$\underset{\Gamma_M}{arg\ max} \left\{ \frac{E_z^{\Omega^3}(x,y,\omega)}{E_z^{\Omega^{shadow}}(x,y,\omega)} \right\} \tag{9.12}$$

alone are retained for field measurements. In (9.12), $\Omega^{shadow} = \Omega^1 \cup \Omega^2$ defines the shadow region, $E_z^{\Omega^1}(x,y,\omega)$ is the total field inside the domain of interest that corresponds to the location of the breast during data acquisition and $E_z^{\Omega^{shadow}}(x,y,\omega)$ is the total field in the shadow regions in Figure Figure 9.7. The criterion (9.12), assures that most of the EM field reflected by the deformable mirror is steered towards the

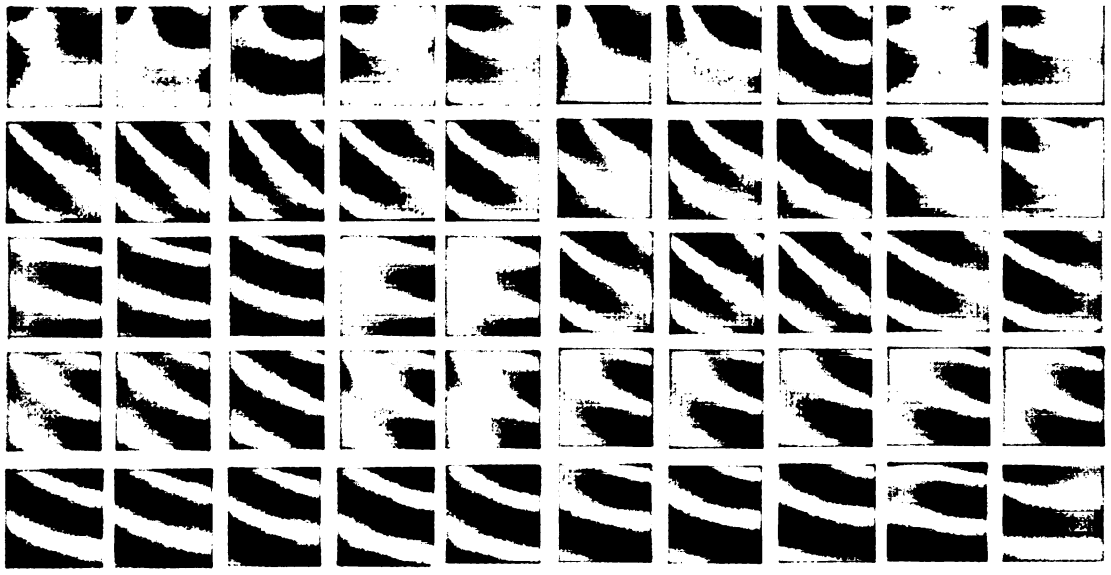

Figure 9.9. $\hat{z} \cdot \vec{\mathcal{E}}(x, y, z; t = 0)$ maintained by deformations $f(u)$ that satisfy (9.7),(9.12).

breast with minimal amount of field leaking into the shadow regions and else where inside the imaging tank. Figure Figure 9.9 shows the field pattern produced by a subset of the useful mirror deformations that satisfy (9.7) and (9.12). A total of 133 deformations that satisfied (9.7) and (9.12) were identified as useful shapes for breast imaging.

9.5 Redundancy Elimination

The criterion, (9.12) guarantees that the mirror surfaces $\{\Gamma_M\}_{i=1}^{K}$ yield useful field measurements with the breast positioned inside Ω^3. However, the field maintained by useful mirrors could yield similar field pattern in the domain of interest resulting in redundant field measurements. The redundancy in the measurements is minimized by applying pattern classification tools such as feature extraction and classification to the total field, $E_z^{\Omega^3}(x, y, \omega)$ maintained by the mirror deformations that satisfy (9.12).

9.5.1 Feature Extraction

To eliminate redundancy in field measurements, a feature set is computed for the field maintained by each useful mirror shape in the absence of the breast inside Ω^3. Besides dimensionality reduction, the objective of feature extraction is to identify attributes of the total field, $E_z^{\Omega^3}(x, y, \omega)$ that carry discriminatory information. The features extracted from fields due to individual mirror deformations aid in excluding the redundant mirror deformations. Features such as,

1. Correlation coefficient ρ
2. Chebychev distance $d^c(x, y)$ and
3. Power distance $d^p(x, y)$

were calculated for $E_z^{\Omega^3}(x, y, \omega)$ maintained by the individual mirror shapes. The features computed for the phasor field $E_z^i(x, y, \omega)$ for the i^{th} mirror shape inside Ω^3 are given by the equations [169],

$$\rho_{ij} = \frac{\left(E_z^i - \overline{E_z^i}\right)^T \left(E_z^j - \overline{E_z^j}\right)}{\sigma_{E_z}^i \sigma_{E_z}^j} \tag{9.13a}$$

$$d_{ij}^c = \frac{d_{ij}}{max\left\{d_{ij}\right\}}, \quad d_{ij} = max|E_z^i - E_z^j| \tag{9.13b}$$

$$d_{ij}^p = \frac{d_{ij}}{max\left\{d_{ij}\right\}}, \quad d_{ij} = \left(\sum_n |E_{z,n}^i - E_{z,n}^j|^p\right)^{1/r} \tag{9.13c}$$

In (9.13a)-(9.13c), p and r are non-negative integers, $\sigma_{E_z}^i$ is the standard deviation of phasor field for the i^{th} mirror shape and E_z^i is a complex vector containing the total field inside the domain of interest, Ω^3. Mirrors that yield similar field pattern have ρ_{ij} close to unity and distance metrics d_{ij}^c and d_{ij}^p close to zero. During redundancy

elimination, features were calculated for the real, imaginary and complex quantities of $E_z(x, y, \omega)$ produced by all admissible mirror deformations.

Correlation Coefficient

In computing the correlation coefficient, the real and imaginary parts of the phasor field $E_z^{\Omega^3}$ were concatenated into a single vector. The correlation coefficient defined in (9.13a), is a symmetric operation i.e., $\rho_{ij} = \rho_{ji}$. Figure Figure 9.10 shows the symmetric correlation matrix computed for the 133 mirror deformations. In Figure Figure 9.10, each mirror shape has a row with 133 column entries. The i^{th} row in the feature matrix contains the correlation between E_z^i and the field maintained by the remaining 132 mirror shapes. An entry in the i^{th} row with $\rho_{ij} \rightarrow 1$ imply that mirrors i and j yield redundant field patterns. Entries with $\rho_{ij} \rightarrow -1$ imply mirrors i and j yield negatively correlated field patterns, i.e., the deformations maintains complementary field patterns. Correlation matrix entries in which, $\rho_{ij} \backsimeq 0$ indicate that the i^{th} and j^{th} mirror deformations are independent. Thus, the correlation matrix can be used to eliminate redundant mirror deformations.

Distance Metrics

Distance metrics such as Euclidean, city-block, power and Chebychev are widely used in computer vision and artificial intelligence for neighborhood measures [169]. Of these distance metrics, the Chebychev and power distance computed for the total field E_z^{Ω} yielded good discrimination between fields due to different mirror surfaces, Γ_M. Unlike the Euclidean distance, Chebychev distance in (9.13b) retains only the maximum distance between two field patterns along any one dimension of the total field. The distance measure in (9.13b) can be used to identify mirror shapes that produce dissimilar fields. Figure Figure 9.11 shows the normalized Chebychev distance matrix of the complex field for the 133 mirror shapes. In Figure Figure 9.11, the i^{th} row in the Chebychev distance matrix with $d_c^{ij} \rightarrow 0$ indicate that the i^{th}

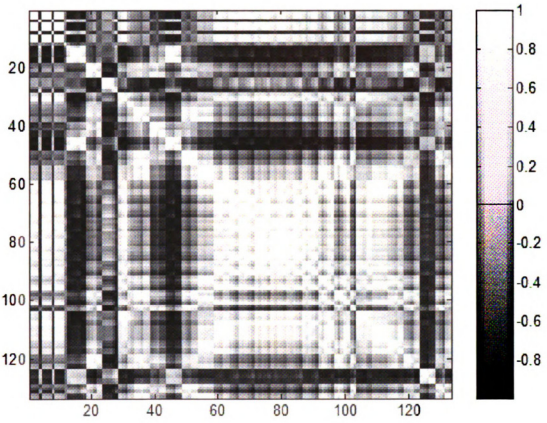

Figure 9.10. Correlation coefficient matrix for useful mirror shapes.

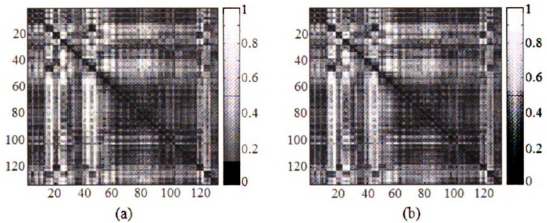

Figure 9.11. Normalized Chebychev distance metrics for (a)$\Re e\{E_z\}$ (b) $\Im m\{E_z\}$

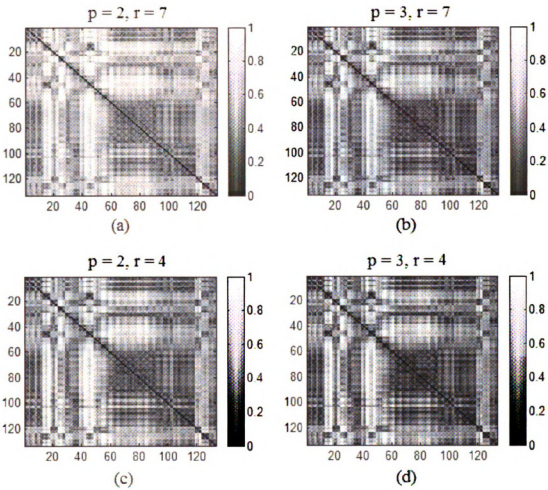

Figure 9.12. Normalized power distance of E_z for (a) $p = 2, r = 7$ (b) $p = 3, r = 7$ (c) $p = 2, r = 4$ and (d) $p = 3, r = 4$ of the useful mirror deformations.

and j^{th} mirror deformations yield redundant field measurements. Matrix entries in Figure Figure 9.11 with $d_c^{ij} \rightarrow 1$ indicate mirror deformations with dissimilar field. Power distance metric is often used to vary the progressive weight placed on the feature dimensions on which two objects or patterns vary. The progressive weighting is achieved in (9.13c) using the non-negative parameters r and p. The parameter p determines the weight for the differences on individual dimensions while the parameter r determines the weight placed on larger differences between objects or patterns. When p and r equals 2, (9.13c) reduces to the Euclidean distance measure. Figure

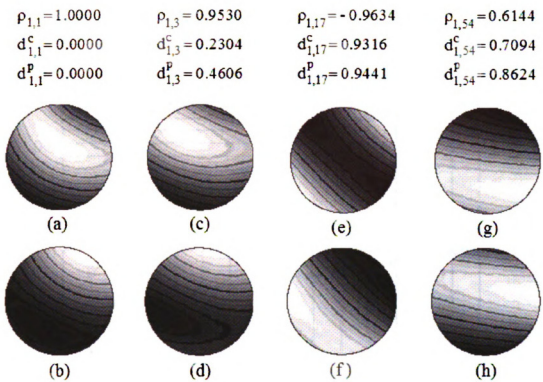

Figure 9.13. Field pattern and features computed for Mirror deformations 1, 3, 17 and 54 (a) $\Re e(E_z)$ and (b) $\Im m(E_z)$ for Mirror 1, (c) $\Re e(E_z)$ and (d) $\Im m(E_z)$ for Mirror 3 (e) $\Re e(E_z)$ and $\Im m(E_z)$ for Mirror 17, (g) $\Re e(E_z)$ and $\Im m(E_z)$ for Mirror 54 (p=2 and r=7 in 9.13c).

Figure 9.12 shows the normalized power distance matrix computed for the complex time harmonic field due to mirror deformations, $\{\Gamma_M\}_{i=1}^K$ for different values of p and r. Figure Figure 9.12 clearly elucidates the advantage of power distance for eliminating redundant mirror shapes. Figure Figure 9.13 shows an example of the real and imaginary parts of $E_z(x, y, \omega)$ due to four randomly picked mirror deformations and their feature values. The correlation coefficient and distance metrics computed between E_z^1 and $E_z^j, j = 3, 17, 54$ indicate that mirror deformations 1 and 3 yield similar field and hence will result in very similar field measurements. A visual comparison of the fields in Figure Figure 9.13 confirms the prediction of the features selected for redundancy elimination. This demonstrates that the correlation coefficient and

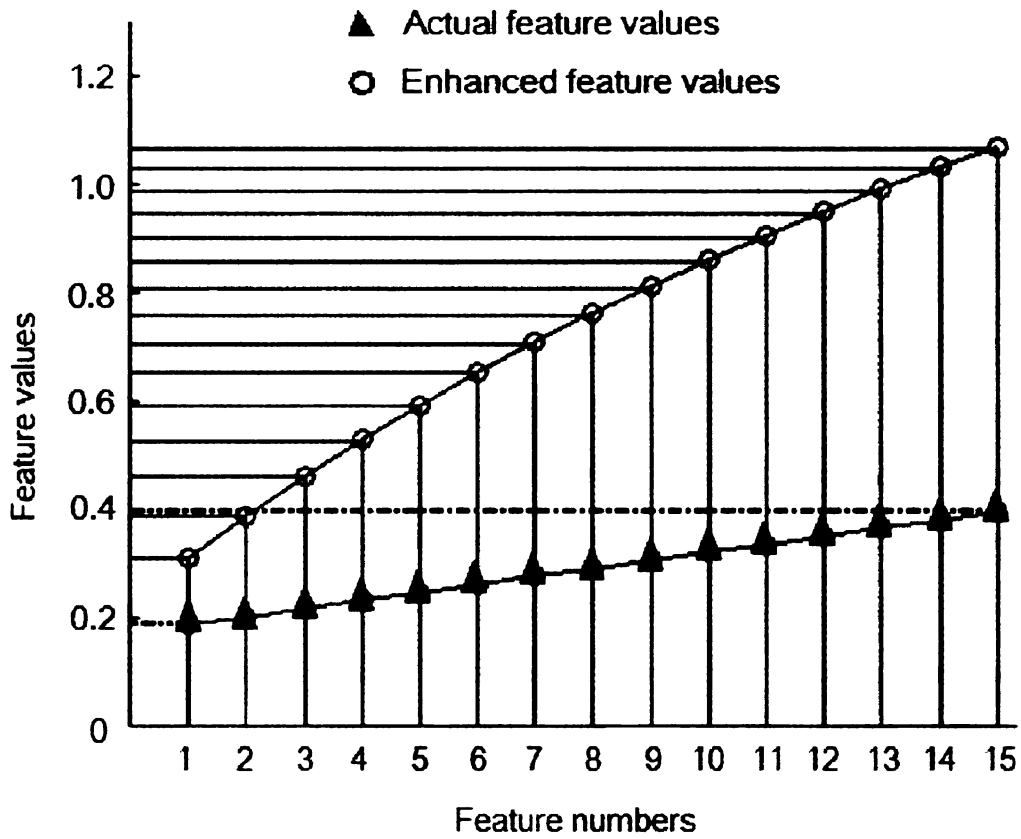

Figure 9.14. Feature contrast enhancement for mirrors a and b.

distance metrics contain discriminant information about the field maintained by the mirror deformations and can be utilized to identify redundant mirror shapes.

9.5.2 Clustering

Clustering is the UN-supervised classification of observations or feature vectors into groups or clusters [169]. The goal of clustering is to automatically identify the intrinsic similarity between feature vectors and to group them into clusters. Clustering algorithms can be used to identify the similar mirror deformations that yield redundant field measurements inside Ω^3. The distance and correlation features forms the observations for the clustering algorithm. The simplest *nearest neighbor* clustering routine is implemented to independent mirror deformations for multi-view field measurements.

Contrast Enhancement

Prior to clustering, features computed from the field distribution are enhanced to improve the performance of the clustering algorithm. In (9.13b)-(9.13c), the distance metrics are normalized by the maximum distance computed for the admissible set of mirror deformations $\{\Gamma_M\}_{i=1}^{K}$. Thus, the distances are standardized with respect to the farthest field patterns or the most dissimilar fields. The farthest feature vector behaves like an outlier that contracts the distance contrast or the spread between mirror shapes that yield dissimilar field patterns. To overcome such scenario, the range within the distance metrics is enhanced using a logarithmic mapping to stretch the contrast within feature vectors of dissimilar fields that are masked by the outliers. Figure Figure 9.14 shows the histogram of few of the features computed between mirrors a and b before and after contrast enhancement.

Nearest Neighbor Clustering

The enhanced feature vector is used in the *nearest neighbor* clustering algorithm to group similar field patterns produced by the mirror deformations, $\{\Gamma_M\}_{i=1}^{K}$. In the clustering routine, the i^{th} row in the enhanced power or Chebychev distance matrices or the correlation matrix is the feature vector, $\mathbf{x}_i$ of the field due to i^{th} mirror deformation Γ_M^i. The clustering procedure is iterated and new clusters are created until the minimum Euclidean distance between the cluster centers are above a prescribed threshold. After clustering, the mirror deformations with feature vector closest to the cluster center are eliminated and the rest are retained for tomography. The pseudo code for the nearest neighbor clustering algorithm is as follows.

1. Set $i = 1, k = 1$ and assign $\mathbf{x}_i$ to cluster C_k.

2. Increment i by $i + 1$ and compute the Euclidean distance, $d_{i,k}$ between $\mathbf{x}_i$ and cluster center C_k.

3. If $d_{i,k} < \tau_f$

- Assign $\mathbf{x}_i$ to C_k and re-compute the cluster center for the k^{th} cluster

4. If $d_{i,k} > \tau_f$

   - Increment k by $k+1$ and set $\mathbf{x}_i$ as the new cluster center.

5. Repeat steps (1)-(3), until all I feature vectors are clustered.

6. After clustering all feature vectors once, compute the Euclidean inter-cluster distance $d_c^{mn}, \forall m, n = 1, 2, ..., K$ for all K cluster centers.

7. If $d_c^{mn} < \tau_c$

   - Identify new cluster centers

8. Set $i = 0$ and iterate steps (6)-(7) with the new set of cluster centers until the minimum Euclidean distance between all clusters are above a predetermined threshold tau_c.

During clustering, the correlation, power and Chebychev feature vectors are treated separately. The outcomes of the three clustering process are combined to determine the mirror deformations for multi-view field measurements of the breast.

9.6 Implementation of Mirror Deformations

The optimal mirror deformations that produce independent field patterns are used to acquire multi-view measurements from the breast. These predetermined mirror deformations are realized by applying appropriate potential distribution $V(x,y)$ to the actuator array beneath the membrane mirror as explained in section 7.2. The mirror deformation under the influence of an applied actuator potential distribution, $V(x,y)$ is given by (7.5)-(7.6). The mirror deformations identified for tomography can be accomplished using the membrane deformable mirror by following the iterative computational procedure in Figure Figure 9.15. The potential distribution applied

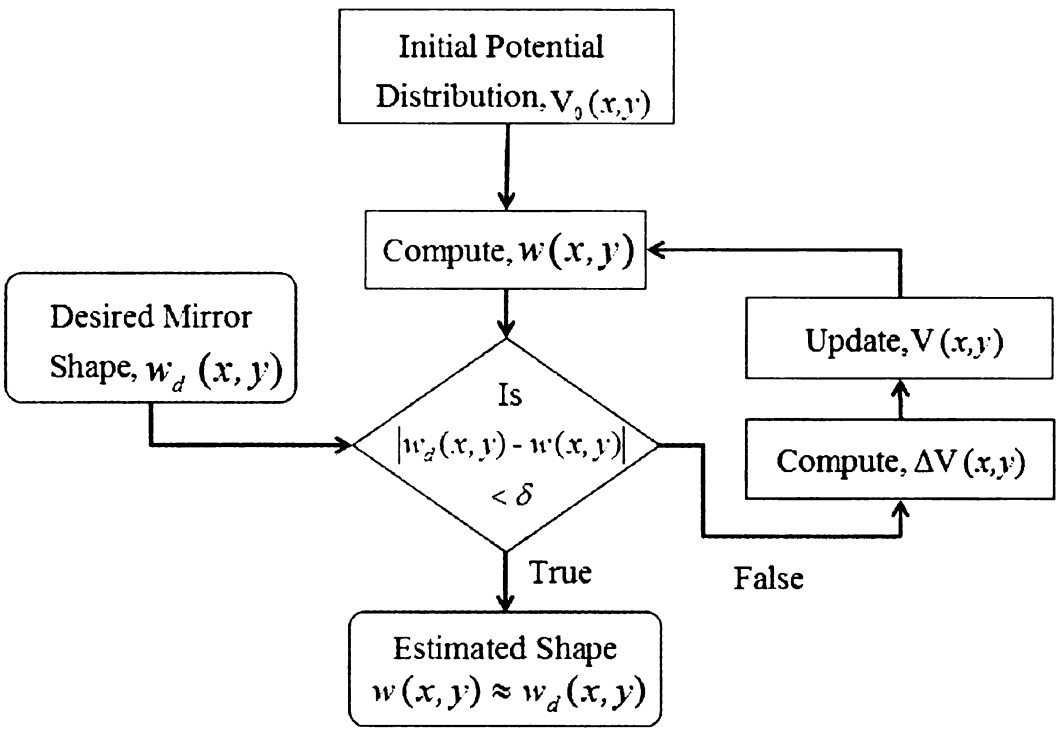

Figure 9.15. Iterative procedure for estimating the mirror actuator potentials.

to the actuator array establishes a electrostatic force between the actuator and the membrane which, causes the membrane to deflect. The mirror deflection is directly proportional to the electrostatic force and hence the applied actuator potential distribution $V(x, y)$ by (7.6). The iterative procedure begins with an initial potential distribution $V_0(x, y)$ and solves (7.5)-(7.6) with appropriate boundary conditions for the desired membrane deformation, $w(x, y)$. Using gradient search method, the error between the obtained and desired mirror deformations is minimized iteratively until the error is below the tolerance level, δ.

Estimation of the actuator potential distributions that produce the optimal mirror surfaces for tomography is a one time process which is carried off line prior to data acquisition. In fact, many adaptive optics systems employing membrane deformable mirror, control the mirror shape in real time by adaptively changing the actuator potential distribution in a feedback loop [136, 143] which, indicate the feasibility of the off line determination of mirror deformations/shapes for breast imaging. During data acquisition, the predetermined actuator potentials are applied to the membrane mirror in sequence to obtain multi-view field measurements from the breast. These predetermined actuator potential distributions are independent of the physical dimension and pathological state of the breast.

9.7 Conclusions

Following the above strategies, optimal mirror deformations that yield unique multi-view field measurements for microwave breast tomography were identified. Determination of optimal mirror shapes is summarized in the below pseudo code.

1. Fix the source, mirror and breast locations namely, (x_s, y_s), Ω_M, Ω_P and Ω^3
2. Fit Bezier curves, $f_(u) \in \Omega_M$
3. For each mirror surface, $f_j(u)$

(a) Compute total electric field $E_z(x, y\omega)^{\Omega^3}$ using (9.10)

(b) Retain mirror deformation, $f_j(u)$ if (9.7) is satisfied

4. For mirror shapes that satisfy (9.7)

   (a) Compute features using (9.13a)-(9.13c)

   (b) Employ nearest neighbor clustering to identify redundant mirror deformations

5. Dissimilar field patterns identified by the clustering algorithm yield unique multi-view field measurements for breast imaging

The identified optimal mirror deformations steer the incident field towards the breast at different angles to yield multi-view field measurements to recover the unknown spatial permittivity distribution inside the breast. The optimal mirror shapes once determined can be used for imaging any penetrable object placed in the imaging region.

CHAPTER 10

MICROWAVE BREAST IMAGING USING DEFORMABLE MIRROR

Introduction

This section deals with the mathematics and numerical implementation of breast permittivity reconstruction for the deformable mirror setup illustrated in Figure Figure 9.1. The optimal mirror deformations determined following the procedure detailed in the previous chapter are used to obtain multi-view scattered field measurements from the breast. Computational feasibility of the deformable mirror tomography technique for breast cancer detection and other potential applications are investigated using two dimensional models with varying spatial electrical property.

Section 10.1 deals with the EM theory that dictates the field maintained by the deformable mirror tomography setup in the presence of the heterogeneous breast. The field measurements maintained by the two-dimensional computational model is presented in section 10.2. The iterative permittivity inversion procedure and regularization of the ill-posed inverse problem are covered in section 10.3. Computational feasibility study of the proposed breast imaging technique is investigated in section 10.4 for different heterogeneous 2D breast models. The outcome of the numerical simulations for the heterogeneous mathematical breast models are discussed in section 10.5. Besides breast imaging, the mirror based microwave tomography technique proposed in this thesis can also be used for material characterization and non-invasive inspection of in-animate objects. Numerical simulations conducted for weak and strong scatterers demonstrating the potential application of deformable mirror microwave tomography for near field imaging are presented in section 10.6.

10.1 Theory

The field maintained by deformable mirror tomography setup in the presence of the breast is computed using finite element boundary integral (FEBI) method for continuous excitation. The FEBI method employs boundary integral equation for the field inside therapy tank and external to the breast. The field inside the heterogeneous breast is modeled using finite element analysis [50]. For source free case, the vector wave equation in (4.31) reduces to

$$\left(\nabla^2\mathbf{E} + k^2\mathbf{E}\right) = 0 \tag{10.1}$$

where $\nabla^2 = \left(\partial^2/\partial x^2 + \partial^2/\partial y^2 + \partial^2/\partial z^2\right)$ and $k(x,y)$ is the wave number inside the finite element breast model. The integral equation solution for field inside the imaging tank in the presence of breast is expressed in terms of potentials (4.49)-(4.50). In the absence of charge accumulation, (4.49) reduces to,

$$\mathbf{E}(\mathbf{r},\omega) = -j\omega\mathbf{A}(\mathbf{r},\omega) - \frac{1}{\epsilon}\nabla \times \mathbf{F}(\mathbf{r},\omega) \tag{10.2}$$

In (10.2), μ and ϵ are the permeability and permittivity of the couplant in the imaging tank and $\mathbf{A}$ and $\mathbf{F}$ are the magnetic and electric vector potentials explained in section 4.7. Equation 10.2 can be rewritten as,

$$\mathbf{E}(\mathbf{r},\omega) = -j\omega\mu\mathbf{J}(\mathbf{r},\omega) * g_{3D}(\mathbf{r},k_b) - \frac{1}{\epsilon}\nabla \times (\epsilon\mathbf{M}(\mathbf{r},\omega) * g_{3D}(\mathbf{r},k_b)) \tag{10.3}$$

where $g_{3D}(\mathbf{r},k_b)$ is the 3D scalar Greens function for field in the homogeneous coupling solution. Substituting (4.52)-(4.53) for the magnetic and electric vector poten-

tials in 10.3 yields,

$$\begin{aligned}\mathbf{E}(\mathbf{r},\omega) = & - j\omega\mu \iiint_V \mathbf{J}(\mathbf{r}')g(\mathbf{r},\beta;\mathbf{r}')dv' \\ & - \nabla \times \iiint_V \mathbf{M}(\mathbf{r}')g(\mathbf{r},\beta;\mathbf{r}')dv' \end{aligned} \tag{10.4}$$

With the knowledge of electric field, the magnetic field can be obtained using (4.2a). In (10.4), $\mathbf{J} = \mathbf{J}_i + \mathbf{J}_{eq}$ and $\mathbf{M} = \mathbf{M}_{eq}$ are the impressed and equivalent electric and magnetic current densities. The equivalent current densities are contributions from the perfectly conducting mirror, EM source and the penetrable heterogeneous dielectric breast. These equivalent currents obey the fundamental equivalence theorems explained in chapter 3.

Equation (10.4) implies that the total field anywhere outside the breast can be obtained with the knowledge of impressed and equivalent electric and magnetic current sources. The equivalent current sources maintained by the dielectric scatterer are computed by solving (10.1) and (10.4) with Dirichlet boundary conditions given by,

$$\hat{n} \times \mathbf{E}(\mathbf{r},\omega) = 0 \tag{10.5}$$

on the surface of the deformable mirror and aperture source. The FEBI method truncates the computational model by imposing the radiation boundary condition close to the breast and models the heterogeneous breast using finite element analysis thereby reducing the number of unknowns in the computational domain.

10.2 Forward Problem - Data Acquisition

Feasibility of the proposed deformable mirror based tomography technique for breast imaging is demonstrated via two-dimensional imaging setup as illustrated in Figure Figure 10.1. The two-dimensional wave propagation model solves the field equations

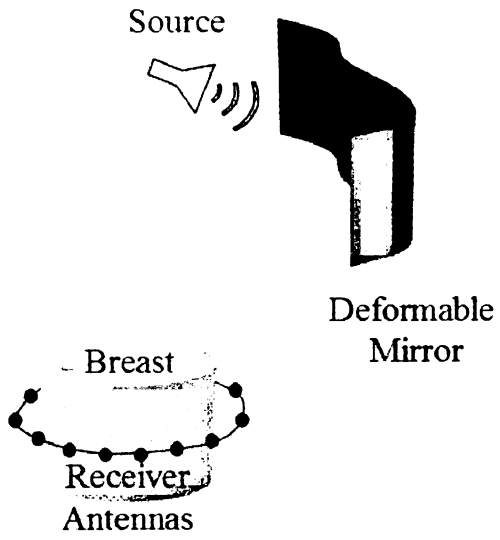

Figure 10.1. Illustration of deformable mirror microwave tomography system in 2D.

for TM^z polarization. Figure Figure 10.2 shows the computational geometry of the 2D imaging setup in Figure Figure 10.1. The deformable mirror is modeled as a thin perfectly conducting flexible metallic strip and the directional electromagnetic source is approximated by a constant line current source with a metal backing to direct the emanating field towards the flexible membrane mirror. In Figure Figure 10.2, the deformable mirror and source metal backing surfaces are defined by Γ^M and Γ^P respectively and the heterogeneous breast is described by the closed region S bounded by external contour ∂S.

10.2.1 Field Equations in 2D

In Figures Figure 10.1 - Figure 10.2, axis of the arbitrary shaped conducting and dielectric scatterers are parallel to the z axis with no variation along z i.e., $\partial/\partial z = 0$. The infinitely long, constant line current source maintains a z-directed current and supports $\hat{z} \cdot \mathbf{A}$. The TM^z polarized fields emanating from the line source induces z-directed equivalent surface currents on the membrane mirror, source metal backing and inside the heterogeneous penetrable breast. Let $\mathbf{J}_i$ be the impressed current den-

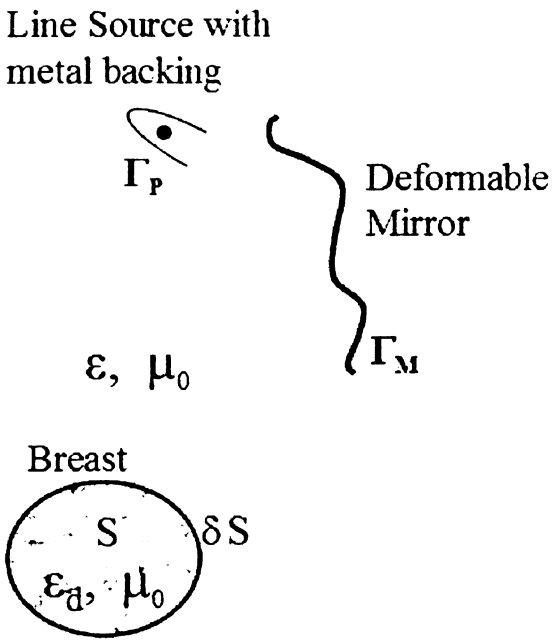

Figure 10.2. Two-dimensional computational model.

sity that maintains the equivalent current densities $\mathbf{J}_m$, $\mathbf{J}_p$ on the mirror and source metal backing respectively and $\mathbf{J}_d$, $\mathbf{M}_d$ on ∂S of the breast. These equivalent and impressed currents radiating inside the imaging tank maintains the TM^z polarized electric field at the receiver locations surrounding the breast. For the 2D TM^z case, (10.4) reduces to,

$$\begin{aligned}
\hat{z}\cdot\mathbf{E}(x,y,\omega) = &- \hat{z}\cdot\frac{\omega\mu}{4}\int_{\Gamma_M}\mathbf{J}_m(x',y')H_0^{(2)}(k_b,x,y;x',y')dx'dy' \\
&- \hat{z}\cdot\frac{\omega\mu}{4}\int_{\Gamma_P}\mathbf{J}_p(x',y')H_0^{(2)}(k_b,x,y;x',y')dx'dy' \\
&- \hat{z}\cdot\frac{\omega\mu}{4}\int_{\partial S}\mathbf{J}_d(x',y')H_0^{(2)}(k_b,x,y;x',y')dx'dy' \\
&- \hat{z}\cdot\nabla\times\int_{\partial S}\mathbf{M}_d(x',y')H_0^{(2)}(k_b,x,y;x',y')dx'dy' \\
&- \frac{\omega\mu}{4}I_0H_0^{(2)}(k_b|x-x_s,y-y_s|) \qquad (10.6)
\end{aligned}$$

In (10.6), k_b is the wave number of couplant in the imaging tank, $(x_s, y_s, z = 0)$ is the location of line source that yields the incident field, $E_z^{in} = -\frac{\omega\mu}{4} I_0 H_0^{(2)}(k_b|x - x_s, y - y_s|)$. The total field inside heterogeneous breast is given by the scalar wave equation,

$$\left(\nabla_\tau^2 + k^2(x,y)\right) E_z(x,y,\omega) = 0, \quad (x,y) \in S \tag{10.7}$$

where $\nabla_\tau = \left(\partial^2/\partial x^2 + \partial^2/\partial y^2\right)$ is the Laplacian operator in transverse XY plane and $k(x,y)$ is the wave number inside the breast. The contribution of $\mathbf{J}_d$ in (10.6) can be simplified as,

$$\begin{aligned}
\mathbf{J}_d &= \hat{z} J_d \\
&= \hat{n} \times \mathbf{H} \\
&= -\frac{1}{j\omega\mu} \hat{n} \times (\nabla_\tau \times [\hat{\tau} E_\tau + \hat{z} E_z]) \\
&= -\frac{1}{j\omega\mu} \hat{n} \times (\nabla_\tau \times \hat{z} E_z) \\
&= \frac{1}{j\omega\mu} \hat{z} E_z (\hat{n} \cdot \nabla_\tau), \quad \because \mathbf{A} \times (\mathbf{B} \times \mathbf{C}) = (\mathbf{A} \cdot \mathbf{C})\mathbf{B} - (\mathbf{A} \cdot \mathbf{B})\mathbf{C}, \hat{n} \times \hat{\tau} = \hat{z} \\
&= \frac{1}{j\omega\mu} \hat{z} \, (\hat{n} \cdot \nabla_\tau E_z)
\end{aligned} \tag{10.8}$$

Substituting $\mathbf{M}_d = \hat{n} \times \mathbf{E}$ and invoking vector identities simplifies the contribution of the surface magnetic current density to,

$$\begin{aligned}
\nabla \times \int_{\partial S} \mathbf{M}_d H_0^{(2)}(k_b, x, y; x', y') dS' &= 4j \nabla_\tau \times \int_{\partial S} \left(\hat{n}' \times \mathbf{E}(x', y', \omega)\right) G_{2D} dS' \\
&= 4j \int_{\partial S} \nabla_\tau \times \left(\hat{n}' \times \hat{z} E_z'\right) G_{2D} dS'
\end{aligned} \tag{10.9}$$

Invoking vector identities and $\left[\nabla G_{2D} = -\nabla' G_{2D}\right]$ yields,

$$\begin{aligned}
\nabla_\tau \times \left(\hat{n}' \times \mathbf{E}_z'\right) G_{2D} &= \nabla_\tau G_{2D} \times \left(\hat{n}' \times \mathbf{E}_z'\right) + G_{2D} \left(\nabla_\tau \times \left(\hat{n}' \times \mathbf{E}_z'\right)\right) \\
&= \nabla_\tau G_{2D} \times \left(\hat{n}' \times \mathbf{E}_z'\right), \quad [\nabla_\tau = \partial/\partial x + \partial/\partial y]
\end{aligned}$$

$$= -\left(\nabla' G_{2D} \cdot \hat{z} E'_z\right) \hat{n}' + \left(\hat{n}' \cdot \nabla' G_{2D}\right) \hat{z} E'_z$$
$$= \left(\hat{n}' \cdot \nabla' G_{2D}\right) \hat{z} E'_z \qquad (10.10)$$

Substituting (10.10) into (10.9) gives,

$$\nabla \times \int_{\partial S} \mathbf{M}_d G_{2D} dx' dy' = \hat{z} 4j \int_{\partial S} \left(\hat{n}' \cdot \nabla' G_{2D}\right) E'_z(x', y', \omega) dx' dy' \qquad (10.11)$$

Substituting $\mathbf{J}_m = \hat{z} J_m$, $\mathbf{J}_p = \hat{z} J_p$ and (10.8), (10.11) into 10.6 yields the electric field boundary integral equation,

$$\begin{aligned} E_z(x, y, \omega) = & - \frac{\omega\mu}{4} \int_{\Gamma_M} J_m(x', y') H_0^{(2)}(k_b, x, y; x', y') dx' dy' \\ & - \frac{\omega\mu}{4} \int_{\Gamma_P} J_p(x', y') H_0^{(2)}(k_b, x, y; x', y') dx' dy' \\ & - \int_{\partial S} \left(\hat{n}' \cdot \nabla'_\tau E_z(x', ' y', \omega)\right) \frac{1}{4j} H_0^{(2)}(k_b, x, y; x', y') dx' dy' \\ & + \int_{\partial S} \left(\hat{n}' \cdot \nabla' \frac{1}{4j} H_0^{(2)}(k_b, x, y; x', y')\right) E'_z(x', ' y, \omega) dx' dy' \\ & - \frac{\omega\mu}{4} I_0 H_0^{(2)}(k_b | x - x_s, y - y_s|) \end{aligned} \qquad (10.12)$$

Equations (10.7), (10.12) are solved with the boundary conditions,

$$E_z(x, y, \omega) = 0, \quad \forall (x, y) \in \Gamma_M, \Gamma_P \qquad (10.13)$$

for the unknown induced current densities and total field, $E_z(x, y, \omega)$ in the 2D computational model in Figure Figure 10.2. From the field and current densities, field measurements at the receiver locations can be calculated using (10.12).

10.2.2 Computational Method

Solution to the boundary value problem given by (10.7), (10.12)-(10.13) is obtained using the finite element boundary integral (FEBI) numerical technique. The FEBI method commonly referred as the hybrid method solves the integro-differential equations using the finite element and method of moments techniques [50, 51]. In both numerical techniques, solution to the integral or differential equation involves,

1. Domain discretization
2. Selection of the subdomain interpolation or basis functions
3. Formulation of the system of equations
4. Solution to the system of equations

The FEBI formulation for the field maintained by the breast is derived in the subsequent section.

10.2.2.1 FEBI Formulation

Finite element analysis is a widely used numerical technique for solving boundary value problems in engineering, physics and mathematics [170, 171, 50]. In finite element technique, the computational domain is discretized in to smaller local domains where the solution is represented using subdomain basis or interpolation functions. Solution to a boundary value problem is obtained by solving a system of equations for the unknown coefficients of the interpolation function. Let the total field $E_z(x, y, \omega)$ be represented by ϕ for ease of notation. Then, the scalar wave equation can be rewritten as,

$$\left(\frac{\partial^2}{\partial^2 x} + \frac{\partial^2}{\partial^2 y} + k_b^2 \epsilon_d(x, y) \right) \phi = 0, \quad (x, y) \in S. \tag{10.14}$$

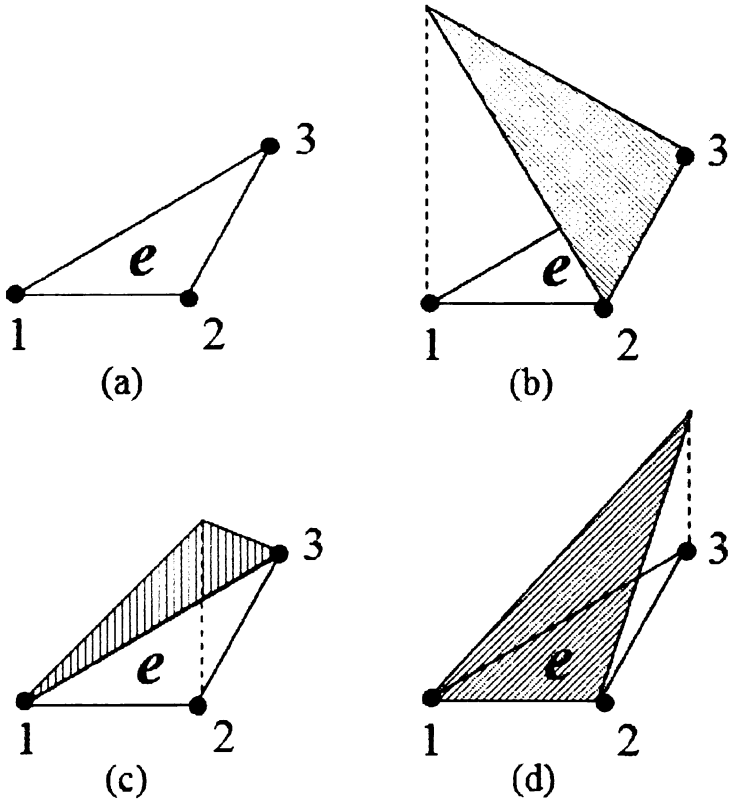

Figure 10.3. Finite element and interpolation functions (a) Linear triangular element (b) N_1^e (c) $N_2 1^e$ (d) N_3^e.

Let the computational domain S be divided into M small elements and ∂S be divided into M_s boundary segments. The field inside the individual element is expressed as,

$$\begin{aligned} \phi^e(x,y) &= \sum_{i=1}^{3} N_i^e(x,y)\phi_i^e \\ &= \{N^e\}^T \{\phi^e\} = \{\phi^e\}^T \{N^e\} \end{aligned} \tag{10.15}$$

and the field on the boundary is expressed as,

$$\phi^s(x,y) = \sum_{i=1}^{2} N_i^s(x,y)\phi_i^s. \tag{10.16}$$

The Galerkin's method applied to a single element shown in Figure Figure 10.3

defined by Ω^e yields the weighted residue [50, 51],

$$\begin{aligned} R_i^e &= \iint_{\Omega^e} N_i^e r dx dy \\ &= \iint_{\Omega^e} \left[\nabla^2\phi + k_b^2\epsilon_d(x,y)\right] N_i^e(x,y) d\Omega = 0 \end{aligned} \tag{10.17}$$

Substituting $\nabla^2 = \frac{\partial^2}{\partial x^2} + \frac{\partial^2}{\partial y^2}$ and invoking the identities,

$$N_i^e \frac{\partial^2}{\partial x^2} = \frac{\partial}{\partial x}\left[N_i^e \frac{\partial\phi}{\partial x}\right] - \frac{\partial N_i^e}{\partial x}\frac{\partial\phi}{\partial x} \tag{10.18}$$

$$N_i^e \frac{\partial^2}{\partial y^2} = \frac{\partial}{\partial y}\left[N_i^e \frac{\partial\phi}{\partial y}\right] - \frac{\partial N_i^e}{\partial y}\frac{\partial\phi}{\partial y} \tag{10.19}$$

and the divergence theorem,

$$\iint_{\Omega^e} \left(\frac{\partial U}{\partial x} + \frac{\partial V}{\partial y}\right) d\Omega = \int_{\partial\Gamma^e} (U\hat{x} + V\hat{y}) \cdot \hat{n} d\Gamma \tag{10.20}$$

reduces 10.17 to,

$$\begin{aligned} R_i^e &= \iint_{\Omega^e} \left[\frac{\partial N_i^e}{\partial x}\frac{\partial\phi}{\partial x} + \frac{\partial N_i^e}{\partial y}\frac{\partial\phi}{\partial y} - k_b^2\epsilon_d\right] d\Omega' + \int_{\Gamma^e} (\nabla\phi \cdot \hat{n})\, N_i^e d\Gamma \\ &= 0 \end{aligned} \tag{10.21}$$

Let $\nabla\phi \cdot \hat{n} = \psi$ on the element boundary be expressed as,

$$\psi^s(x,y) = \sum_{i=1}^{2} N_i^s(x,y)\psi_i^s. \tag{10.22}$$

Substituting (10.16) and (10.22) into (10.22) for each element gives the augmented linear system of equations,

$$[K]\{\phi\} + [C]\{\psi\} = \{0\} \tag{10.23}$$

In (10.23), the matrices $[K]$ and $[C]$ are given by,

$$\begin{aligned}
[K] &= \sum_{m=1}^{M} [K^e] \\
&= \sum_{m=1}^{M} \left[\iint_{\Omega^e} \left[\frac{\partial N_i^e}{\partial x}\frac{\partial \phi}{\partial x} + \frac{\partial N_i^e}{\partial y}\frac{\partial \phi}{\partial y} - k_b^2 \epsilon_d \{N^e\}\{N^e\}^T \right] d\Omega' \right] \qquad (10.24a) \\
[C] &= \sum_{t=1}^{M_s} \left[C^t\right] \\
&= \sum_{t=1}^{M_s} \left[\int_{\Gamma_t} \left\{N^t\right\}\left\{N^t\right\}^T d\Gamma' \right] \qquad (10.24b)
\end{aligned}$$

In the boundary integral equation, let the induced current densities in each boundary segment be expressed as,

$$J_m^s(x,y) = \sum_{i=1}^{2} N_i^s(x,y) J_{m,i}^s, \quad s = 1,2,...,N1 \tag{10.25a}$$

$$J_p^s(x,y) = \sum_{i=1}^{2} N_i^s(x,y) J_{p,i}^s, \quad s = 1,2,...,N2 \tag{10.25b}$$

where $N1$ and $N2$ are the number of line segments on Γ_M and Γ_P respectively. Substituting (10.16), (10.22) and (10.25a) -(10.25b) into (10.12) yields,

$$E_z(x,y,\omega) = -\frac{\omega\mu}{4} \sum_{t=1}^{N1} \int_{\Gamma_M^t} \left\{N^t\right\}^T \left\{J_m^t\right\} H_0^{(2)}(k_b, x, y; x', y') d\Gamma'$$

$$
\begin{aligned}
&- \frac{\omega\mu}{4}\sum_{t=1}^{N2}\int_{\Gamma_P^t}\left\{N^t\right\}^T\left\{J_p^t\right\}H_0^{(2)}(k_b,x,y;x',y')d\Gamma' \\
&+ \sum_{t=1}^{M_s}\int_{\partial S^t}\left[\left\{N^t\right\}^T\{\psi\}G_{2D}+\left\{N^t\right\}^T\{E_z\}\frac{\partial G_{2D}}{\partial n'}\right]d\Gamma' \\
&+ E_z^{inc}(x,y,\omega) \qquad (10.26)
\end{aligned}
$$

where $\psi = -\hat{n}'\cdot(\nabla' E_z)$. The unknown quantities in (10.26) are obtained by evaluating the inner product of (10.26) with test functions at points along the three different boundaries, Γ_M, Γ_P and ∂S [51]. When evaluating the inner products on Γ_M, Γ_P, boundary conditions (10.13) are imposed. The resulting equations are represented in matrix form as,

$$
\begin{aligned}
[C]^T\{E_z\} = &- \left[Z_m^1\right]\{J_m\} - \left[Z_p^1\right]\{J_p\} + [Q_1]\{\psi\} \\
&+ [P_1]\{E_z\} + \left\{E_{z,d}^i\right\}, \quad (x,y)\in S \qquad (10.27a)\\
\{0\} = &- \left[Z_m^2\right]\{J_m\} - \left[Z_p^2\right]\{J_p\} + [Q_2]\{\psi\} \\
&+ [P_2]\{E_z\} + \left\{E_{z,m}^i\right\}, \quad (x,y)\in \Gamma_M \qquad (10.27b)\\
\{0\} = &- \left[Z_m^3\right]\{J_m\} - \left[Z_p^3\right]\{J_p\} + [Q_3]\{\psi\} \\
&+ [P_3]\{E_z\} + \left\{E_{z,p}^i\right\}, \quad (x,y)\in \Gamma_P \qquad (10.27c)
\end{aligned}
$$

Equations (10.23) and (10.27) form a linear system with $M + M_s + N1 + N2$ number of unknowns. Solution for the field is obtained by using triangular basis functions in (10.23) and pyramidal basis functions in (10.27). In both finite element and boundary integral equations, the basis and testing functions were the same. For each mirror deformation, the linear system of equations (10.23) and (10.27) is solved for the unknown field and induced current densities. From the knowledge of field and current densities, field measurements for each predetermined optimal mirror shapes, $\{\Gamma_M\}_{i=1}^K$ are computed by evaluating (10.12) at the receiver locations $(x_r, y_r), r = 1, 2, .., L$.

In matrix form, the field measurements due to breast and deformable mirror at the receiver locations is given by,

$$\{E_z\}|_{(x_r,y_r)} = -\left[Z_m^r\right]\{J_m\} - \left[Z_p^r\right]\{J_p\} + [Q_r]\{\psi\} + [P_r]\{E_z\} + \left\{E_{z,r}^i\right\} \quad (10.28)$$

Field measurements calculated for all optimal mirror shapes using (10.28) are used in permittivity imaging of the breast.

10.3 Inverse Problem - Breast Imaging

The inversion process is a classical optimization problem that aims to minimize the error between measured and computed fields at the receiver locations for all optimal mirror deformations. The objective is to find the minimizer of the cost function,

$$\underset{\epsilon^{sol}}{argmin}\ C(\epsilon_d)$$

$$C(\epsilon_d) = \frac{1}{2}\|E_z^{meas} - E_z^{cal}\|^2 \quad (10.29)$$

In (10.29), $E_z^{meas} = E_z^{rx} + noise$ is the noisy measurement data and $\hat{E_z}^{rx}$ is the field calculated at receiver locations for the estimated permittivity distribution, $\hat{\epsilon_d}(x,y)$ in the breast. Fields measured for all optimal mirror deformations are used in the inversion process.

10.3.1 Permittivity Inversion

The iterative permittivity inversion process is illustrated in Figure Figure 10.4. The iterative procedure starts with an initial estimate $\hat{\epsilon}$ and computes the field, $\hat{E_z}^{rx}$ at the receiver locations for the optimal mirror deformations, $\{\Gamma_M\}_{i=1}^K$ using (10.23) and (10.27). If the error between E_z^{meas} and $\hat{E_z}^{rx}$ is above the tolerance level δ, the permittivity estimate is updated to minimize the measurement error. The

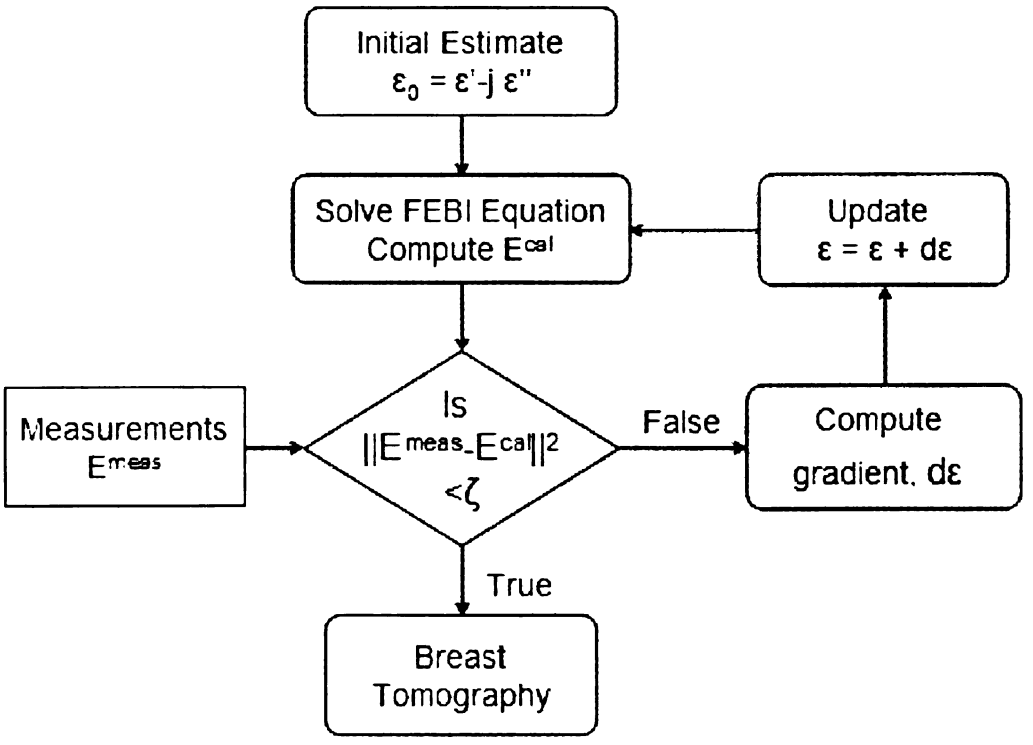

Figure 10.4. Iterative permittivity reconstruction procedure.

permittivity estimate is updated iteratively as illustrated in Figure Figure 10.4 until the measurement error is minimized.

A Taylor series expansion of E_z^{meas} about the solution yields,

$$E_z^m(\hat{\epsilon} + \triangle\epsilon) = E_z^m(\hat{\epsilon}) + \frac{dE_z^m}{d\hat{\epsilon}} \triangle \hat{\epsilon} + \frac{d^2E_z^m}{d\hat{\epsilon}^2} \frac{\triangle\hat{\epsilon}^2}{2} + O_n \tag{10.30}$$

where O_n in (10.30) represents the higher order derivatives in the Taylor series expansion. Neglecting the higher order derivatives, a linearized Taylor series expansion of the form,

$$\frac{dE_z^m}{d\hat{\epsilon}} \triangle \hat{\epsilon} = E_z^m(\hat{\epsilon} + \triangle\epsilon) - E_z^m(\hat{\epsilon}) \tag{10.31}$$

is used to solve for the unknown permittivity distribution. Equation (10.31) can be

rewritten as,

$$J \triangle \hat{\epsilon} = \triangle E_z^m \tag{10.32}$$

where $\triangle E_z^m = E_z^m(\hat{\epsilon} + \triangle\epsilon) - E_z^m(\hat{\epsilon})$ and J is the Jacobian matrix containing the first derivative of E_z^m with respect to ϵ. The first derivative of the field measurements with respect to the k^{th} element's permittivity inside the discretized computational domain is computed using (10.28) as,

$$\left\{\frac{E_z^m}{d\epsilon_k}\right\} = -\left[Z_m^r\right]\left\{\frac{dJ_m}{d\epsilon_k}\right\} - \left[Z_p^r\right]\left\{\frac{dJ_p}{d\epsilon_k}\right\} + [Q_r]\left\{\frac{d\psi}{d\epsilon_k}\right\} + [P_r]\left\{\frac{dE_z}{d\epsilon_k}\right\} \tag{10.33}$$

In (10.33), the derivatives of E_z, ψ, J_m and J_p are obtained by differentiating (10.23) and (10.27). Differentiating (10.23) and (10.27) with respect to the k^{th} element's permittivity yields the linear system of equations,

$$\{0\} = + \frac{d[K]}{d\epsilon_k}\{E_z\} + [K]\frac{dE_z}{d\epsilon_k} + [C]\left\{\frac{d\psi}{d\epsilon_k}\right\}, (x,y) \in S \tag{10.34a}$$

$$[C]^T\left\{\frac{dE_z}{d\epsilon_k}\right\} = - \left[Z_m^1\right]\left\{\frac{dJ_m}{d\epsilon_k}\right\} - \left[Z_p^1\right]\left\{\frac{dJ_p}{d\epsilon_k}\right\} + [Q_1]\left\{\frac{d\psi}{d\epsilon_k}\right\} + [P_1]\left\{\frac{dE_z}{d\epsilon_k}\right\}, \quad (x,y) \in S \tag{10.34b}$$

$$\{0\} = - \left[Z_m^2\right]\left\{\frac{dJ_m}{d\epsilon_k}\right\} - \left[Z_p^2\right]\left\{\frac{dJ_p}{d\epsilon_k}\right\} + [Q_2]\left\{\frac{d\psi}{d\epsilon_k}\right\} + [P_2]\left\{\frac{dE_z}{d\epsilon_k}\right\}, \quad (x,y) \in \Gamma_M \tag{10.34c}$$

$$\{0\} = - \left[Z_m^3\right]\left\{\frac{dJ_m}{d\epsilon_k}\right\} - \left[Z_p^3\right]\left\{\frac{dJ_p}{d\epsilon_k}\right\} + [Q_3]\left\{\frac{d\psi}{d\epsilon_k}\right\} + [P_3]\left\{\frac{dE_z}{d\epsilon_k}\right\}, \quad (x,y) \in \Gamma_P \tag{10.34d}$$

for the unknown derivatives of E_z, ψ, J_m and J_p. Using (10.24a) and the Cauchy-Riemann equations for complex differentiation, (10.34a) is expressed as [172],

$$\frac{d[K^e]}{d\epsilon_k} = -k_b^2 \iint_{\Gamma^e} \{N^e\}\{N^e\}^T d\Omega' \tag{10.35}$$

The Jacobian matrix is assembled using the chain rule and Cauchy-Riemann rule for complex differentiation for the optimal mirror deformations, $\{\Gamma_M\}_{i=1}^{K}$.

The iterative inversion procedure solves,

$$J^T J \triangle \hat{\epsilon} = J^T \triangle E_z^m \tag{10.36}$$

for the permittivity update, $\triangle\hat{\epsilon}$ to obtain the permittivity estimate

$$\epsilon^{new} = \epsilon^{old} + \alpha\hat{\epsilon}, \quad \alpha > 0. \tag{10.37}$$

For the new estimate ϵ^{new}, field at the receiver locations are calculated using (10.28). A better estimate for the unknown permittivity is obtained using (10.34)-(10.37) until one of the following stopping criteria,

$$\frac{\|E_z^{meas} - E_z^{cal}\|^2}{\|E_z^{meas}\|^2} \leq \delta_E \tag{10.38a}$$

$$\|\epsilon^{new} - \epsilon^{old}\|^2 \leq \delta_\epsilon \tag{10.38b}$$

is satisfied. In (10.38a)-(10.38b), δ_E and δ_ϵ are positive real numbers that determine the error in reconstructed spatial permittivity distribution inside the breast.

10.3.2 Regularization

Inverse scattering problems are ill-posed and yields a highly ill-conditioned Jacobian matrix. The ill-conditioned Jacobian matrix results in unstable solutions. The instability in the solution is minimized by solving the regularized problem [162, 76],

$$\left[J^T J + \gamma L^T L\right] \triangle \hat{\epsilon} = J^T \triangle E_z^m, \quad \gamma > 0 \tag{10.39}$$

which is a solution to the minimization problem,

$$\triangle\epsilon = argmin\|J^T J - J^T \triangle E_z^m\|^2 + \gamma\|L\| \triangle \epsilon^2 \tag{10.40}$$

In (10.40), γ is the regularization parameter which, is determined empirically and L is the penalty function that is used to impose priori constraints to the solution. When L equals the identity matrix, (10.40) corresponds to the zeroth order regularization. The inversion algorithm iteratively solves the linearized regularization problem until the error between the measured and computed field is below the desired tolerance.

10.4 Tomography - Simulations

The feasibility of tomographic reconstruction of the heterogeneous breast permittivity using deformable mirror is investigated via numerical simulations. The multi-view measurements computed for $\{\Gamma_M\}_{i=1}^K$ are used in permittivity estimation. Solution to the ill-posed inverse scattering problem was achieved using the regularized inverse problem for the unknown permittivity distribution inside the breast. Robustness of the reconstruction technique was evaluated in the presence of additive random noise with the coupling solution as the initial estimate.

10.4.1 Piecewise Continuous Scatterer - Model A

In the 2D simulations, field produced by a 9 cm diameter inhomogeneous breast model was computed at 24 locations on a 12 cm diameter annular ring surrounding the breast. Field calculated for the optimal mirror shapes, $\{\Gamma_M\}_{i=1}^K$ were used for permittivity reconstruction. The heterogeneous 2D mathematical phantom was discretized into 300 triangular elements with 205 elements with unknown material property. Figure Figure 10.5 shows the 2D FEBI mesh of the inhomogeneous breast model with background permittivity, ϵ. The permittivity of the scatterer is ϵ_1 in the periphery and gradually increases to ϵ_4. The permittivity values assigned to

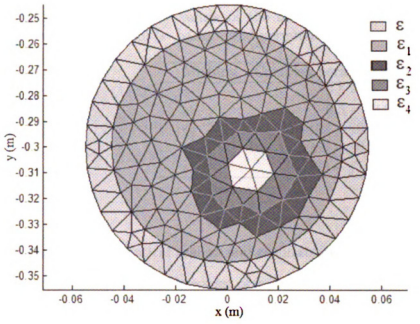

Figure 10.5. Two dimensional mesh of the heterogeneous breast.

the heterogeneous breast model in Figure Figure 10.5 are listed in Table Table 10.1. The tissue conductivity listed in Table Table 10.1 is relatively lower compared to the experimental data reported in [47]. Thus, the contrast between the real and imaginary parts of the dielectric constant is more than an order of magnitude for model A. The permittivity distribution was chosen to evaluate the ability of the near field deformable mirror tomography to reconstruct permittivity profiles with huge contrast between the real and imaginary parts and to investigate the impact of choice of mirror deformations on permittivity reconstructions.

10.4.1.1 Multiple Mirror Deformations - Model A

The minimal number of mirror shapes required for reliable permittivity reconstruction was investigated for dielectric model A using field measurements from 8, 12 and 16 mirror shapes belonging to $\{\Gamma_M\}_{i=1}^{K}$. In all simulations, the inversion algorithm was initialized with the background permittivity and the permittivity profile estimated after each iteration was constrained using a generous upper and lower bounds. For

Table 10.1. Permittivity values of the inhomogeneous breast model using Debye dispersion model [163] (ϵ background permittivity).

Medium	Complex permittivity
ϵ	$9.5 - j0.20$
ϵ_1	$9.5 - j0.23$
ϵ_2	$15.1452 - j0.5229$
ϵ_3	$28.5263 - j0.9833$
ϵ_4	$49.6133 - j1.3233$

fair comparison, identical scaling and regularization parameters, α and γ were used during inversion for the different set of mirror shapes. Figure Figure 10.6 compares the tomographic images reconstructed using 8, 12 and 16 mirrors at the 68^{th} iteration for the zeroth order regularization technique. Figure Figure 10.7-Figure 10.9 compares the permittivity profiles along horizontal, vertical and diagonal transects through the breast model after same number of iterations. The inherent low-pass filtering property of the regularization technique [76] results in a smoothed reconstruction of the permittivity profile. Tomographic reconstructions shown in Figures Figure 10.6-Figure 10.9 imply that the inversion result improves with increase in the number of mirror shapes though acceptable results can be obtained even with 8 mirrors shapes. Unlike conventional technique, in the proposed tomography technique the ability to acquire more field measurements is not limited by the number of transceiver antennas. With the aid of deformable mirror a multitude of field measurements can be acquired for image reconstruction.

10.4.2 Piecewise Continuous Scatterer - Breast Model B

In Model B, the mesh in Figure Figure 10.5 was used for the breast tissue properties reported in [47]. The permittivity values assigned to the finite element mesh are listed in Table Table 10.2. The permittivity values in Table Table 10.2 are higher than the first order Debye dispersion model. Simulations were carried out using the

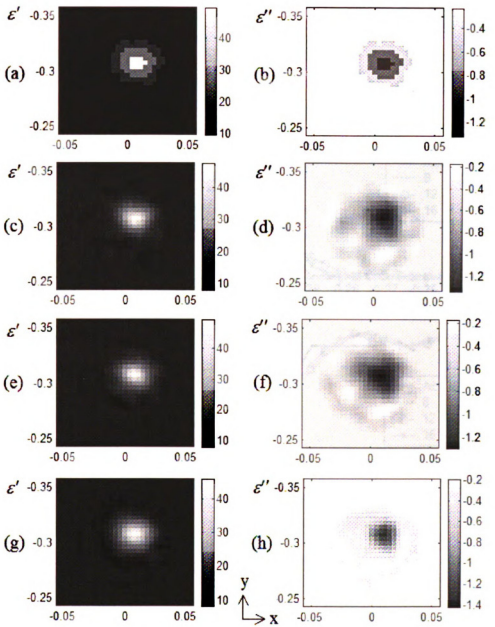

Figure 10.6. Reconstruction at 68^{th} iteration. (a) ϵ' (b) ϵ'' of true solution; (c) ϵ' (d) ϵ'' for 8 mirrors; (e) ϵ' (f) ϵ'' for 12 mirrors; (g) ϵ' (h) ϵ'' for 16 mirrors [167].

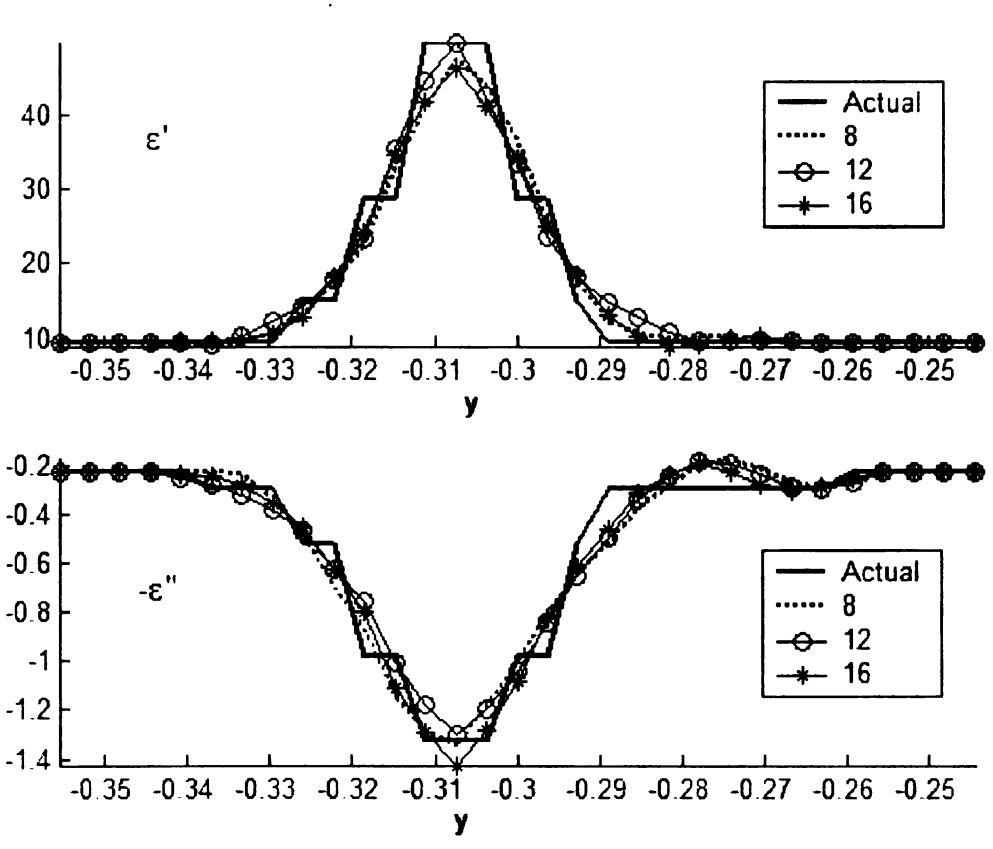

Figure 10.7. Reconstructed permittivity profile along x=0 for 8, 12 and 16 mirror deformations.

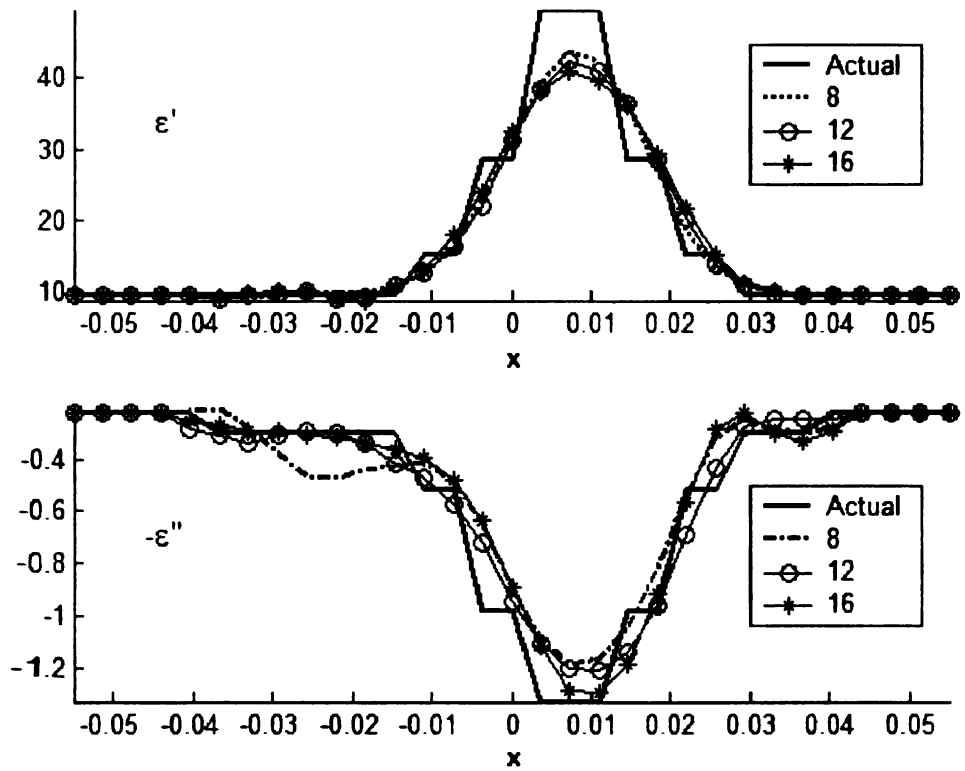

Figure 10.8. Reconstructed permittivity profile along y=-0.304 for 8, 12 and 16 mirror deformations.

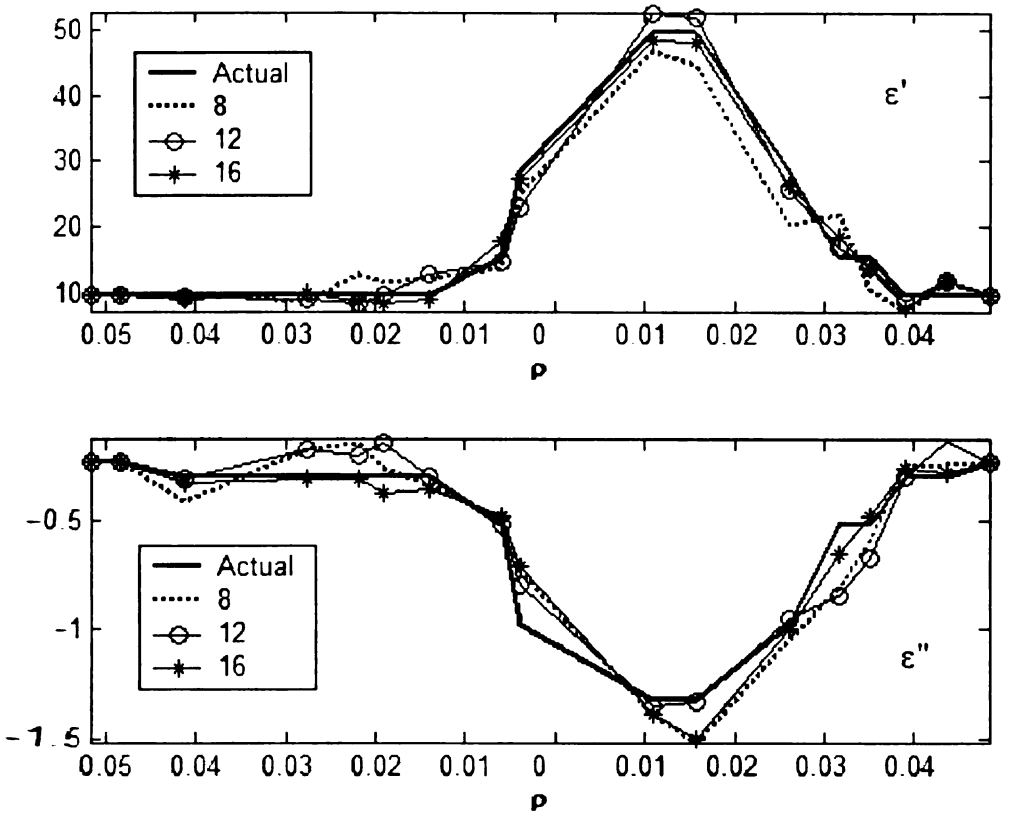

Figure 10.9. Reconstructed permittivity profile along the diagonal for 8, 12 and 16 mirror deformations.

Table 10.2. Permittivity values of the inhomogeneous breast model [47] (ϵ background permittivity).

Medium	Complex permittivity
ϵ	$14.8500 - j3.47$
ϵ_1	$16.5000 - j3.8500$
ϵ_2	$26.7000 - j9.3700$
ϵ_3	$47.1000 - j20.4200$
ϵ_4	$57.3000 - j25.9400$

values in [47] to evaluate the feasibility of permittivity imaging with variations in tissue properties.

10.4.2.1 Inversion - Noise Free Measurements

As discussed earlier, field measurements computed at 24 receiver positions for TM^z polarization at 700 MHz were used for permittivity inversion. The total field maintained by 25 mirror shapes were used to reconstruct the permittivity of the computational breast model, B. An additional constraint on the permittivity update was imposed by setting L to be the Laplacian differentiation operator, $\mathcal{L}$ in 10.39. Figure Figure 10.10 shows the reconstructed permittivity distribution for the breast model B. The least square reconstruction error calculated during the iterative procedure is shown in Figure Figure 10.11. A comparison of the reconstructed permittivity profiles along the horizontal and vertical transects through the tumor center are shown in Figures Figure 10.12-Figure 10.13. The additional constraint imposed by the Laplacian operator penalizes permittivity updates with abrupt variation and ensures smooth and stable solution. From Figures Figure 10.10-Figure 10.11, it can be observed that regularization of the problem for a stable solution results in the smooth reconstruction.

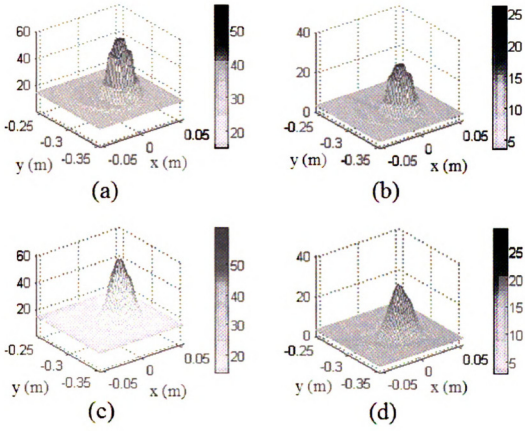

Figure 10.10. Permittivity reconstruction of noise free measurements for the regularized problem (a) ϵ' and (b) -ϵ'' for the true distribution, (c) ϵ' and (b) -ϵ'' estimated reconstruction [166].

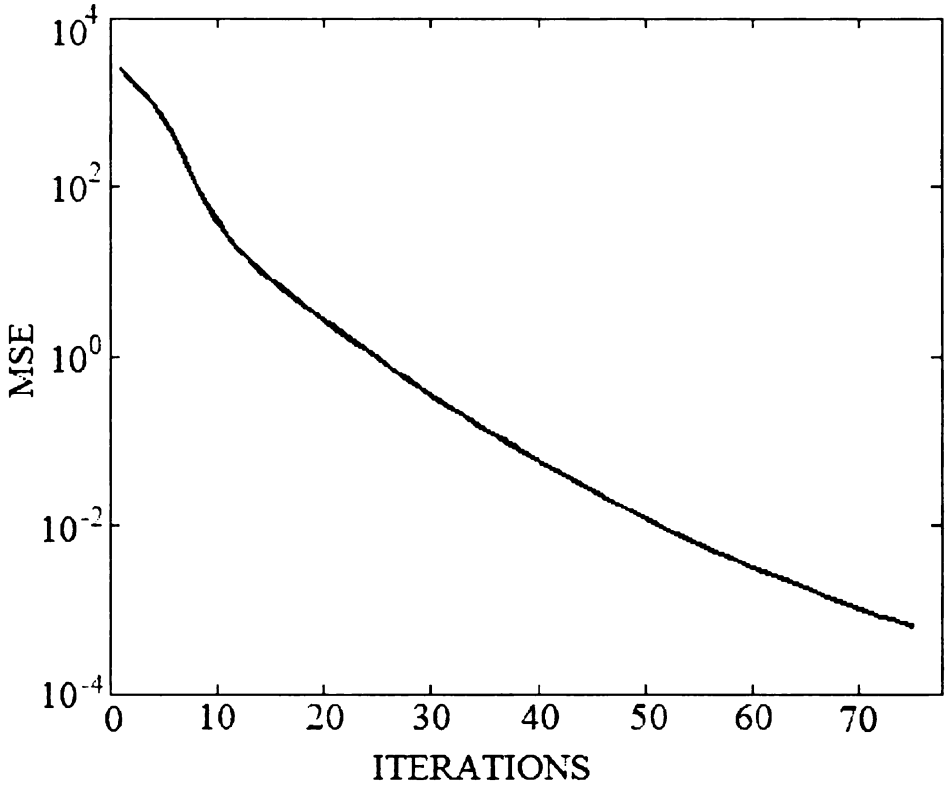

Figure 10.11. Reconstruction error for the noise free measurements.

10.4.2.2 Inversion - 2% Noise Measurements

The robustness of the proposed tomographic technique was investigated by adding zero mean random noise to the field measurements. The amount of noise added to the measurement field was quantified using the ratio of $\updownarrow^2$ norm,

$$\frac{\|n(x_r, y_r)\|}{\|E_z^r\|}\% \tag{10.41}$$

In the presence of noise, the reconstruction was noisy and often stagnated in local minima. To ensure stable solution, additional constraint was imposed using the Laplacian differentiation operator. Figure Figure 10.14 shows the breast permittivity estimated by the inversion process in the presence of 2% random noise for different Laplacian masks and identical regularization parameter γ. The reconstruction result

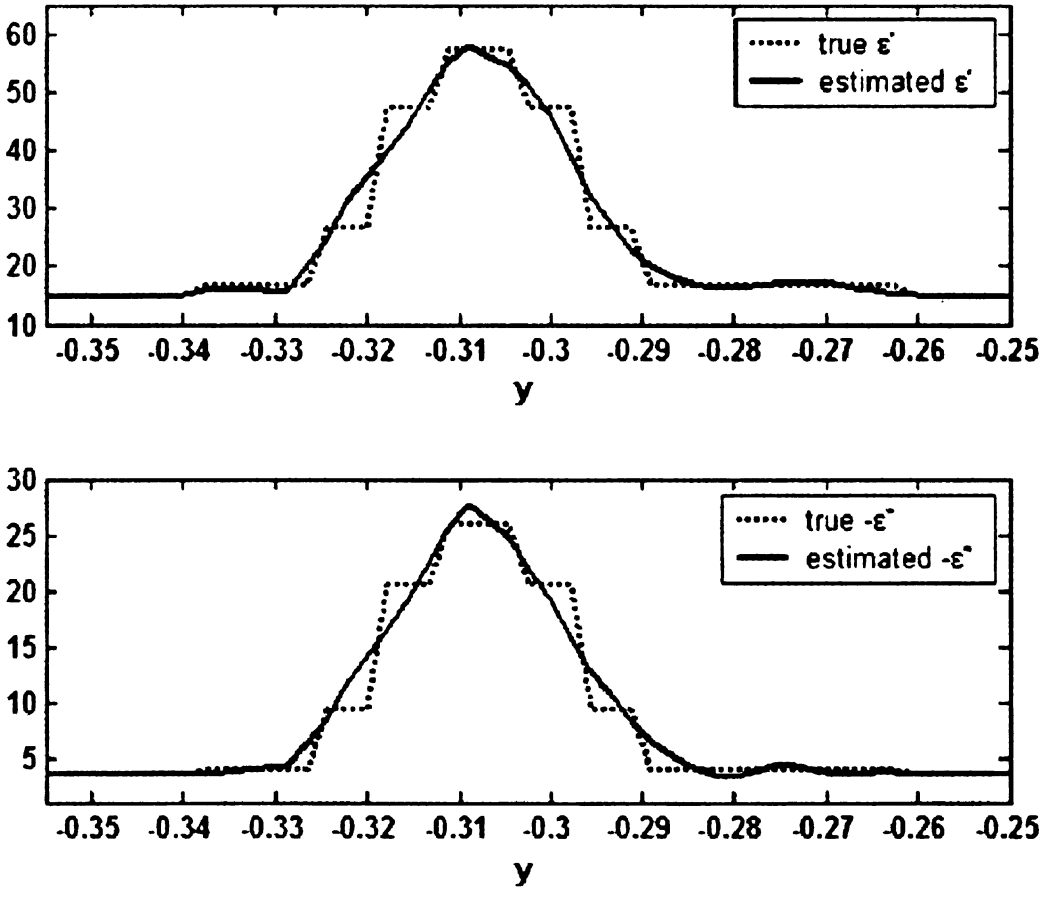

Figure 10.12. Reconstructed permittivity profile for noise free measurements along x=0.

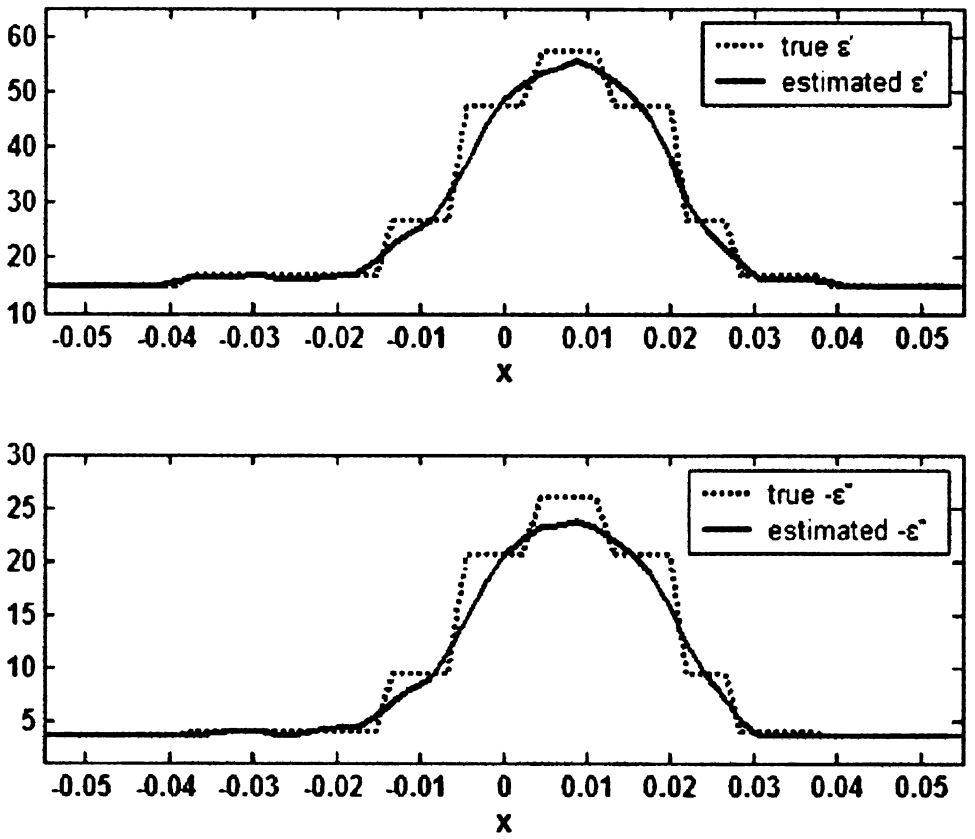

Figure 10.13. Reconstructed permittivity profile along y=-0.304.

is acceptable for field measurements with 2% random noise. The error in field measurements for the estimated permittivity distribution computed during the iterative inversion process is shown in Figure Figure 10.15. In Figure Figure 10.15, as the iteration increases the reconstruction error decreases and the permittivity estimate converges to the true solution.

10.4.3 Continuous Scatterer - Breast Model C

A lossy inhomogeneous breast model with a smooth dielectric profile was considered for tomographic reconstruction using 16 mirror shapes. Field measurements computed for continuous wave excitation at 700 MHZ was used during inversion. The spatial permittivity inside the breast model is given by the expression [173],

$$\begin{aligned} \epsilon' &= \epsilon'_0 + \left(\epsilon'_0\right)^a e^{-\frac{1}{b}\left[(x-x_0)^2+(y-y_0)^2\right]} \\ \epsilon'' &= \epsilon''_0 + \left(\epsilon'_0\right)^c e^{-\frac{1}{d}\left[(x-x_0)^2+(y-y_0)^2\right]} \end{aligned} \tag{10.42}$$

where a, b, c, d are real numbers and are the real and imaginary components of the background medium and $\epsilon_d = \epsilon' - j\epsilon''$. In (10.42), ϵ'_0 and ϵ''_0 are the real and imaginary components of the permittivity of benign breast tissue at 700 MHz reported in [47]. The permittivity profile of the scatterer obtained using (10.42) is shown in Figure Figure 10.16.

10.4.3.1 Inversion - Noise Free Measurements

Field measurements at 24 receiver locations computed for 16 mirror shapes were used to reconstruct the permittivity of 168 unknown elements inside the scatterer. The permittivity reconstruction for the noise free measurements is shown in Figure Figure 10.17. In the absence of noise, the reconstruction converged rapidly to the true solution for the first order regularization problem.

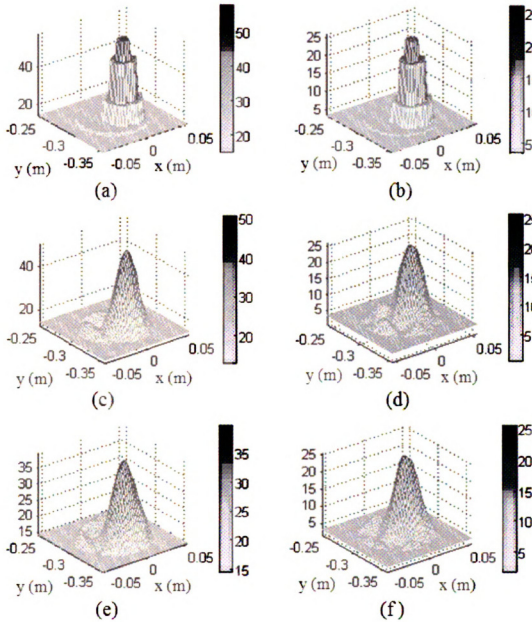

Figure 10.14. Reconstruction results with 2% additive random noise (a) true ϵ' distribution (b) true $-\epsilon''$ distribution (c) ϵ' and (d) $-\epsilon''$ for L1 (e) ϵ' and (f) $-\epsilon''$ for L2.

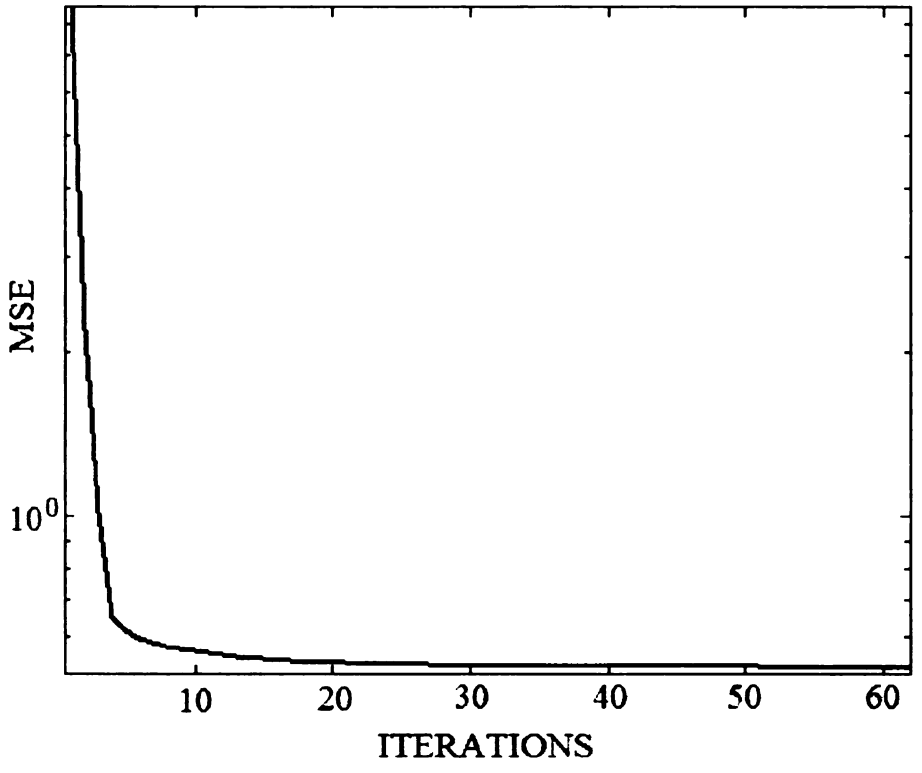

Figure 10.15. Reconstruction error for L1 in the presence of 2% additive random noise.

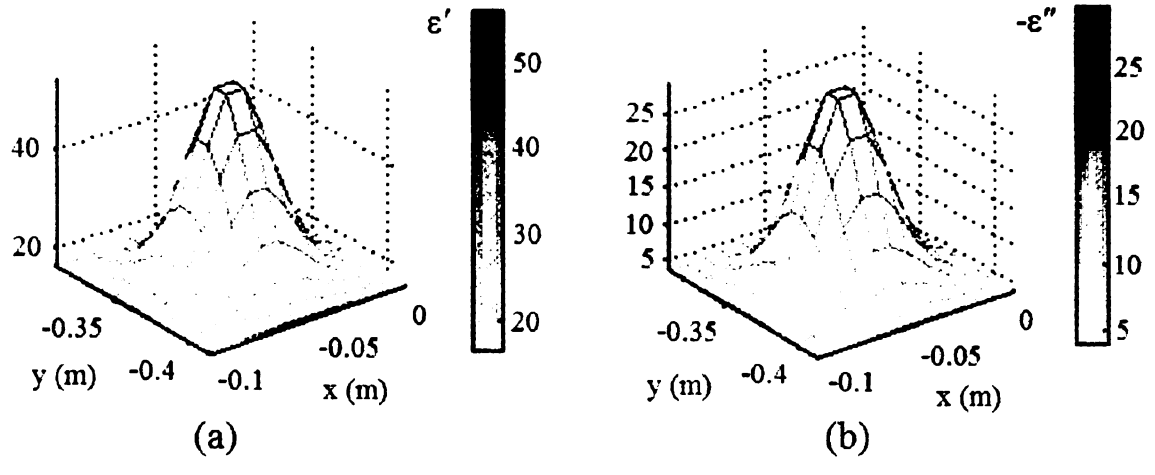

Figure 10.16. Permittivity distribution of a scatterer with smooth profile, $\epsilon = \epsilon' - j\epsilon''$.

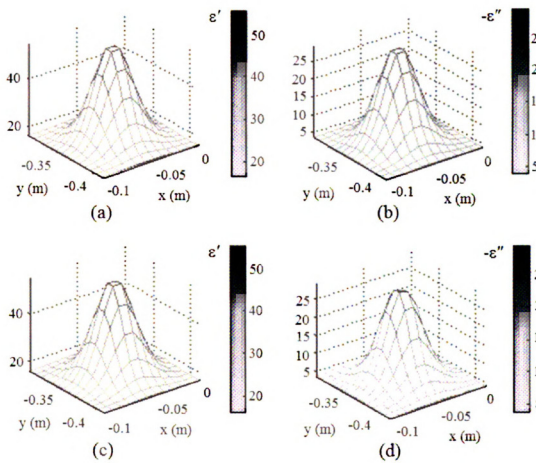

Figure 10.17. Tomographic reconstruction of noise free measurements using 16 mirror shapes (a) ϵ' and (b) $-\epsilon''$ of the true profile, (c) ϵ' and (d) $-\epsilon''$ of the reconstructed profile ($\epsilon_{bgnd} = 16.50 - j3.85$) [173].

10.4.3.2 Inversion - Noisy Measurements

Zero mean random noise was added to the field measurements computed for the 16 mirror shapes. Inversion results for the noisy field measurements were studied for 1.5%, 5% and 10% noise levels [173]. The reconstructions were obtained for the noisy measurements by including the Laplacian penalty function in the optimization problem. The reconstruction result for a 1.5% random noise is shown in Figures Figure 10.18(c)-(d). The reconstruction is comparable to the true solution and improved with increase in the number of iterations. Figures Figure 10.19(c)-(d) shows the reconstructed spatial permittivity distribution for measurements with 5% random noise. With increase in iteration number, the inversion yields permittivity estimates closer to the true profile. The reconstruction error computed during the iterative inversion is shown in Figure Figure 10.20. The reconstructed permittivity in the presence of 10% random noise is shown in Figures Figure 10.21(c)-(d). With the background permittivity as the initial estimate, the permittivity distribution inside the mathematical breast model was reconstructed for 16 mirror shapes in the presence of different noise levels. The reconstruction results in Figures Figure 10.18-Figure 10.21 demonstrate the robustness and feasibility of the proposed deformable mirror tomography system.

10.4.3.3 Choice of regularization parameter, γ

For a 5% additive random noise, simulations were carried out for a wide range of γ and the inversion results were used to construct an error curve of measurement discrepancy versus penalty. The iterative inversion process was continued until the solution was either below the tolerance level or if the cost function $C(\epsilon)$ ceased to vary with iteration. Figure Figure 10.22 shows the error curve constructed for data with 5% measurement noise. For $0.05 \leq \gamma \leq 1.0$, both the measurement error and the penalty function are minimized and for these values of γ, the reconstructions

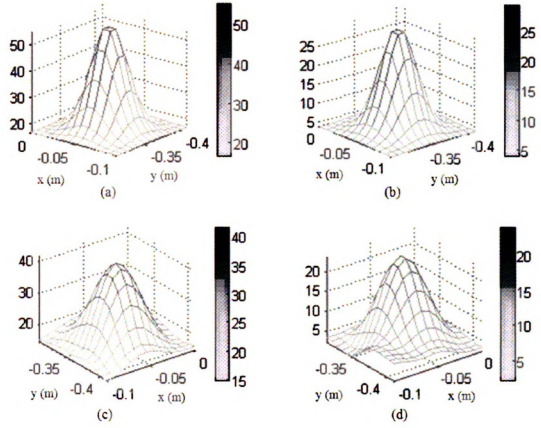

Figure 10.18. Tomography reconstruction in the presence of 1.5% additive random noise (a) ϵ' and (b) -ϵ'' of the true distribution, (c) ϵ' and (d) -ϵ'' of the reconstructed distribution.

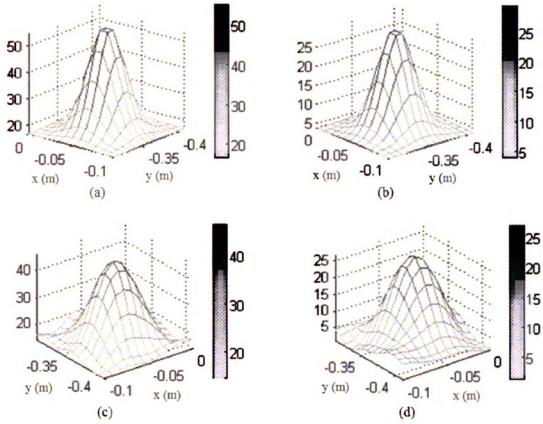

Figure 10.19. Tomography reconstruction in the presence of 5% additive random noise (a) ϵ' and (b) $-\epsilon''$ of the true distribution, (c) ϵ' and (d) $-\epsilon''$ of the reconstructed distribution.

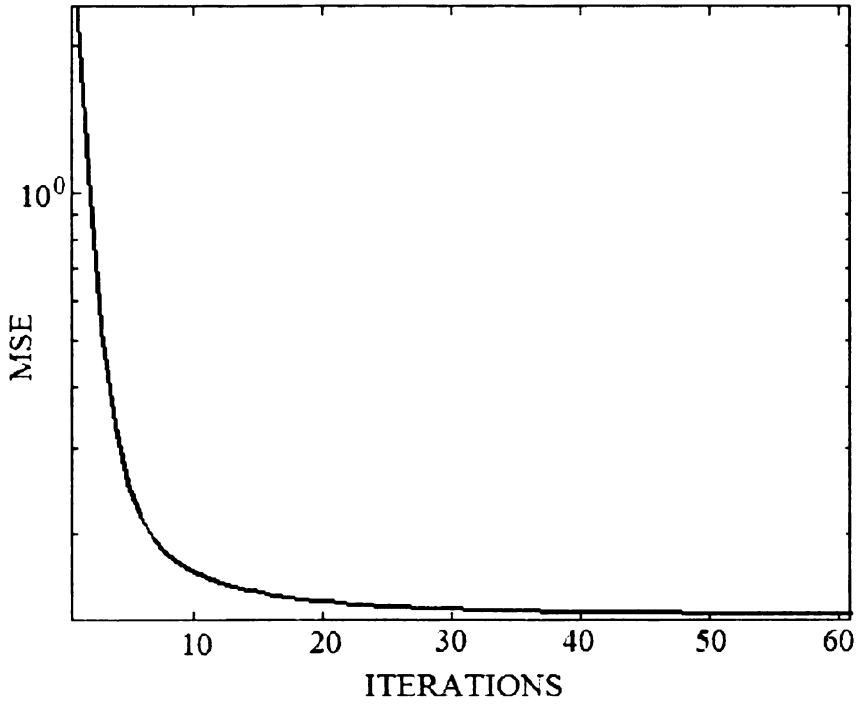

Figure 10.20. Reconstruction error in the presence of 5% additive random noise.

are comparable to the true solution. Tomographic reconstructions are promising and illustrate the feasibility of the mirror based technique for breast imaging.

10.5 Discussions

A novel deformable membrane mirror based microwave tomographic system is proposed for breast cancer imaging. The functionality and mathematical principles of the proposed system to image 2D mathematical breast models are presented. The efficiency of the mirror based tomography technique in improving the solution stability without the need to increase the number of transceiver antennas is demonstrated through 2D inversion simulations for a strong scatterer with discontinuous permittivity distribution using 8, 12 and 16 mirror shapes. Simulation results obtained for the different breast models (A, B, C) in the presence of additive random noise demonstrate the robustness of the proposed technique for breast imaging. In all sim-

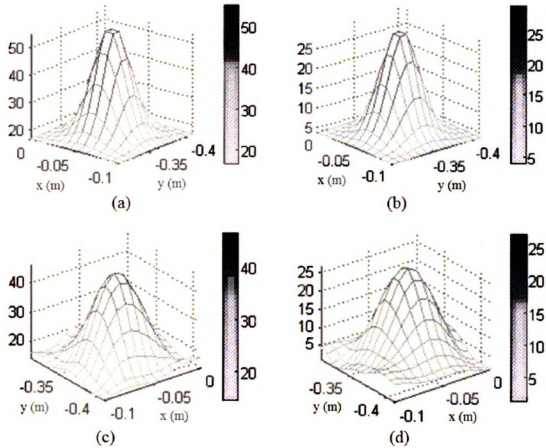

Figure 10.21. Tomography reconstruction in the presence of 10% additive random noise (a) ϵ' and (b) $-\epsilon''$ of the true distribution, (c) ϵ' and (d) $-\epsilon''$ of the reconstructed distribution.

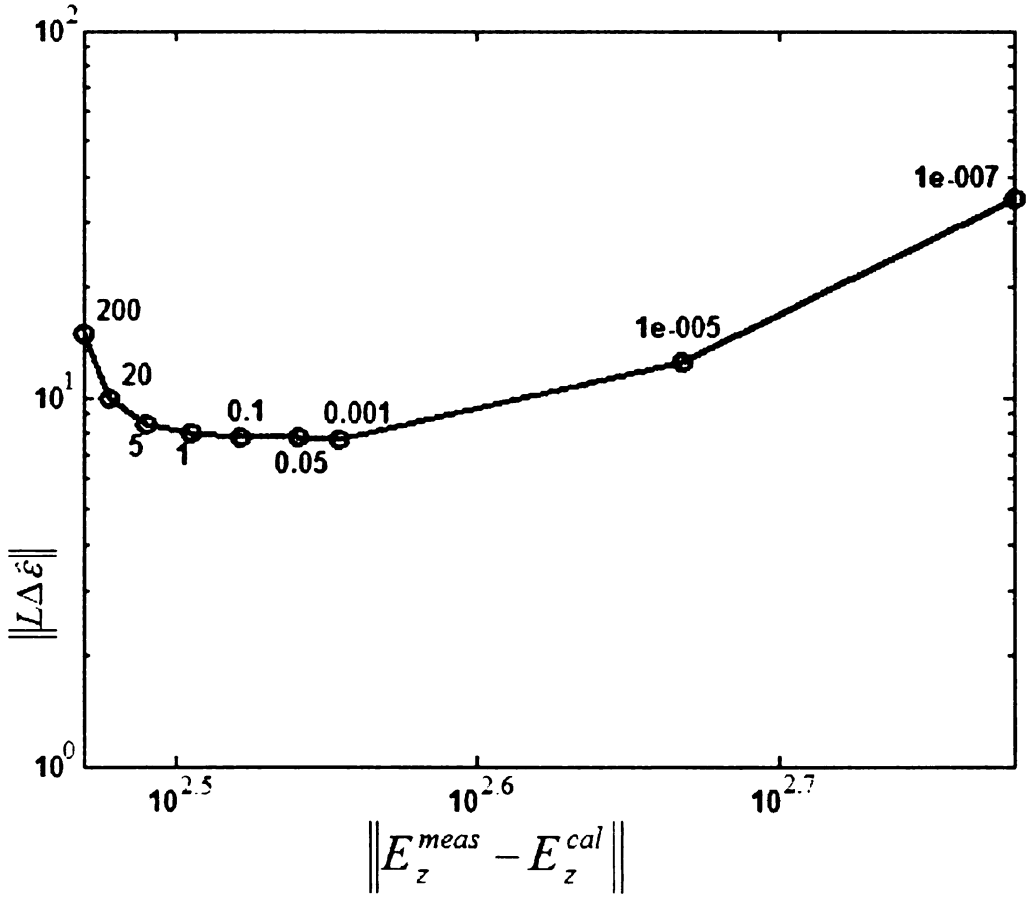

Figure 10.22. L-curve test for 5% noisy measurements [173].

ulations, the initial permittivity estimate was assumed to be equal to the background permittivity which, in this case would be permittivity of coupling solution inside the imaging tank.

The error curve constructed for the inversion process for 5% measurement noise illustrates the importance of regularization parameter, γ. During inversion simulations, the inclusion of penalty function yielded stable solution in the presence of noise. The convergence and stability of the inversion algorithm can be further improved by updating the parameters α and γ during the iterative process and by incorporating problem dependent a-priori information. The inverse scattering problem proposed using deformable mirror tomography for breast imaging is robust in that the system

- Provides information rich multi-view field measurements with a fixed transmit antenna and continuously deformable mirror
- Yields reconstruction with acceptable resolution and accuracy
- Reconstructs strong lossy inhomogeneous dielectric scatterers with
    - Discontinuous and
    - Continuous permittivity profile
- Yields improved reconstruction with incorporation of prior constraints and
- Provides stable solution in the presence of noise

In the proposed system, the complexities associated with multiple transceiver antenna arrangement, antenna switching and cross talk compensation does not exist and multi-view data for reliable reconstruction of the unknown permittivity can be obtained using predetermined optimal mirror deformations. The simulation studies broadens the horizon of the adaptive mirror technology widely used in astronomy, document scanners, retinal imaging, projection display, digital cinema and high definition TV

Table 10.3. 2D Dielectric scatterer models.

2D Models	I	II	III	IV
Scatterer type	Two-layer Homogeneous	Weak, Heterogeneous	Off-center, strong, Heterogeneous	Strong, centered Heterogeneous
Excitation	700 MHz	700 MHz	700 MHz	700 MHz
Mirror shapes	25	16	16	12
Receivers	24	24	24	24
Background, ϵ_b	9.5-0.23j	1.0	5.20 -1.03j	4.55 -0.90j

to noninvasive imaging of penetrable objects such as the heterogeneous human breast using microwaves. The simulation studies of the deformable mirror based tomography system are promising and demonstrate the applicability of a new tomographic imaging system for breast cancer detection. The convergence and stability of the inversion algorithm can be further improved by updating the regularization parameter during inversion and by incorporating additional problem dependent a-priori information.

10.6 Potential Applications

Besides breast imaging, the deformable mirror microwave tomography can be extended for material characterization and near field noninvasive inspection of inanimate objects in material science and engineering. The ability of the proposed imaging technique to invert scatterer permittivity with varying dielectric contrast was investigated using 2D dielectric models with a wide variation in the permittivity profile. The different dielectric models investigated are tabulated in Table Table 10.3.

10.6.1 Layered Media - Discontinuous Strong Scatterer

A lossy two-layer circular dielectric cylinder was chosen for permittivity inversion using the near field deformable mirror imaging technique. Homogeneous dielectric media with discontinuous permittivity profile are challenging to invert unlike dielectric scatterers with continuous or piecewise smooth permittivity variations. Inversion

of layered media dielectric model was conducted to evaluate the potential of the proposed tomography technique for multi-layer dielectric objects commonly encountered in EM applications. Figures Figure 10.23 (a)-(b) show the real and imaginary parts of the permittivity distribution inside the 2D lossy two-layer circular cylinder. Field measurements of 15 mirror deformations were used in the zeroth Tikhonov regularization to recover the discontinuous dielectric profile. Figures Figure 10.23 (c)-(d) show the reconstructed permittivity distribution, $\epsilon_{est} - \epsilon_b$ in the absence of measurement noise. Histogram of the recovered permittivity values were used to locate the two layer regions and the mean permittivity in each region was assigned as the permittivity estimate. Figures Figure 10.24 (c)-(d) show the processed permittivity estimate, $\widetilde{\epsilon}_{est} - \epsilon_b$ for the dielectric model in Figures Figure 10.24 (a)-(b). The estimated permittivity for the layered dielectric cylinder is acceptable and can be improved further by incorporating additional constraints during inversion.

10.6.2 Continuous Profile - Weak Scatterer

Simulations were conducted to invert the inhomogeneous permittivity distribution of a 2D weak scatterer in free space at 700 Hz continuous wave excitation. The real and imaginary parts of the 2D weak scatterer are shown in Figures Figure 10.25(a)-(b). As with the other simulations, the inversion process started with the background permittivity, ϵ_b as the initial guess and was iterated until (10.38a) or (10.38b) was satisfied. First order Tikhonov regularization with $L = D^1$ where D^1 is the first order spatial derivative was used to penalize oscillating solutions. Permittivity inversion obtained in the absence of noise is shown in Figures Figure 10.25(c)-(d) and the reconstruction error is shown in Figure Figure 10.26. As expected, for noise free measurements, the permittivity estimate reaches the solution rapidly.

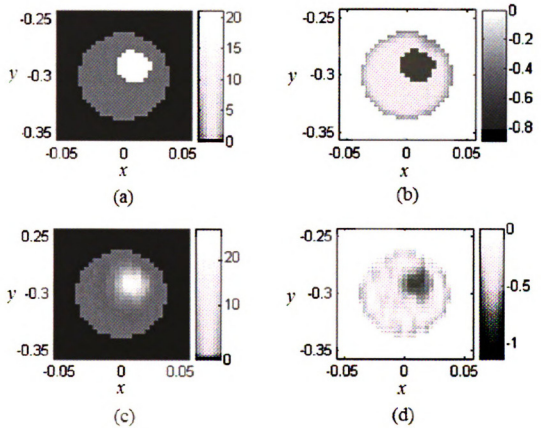

Figure 10.23. Permittivity inversion for two-layer dielectric cylinder (a) $\Re\{\epsilon_{soln} - \epsilon_b\}$ (b) $\Im\{\epsilon_{soln} - \epsilon_b\}$ (c) $\Re\{\epsilon_{est} - \epsilon_b\}$ (d) $\Im\{\epsilon_{est} - \epsilon_b\}$; ϵ_b : background permittivity.

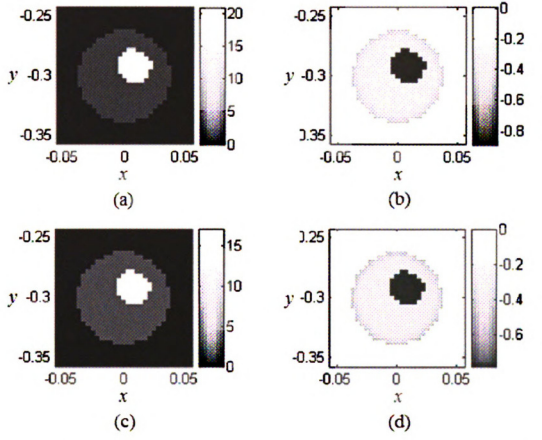

Figure 10.24. Permittivity inversion for two-layer dielectric cylinder after post-processing(a) $\Re\{\epsilon_{soln} - \epsilon_b\}$ (b) $\Im\{\epsilon_{soln} - \epsilon_b\}$ (c) $\Re\{\bar{\epsilon}_{est} - \epsilon_b\}$ (d) $\Im\{\bar{\epsilon}_{est} - \epsilon_b\}$; ϵ_b : background permittivity.

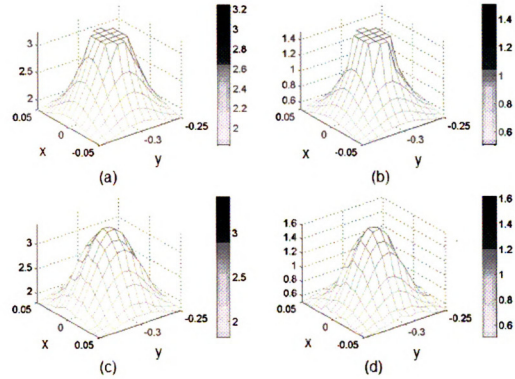

Figure 10.25. Permittivity inversion for weak dielectric cylinder (a) $\Re\{\epsilon_{soln}\}$ (b) $\Im\{\epsilon_{soln}\}$ (c) $\Re\{\epsilon_{est}\}$ (d) $\Im\{\epsilon_{est}\}$; $\epsilon = \epsilon' - j\epsilon''$, $\epsilon_b = 1.0$.

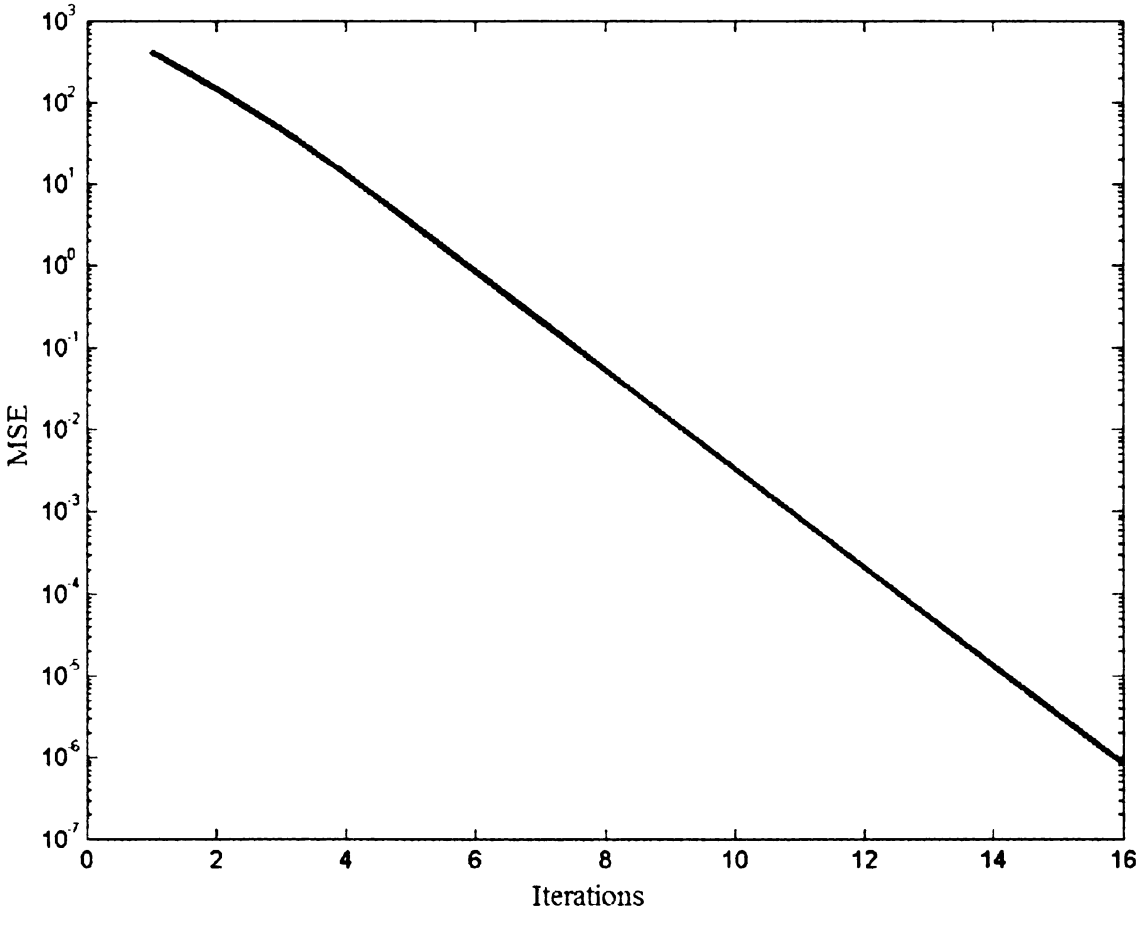

Figure 10.26. Reconstruction error for a 2D weak dielectric cylinder.

10.6.3 Continuous Profile - Strong Scatterer

Heterogeneous dielectric cylinder with continuous and high-contrast dielectric profile was used for near field imaging using the deformable mirror tomography computational model. Two dielectric scatterers were investigated in the simulations; model 'III' where the peak dielectric constant is off-center and model 'IV' where the peak is centered. Figures Figure 10.27 (a)-(b) show the real and imaginary parts of dielectric model 'III' and Figures Figure 10.27 (c)-(d) are the real and imaginary components of scatterer model 'IV' used in the simulations. Permittivity reconstructions for model 'III' and 'IV' in the absence of measurement noise are shown in Figures Figure 10.28 (a)-(b) and (c)-(d) respectively. The robustness of the mirror based tomography technique to measurement noise was investigated via numerical simulations for Model III. A 6% additive white noise was added to the field measurements computed for Model 'IV' dielectric scatterer listed in Table Table 10.3. The outcome of the first order Tikhonov regularization is shown in Figure Figure 10.29. Figures Figure 10.29 (c)-(d) show the real and imaginary components of the reconstructed dielectric profile in the presence of 6% measurement noise. The reconstruction error of the iterative permittivity recovery process is shown in Figure Figure 10.30. The permittivity reconstruction and residual error in Figures Figure 10.29-Figure 10.30 appear promising and can be further improved by imposing additional constraints along the scatterer boundary and by incorporating prior knowledge in the inverse procedure.

10.6.4 Conclusions

Numerical simulations for dielectric scatterer with different permittivity profiles demonstrate the potential applications of the novel near field deformable mirror inverse scattering technique for material characterization and imaging penetrable inanimate objects. Simulation studies indicate that the deformable mirror arrangement is capable of providing multi-view data for reliable reconstruction even in the presence

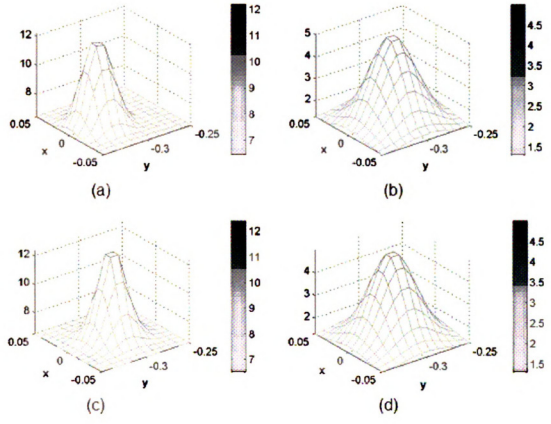

Figure 10.27. Permittivity distribution of strong scatterer (a) Model III, $\Re\{\epsilon_{soln}\}$ (b) Model III, $\Im\{\epsilon_{soln}\}$ (c) Model IV, $\Re\{\epsilon_{soln}\}$ (d) Model IV, $\Im\{\epsilon_{soln}\}$.

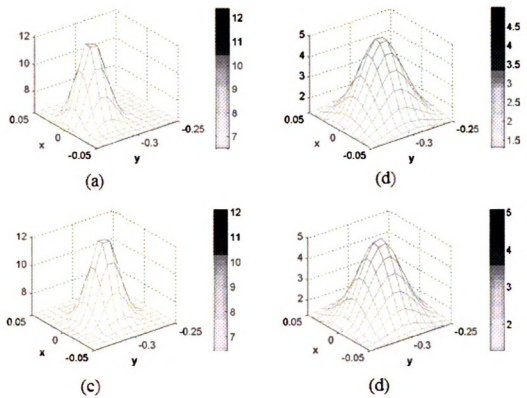

Figure 10.28. Estimated permittivity distribution of strong scatterer (a) Model III, $\Re\{\epsilon_{soln}\}$ (b) Model III, $\Im\{\epsilon_{soln}\}$ (c) Model IV, $\Re\{\epsilon_{est}\}$ (d) Model IV, $\Im\{\epsilon_{est}\}$; $\epsilon_{est} = \epsilon' - j\epsilon''$.

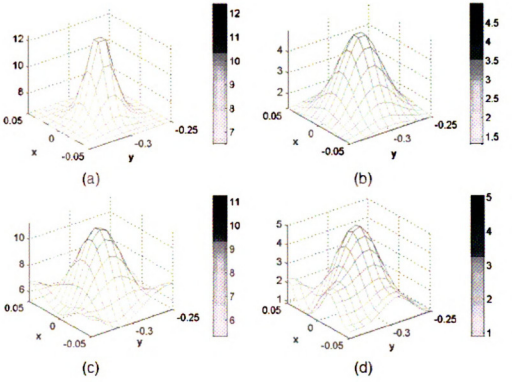

Figure 10.29. Permittivity reconstruction for 6% measurement noise (a) Model 'E', $\Re\{\epsilon_{est}\}$ (b) Model, 'E' $\Im\{\epsilon_{est}\}$.

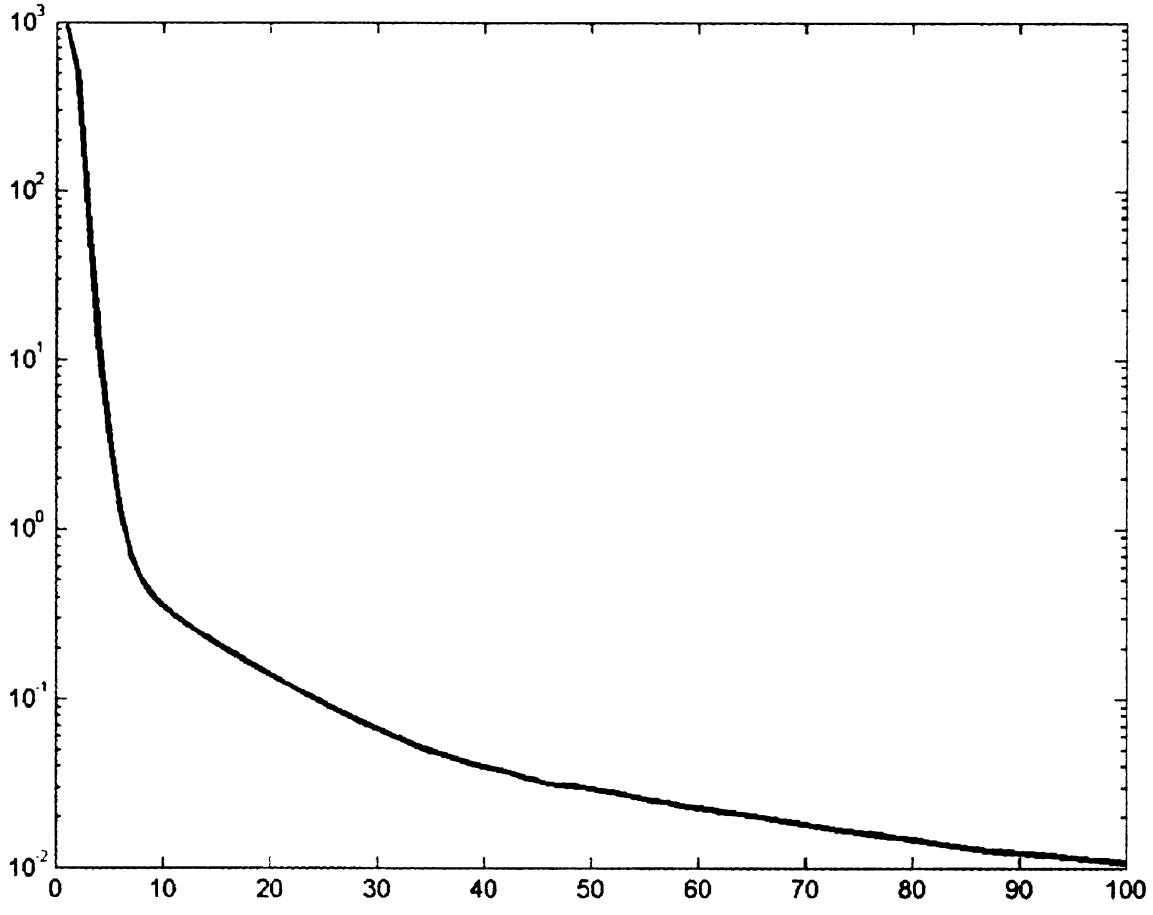

Figure 10.30. Reconstruction error for Model 'E' in the presence of 6% noise.

of additive white measurement noise.

DATE DUE	DATE DUE	DATE DUE
JAN 1 2 2008		

INVESTIGATION OF A DEFORMABLE MIRROR MICROWAVE IMAGING AND THERAPY TECHNIQUE FOR BREAST CANCER

VOLUME II

By

Kavitha Arunachalam

A DISSERTATION

Submitted to
Michigan State University
in partial fulfillment of the requirements
for the degree of

DOCTOR OF PHILOSOPHY

Department of Electrical and Computer Engineering

2007

CHAPTER 11

BREAST CANCER THERMOTHERAPY USING DEFORMABLE MIRROR

Introduction

In the United States, breast cancer is the second leading cause of cancer deaths amongst women and it is anticipated that one in every eight American women will succumb to breast cancer in their lifetime [13]. The increase in incidence and mortality rate of breast cancer is a significant health concern in the United States and elsewhere in the world. Surgery or surgery combined with radiation therapy are the most common treatment modalities for breast cancer. In recent years, hyperthermia and radiofrequency ablation techniques have been actively pursued as an alternative or adjuvant to radiation (high energy X-rays) and chemotherapy treatments of breast carcinoma. The application of electric field heating in medicine for destruction and growth control of cancer cells dates back to 1800s [26]. The efficacy of thermal treatment for destroying tumor cells and the use of thermal techniques for breast imaging are well known and documented in the literature [16], [26], [174]. In hyperthermia treatment, tissue is exposed to high power electromagnetic (EM) radiation wherein the temperature of tumor tissue is elevated above 42° for a prolonged time duration. On the other-hand, in ablation, temperature of tumor tissue is selectively elevated above 55° for few minutes. The impact of thermal deposition on tissue damage due to such electromagnetic therapies are summarized in [175].

Several minimally invasive image guided therapy techniques such as focused ultrasound, laser and radiofrequency interstitial, and microwave ablation have been proposed as an alternative to invasive surgical treatments [176]-[180]. Research involving numerical simulations and prototype experimental studies indicate the merit of mi-

crowave and ultrasound hyperthermia as an adjuvant technique for radiation therapy [181]-[186]. The widely proposed phased array microwave hyperthermia techniques often utilize either coherent or incoherent electromagnetic applicators to control the phase and amplitude of the incident field in a feedback mode for optimal power deposition without appreciable hot spots in the surrounding benign tissue. Several optimization techniques have been proposed in the literature to control the EM energy deposited by such array applicators [187]-[193]. For a given phased array applicator design, an increase in the number of antenna elements improves the field pattern inside the tissue along with an increase in the complexity of the power optimization routine.

This chapter presents the computational feasibility study of an alternative mode of EM therapy for breast cancer treatment using membrane deformable mirror [194]. The proposed system employs fixed directional electromagnetic sources and continuously deformable flexible mirror with reflective coating similar to that used in the breast imaging system. The deformable mirror with reflective coating functions as an adaptive focusing mirror and delivers preferential energy deposition at the tumor site in the breast. The proposed microwave hyperthermia technique does not require amplitude and phase optimization for regional focusing. The mirror functions like a continuum of radiating elements and maintains continuous magnitude and phase variations on the mirror surface and offers effective scan coverage inside the breast with efficient field focusing at the tumor site. The feasibility of the proposed technique is evaluated via numerical simulations on a two-dimensional breast phantom. The EM energy deposited by the therapy setup is used in the bio-heat transfer equation to quantify the steady state temperature distribution inside the breast phantom. Numerical simulation on the feasibility of extending the proposed technique for non-invasive ablation of the tumor is also presented in this chapter. Figure Figure 11.1 shows the different modules in the therapy computational model. As indicated in

Figure Figure 11.1, the key modules in the therapy model include

- Mirror shape estimation to focus EM field at the tumor site
- Computation of electric field inside the breast to evaluate EM energy deposition
- Thermal module to calculate steady state temperature distribution inside the breast for cancer therapy

The mathematical theory, approach and the implementation of each module is explained in the following sections. The proposed system with single and dual mirrors and the system functionality are explained in section 11.1. The mathematical equations that govern the EM fields in the computational model are covered in section 11.2. The electric field focusing strategy and mirror shape estimation for tumor temperature elevation are discussed in section 11.3. The bio-heat transfer equation (BHTE) that governs the steady state temperature distribution inside the breast, the computational model and tumor temperature elevation for cancer therapy are detailed in section 11.4. Comparison of the computer simulations of single and dual mirror assemblies for two dimensional breast phantom is presented in section 11.5. Steady state temperature distribution maintained by the dual mirror assembly inside two dimensional mathematical breast phantoms with tumors of varying shapes located at different regions inside the breast are also presented in section 11.5. The outcome of the computational feasibility study are summarized in section 11.6.

11.1 Deformable Mirror Therapy Setup

The novelty of the proposed approach lies in the use of the continuously deformable membrane mirror for selective EM energy deposition at the tumor location inside the breast. The deformable mirror used to steer the low power EM field for breast imaging could be used to focus the high power EM field at the tumor site for selective tissue heating. The therapy model relies on the ability of the deformable mirror

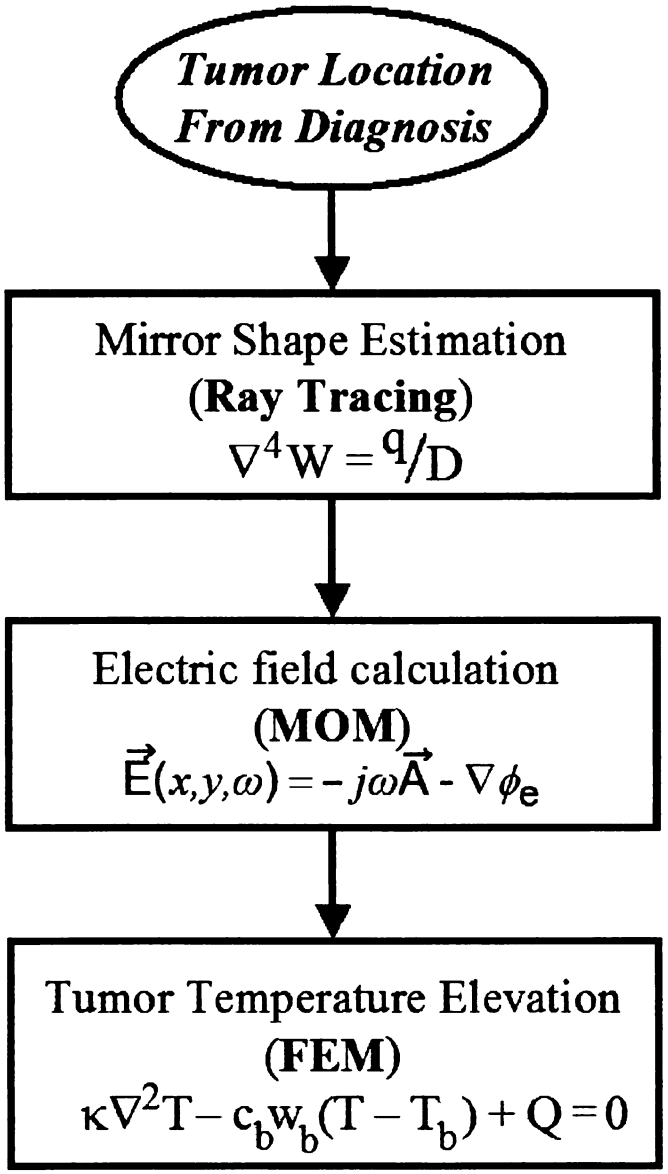

Figure 11.1. Computational modules in therapy simulations.

to conform to a predetermined shape for EM field focusing during cancer therapy. Two therapy models are investigated in this chapter using two dimensional numerical breast phantoms. The operation of both therapy schemes and the governing equations used in the computational model are explained here.

11.1.1 Single Deformable Mirror Assembly

Figure Figure 11.2 (a) shows a schematic illustration of the therapy technique that employs a deformable mirror for tumor tissue heating. The setup consists of a directional EM source such as a horn or an aperture antenna emanating continuous wave excitation and a deformable mirror both submerged inside the treatment tank filled with the coupling solution. Prior to EM thermal therapy, the shape of the deformable mirror is estimated using clinical findings of the tumor size and location such that the mirror focuses the incident EM field at the tumor site. During therapy, the field emanating form the directional source gets reflected by the deformble mirror and is focused at the tumor. The field strength is increased gradually until the desired temperature distribution is achieved in the lesion for effective cancer therapy. In the simple and less complex single mirror therapy model, the breast is exposed to high power EM radiation from one side alone. The advantages of the single mirror therapy setup is investigated via computer simulations.

11.1.2 Dual Deformable Mirror Assembly

A schematic representation of the dual mirror localized hyperthermia setup for breast cancer treatment is shown in Figure Figure 11.2 (b). The therapy set up consists of two sets of fixed directional microwave source and deformable membrane mirror inside the treatment tank filled with the coupling solution [195]. In the dual mirror assembly, the breast is illuminated by two deformable mirrors positioned on either side of the breast. The therapy setup with dual deformable mirrors provides selective energy deposition inside the lesion within a shorter time duration. Breast illumination from

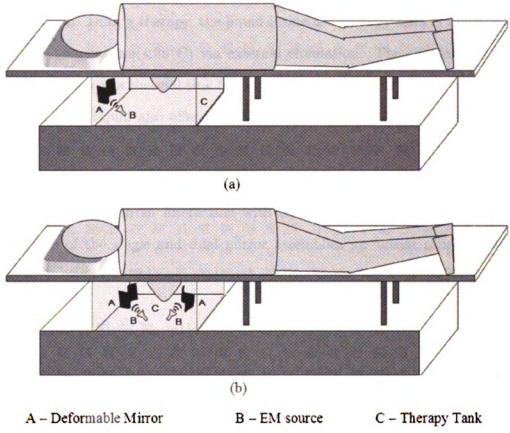

Figure 11.2. Schematic illustration of the deformable mirror therapy model for breast cancer thermotherapy (a) single mirror model (b) dual mirror model.

both sides might also help reduce undesired skin burns anticipated with the simple single mirror therapy model. The location and size of the tumor obtained from diagnostic breast images are used to estimate the deformation of the flexible mirrors to deposit preferential EM energy at the tumor site. During therapy, both mirrors are illuminated simultaneously by the respective EM sources until the temperature inside the tumor elevates to the therapeutic level. In both deformable mirror therapy setups, prior knowledge about the spatial location of the tumor is utilized to control the potential distribution of the deformable mirror actuator circuits to focus the incident EM field at the tumor location. The deformable mirror size is chosen large enough

such that the electric field reflected at the mirror surface is primarily focused at the tumor location. During therapy, the liquid inside the therapy tank is maintained at a constant temperature($<38^{\circ}$C) via external circulation. The circulating coupling solution functions as a thermal sink for the skin and reduces undesired hot spots and skin burns. The liquid also offers low impedance mismatch for the emanating EM field and efficiently couples the EM energy inside the breast. The high loss tangent of the couplant damps spurious scattering from the mirror edges and backscattered field from the breast from interacting with the metal coated mirror surface. The performance of the single and dual mirror assemblies for breast cancer therapy is investigated using the EM computational model discussed in 11.2.

11.2 Electric Field Equations

To study the feasibility of the deformable mirror setup for cancer treatment, it is essential to quantify the EM energy deposited inside the breast. The electric field equations used in the computational model to quantify EM energy deposition is explained in this section. To obtain some preliminary insights, two-dimensional numerical simulations are conducted to investigate the plausibility of using a deformable mirror for noninvasive breast cancer thermal therapy. In the computational model, the field maintained by the deformable mirror setup inside the two-dimensional breast phantom is analyzed for TM^z polarization in the time harmonic regime and the integral equation solution to the electric field is derived using method of moments.

11.2.1 Computational Model

The therapy setup that consists of metal coated deformable mirror(s), aperture sources and the penetrable lossy dielectric breast is modeled using the equivalence theorems explained in sections 4.5.4 and 4.5.5. An equivalent 2D scattering problem that is used to solve the field maintained by the deformable mirror therapy model is shown in Figure Figure 11.3. In the computational model shown in Figure Figure 11.3,

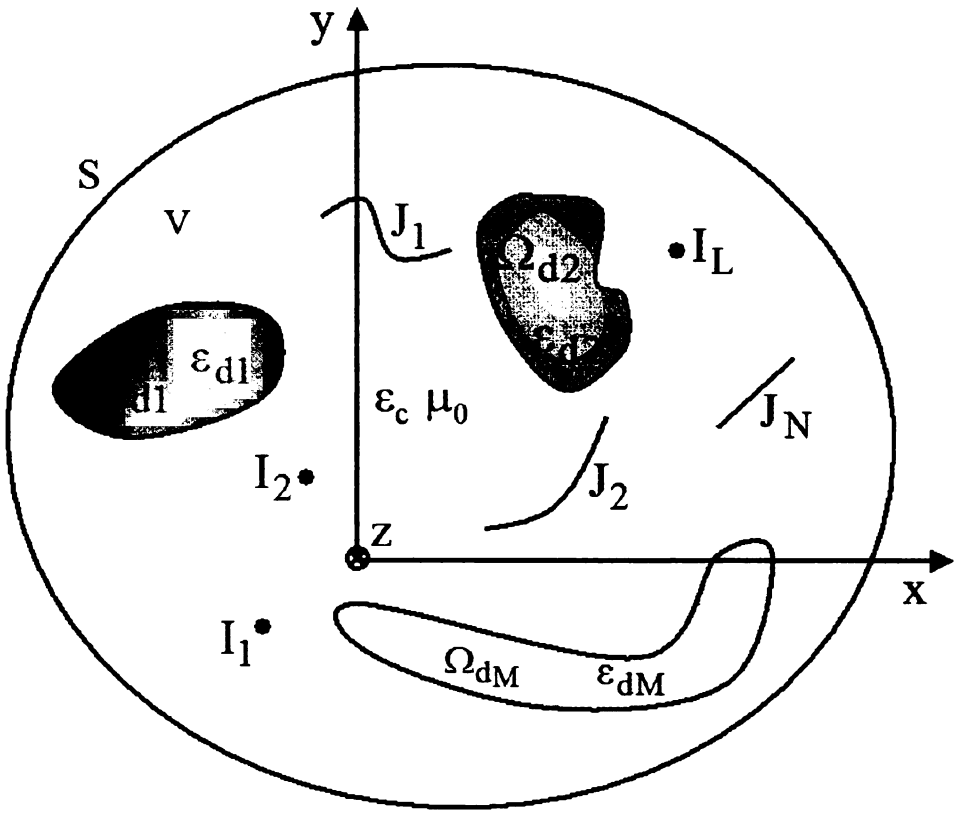

Figure 11.3. Equivalent scattering problem for the field maintained by the two-dimensional deformable mirror therapy model.

the impressed line currents $\left\{\mathbf{J}_i^l\right\}_{l=1}^{L}$ induce the surface currents, $\{\mathbf{J}_s^n\}_{n=1}^{N}$ on the thin metallic strip defined by $\{\Gamma_n\}_{n=1}^{N}$ and maintain the volume currents, $\left\{\mathbf{J}_d^m\right\}_{m=1}^{M}$ inside arbitrary shaped dielectric scatters with closed surfaces, $\{\Omega_m\}_{m=1}^{M}$. In the 2D TM^z computational model, the z-directed line currents induce z-directed equivalent currents and together they maintain the electric field, $E_z(x,y,\omega)$ inside the computational domain V. For TM^z polarization, the total electric field in (4.49) reduces to,

$$E_z(x,y,\omega) = -j\omega A_z(x,y,\omega) \tag{11.1}$$

where A_z is the z-directed magnetic vector potential defined in (4.52). The magnetic vector potential in (11.1) represents contributions of both the impressed and induced current densities inside V. The contribution of the impressed line currents is given by the equation,

$$\begin{aligned} A_{z_i}(x,y,\omega) &= \mu_0 \sum_{l=1}^{L} J_i^l(\mathbf{r}) * g(\mathbf{r},\beta;\mathbf{r}') \\ &= \mu_0 \sum_{l=1}^{L} I_l \delta(\mathbf{r}-\mathbf{r}_s) * g(\mathbf{r},\beta;\mathbf{r}'), \quad \mathbf{r}_s = (x_s,y_s,0) \\ &= \frac{\mu_0}{4} \sum_{l=1}^{L} I_l H_0^{(2)}(\beta|\mathbf{r}-\mathbf{r}_s|), \quad \mathbf{r}_s = (x_s,y_s,0) \end{aligned} \tag{11.2}$$

The field maintained by the induced surface currents on the thin perfectly conducting strips is obtained using the magnetic vector potential expression,

$$A_{z_s}(x,y,\omega) = \frac{\mu_0}{4j} \sum_{n=1}^{N} \int_{\Gamma_n} J_s^n(\mathbf{r}') H_0^{(2)}(\beta|\mathbf{r}-\mathbf{r}'|) dx'dy' \tag{11.3}$$

The TM^z electric field maintained by the current source is partly reflected and partly transmitted by the penetrable dielectric scatterer. The penetrating field inside dielectric scatterer undergoes multiple reflections at the scatterer-background boundary.

The total field inside the dielectric scatterer which also contributes to the electric field in the external medium is expressed in terms of the magnetic vector potential as,

$$A_{z_d}(x,y,\omega) = \frac{\mu_0}{4j}\sum_{m=1}^{M}\iint_{\Omega_d} J_d^m(\mathbf{r}')H_0^{(2)}(\beta|\mathbf{r}-\mathbf{r}'|)dx'dy' \tag{11.4}$$

Substituting the equivalent volume current in (5.16) into (11.4) yields,

$$A_{z_d}(x,y,\omega) = \frac{\mu_0}{4j}\sum_{m=1}^{M}\iint_{\Omega_d} j\omega\epsilon_0\left(\epsilon_d-\epsilon_c\right)E_d(\mathbf{r}')H_0^{(2)}(\beta|\mathbf{r}-\mathbf{r}'|)dx'dy' \tag{11.5}$$

In (11.5), ϵ_c is the dielectric permittivity of the external couplant inside the therapy tank and $\epsilon_d(x,y,\omega)$ is the spatial permittvity distribution inside the dielectric scatterer. Substituting (11.2)-(11.5) into (11.1) yields the total field inside V,

$$\begin{aligned} E_z(x,y,\omega) = & -\frac{\omega\mu_0}{4}\sum_{l=1}^{L} I_l H_0^{(2)}(\beta|\mathbf{r}-\mathbf{r}_s|) \\ & -\frac{\omega\mu_0}{4}\sum_{n=1}^{N}\int_{\Gamma_n} J_s^n(\mathbf{r}')H_0^{(2)}(\beta|\mathbf{r}-\mathbf{r}'|)dx'dy' \\ & -\frac{j\beta^2}{4}\sum_{m=1}^{M}\iint_{\Omega_{d_m}}\left(\frac{\epsilon_d}{\epsilon_c}-1\right)E_d(\mathbf{r}')H_0^{(2)}(\beta|\mathbf{r}-\mathbf{r}'|)dx'dy' \end{aligned} \tag{11.6}$$

where $\beta = \omega\sqrt{\epsilon_0\epsilon_c\mu_0}$ is the wave number in the coupling medium. A unique solution to the scattering problem is obtained by imposing the boundary condition,

$$E_z(x,y,\omega) = 0, \quad (x,y) \in \Gamma_n \forall n = 1,..,N \tag{11.7}$$

on the contours of the perfectly conducting obstacles. Equation 11.6, is generalization of (5.20) explained in section 5.4 for multiple perfectly conducting and penetrable scatterers.

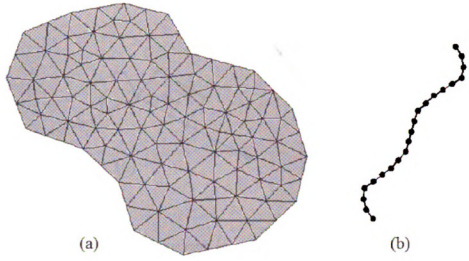

Figure 11.4. Domain discretization for computational method (a) penetrable scatterer (b) perfectly conducting strip.

11.2.2 Computational Method

The integral equation in (11.6) is solved using method of moments by discretizing the computational domain. Figure Figure 11.4 illustrates typical domain discretization of arbitrary shaped penetrable and impenetrable scatterers used in the method of moments numerical code for the unknown electric field, $E_z(x, y, \omega)$. In the computational method, the current density induced on the perfectly conducting obstacle is approximated by a linear superposition of the subsectional pulse basis functions [51]

$$J_s^n \cong \sum_{p=1}^{P^n} j_{s,p}^n b_p(t) \tag{11.8}$$

The pulse basis illustrated in Figure Figure 11.5 (a) is given by the expression,

$$b_p(t) = \left\{ \begin{array}{ll} 1 & t \in cell_p \\ 0 & otherwise \end{array} \right\} \tag{11.9}$$

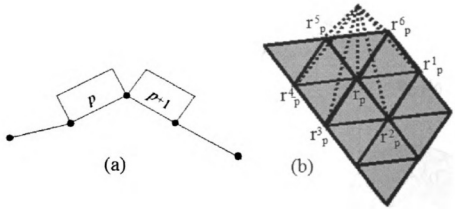

Figure 11.5. Basis functions (a) pulse basis (b) pyramidal basis.

The total field inside the dielectric scatterer given by the equivalent volume current is expanded by a linear superposition of the subdomain linear pyramidal basis functions,

$$c_p(\mathbf{r}) = \frac{|\mathbf{r} - \mathbf{r}_p^l|}{|\mathbf{r}_p - \mathbf{r}_p^l|}, \quad l = 1, 2, ..., N^p \tag{11.10}$$

such that,

$$E_d^n \cong \sum_{p=1}^{L^n} e_{d,p}^n c_p(\mathbf{r}) \tag{11.11}$$

In 11.10, N^p is the number of neighboring nodes for the p^{th} node. Figure Figure 11.5 (b) shows the pyramidal basis function centered at p^{th} node in the discretized computational domain with $N^p = 6$. Substituting (11.8) and (11.11) for the induced surface and volume equivalent currents into (11.6) yields,

$$\begin{aligned} E_z(x,y,\omega) = & - \frac{\omega\mu_0}{4} \sum_{l=1}^{L} I_l H_0^{(2)}(\beta|\mathbf{r} - \mathbf{r}_s|) \\ & - \frac{\omega\mu_0}{4} \sum_{n=1}^{N} \int_{\Gamma_n} \sum_{p=1}^{P^n} j_{s,p}^n b_p(x',y') H_0^{(2)}(\beta|\mathbf{r} - \mathbf{r}'|) dx'dy' \end{aligned} \tag{11.12}$$

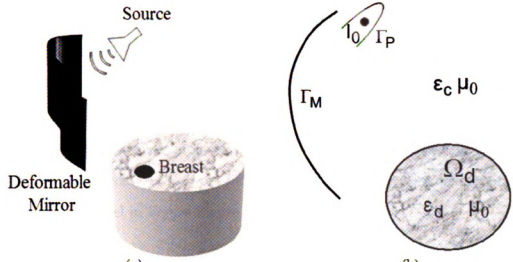

Figure 11.6. Single mirror therapy setup (a) 2D computational model (b) Model geometry.

$$- \frac{j\beta^2}{4} \sum_{m=1}^{M} \iint_{\Omega_{dm}} \sum_{p=1}^{L^n} \left(\frac{\epsilon_{d,p}}{\epsilon_c} - 1 \right) e^n_{d,p} c_p(\mathbf{r}') H_0^{(2)}(\beta|\mathbf{r} - \mathbf{r}'|) d\Omega'$$

Solution to 11.12 is obtained by evaluating the inner product between 11.12 and test functions $v_s(\mathbf{r})$,

$$\langle E_z(x, y, \omega), v_s(x, y) \rangle, \quad (x, y) \in \Gamma_n, \Omega_{dm}. \tag{11.13}$$

The inner product in 11.13 yields a linear system of equations for the unknown current densities and total electric field. The linear system of equations are simultaneously solved for the unknown current densities and total electric field inside the breast by imposing the boundary conditions in (11.7).

11.2.3 Single Mirror Therapy Model

In the 2D simulations, the microwave aperture antenna is approximated by an infinite line source with metal backing to maintain directional field pattern and the deformable

membrane mirror with reflective coating is modeled as a thin perfectly conducting arbitrarily shaped smooth strip. The 2D computational model for therapy setup employing single deformable mirror is shown in Figure Figure 11.6. In Figure Figure 11.6, Γ_P defines the contour of the metal backing for the line current and Γ_M defines the contour of the deformable mirror with thin metallic coating. The breast irradiated by the deformable mirror is modeled as a heterogeneous lossy dielectric cylinder of arbitrary shape. From (11.12), the field maintained by the two-dimensional single mirror therapy model in Figure Figure 11.6 is given by,

$$\begin{aligned} E_z(x,y,\omega) = & -\frac{\omega\mu_0}{4} I_0 H_0^{(2)}(\beta|\mathbf{r}-\mathbf{r}_s|) \\ & -\frac{\omega\mu_0}{4}\int_{\Gamma_M} J_M H_0^{(2)}(\beta|\mathbf{r}-\mathbf{r}'|)dx'dy' \\ & -\frac{\omega\mu_0}{4}\int_{\Gamma_P} J_P H_0^{(2)}(\beta|\mathbf{r}-\mathbf{r}'|)dx'dy' \\ & -\frac{j\beta^2}{4}\iint_{\Omega_d}\left(\frac{\epsilon_d(\mathbf{r}')}{\epsilon_c}-1\right) E_d(\mathbf{r}') H_0^{(2)}(\beta|\mathbf{r}-\mathbf{r}'|)dx'dy' \quad (11.14) \end{aligned}$$

satisfying the boundary conditions,

$$E_z(x,y,\omega) = 0, \quad (x,y) \in \Gamma_M, \Gamma_P \quad (11.15)$$

In (11.14), J_M and J_P are the z-directed surface current densities induced on the deformable mirror, Γ_M and the line source's metal backing, Γ_P respectively. The total field inside the 2D computational model in Figure Figure 11.6 therapy tank is obtained by solving (11.14) - (11.15) using (11.9)-(11.10).

11.2.4 Dual Mirror Therapy Model

The two-dimensional computational model for the dual mirror therapy setup is illustrated in Figure Figure 11.7. In the computational model, the individual source-

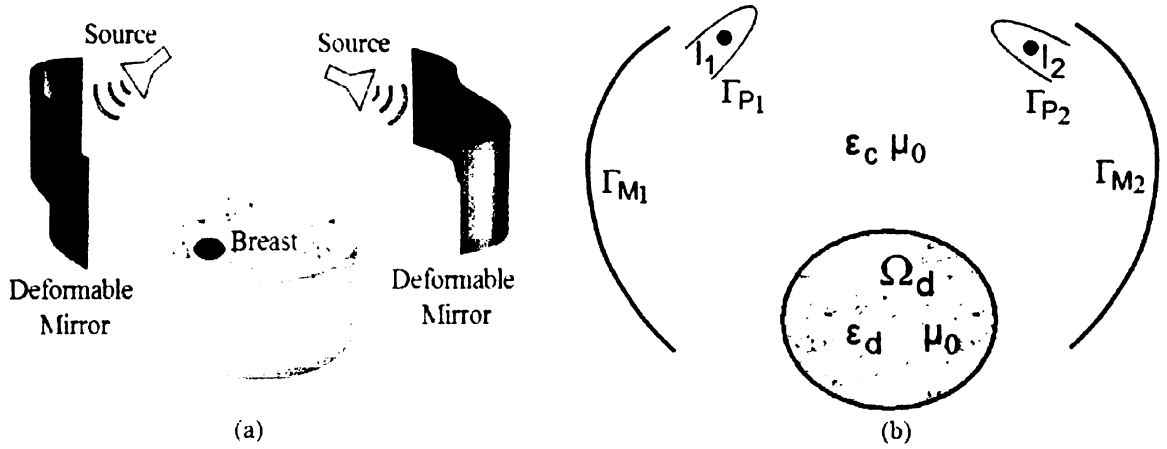

Figure 11.7. Dual mirror therapy setup (a) 2D computational model (b) Model geometry.

mirror pair is approximated as in the single mirror therapy model. In Figure Figure 11.7, the contours of the line source metal backing defined by Γ_{P_1} and Γ_{P_2} maintain the induced surface current densities J_1 and J_2 respectively. The contours of the deformable mirrors that support induced current densities are defined by Γ_{M_1} and Γ_{M_1}. The field maintained by the dual mirror assembly inside the 2D computational domain in Figure Figure 11.7 is given by the expression,

$$\begin{aligned} E_z(x,y,\omega) = & - \frac{\omega\mu_0}{4} I_1 H_0^{(2)}(\beta|\mathbf{r}-\mathbf{r}_{s_1}|) - \frac{\omega\mu_0}{4} I_2 H_0^{(2)}(\beta|\mathbf{r}-\mathbf{r}_{s_2}|) \\ & - \frac{\omega\mu_0}{4} \sum_{n=1}^{2} \int_{\Gamma_{M^n}} J_M^n H_0^{(2)}(\beta|\mathbf{r}-\mathbf{r}'|)dx'dy' \\ & - \frac{\omega\mu_0}{4} \sum_{n=1}^{2} \int_{\Gamma_{P^n}} J_P^n H_0^{(2)}(\beta|\mathbf{r}-\mathbf{r}'|)dx'dy' \\ & - \frac{j\beta^2}{4} \iint_{\Omega_d} \left(\frac{\epsilon_d(\mathbf{r}')}{\epsilon_c} - 1\right) E_d(\mathbf{r}') H_0^{(2)}(\beta|\mathbf{r}-\mathbf{r}'|)dx'dy' \quad (11.16) \end{aligned}$$

Equation (11.16) with the boundary condition,

$$E_z(x, y, \omega) = 0, \quad (x, y) \in \Gamma_{M1}, \Gamma_{M2}, \Gamma_{P1}, \Gamma_{P2} \tag{11.17}$$

is solved using the method of moments for the unknown total field in the dual mirror therapy model.

11.3 Electric Field Focusing

The objective is to determine a mirror shape such that the EM field incident on the mirror is focused at the known tumor site. The location and size information of the tumor obtained from clinical findings are used to estimate the mirror shape required for field focusing. The large physical dimension of the deformable mirror ($\geq 2\lambda_{tank}$) compared to the wavelength in high dielectric constant couplant inside the therapy tank enables the use of ray tracing technique to approximate wave interaction with the mirror surface. The high loss tangent of the coupling solution also enables return reflections from the breast to be neglected in the ray tracing model. With these assumptions, the mirror deformation for field focusing is estimated by employing ray tracing technique.

11.3.1 Focusing Strategy

Let $S_t(\mathbf{r})$ and $S_b(\mathbf{r})$ define the known tumor and benign breast tissue volumes obtained from the clinical breast images and let $p_s(\mathbf{r})$ be the location of the directional microwave source and $p_t(\mathbf{r})$ be the center or eye of the tumor tissue volume $S_t(\mathbf{r})$. For a given tumor and EM source location, the objective is to estimate a mirror surface $f(u)$ such that maximum EM energy is deposited inside $S_t(\mathbf{r})$ compared to that in the volume $S_b(\mathbf{r})$. This is achieved by employing ray tracing technique to find a mirror deformation, $f(u)$ comprising contiguous points $p_i(\mathbf{r})$ inside the search region, S near the source such that $f(u)$ effectively focuses the incident EM field at the tumor

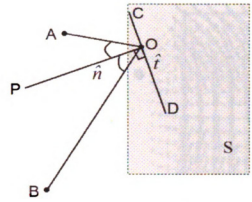

Figure 11.8. Field focusing using ray tracing.

location, $p_t(\mathrm{r})$. The search space, S is determined such that the mirror surface is away from the breast tissue to avoid direct irradiation of the breast by the directional EM source. The search region is chosen large enough to ensure the validity of the ray tracing method used in mirror shape estimation.

11.3.2 Mirror Shape Estimation

Figure Figure 11.8 illustrates the strategy underlying the mirror shape estimation procedure for breast cancer therapy. In Figure Figure 11.8, let the coordinates **A** and **B** represent the locations of the EM source and tumor center respectively. The goal is to fit a curve, $f(u)$ inside the search space denoted by the bounded dotted lines such that the rays emitting from **A** are focused at **B** after reflection from the mirror surface, $f(u) \in S$. The mirror deformation, f(u) re-directs the incident ray towards **B** only if the angle of incidence is equal to the angle of reflection i.e.,

$$\angle AOP = \angle POB \tag{11.18}$$

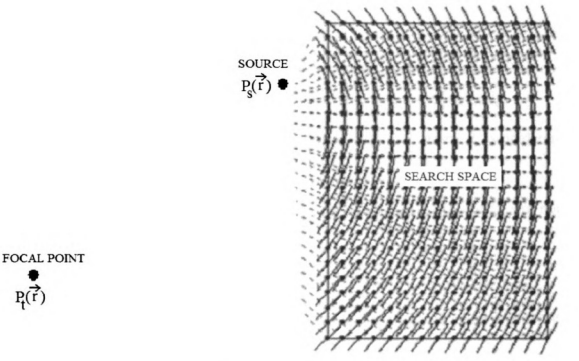

Figure 11.9. Surface tangents and normals within the search space determined for a given $p_s(\mathbf{r})$ and $p_t(\mathbf{r})$.

Condition (11.18) requires a normal at **O** such that the normal vector */overrightarrowOP* bisects the angle subtended by $\angle AOB$ as shown in Figure Figure 11.8. The vector tangent to $\overrightarrow{OP}$ and passing through **O** denoted by $\overrightarrow{CD}$ focuses the ray emanating from **A** to the desired location **B**. Following this procedure, the tangent vectors that focus the incident field at **B** are determined for all points inside the discretized search space, S. Figure Figure 11.9 shows the surface tangents and normals inside the search space that can focus rays from the source at the focal point. The next step in mirror shape estimation is to fit a curve through the surface tangents inside the search space such that the resulting surface is at least piecewise continuous for efficient field focusing. For 2D case, this is accomplished by following the below procedure.

- Start with an initial coordinate, (x_i, y_i) inside S usually, near the source at the top left corner of S

    1. Find the angle between surface tangent vector, $\hat{t}_i$ and its neighboring tangential vectors denoted by $\left\{\hat{t}_i^-\right\}$, subtending angle $\left\{\theta_t^i\right\}$ with $\hat{t}_i$
    2. Retain surface tangents, $\left\{\hat{t}_i^-\right\}$ for which, $\left\{\theta_t^i\right\} < \theta_\epsilon$ where θ_ϵ is predetermined threshold
    3. Find the closest surface tangent, $\hat{t}_i^-$ such that vectors $\hat{t}_i$ and $\hat{t}_i^-$ are not collinear
    4. If such a surface tangent vector, $\hat{t}_i^-$ exists then
        (a) Increment i, $i = i+1$ and assign (x_i^-, y_i^-) as (x_{i+1}, y_{i+1}), a contiguous point to (x_i, y_i)
        (b) Repeat steps (1)-(4) until x_i and y_i are less than the x and y bounds of the search space, S.
    5. else, stop the search process

A contiguous set of such surface tangents identified using the above steps yield the mirror shape, $f(u)$ that could be used to focus the incident field at the desired location. Figure Figure 11.10 shows one possible mirror shape for field focusing. During therapy, the actuator potential distribution, $V(x, y)$ that yields the estimated mirror deformation, $f(u)$ could be determined using an iterative minimization approach shown in Figure Figure 11.11. As shown in Figure Figure 11.11, the desired mirror deformation, $f(u)$ is achieved by iteratively estimating the actuator potential distribution such that the error,

$$C(f) = min|f(u) - \hat{f}(u)| \tag{11.19}$$

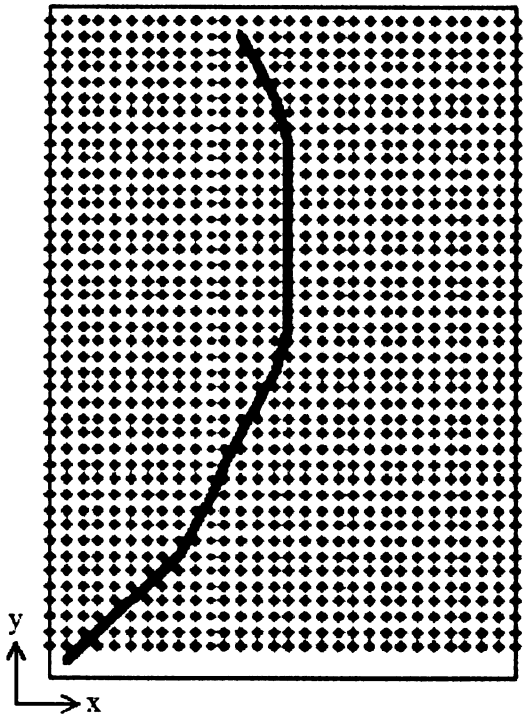

Figure 11.10. Mirror surface estimated using ray tracing for field focusing.

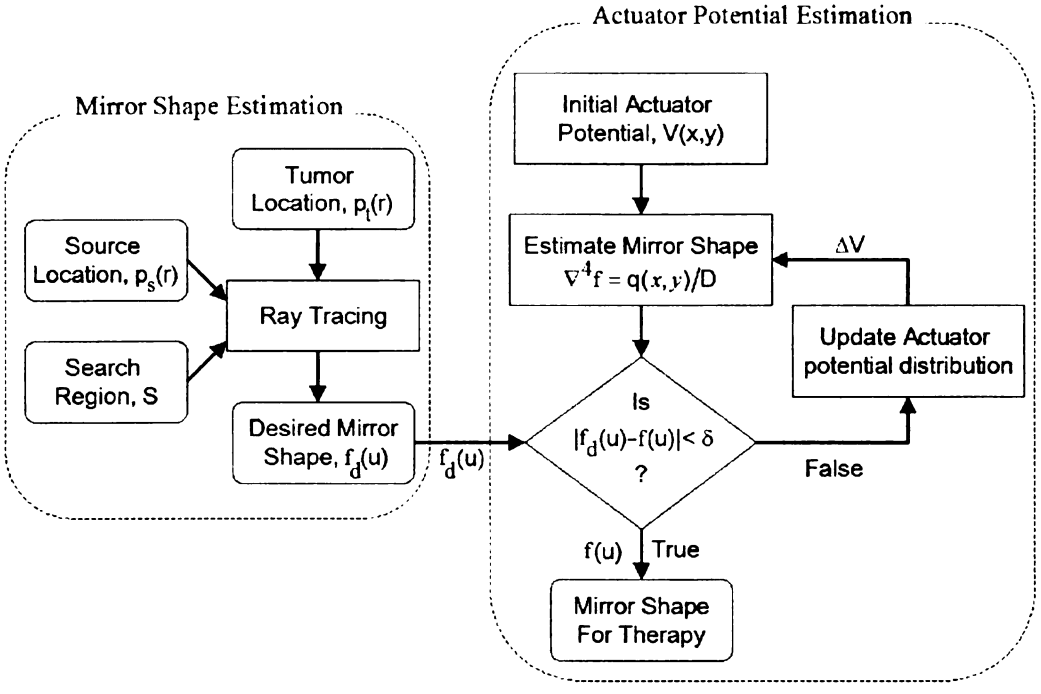

Figure 11.11. Iterative minimization procedure to determine the actuator potential for the estimated mirror deformation.

is minimized. The minimizer of (11.19) yields the actuator potential distribution, $V(x,y)$ that maintains the mirror deformation to deposit preferential amount of EM energy inside the tumor location.

11.3.3 Electric Field Inside Therapy Tank

Prior to field calculations in the presence of breast phantom, the electric field pattern maintained by the deformable mirror assembly inside the therapy tank were calculated to determine the operating frequency and to evaluate the focusing ability of the mirror shape estimated using ray tracing. In the 2D computational model, the mirror deformation was estimated to focus the electric field, $E_z(x,y,\omega)$ at x=-0.2 m and y=-0.2 m inside the therapy tank. Substituting $\epsilon_d = \epsilon_c$ into (11.6) yields the total field inside the therapy tank in the absence of breast.

Case ii: Single Mirror

For the single mirror therapy setup, the total field inside the therapy tank in (11.14) reduces to the form

$$\begin{aligned} E_z(x,y,\omega) = & - \frac{\omega\mu_0}{4} I_0 H_0^{(2)}(\beta|\mathbf{r}-\mathbf{r}_s|) \\ & - \frac{\omega\mu_0}{4} \int_{\Gamma_M} J_M H_0^{(2)}(\beta|\mathbf{r}-\mathbf{r}'|)dx'dy' \\ & - \frac{\omega\mu_0}{4} \int_{\Gamma_P} J_P H_0^{(2)}(\beta|\mathbf{r}-\mathbf{r}'|)dx'dy' \end{aligned} \tag{11.20}$$

Equation (11.20) with the boundary conditions in (11.15) yields the field in the absence of the breast.

Case ii: Dual Mirror

Electric field maintained by the dual mirror model in the absence of breast is obtained by substituting $\epsilon_d = \epsilon_c$ into (11.16) for $L = M = N = 2$. The total z-directed electric

field for the 2D computational model given by

$$
\begin{aligned}
E_z(x,y,\omega) = & - \frac{\omega\mu_0}{4} I_1 H_0^{(2)}(\beta|\mathbf{r}-\mathbf{r}_{s_1}|) - \frac{\omega\mu_0}{4} I_2 H_0^{(2)}(\beta|\mathbf{r}-\mathbf{r}_{s_2}|) \\
& - \frac{\omega\mu_0}{4} \sum_{n=1}^{2} \int_{\Gamma_{M^n}} J_M^n H_0^{(2)}(\beta|\mathbf{r}-\mathbf{r}'|) dx' dy' \\
& - \frac{\omega\mu_0}{4} \sum_{n=1}^{2} \int_{\Gamma_{P^n}} J_P^n H_0^{(2)}(\beta|\mathbf{r}-\mathbf{r}'|) dx' dy' \qquad (11.21)
\end{aligned}
$$

is solved by imposing the boundary conditions in (11.17). Equations (11.20) and (11.21) are respectively solved with boundary conditions (11.15) and (11.17) using method of moments briefly explained in section 11.2.2.

11.3.3.1 Frequency Selection

The total field inside the therapy tank was calculated for the 2D TM^z model for several operating frequencies in the flat region of the dielectric spectrum shown in Figure Figure 3.1. Simulations were carried for frequencies between 500-900 MHz. The mirror shape estimated for E-field focusing at (-0.2, -0.2) for the single mirror therapy model is shown in Figure Figure 11.12. Figure Figure 11.13 shows the corresponding TM^z electric field distribution in the therapy tank due to the deformable mirror in Figure Figure 11.12 at 500, 700 and 900 MHz. The E-field pattern for each excitation frequency is obtained using (11.20) and (11.15). The field reflected at the deformable mirror surface add in phase and maintain a focal peak at (-0.2, -0.2) as seen in Figure Figure 11.13. In Figure Figure 11.13, it can be observed that with increase in the operating frequency the field pattern becomes sharper. The increase in field strength at higher frequencies in Figure Figure 11.13 is due to the presence of the term 'ω' in (11.20). For normalized field, the strength of the EM field reduces with increase in frequency due to "*skin depth*". At frequencies above 900 MHz, the loss tangent of breast tissue varies nonlinearly as shown in Figure Figure 3.1 [47],

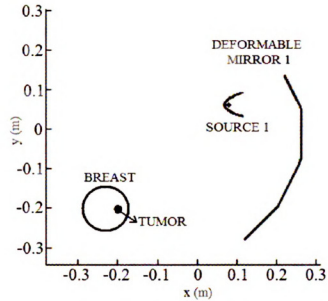

Figure 11.12. 2D single mirror therapy model for E-field focusing.

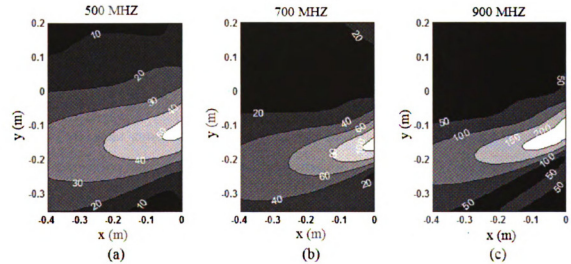

Figure 11.13. Field pattern, $|Ez|$ inside therapy tank for single mirror model (a) 500 MHz (b) 700 MHz and (c) 900 MHz (ϵ_c=43.76 j22.82).

[46]. Thus, frequencies above 900 MHz yield poor field penetration leading to poor energy deposition at tumor site and may result in undesired superficial heating and skin burns. The very high loss tangent of breast at higher frequencies and skin depth outweigh the focal resolution above 900 MHz. Hence, further numerical simulations are investigated at 500 MHz.

11.4 Tissue Thermal Map

The high water content of the tumor compared to the benign tissue results in preferential EM energy deposition at the tumor site. The EM energy deposited inside the breast forms the input for the thermal model. The EM energy deposited by the therapy setup is used in the bio-heat transfer equation (BHTE) to quantify the steady state temperature distribution inside the mathematical breast model. The computational model implemented to investigate heat transfer inside breast employs the widely used Penne's BHTE under steady state condition [35]. The steady state temperature distribution inside the breast models are analyzed using the 2D computational thermal model explained in this section.

11.4.1 Steady State BHTE

In the bio-heat transfer model, the temperature distribution inside living tissue is determined by external power deposition, heat exchange due to convection and conduction and heat generation due to metabolic activity. In the presence of external power deposition, the metabolic heat generation is negligible and hence was dropped in the steady state Penne's BHTE,

$$\kappa \nabla^2 T(x,y) + \omega_b c_b \left(T_a - T(x,y)\right) + Q_r(x,y) = 0 \tag{11.22}$$

where κ is the tissue thermal conductivity (W/m/°C); ω_b, c_b are the perfusion rate (kg/m^3/s) and specific heat (J/kg/°C) of blood; T_a is the arterial temperature (°C)

assumed to be constant; Q_r is the power (W/m^3) deposited due to spatial tissue heating and T is the temperature distribution inside the living tissue in (°C). The spatial tissue heating due to electromagnetic irradiation is given by the specific absorption rate as,

$$\begin{aligned} SAR &= \sigma \frac{|E^{rms}|^2}{\rho} \\ &= 2\rho Q_r \end{aligned} \tag{11.23}$$

In (11.23), σ and ρ are the tissue conductivity and density respectively and E^{rms} is the root mean square value of the electric field. The electromagnetic energy, Q_r in (11.23) is the heat source for the steady state BHTE (11.23). The field maintained by the deformable mirror assembly inside the breast given by (11.6) is used to calculate the tissue specific absorption rate in (11.23). The 2D steady state thermal power balance equation (11.22) is solved using (11.23) and the boundary condition,

$$T(x,y) = T_0, \quad (x,y) \in \partial\Omega_{breast}. \tag{11.24}$$

The boundary condition in 11.24 maintains the temperature in the therapy tank well below the therapeutic temperature and acts as a thermal sink.

In the 2D numerical model, the computations are for an infinitely long cylinder with spatial property invariance along the axis of the cylinder. Thus, the units of the EM energy deposited inside the breast defined in (11.23) with units (Watts/kg) has to be modified for a meaningful interpretation of the SAR values. Thus the tissue SAR calculated for an infinitely long cylinder in the 2D computational model should be multiplied by a finite height, d. Thus, in the 2D numerical simulations, a maximum SAR of $42.86(W/kg/m)$ equals 4.286 (Watts/kg) for $d = 10cm$.

11.4.2 Computational Method

The differential equation for bio-heat transfer inside the breast given by (11.22) is solved using the finite element model. The finite element method is a valuable computational tool for modeling complex, heterogeneous geometries commonly encountered in hyperthermia treatment planning [185], [187], [191]. In the finite element method, the computational breast model is discretized into triangular elements and the temperature distribution is approximated using linear subdomain basis functions $\{N_i^e(x,y)\}_{i=1}^3$. The variational formulation of (11.22) yields the elemental equation [50],

$$\left\{ \iint\limits_{\Omega^e} \left[\kappa^e \left(\frac{\partial N_i^e}{\partial x}\frac{\partial N_j^e}{\partial x} + \frac{\partial N_i^e}{\partial y}\frac{\partial N_j^e}{\partial y} \right) - c_b^e w_b^e N_i^e N_j^e \right] dx'dy' \right\} T_j^e + \iint\limits_{\Omega^e} \left[c_b^e w_b^e T_a + Q_r^e \right] N_j^e dx'dy' = 0 \qquad (11.25)$$

In (11.25), the quantities with subscript 'e' refer to the tissue properties of element, e inside the discretized breast model. The temperature inside the element is approximated by the linear basis functions as,

$$T^e(x,y) = \sum_{i=1}^{3} N_i^e(x,y) T_i^e \qquad (11.26)$$

Using (11.26), the variational form of BHTE in (11.25) is solved for the Dirichlet's boundary condition (11.24).

11.4.3 Temperature Elevation For Therapy

During thermal therapy, temperature of the coupling solution surrounding the breast phantom is maintained at a fixed temperature, $T_0^\circ C$ to avoid superficial heating of the skin. In the computational model, SAR and temperature distributions inside the breast model are controlled by impressed line current density. Thus, in the numerical

simulations, the E-field and SAR necessary for therapeutic temperature (above $42^{\circ}C$) are determined by incrementally increasing the amplitude of the impressed current density. The temperature elevation process starts with an initial current density for the line currents and solves equations (11.6) - (11.7) for the electric field distribution and computes the steady state temperature distribution inside the breast model using (11.22) - (11.24). For a given current amplitude, thermal metrics such as mean and maximum temperatures inside the benign and lesion tissue regions are calculated. The electric field and steady state thermal computations are iterated and the current density is increased during each iteration until the thermal metrics inside the breast meet the desired therapeutic thermal distribution. The tumor temperature elevation process employed in the 2D computational model is depicted in the flowchart shown in Figure Figure 11.14.

11.5 Computer Simulations - Breast Cancer Therapy

This section presents the outcome of the steady state thermal computational model employing deformable mirror on 2D numerical breast models with lesions of varying size at different spatial locations. The thermal mapping inside the breast models are studied for two different ambient temperatures inside the therapy tank in an attempt to reduce the skin/surface temperature during therapy. The feasibility of extending the mirror based therapy setup for noninvasive tumor ablation is also investigated via computer simulations.

11.5.1 Computational Breast Models

In the numerical simulations, the breast is modeled as a circular dielectric cylinder of 6.2 cm radius with 2 mm skin of uniform thickness. Circular and elliptic tumors of different physical dimensions at different spatial locations are analyzed in the numerical simulations. Figure Figure 11.15 shows the different computational breast models that were used in the computational feasibility study. The physical dimensions of

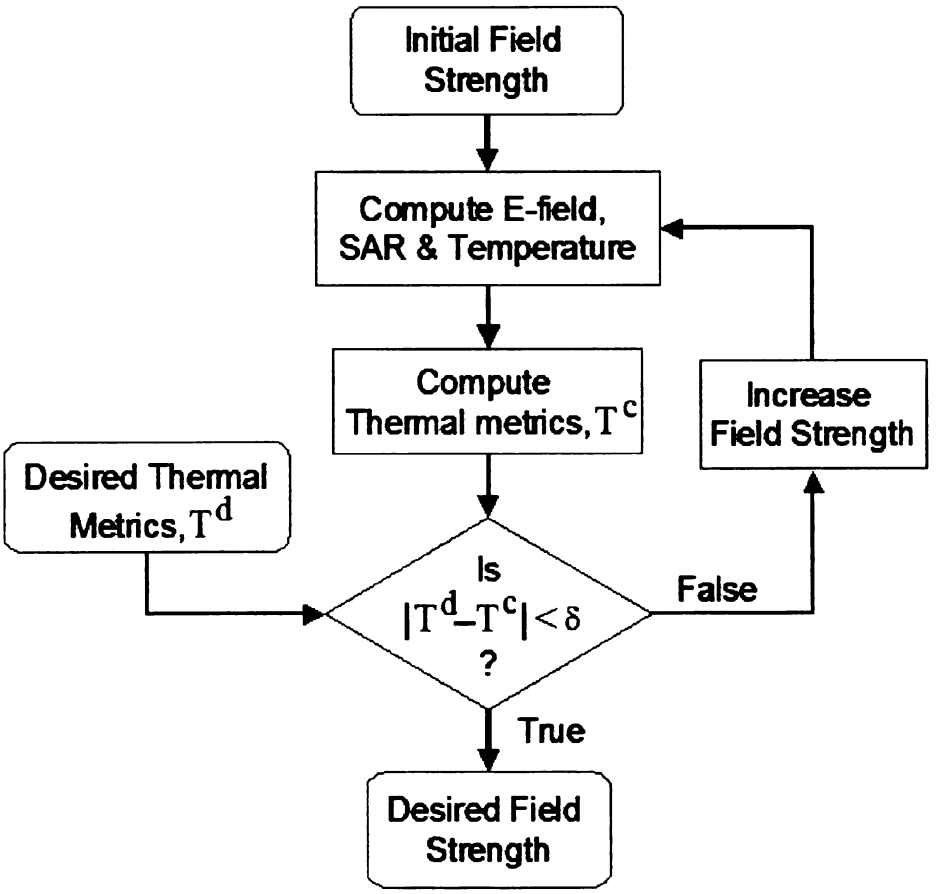

Figure 11.14. Feedback control for tumor temperature elevation.

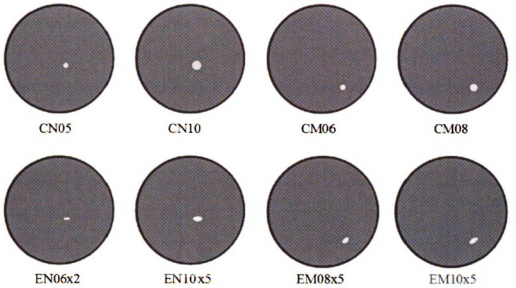

Figure 11.15. Computational breast models with tumors of varying size and shapes at different spatial locations (skin thickness = 2mm).

tumor and breast tissues are listed in Table Table 11.1. For each breast model in Figure Figure 11.15, appropriate mirror shapes were determined using the ray tracing technique explained in section 11.3.2. For the estimated mirror shapes, EM energy absorption inside the breast phantom is computed using (11.6) and (11.7). The SAR inside 2D breast phantoms calculated using (11.23) is substituted into (11.22) to determine the steady state thermal distribution inside the breast models. The steady state temperature inside the breast model is obtained using the tissue electrical and thermal properties listed in Table Table 11.2 for $c_b = 4000$. The temperature of the coupling liquid in the therapy tank is maintained at two different temperatures, $T_0 = 32°C$ and $T_0 = 37°C$. There is very limited literature on the dielectric properties of the breast tissue in the electromagnetic spectrum [45]-[47]. Experimental values reported in literature vary widely due to the inherent difference in the experimental procedures and the histological properties of the heterogeneous breast tissue

Table 11.1. Breast models used in the therapy computational feasibility study.

Computational Breast Models					
Model ID	Breast radius (mm)	Origin (mm)	Tumor size (mm)	Tumor center (mm)	Location from center (mm)
CN05	62 x 62	(-210, -190)	2.5 x 2.5	(-200, -200)	(10, -10)
CN10	62 x 62	(-210, -190)	5 x 5	(-200, -200)	(10, -10)
CM08	62 x 62	(-210, -190)	4 x 4	(-186, -222)	(24, -32)
CM06	62 x 62	(-210, -190)	3 x 3	(-186, -222)	(24, -32)
EN06x2	62 x 62	(-210, -190)	3 x 1	(-200, -200)	(10, -10)
EN10x5	62 x 62	(-210, -190)	5 x 2.5	(-200, -200)	(10, -10)
EM08x5	62 x 62	(-210, -190)	4 x 2.5	(-186, -222)	(24, -32)
EM10x5	62 x 62	(-210, -190)	5 x 2.5	(-186, -222)	(24, -32)

Table 11.2. Dielectric and thermal properties of breast tissue [47], [42], [196]-[197]($\epsilon = \epsilon_r - j\sigma/\omega\epsilon_0''$, ϵ_c=43.76-j22.82, c_b=4000, $T_b = 37°$C, f=500MHz)

Tissue type	ϵ_r	σ(S)	κ (W/m/°C)	w_b(kg/m^3/s)	ρ(kg/m^3)
Benign	18.00	0.12	0.22	1.1	888
Malignant	57.60	0.77	0.56	1.8	1050
Skin	48.63	0.705	0.42	2.275	1040

samples. Irrespective of the variations within the reported values, all findings reveal a significant contrast in the dielectric constant and conductivity of cancerous tissue compared to the benign tissue. The dielectric property of freshly excised benign and malignant breast tissues reported in [47] over 50-900 MHz frequency range is used in the computational feasibility study. Table Table 11.2 lists the tissue dielectric properties used in the numerical simulations.

11.5.2 Single Vs Dual Mirror Therapy Model

The thermal profiles maintained by single and dual mirror assemblies were investigated for the breast model CN10 shown in Figure Figure 11.15. Figures Figure 11.12 and Figure 11.16 show the computational model and mirror shapes used in therapy simulations. The specific absorption rate given by (11.23) was computed using equations (11.14) - (11.15) and (11.16) - (11.17) respectively for the single and deformable mirror setup. In both therapy models, impressed current amplitude was iteratively increased until tumor tissue temperature was elevated above 42°C. Thus, the impressed current amplitude required for the two models are different. Figures Figure 11.17 (a)-(b) show the SAR inside CN10 for which, $T_{tumor} > 42°C$ conducive for hyperthermia. Figures Figure 11.19-Figure 11.20 show the steady state thermal distribution inside CN10 maintained by single and dual mirror therapy models for $T_0 = 32°C$ and $T_0 = 37°C$ respectively. In Figures Figure 11.19-Figure 11.20, the impressed current amplitudes are iteratively increased until the tumor tissue temperature was elevated above 42°C. The steady state temperature inside CN10 for the single and dual mirror setup are compared along four different transects through the tumor shown in Figure Figure 11.18. Figures Figure 11.21 - Figure 11.22 compare the steady state thermal profiles maintained by the single and dual mirror therapy models for the transects shown in Figure Figure 11.18. From Figures Figure 11.17-Figure 11.22, it can be observed that the performance of the dual mirror assembly is better than the single mirror model for field focusing. The single mirror assembly

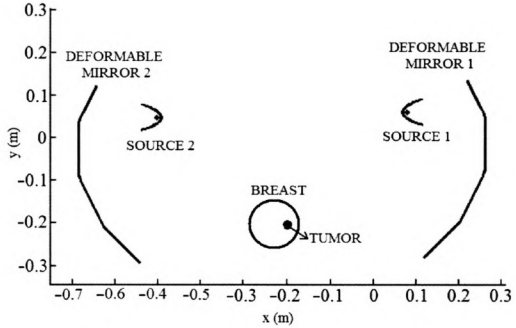

Figure 11.16. Computational model of (a) single mirror and (b) dual mirror setup.

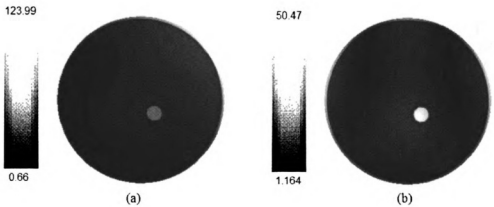

Figure 11.17. Tissue specific absorption rate in CN10 (W/kg/m) (a) single mirror and (b) dual mirror setup.

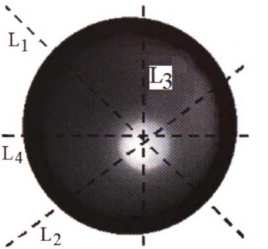

Figure 11.18. Transects through the tumor in the breast models.

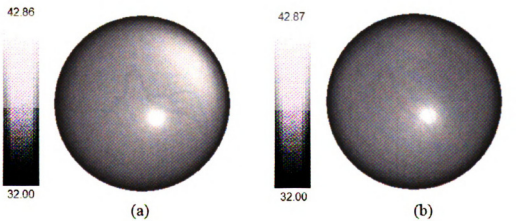

Figure 11.19. Steady state temperature distribution in CN10 for $T_0 = 32°C$(a) single mirror and (b) dual mirror setup.

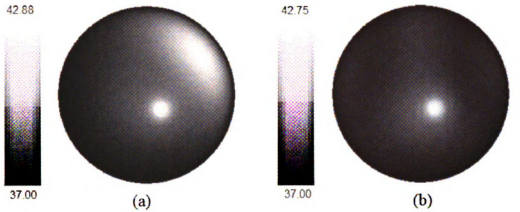

Figure 11.20. Steady state temperature distribution in CN10 for $T_0 = 37^{\circ}C$(a) single mirror and (b) dual mirror setup.

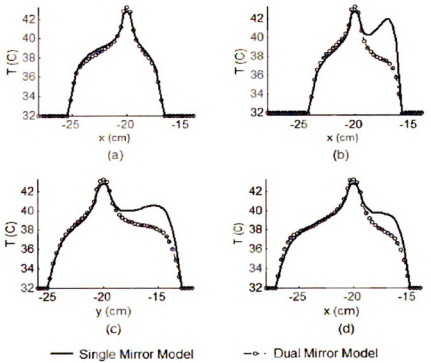

Figure 11.21. Comparison of the steady state temperature in CN10 between single and dual mirror setup for $T_0 = 32^{\circ}C$ (a) L_1 (b) L_2 (c) L_3 (d) L_4.

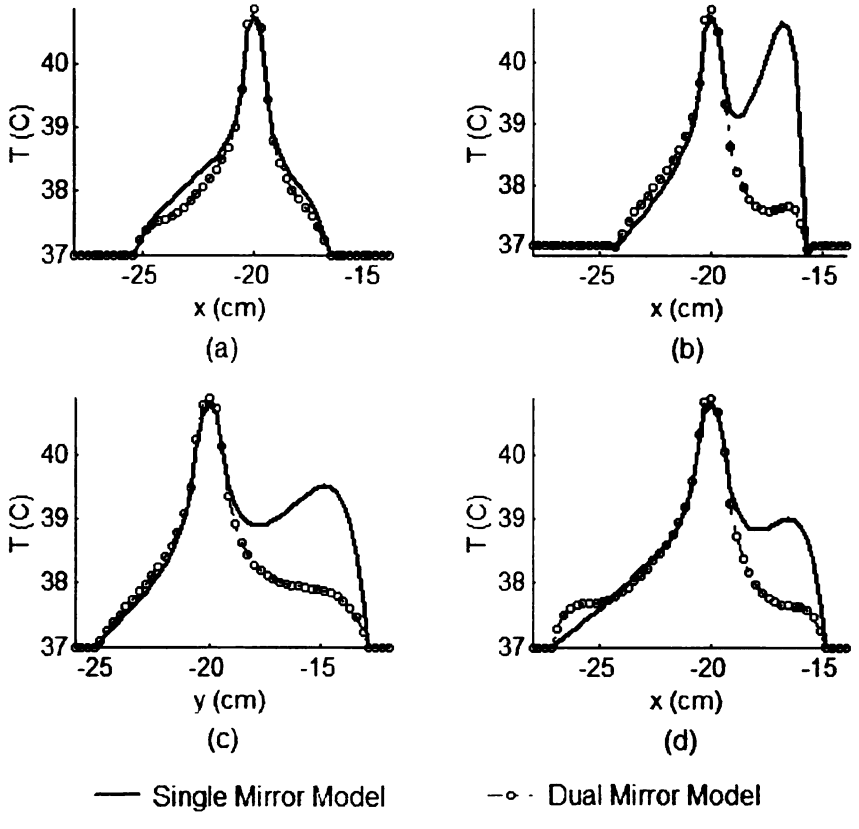

Figure 11.22. Comparison of the steady state temperature in CN10 between single and dual mirror setup for $T_0 = 37°C$ (a) L_1 (b) L_2 (c) L_3 (d) L_4.

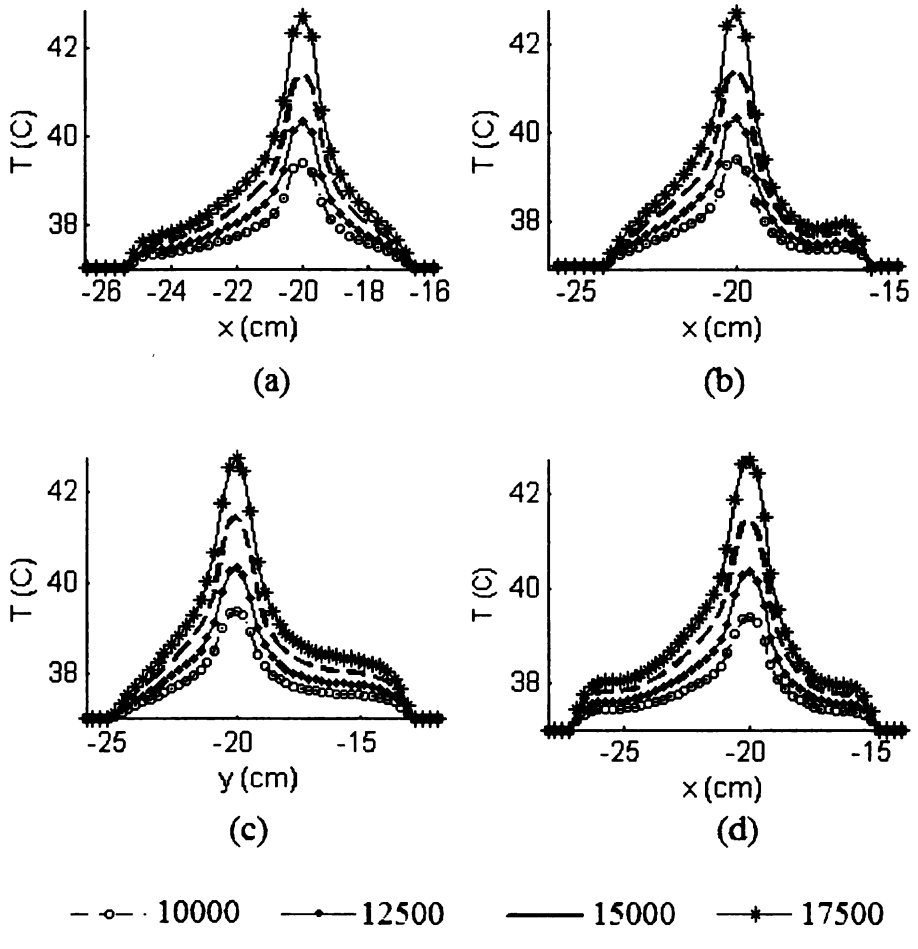

Figure 11.23. Steady state temperature elevation in CN10 for dual mirror setup for $T_0 = 37°C$ (a) L_1 (b) L_2 (c) L_3 (d) L_4.

requires larger impressed current amplitude to achieve $T_0 = 42°C$ unlike the dual mirror assembly. As seen in Figure Figure 11.17, the specific absorption rate inside the benign breast tissue is relatively large for the single mirror model which might lead to undesired hot spots in the surrounding benign tissue and skin burns. In the single mirror model, the breast is irradiated from one side which maintains a strong thermal gradient within the benign breast tissue surrounding the tumor as shown in Figures Figure 11.19 and Figure 11.20. The dual mirror model on the other hand illuminates the breast from both sides and achieves significant EM energy deposition and temperature elevation inside the tumor without any superficial skin heating and within a shorter time duration. A plot of the steady state thermal profiles in CN10 for different impressed current amplitudes in the dual mirror computational model are shown in Figure Figure 11.23 for $T_0 = 37°C$. Computer simulations indicate the merits of dual mirror setup for breast cancer thermal therapy at $T_0 = 32°C$ and $T_0 = 37°C$. Thus, subsequent computer simulations are investigated using the dual mirror therapy setup.

11.5.3 Dual Mirror Hyperthermic Simulations

Simulations were carried out for the remaining breast models in Figure Figure 11.15 using the dual deformable mirror setup for for $T_0 = 32°C$ and $T_0 = 37°C$. Figures Figure 11.24 (a)-(h) show the tissue specific absorption rate for the breast models. The corresponding steady state temperature distributions for $T_0 = 32°C$ and $T_0 = 37°C$ are shown in Figures Figure 11.25 and Figure 11.26 respectively.

Figures Figure 11.27-Figure 11.34 compare the thermal profiles calculated for $T_0 = 32°C$ and $T_0 = 37°C$ for transects through the breast models as illustrated in Figure Figure 11.18. In Figures Figure 11.27-Figure 11.34, though the temperature profiles within the breast is similar for $T_0 = 32°C$ and $T_0 = 37°C$, temperature of the skin is maintained at a much lower level for the former. This observation is true for all models irrespective of the location, size and shape of the tumor. The thermal metrics

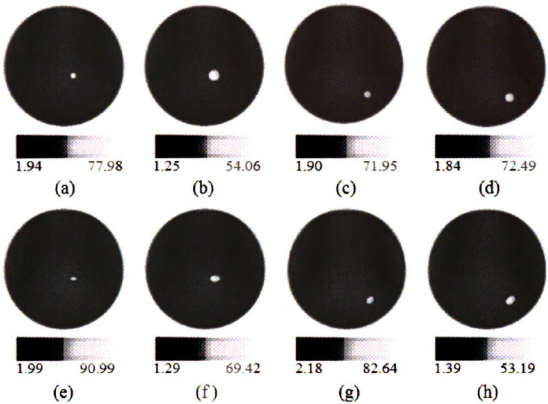

Figure 11.24. Specific absorption rate in breast models (W/kg/m) (a) CN05 (b) CN10 (c) CM06 (d) CM08 (e) EN06x2 (f) EN10x5 (g) EM08x5 (h) EM10x5.

computed for the breast models are summarized in Tables Table 11.3-Table 11.4.

11.5.4 Dual Mirror Ablation Simulations

Experimental studies on the use of microwave interstitial applicators for destroying and controlling tumor cells in various body organs have shown that high vascular tumor cells are subjected to irreversible cell necrosis at elevated temperatures [174] . Microwave ablation technique involves elevating the tumor temperature to $55-100^{\circ}C$ for few minutes unlike the prolonged E-field exposure to maintain the tumor temperature over a narrow therapeutic range of $42-45^{\circ}C$ widely practiced in adjuvant hyper-

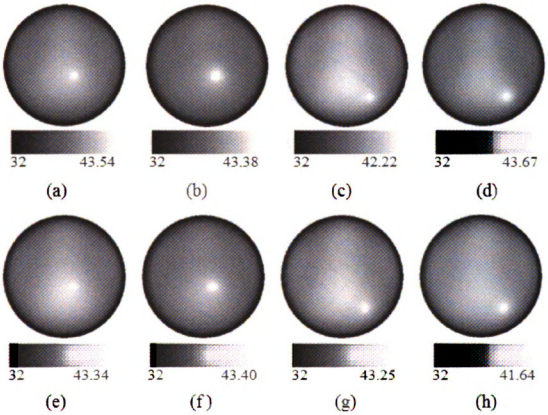

Figure 11.25. Steady state temperature in breast models for $T_0 = 32^{\circ}C$ (a) CN05 (b) CN10 (c) CM06 (d) CM08 (e) EN06x2 (f) EN10x5 (g) EM08x5 (h) EM10x5.

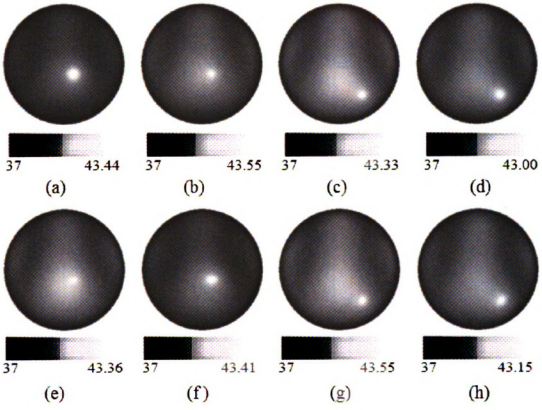

Figure 11.26. Steady state temperature in breast models for $T_0 = 37°C$ (a) CN05 (b) CN10 (c) CM06 (d) CM08 (e) EN06x2 (f) EN10x5 (g) EM08x5 (h) EM10x5.

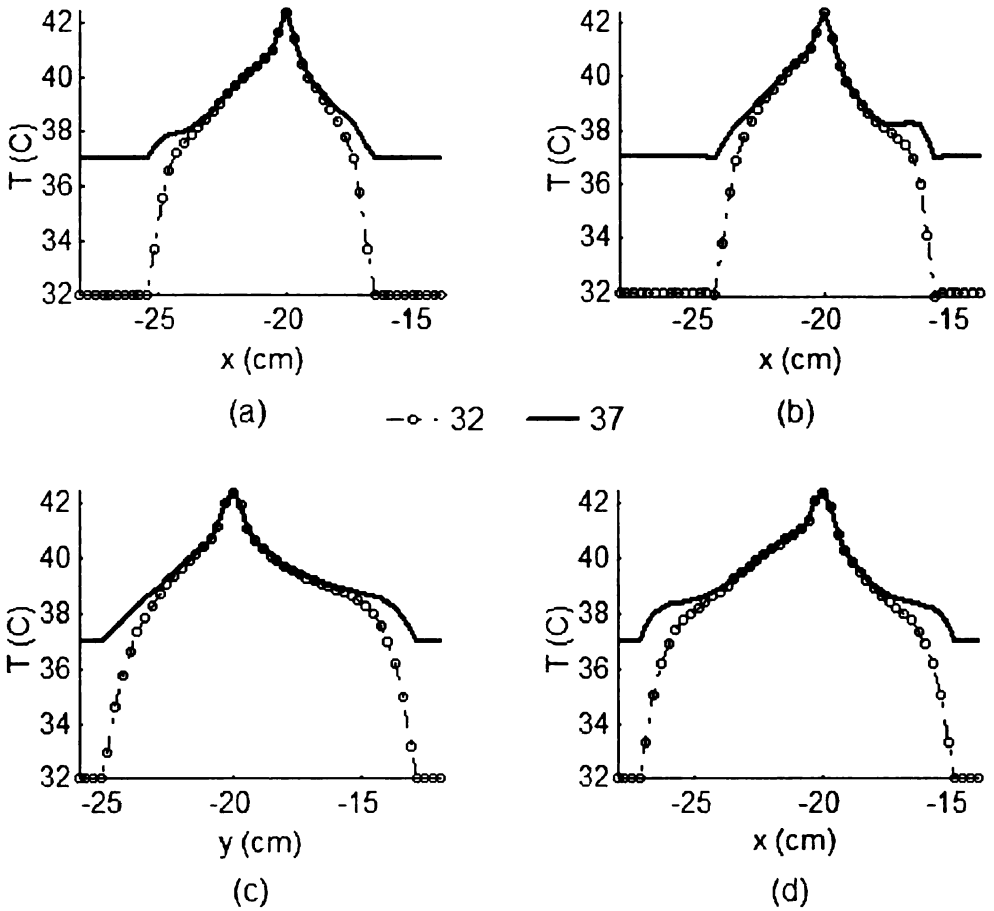

Figure 11.27. Steady state temperature in CN05 (a) L_1 (b) L_2 (c) L_3 (d) L_4.

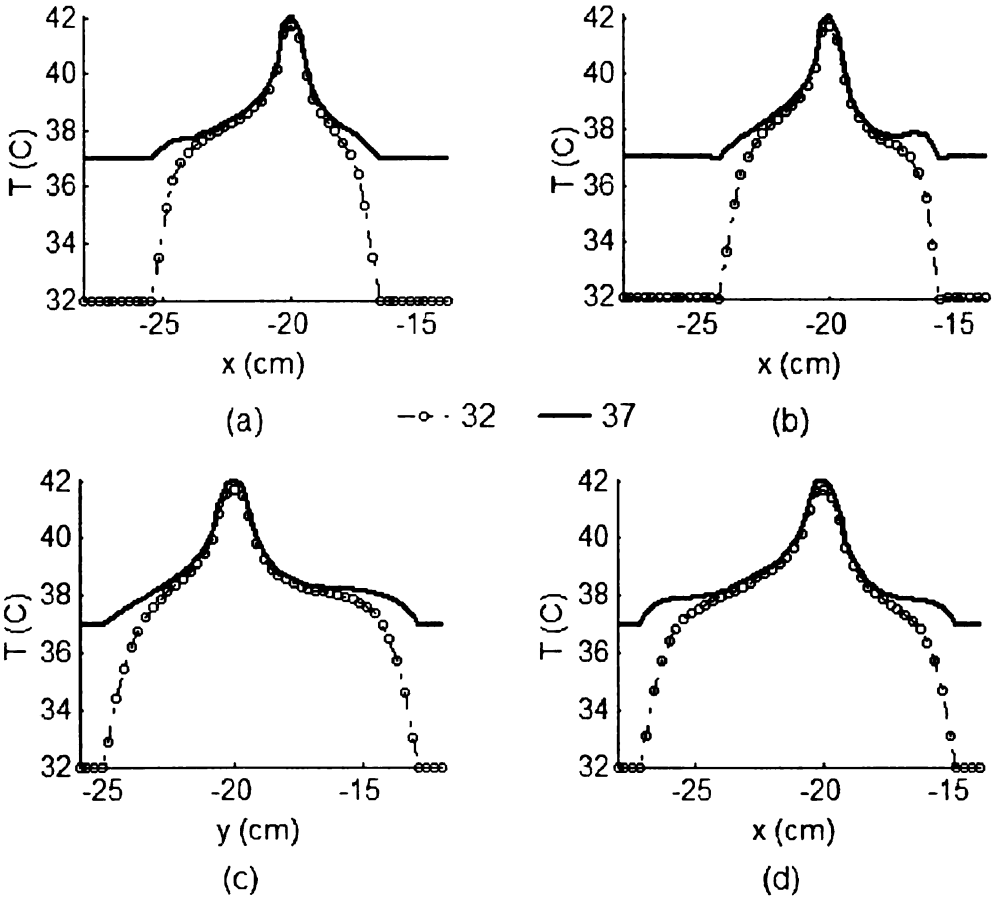

Figure 11.28. Steady state temperature in CN10 (a) L_1 (b) L_2 (c) L_3 (d) L_4.

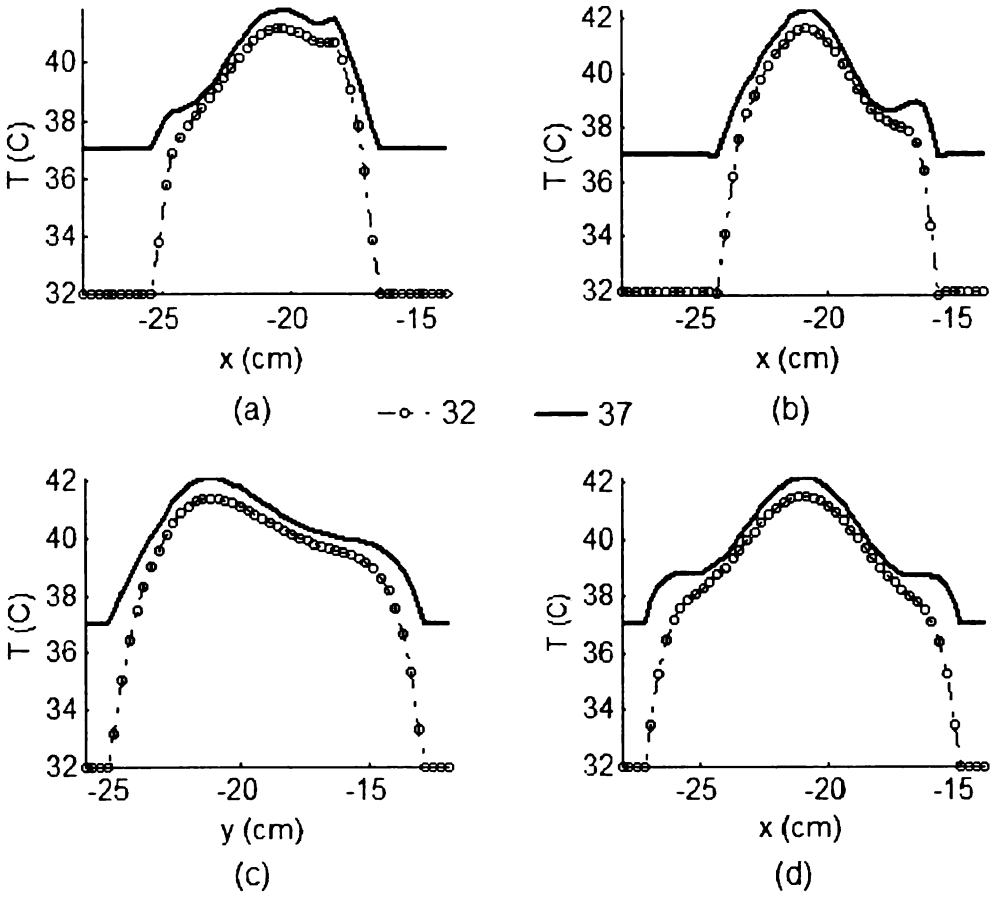

Figure 11.29. Steady state temperature in CM06 (a) L_1 (b) L_2 (c) L_3 (d) L_4.

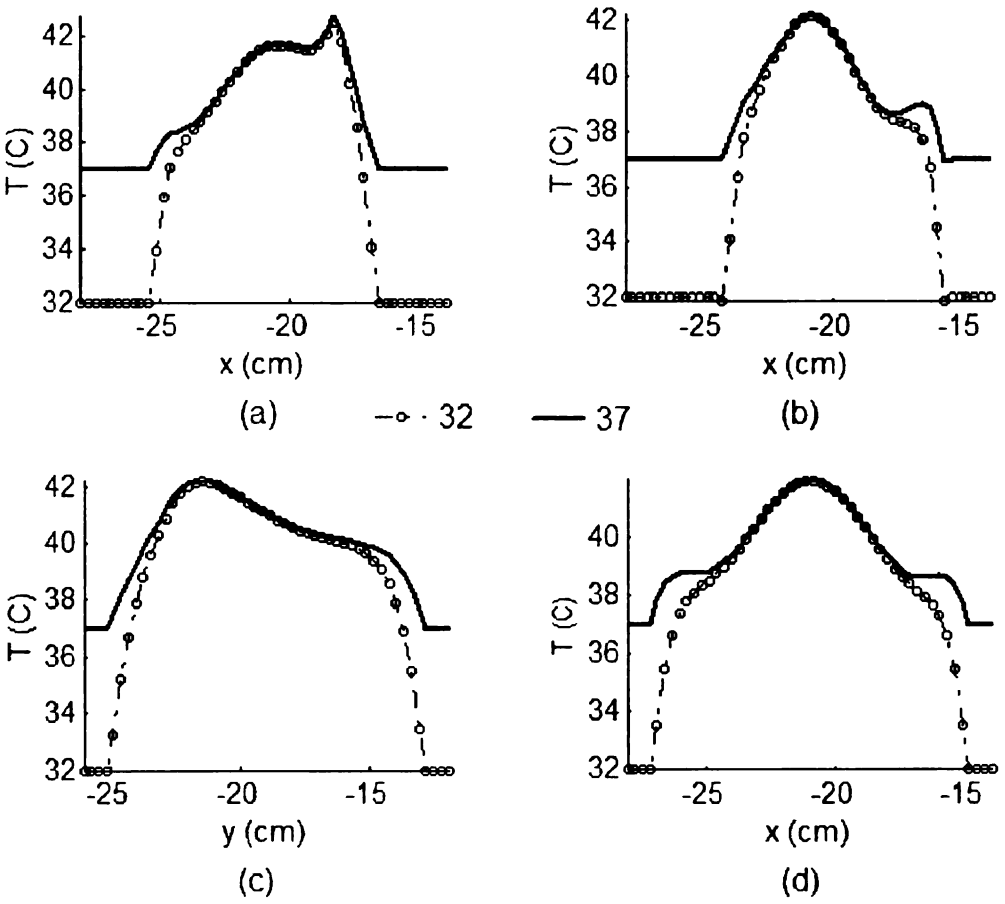

Figure 11.30. Steady state temperature in CM08 (a) L_1 (b) L_2 (c) L_3 (d) L_4.

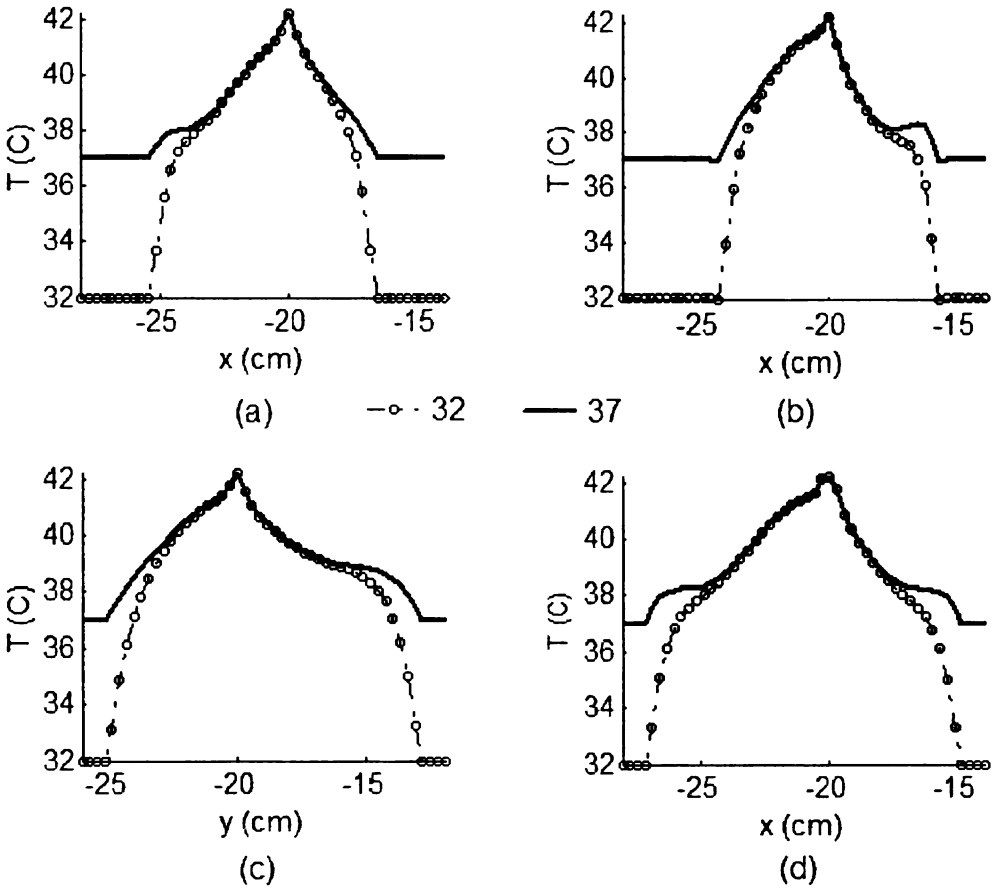

Figure 11.31. Steady state temperature in EN06x2 (a) L_1 (b) L_2 (c) L_3 (d) L_4.

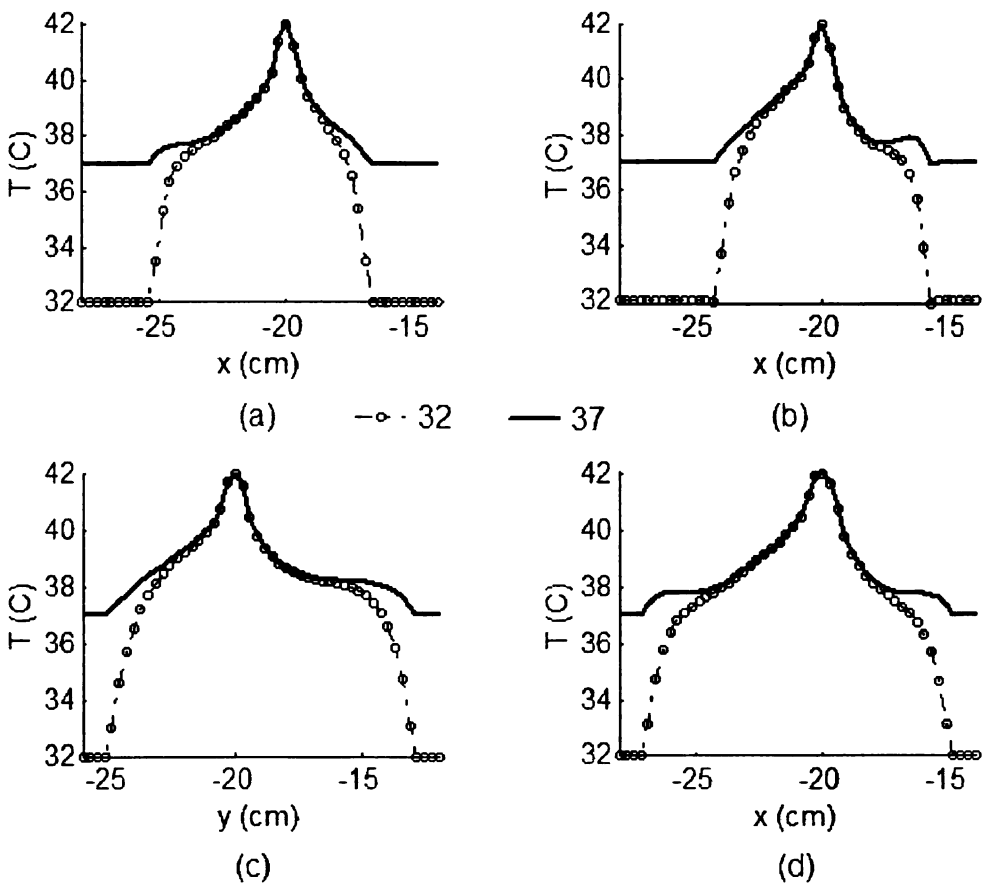

Figure 11.32. Steady state temperature in EN10x5 (a) L_1 (b) L_2 (c) L_3 (d) L_4.

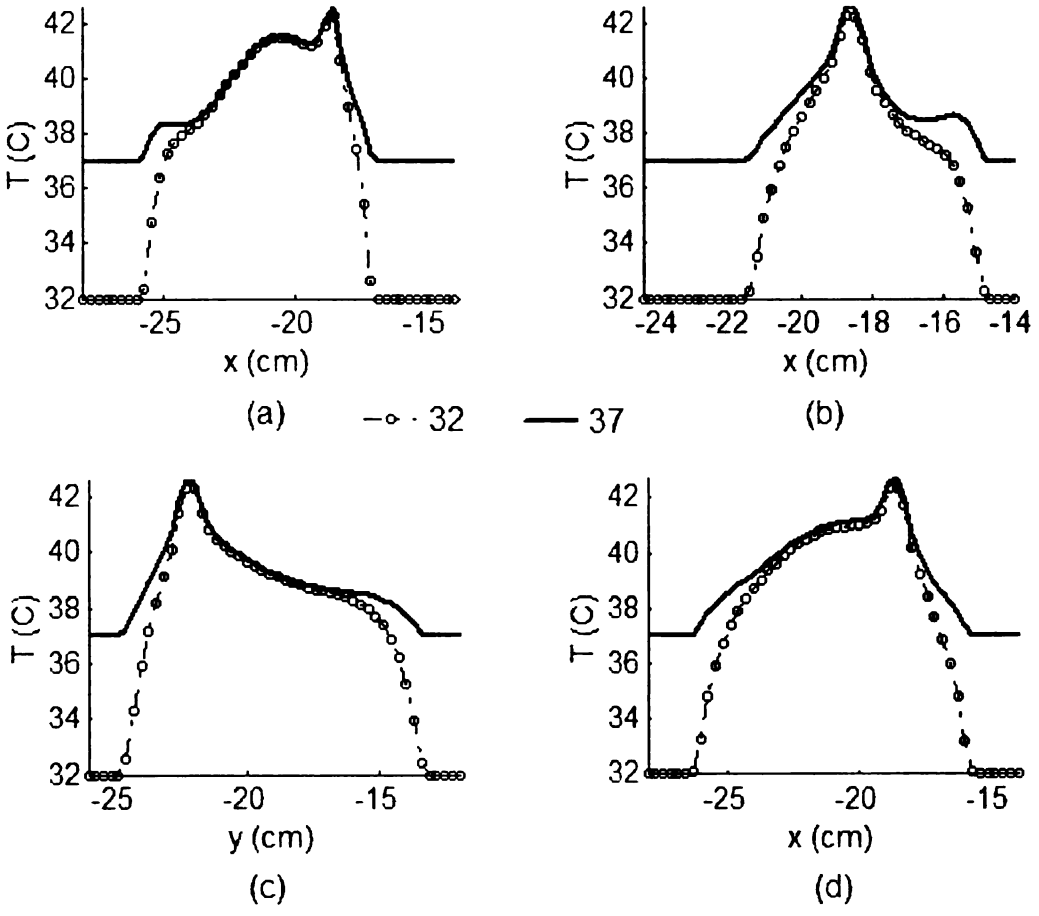

Figure 11.33. Steady state temperature in EM08x5 (a) L_1 (b) L_2 (c) L_3 (d) L_4.

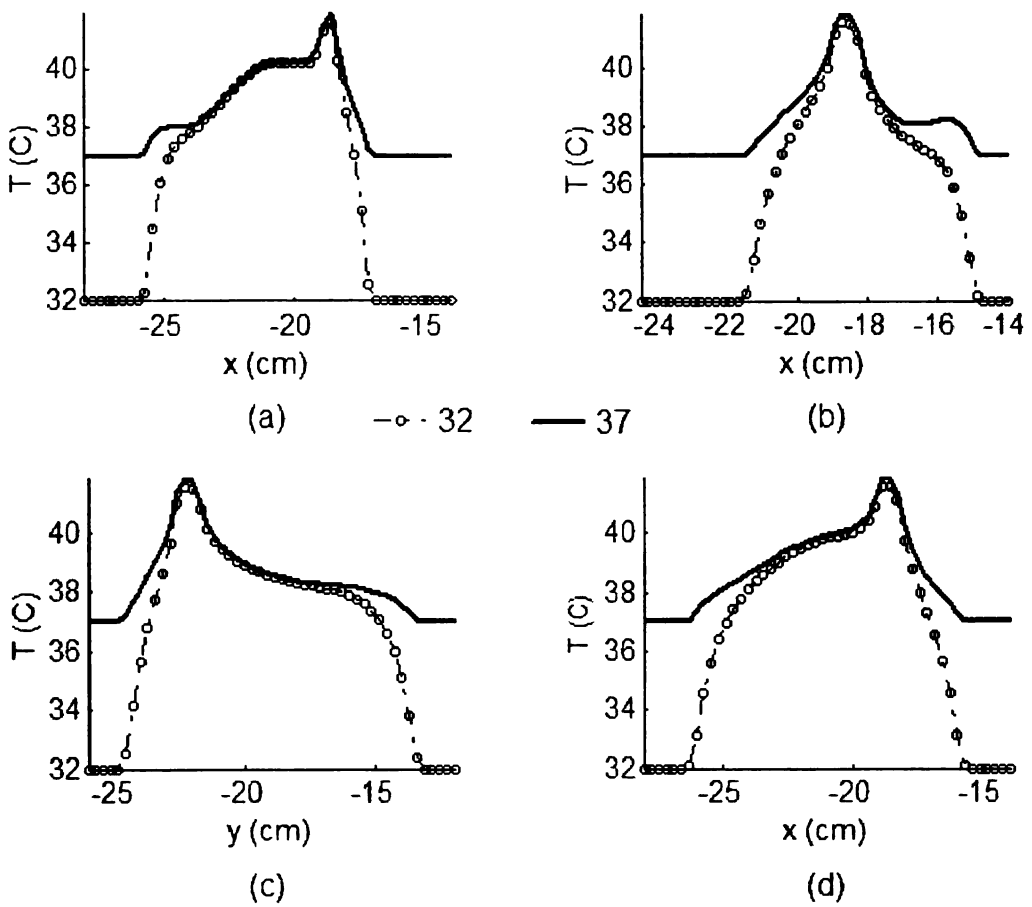

Figure 11.34. Steady state temperature in EM10x5 (a) L_1 (b) L_2 (c) L_3 (d) L_4.

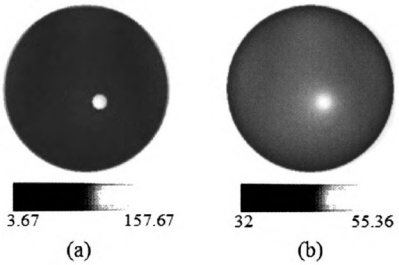

Figure 11.35. CN10 ablation simulations for ($T_0 = 32°C$) (a) SAR (W/kg/m) (b) Steady state temperature (C).

thermia treatments. It is desirable for noninvasive ablation technique to maintain the temperature of the surrounding benign tissue well below $43°C$. The computational feasibility study was extended to investigate the prospects of noninvasive ablation of the tumor using the deformable mirror therapy system. The amplitude of the impressed current in the computational procedure was increased until the maximum temperature inside the lesion was above $55°C$. Figures Figure 11.35 and Figure 11.36 show the SAR and steady state temperature distribution inside CN10 for $T_0 = 32°C$ and $T_0 = 37°C$ respectively for CN10 breast model. The thermal profiles inside the breast model along the four transects in Figure Figure 11.18 are shown in Figure Figure 11.37. The temperature distribution and thermal profiles inside CN10 indicate the feasibility of noninvasive microwave ablation of breast cancer using the deformable mirror therapy setup.

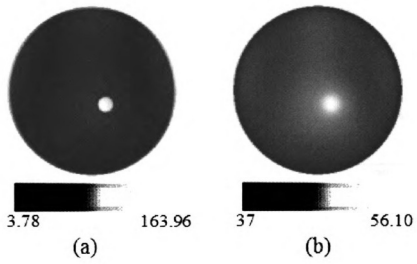

Figure 11.36. CN10 ablation simulations for ($T_0 = 37°C$) (a) SAR (W/kg/m) (b) Steady state temperature (C).

11.6 Conclusions

An alternate and novel microwave hyperthermia treatment approach for breast cancer is investigated via computer simulations on 2D breast models. The proposed technique employs deformable membrane mirrors to focus the incident EM field at the target tumor and achieve selective tumor heating while sparing the surrounding benign tissue. The deformable mirror hyperthermia assembly with fixed microwave sources is a potential alternative to the contemporary methods employing phase-focused, phase-modulated arrays and multiple discrete antennas which require phase and amplitude optimization techniques for field focusing. The large surface of the deformable mirror provides efficient field focusing at the tumor location. The continuously deformable mirror can be viewed as a flexible conformable antenna array, which can scan the breast tissue more effectively and deliver energy preferentially at the tumor site unlike the phased array hyperthermia applicators with limited number of antennas. The computational feasibility study presented for the two dimensional

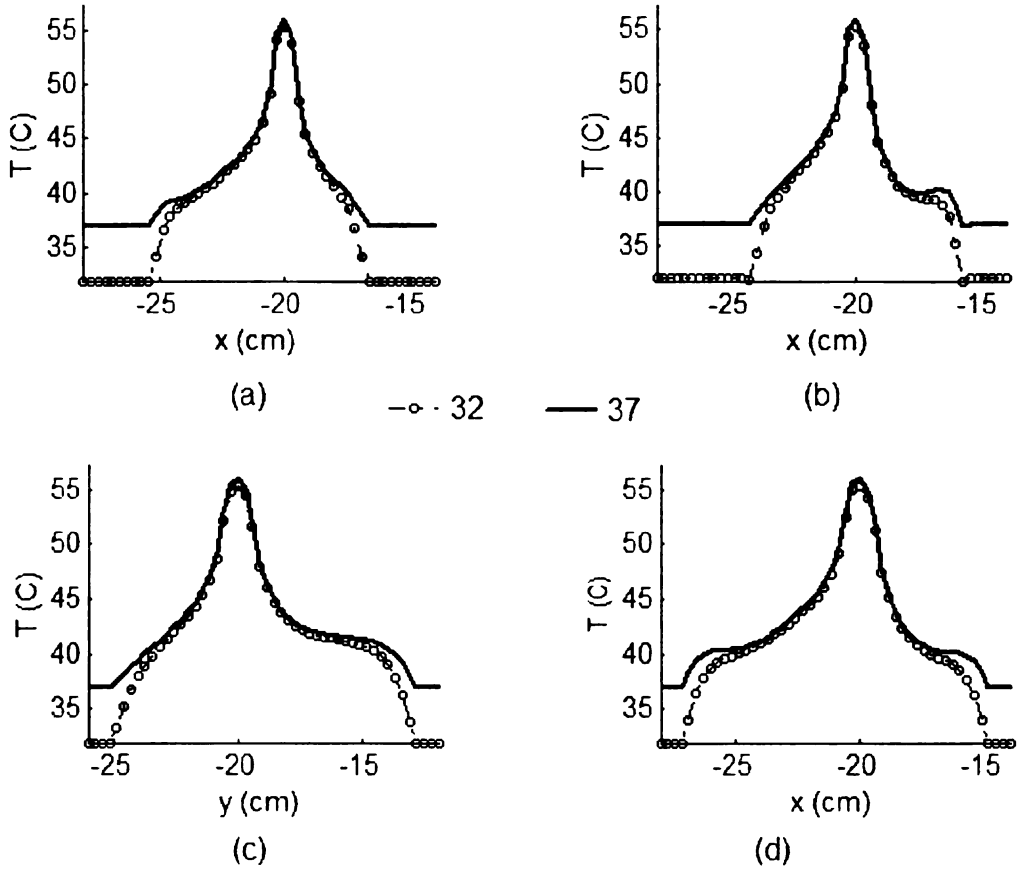

Figure 11.37. Steady state thermal profiles in CN10 (a) L_1 (b) L_2 (c) L_3 (d) L_4.

Table 11.3. Steady state temperature in the breast models for $T_0 = 32°$

Model ID	Skin		Benign Tissue		Tumor Tissue	
	SAR_μ (W/kg/m)	T_μ (°C)	SAR_μ (W/kg/m)	T_μ (°C)	SAR_μ (W/kg/m)	T_μ (°C)
CN05	19.1420	32.3850	5.7227	36.8737	62.3131	42.2141
CN10	15.3437	32.3534	4.2279	36.5831	49.7834	42.8320
CM06	29.5333	32.4745	7.6206	37.4562	67.6219	42.7629
CM08	22.0941	32.4125	5.7592	36.9457	55.6069	42.3774
EN06x2	20.0478	32.3945	6.9426	37.3789	71.4549	42.0499
EN10x5	12.9776	32.3346	3.9961	36.4521	49.6611	41.6419
EM08x5	29.5208	32.4747	7.7137	37.6322	68.0590	42.9053
EM10x5	18.8300	32.3851	4.9587	36.7229	46.1069	41.3142

Table 11.4. Steady state temperature in the breast models for $T_0 = 37°$

Model ID	Skin		Benign Tissue		Tumor Tissue	
	SAR_μ (W/kg/m)	T_μ (°C)	SAR_μ (W/kg/m)	T_μ (°C)	SAR_μ (W/kg/m)	T_μ (°C)
CN05	19.1420	37.1613	5.7227	38.5679	62.3131	42.2288
CN10	13.9955	37.1183	3.8564	38.1136	45.4090	42.3330
CM06	25.7268	37.2186	6.6384	38.8719	58.9062	42.3021
CM08	22.0941	37.1889	5.7592	38.6582	55.6069	42.6981
EN06x2	20.0478	37.1708	6.9426	38.9185	71.4549	42.0649
EN10x5	16.4248	37.1404	5.0576	38.4366	62.8523	42.8941
EM08x5	25.7159	37.2187	6.7195	38.9646	59.2869	42.4234
EM10x5	18.8300	37.1612	4.9587	38.4304	46.1069	41.6345

breast models appear promising and demonstrate the plausibility of the proposed deformable mirror microwave hyperthermia system for breast cancer treatment. Extended simulation studies on the dual mirror assembly for noninvasive tumor ablation indicate the prospects of the deformable mirror setup as a potential cancer ablation tool. At low power levels, the ability of the deformable mirror to scan the breast tissue could be used for breast imaging as shown in chapter and [166]. Numerical results obtained using the iterative tomography inversion scheme in [167]-[168] illustrate the potential of the deformable mirror assembly as a competent tool for imaging and therapy of breast cancer.

CHAPTER 12

THERAPY CASE STUDY USING MRI BREAST DATA

Introduction

Magnetic resonance imaging (MRI) formerly known as *Nuclear Magnetic Resonance* is one of the most commonly used imaging technique in medicine to visualize the pathological and physiological state of living tissues. In this chapter, feasibility of deformable mirror therapy technique is investigated using high resolution MRI data of women reported to have breast malignancy. Section 12.1 briefly covers the basics of MRI technique. MRI Breast imaging, image acquisition and diagnosis are covered in sections 12.2 and 12.3 respectively. The sectional planes of a human body commonly used in medicine for positional reference inside the anatomy that will be used in the description of the MR breast data are briefly explained in section 12.4. Section 12.5 presents MRI image post-processing methods employed to create 2D phantoms for deformable mirror therapy simulations. Therapy simulations on five anonymous patient MRI dataset using deformable mirrors are presented in sections 12.6-12.10. The feasibility of extending the non-invasive hyperthermia technique employing deformable mirrors for ablation is investigated in section 12.11. Finally, the outcome of dual mirror therapy model are discussed in the "Conclusions" section.

12.1 Magnetic Resonance Imaging

MRI is a high resolution imaging technique that relies on the relaxation properties of hydrogen nuclei or proton, found in abundance in biological tissues in the form of water and fat [198]. In the absence of an external magnetic field, the magnetic spins of hydrogen nuclei are randomly oriented and have no net magnetic moment. In the presence of an uniform external field, the hyrdogen nuclei align in parallel or

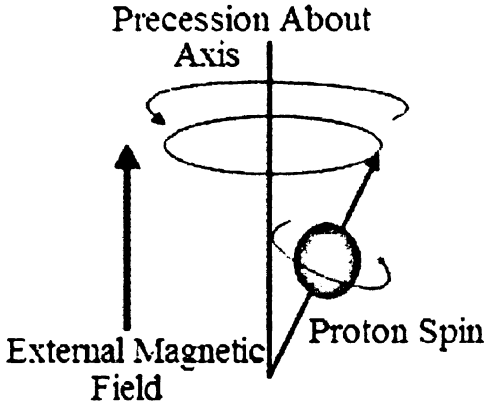

Figure 12.1. Proton precession in the presence of an external static magnetic field [199].

anti-parallel to the longitudinal axis of the static magnetic field. The aligned protons spinning about its own axis, begin to precess or gyrate when exposed to static external magnetic field creating a net magnetic moment. Figure Figure 12.1 shows the proton precessing in the presence of an external static magnetic field. A short radiofrequency(RF) pulse applied in a plane perpendicular to the static magnetic field disrupts the alignment of proton magnetization along the longitudinal axis of the static magnetic field. The degree of proton misalignment depends on the duration and amplitude of the RF excitation pulse. Once the RF pulse is switched off, the protons resume their magnetization and align themselves with the longitudinal axis of the static magnetic field. Figures Figure 12.2 (a)-(b) illustrate the disruption and relaxation of a proton exposed to a short RF burst. The restoration of proton orientation is an exponential process described by an increase in magnetization in the longitudinal plane (T1 relaxation) and decrease in magnetization in the transverse plane (T2 relaxation) [198]. The RF energy emitted by hydrogen nuclei during relaxation is detected by receiver coils for image generation. The relaxation times, T1

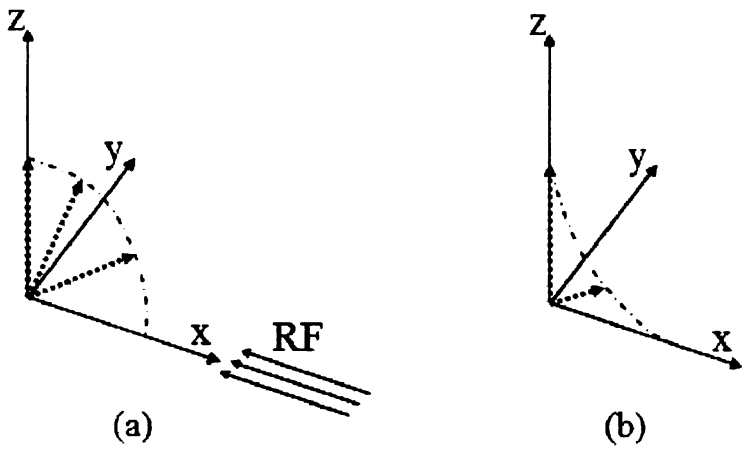

Figure 12.2. Proton relaxation due to RF burst (a) disruption (b) relaxation.

and T2 are unique for each type of tissue and yield the contrast in MR images.

12.2 MR Mammography

12.2.1 Diagnostic Breast Imaging

MR breast mammmograms are obtained on the basis of T1 and T2 relaxation times explained in the previous section. Several variations of RF pulse sequences and external gradient coils are used to obtain 2D and 3D MR contrast images. In MR mammography, dedicated surface coils customed to fit the breast shape are used for imaging. Figure Figure 12.3 shows a bi-lateral breast coil commonly used for simultaneous MR examination of both breasts. Figure Figure 12.4 shows a dedicated breast MR scanner. Prior to sliding the patient into the magnetic bore, the patient lies on the bed in prone position with both breasts pendant inside the breast coil.

During examination, motion artifacts in breast MR images are avoided by compressing the breast using ventral padding of the breast inside the breast coil with specialized inserts of varying sizes. The padding device minimizes motion artifacts

Figure 12.3. Bi-lateral breast surface coil [200].

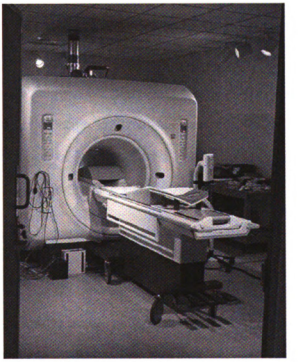

Figure 12.4. Dedicated MR breast scanner [200].

and reduces the effective breast thickness and hence decreases the slice thickness during examination. Both 2D and 3D MR imaging techniques with contrast material functioning at 0.5-1.5T (tesla) are available in commercial breast MR scanners [201]. In the 2D technique, single axial slices of the breast are excited while in the 3D technique, entire breast is excited as a volume.

12.2.2 Paramagnetic Contrast Materials

The T1 and T2 image sequences obtained in MR mammography alone are not adequate to visualize the pathological and physiological state of the living tissue. Thus, sophisticated image acquisition techniques such as fat suppression and administration of contrast agent are used to delineate the areas of interest [201, 202]. In MR imaging, substances with specific magnetic properties are used. The most commonly used paramagnetic contrast material is the gadolinium compound. Gadolinium-enhanced tissues and fluids appear extremely bright on T1-weighted images and provide high sensitivity for detection of vascular tissues such as tumors [201].

12.2.3 Fat Saturation Techniques

During T1 weighted RF sequences, signal intensity of fat tissue can significantly mask the probability of detecting contrast-enhancing lesions. Thus, it is essential to suppress the contribution of fat signal in T1 image sequences. Suppression of fat signal is achieved by employing one of the following [201]:

- Subtracting identical image before and after contrast
- Generating primary fat saturation sequences

The former technique employs image subtraction of identical images before and after contrast infusion. In the later technique, a high frequency fat suppressing impulse is applied to saturate fat tissue before signal measurement. Measurements acquired after the fat-saturation signal does not have contribution of fat tissue.

12.2.4 T2 weighted Sequences

In T2-weighted sequences, hydrous structures in the living tissue emit intense signal. T2-weighted images are mostly obtained after contrast enhanced dynamic measurements. It is possible to recognize small cysts of few mm diameter in T2-weighted breast images. Also, they provide a useful criterion for identifying smooth bordered hyper-vascularized lesions as they emit intense signal. In contrast, carcinomas show a relatively lower signal intensity [201].

12.3 MR Mammography - Diagnostic Criteria

12.3.1 Morphology

Morphological features such as form, margin, pattern of the contrast-enhancing or suspicious regions are the commonly used diagnostic criteria to detect malignancy. Morphological features of the T1 and T2 MR breast images alone cannot be used to reliably detect benign and malignant tumors. MR images obtained after intravenous administration of contrast agent plays a key role in breast diagnosis. The signal intensity changes observed after contrast administration that are used to diagnose MR breast images are briefly explained in this section.

12.3.2 Contrast Kinetics

Temporal distribution of contrast material(CM) during an examination, also known as *"Contrast Kinetics"* serves as diagnostic criteria in breast MRI. Benign lesions usually display a blooming or centrifugal CM distribution; an unchanging distribution is unspecific; a centripetal CM distribution normally indicates carcinomas.

12.3.3 Contrast Dynamics

Enhancement dynamics describes the temporal signal intensity changes occurring in a contrast enhancing region. Signal intensity changes between 1-3 minutes after contrast administration is referred as the *"initial phase"*. The percentage increase in

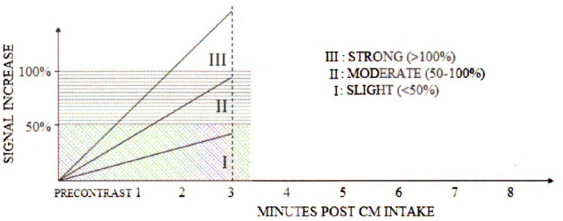

Figure 12.5. Determination of initial signal increase after CM intake [201].

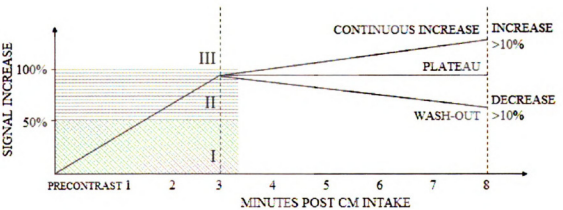

Figure 12.6. Determination of post-initial signal increase after CM administration [201].

Table 12.1. Multi-factor evaluation protocol for malignancy [201].

Criterion	Suspicious for Malignancy	Unspecific
Form	Branching, spiculated	Round
Margins	Indistinct	Well-defined
Pattern	Ring-enhancement	Inhomogeneous
Kinetics	Centripetal	Unchanging
Dynamics (initial)	Strong increase	Moderate increase
Dynamics (post-initial)	Wash-out	Plateau

maximum signal intensity during initial phase when compared to the signal intensity before CM administration serves as an indicator during diagnosis. Figure Figure 12.5 illustrates the determination of initial signal increase after CM intake.

Signal characteristics between 3-8 minutes after contrast administration is known as the *"post-initial phase"*. In post-initial phase, signal intensity value after 8 minutes in relation to the maximum initial phase value is used as a diagnostic criteria for malignancy. The post-initial signal behavior used in diagnosis is illustrated in Figure Figure 12.6. Multi-factor diagnostic criteria such as the one listed in Table Table 12.1 have significantly higher specificity at an equivalent sensitivity than a single factor evaluation protocol. Table Table 12.1 lists the multi-factor diagnostic criteria used in contrast enhancing MR mammography that strongly indicate the presence of malignancy.

12.4 Sectional Planes in Human Body

Anonymous bi-lateral MR breast data were used in the computational feasibility study of the dual deformable mirror therapy technique. For each patient data used in the simulation study, a brief clinical history and MR diagnostic report are presented for clear understanding. In the numerical model, it is essential to know the sectional

planes in human body to locate the suspicious lesions and other signal enhancements mentioned in the MR diagnosis report. This section presents the requisite information to understand the patient MR reports included in this chapter. In medicine, location of a tissue or an organ within the human anatomy is described using the sectional planes namely transverse, coronal and sagittal illustrated in Figure Figure 12.7. In Figure Figure 12.7, the body is erect and the face is forward. When the body is lying face down, the anatomical position is called prone position. When it is lying face up, it is the supine position. The transverse (or axial) sections form a series of slices in the XY plane running top (superior) to bottom (inferior). Often times, superior to inferior is interchangeably used with cranial ('head') to caudal ('tail'). Figure Figure 12.8(a) shows an axial slice of a woman's breast. Coronal sections are slices in the XZ plane running front to back as shown in Figure Figure 12.8 (b). Sagittal sections refer to slices in the YZ plane running from left to right or right to left. A position in the sagittal slice of a human body is often described using terms such as, lateral meaning towards the sides and medial meaning towards the middle. Figure Figure 12.8(c) shows a sagittal section of a woman's breast.

12.5 MRI Image Postprocessing

T2 weighted image sequences with post-contrast enhancement belonging to anonymous patients were used to evaluate the performance of the deformable mirror therapy model for breast cancer treatment. In image postprocessing, firstly, the two dimensional MR breast images were segmented into skin, tumor and benign (fat and glandular) tissues. Later, electrical property of the breast tissue reported in [47] was used to obtain the equivalent permittivity distribution for the MR breast images. Within the fat and glandular tissues, permittivity mapping was achieved using Gaussian distribution function to accommodate gradual variation within tissues of similar type.

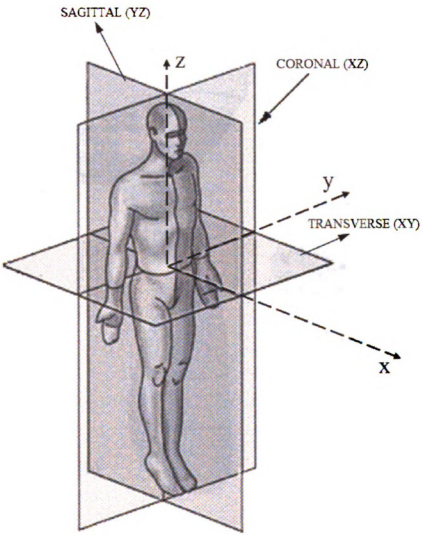

Figure 12.7. Sectional planes in human body [203].

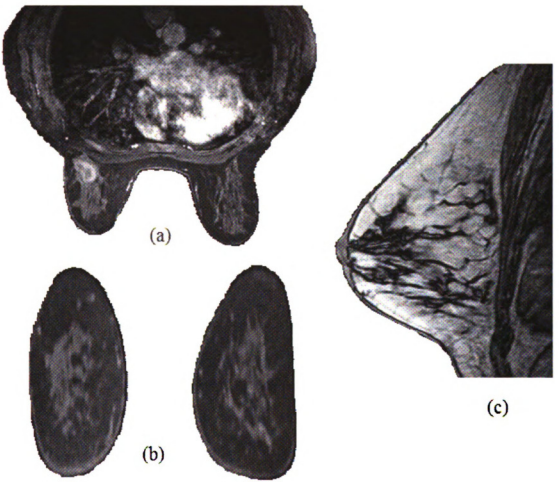

Figure 12.8. Sectional planes of a woman's breast (a) Transverse (b) Coronal (c) Sagittal.

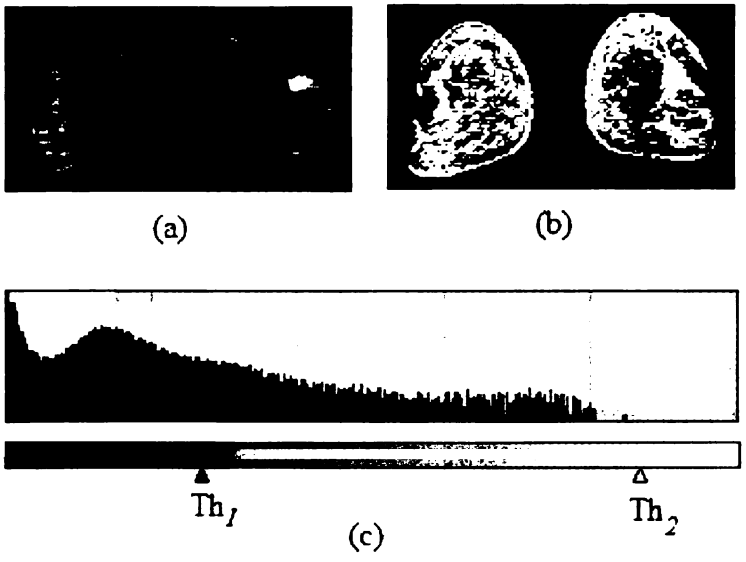

Figure 12.9. Illustration of histogram threshold on breast MR image.

12.5.1 Image Segmentation

Image segmentation was used to identify the different soft tissues in the breast MR images. Precise location of the soft tissues which, are well-defined in T2 weighted post-contrast images were used in image segmentation process. A simple histogram based threshold scheme was used to identify the contour of skin. Figures Figure 12.9(a)-(c) show a coronal section of MR breast image before and after segmentation for a chosen set of histogram thresholds. In Figure Figure 12.9(c), the histogram of the MR image intensity is displayed in logarithmic scale for improved visual perception. The step by step procedure followed to identify skin and tumor contours are illustrated in Figure Figure 12.10. Figure Figure 12.10(a) shows the thresholded image of a MR breast data for the histogram thresholds, Th_1 and Th_2 in Figure Figure 12.10(a). The binary image in Figure Figure 12.10(a) is used to obtain the contour of the breast using *"Laplacian Edge Detector"* [204]. Figures Figure 12.10(c)-(d) show the tumor region identified after histogram threshold and edge detection.

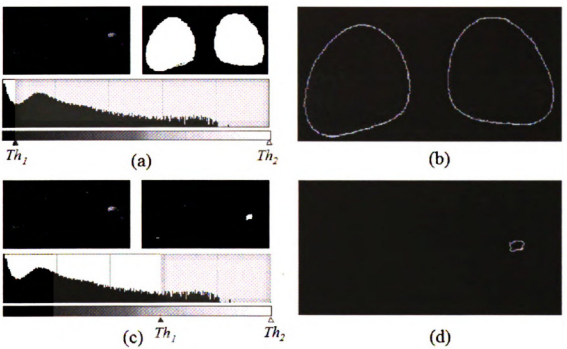

Figure 12.10. Segmentation and identification of soft tissue regions using histogram threshold and edge detection (a) Breast segmentation (b) Breast Contour (c) Tumor segmentation (b) Tumor contour.

12.5.2 Permittivity Map

During simulations, the permittivity values reported in [47], [42] were assigned to the skin and tumor regions of the MR breast data. In the breast region excluding the tumor, $(x, y) \in \Omega_{breast}$ histogram of the pixel intensity was used to assign the tissue electrical property. The most occurring pixel intensity which, correspond to the fat was assigned the permittivity of fat reported in [47]. Permittivity value for the remaining pixels was assigned using a function of the form,

$$exp\left\{-\frac{(I - I_\mu)^2}{2\sigma_I^2}\right\} \tag{12.1}$$

where I is the breast MR pixel intensity; I_μ and σ_I are the mean and standard deviation of the pixel intensity. In (12.1), pixels with signal intensity greater than I_μ are assigned higher permittivity values while those closer to I_μ are assigned values closer to breast fat tissue. Thus, glandular tissues with relatively higher signal intensity in the T2-weighted post-contrast images were assigned permittivity values close to that of tumor. In the microwave regime, fibroglandular tissues are more hydrous than fat and has dielectric permittivity similar to tumor. Figures Figure 12.12 (a)-(b) show the relative permittivity and loss tangent obtained for the MR breast image in Figure Figure 12.11 using (12.1) and [47], [42].

12.6 Patient Case Study I

12.6.1 Clinical History

Patient case study I, was a 54-year old woman with complaints of breast pain and a lump in her left breast. Patient underwent breast biopsy which, revealed the presence of left lobular carcinoma. Multi-planar, multi-sequence MR imaging of the breasts was carried before and after intravenous (IV) infusion of gadolinium contrast.

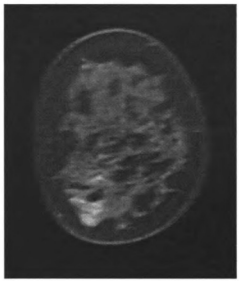

Figure 12.11. T2-weighted post-contrast MR breast image.

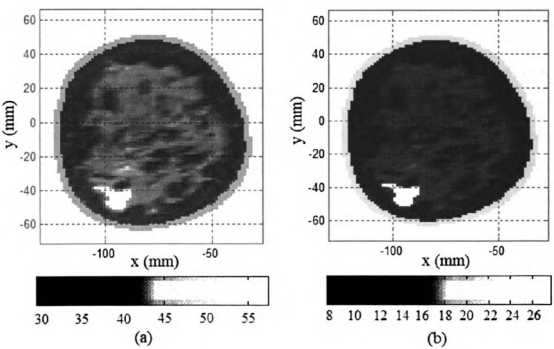

Figure 12.12. Permittivity map for breast tissue at 500 MHz using (12.1) and [47], [42] (a) Relative permittivity, $\epsilon_r(x, y)$ (b) Loss tangent, $\frac{\sigma}{\omega\epsilon_0}$.

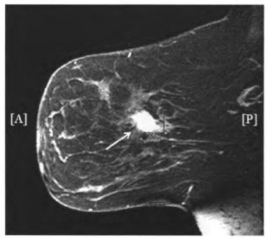

Figure 12.13. Sagittal slice of MR breast image with abnormal enhancement measuring 15x13 mm.

12.6.2 MRI findings

The MR images revealed a markedly abnormal area of enhancement with a spiculated mass in the upper outer quadrant of the left breast. Location of the spiculated enhancement is shown in the sagittal view of the post-contrast T2 weighted image in Figure Figure 12.13. The tumor in Figure Figure 12.13 measures approximately 13 mm in the anterior to posterior dimension and 15 mm in the superior to inferior dimension. Another abnormal enhancement slightly posterior to the above described mass that appears to be an extension was also reported. The second suspicious enhancement measures approximately 30 mm in superior to inferior and 10 mm in anterior to posterior dimensions as indicated in Figure Figure 12.14. Overall the breast had moderate scattered fibroglandular tissue. Sagittal and coronal views of the T2 weighted postcontrast breast image sequences in Figures Figure 12.15 and Figure 12.16 indicate the two suspicious enhancement areas mentioned in the MR diagnostic report which are indicated by little arrows in white. The second lesion marked "B" in Figure Figure 12.15 appear to be a contiguous lesion with anterior-

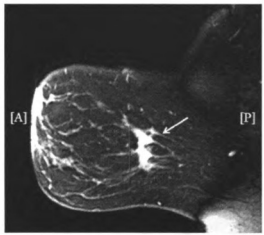

Figure 12.14. Sagittal slice of MR breast image with abnormal enhancement measuring 30x10 mm.

superior portion smaller than the posterior-inferior dimension.

12.6.3 Therapy Simulations

Suspicious lesions reported in the MR findings were used to identify coronal slices with malignancy for therapy simulations. Therapy delivery to the two malignant tissue regions was investigated using dual deformable mirror therapy model for the 2D coronal MR image sequences. The slice thickness of the coronal sections acquired using breast MR scanner was 0.4297 mm. All therapy simulations presented in this chapter were carried out for continuous wave excitation at 500 MHz.

For a known malignant location, mirror deformations for field focusing were determined using ray tracing technique explained in chapter 11. For the estimated mirror deformations, EM energy (SAR) deposited inside the breast tissue was computed. Heat transfer inside the breast tissue was calculated using the tissue SAR. The impressed field strength was increased until the temperature inside the tumor was more than 42 ° C while the rest of the benign breast tissue was maintained below 42 ° C as illustrated in Figure Figure 11.14. Figures Figure 12.17(a)-(b) show the

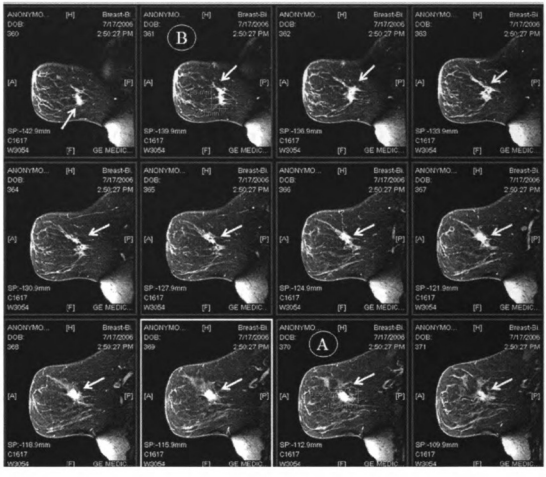

Figure 12.15. Sagittal slices of MR breast image with abnormal enhancement.

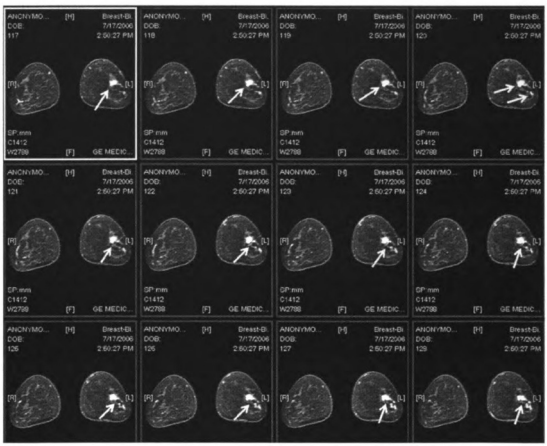

Figure 12.16. Coronal slices of MR breast image with abnormal enhancement.

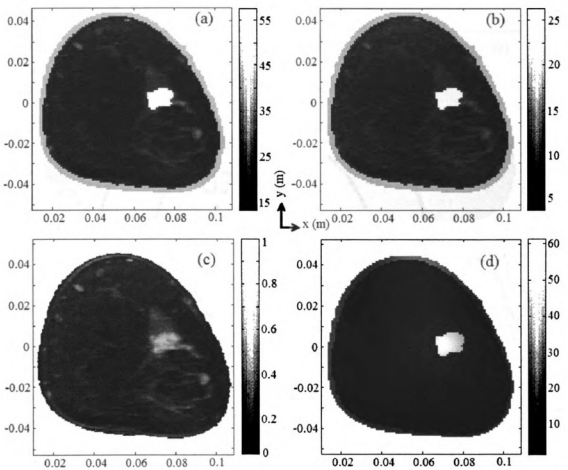

Figure 12.17. Coronal slice of MR data, Ia used in therapy simulations at 500 MHz (a) Relative permittivity, $\epsilon_r(x, y)$ (b) Loss tangent, $\frac{\sigma}{\omega\epsilon_0}$ (c) T2-weighted postcontrast MR image (d) Tissue specific absorption rate (W/kg/m).

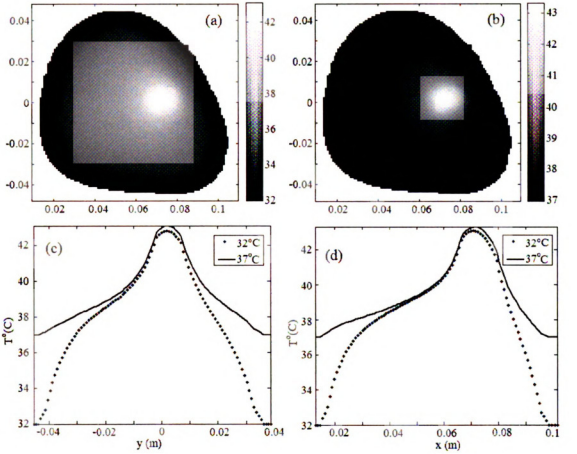

Figure 12.18. Steady state temperature distribution for Ia (a) $T_a = 32°$ C and (b) $T_a = 37°$ C. 1D Thermal profiles along (c) $x = x_c$ and (d) $y = y_c$.

breast tissue permittivity used in therapy simulation for the coronal slice in Figure Figure 12.17(c) with malignancy. The tissue SAR inside the coronal breast slice computed using the dual deformable mirror therapy model is shown in Figure 12.17(d). Preferential amount of EM energy deposited inside the tumor tissue is clearly evident in Figure Figure 12.17(d). Figures Figure 12.18 (a)-(b) show the steady state temperature distributions inside the breast for two different ambient or external temperatures. Temperature profiles along $x = x_c$ and $y = y_c$) where $r_c = (x_c, y_c)$ is the coordinate of the tumor center are shown in Figures Figure 12.18(c)-(d). Thermal distributions in Figures Figure 12.18 (a)-(d) appear promising for selective tumor tissue heating inside the breast. Figures Figure 12.19 (a)-(b) show the permittivity distribution obtained for the 2D coronal left breast data with an extended tumor region as shown in Figure Figure 12.19 (c). The coronal breast slice in Figure Figure 12.19(c) corresponds to the second lesion mentioned in the MR diagnosis. Figure Figure 12.20(a)-(b) show the steady state temperature distribution inside the malignant tissue maintained by the dual deformable mirror therapy model. Thermal profiles for transects running through peak temperature within the two regions corresponding to the tumor marked as '+' are shown in Figures Figure 12.20(c)-(d) and Figure 12.21(c)-(d) respectively. The steady thermal map inside the second lesion indicate an appreciable thermal elevation inside the tumor and its extension without increasing the temperature of surrounding benign tissue and skin.

An additional slice that appears to be an extension of the second lesion reported in the MR findings was also used in the therapy simulations. The permittivity map, T2-weighted postcontrast coronal slice and tissue SAR for this lesion extension are shown in Figures Figure 12.22 (a)-(d). Figures Figure 12.23 (a)-(d) show the steady state temperature maintained by the dual deformable mirror therapy model inside the left breast in Figure Figure 12.22 (c). The tissue SAR and thermal distributions for different coronal sections in Figures Figure 12.18-Figure 12.23 indicate the potential

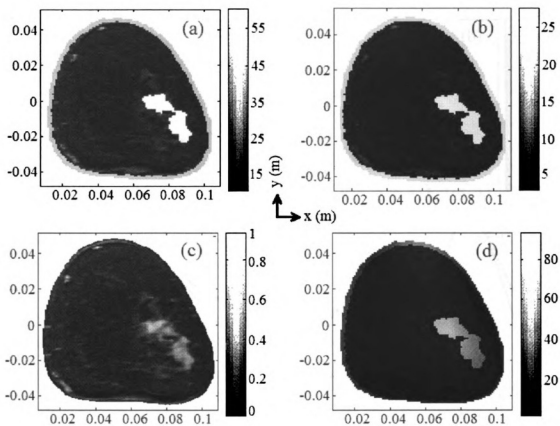

Figure 12.19. Coronal slice of MR data, Ib used in therapy simulations at 500 MHz (a) Relative permittivity, $\epsilon_r(x, y)$ (b) Loss tangent, $\frac{\sigma}{\omega\epsilon_0}$ (c) T2-weighted postcontrast MR image (d) Tissue specific absorption rate (W/kg/m).

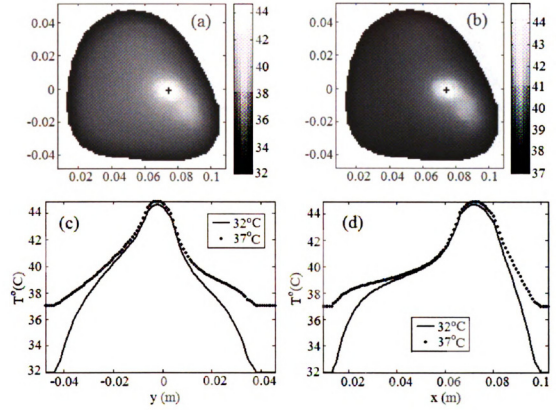

Figure 12.20. Steady state temperature distribution for Ib for transects passing through tumor center marked '+' (a) $T_a = 32°$ C and (b) $T_a = 37°$ C. 1D Thermal profiles along (c) $x = x_{c1}$ and (d) $y = y_{c1}$.

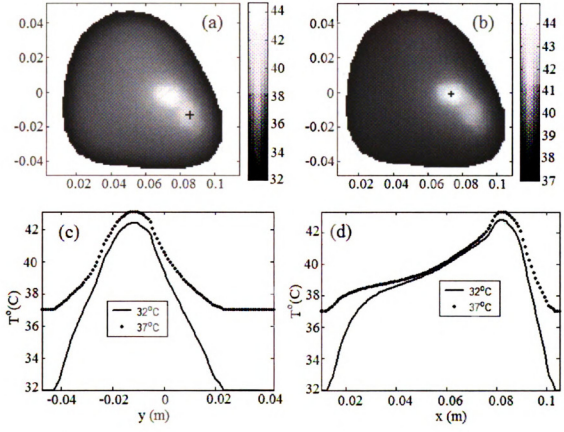

Figure 12.21. Steady state temperature distribution for Ib for transects passing through secondary tumor marked '+' (a) $T_a = 32°$ C and (b) $T_a = 37°$ C. 1D Thermal profiles along (c) $x = x_{c2}$ and (d) $y = y_{c2}$.

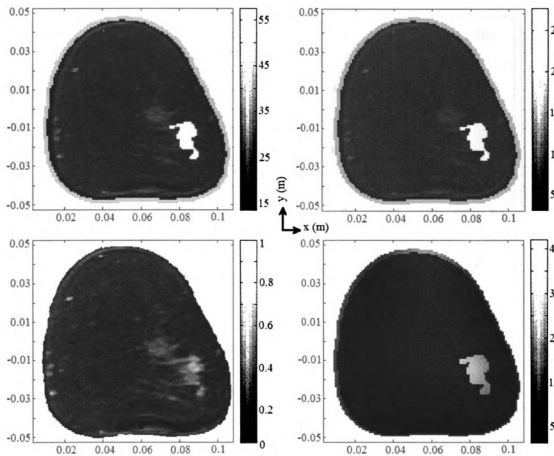

Figure 12.22. Coronal slice of MR data, Ic used in therapy simulations at 500 MHz (a) Relative permittivity, $\epsilon_r(x, y)$ (b) Loss tangent, $\frac{\sigma}{\omega\epsilon_0}$ (c) T2-weighted postcontrast MR image (d) Tissue specific absorption rate (W/kg/m).

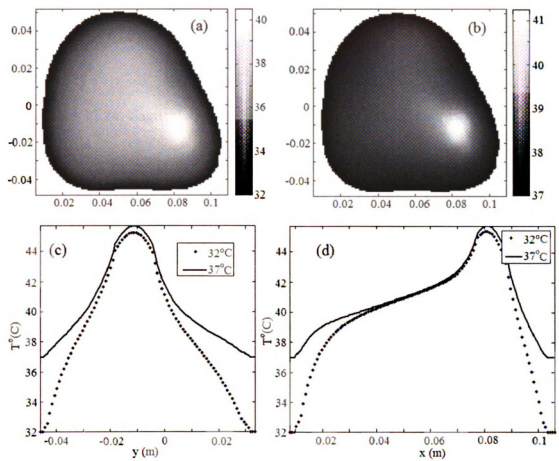

Figure 12.23. Steady state temperature distribution for Ic (a) $T_a = 32°$ C and (b) $T_a = 37°$ C. 1D Thermal profiles along (c) $x = x_c$ and (d) $y = y_c$.

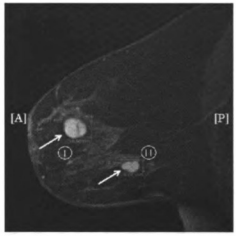

Figure 12.24. Sagittal slice of left breast MR data indicating two lesions.

of the proposed therapy technique as an adjuvant for radiation and chemotherapy of the breast.

12.7 Patient Case Study II

12.7.1 Clinical History

The subject is a 42-year old woman with two lumps on the left breast that were inconclusive in the prior ultrasound study. Multi-sequence MR imaging of both breasts was performed with and without gadolinium contrast administration. A total of 18cc of contrast was administered intravenously during examination.

12.7.2 MRI findings

A moderate amount of scattered fibroglandular tissue with benign enhancement was reported to exist throughout the right breast. A high T2 lesion that corroborates with prior ultrasound study within the anterior depth of the left breast was found. The lesion measuring 19x17x20 mm in the anterioposterior, craniocaudal and transverse dimensions is indicated as (|) in Figure Figure 12.24. Coronal view of the lesion

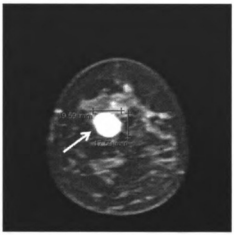

Figure 12.25. Coronal slice of MR left breast image with a lesion measuring 19x17 mm.

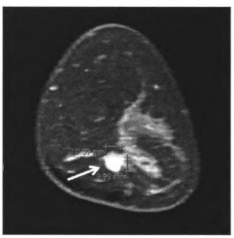

Figure 12.26. Coronal view of MR left breast image with a lesion measuring 10x9 mm.

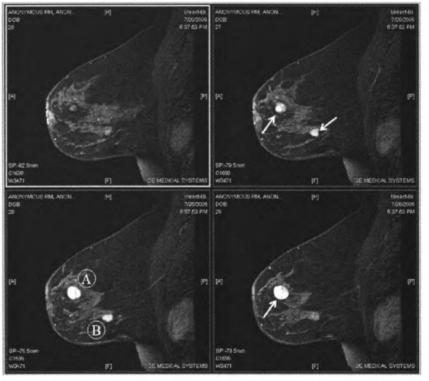

Figure 12.27. Sagittal view of MR left breast images with two lesions.

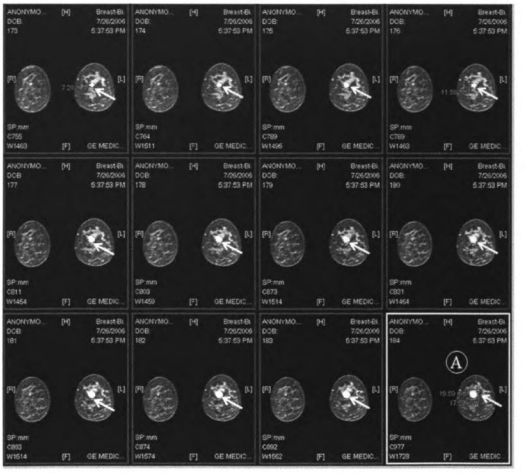

Figure 12.28. Coronal slices of the left breast with abnormal enhancement.

measuring approximately 19x17 mm is shown in Figure Figure 12.25.

The left breast has a moderate scattered fibroglandular tissue with scattered areas of benign enhancement. An additional smaller lesion was reported to exist in the middle depth of the left breast with a more lobulated appearance than the first lesion. This lesion measures 13x9x10 mm in anteroposterior, craniocaudal and transverse dimensions respectively and was not seen in prior ultrasound study. The second lesion is marked as (||) in Figure Figure 12.24. Figure Figure 12.26 shows the coronal section of the second lesion located in the left breast. Figure Figure 12.27 shows the sagittal T2-weighted post-contrast image sequences of the lesions found in the left breast. Coronal views of the lesions are shown in Figure Figure 12.28.

12.7.3 Therapy Simulations

Coronal image sequences corresponding to lesions $'|'$ and $'||'$ were used in the dual mirror therapy model for tumor temperature elevation. Permittivity map for the T2-weighted MR image sequences were obtained following the procedure explained in section 12.5. Figure Figure 12.29 (a)-(d) shows the spatial permittivity distribution, postcontrast MR image and EM energy deposition inside the left breast containing lesion $'|'$. The corresponding steady state temperature distributions achieved by the dual deformable mirror are shown in Figures Figure 12.30 (a)-(d). Additional simulations were carried out for another coronal slice passing through lesion |. Figure Figure 12.31 (c) shows the coronal section containing lesion $'|'$. Figure Figure 12.31 (d) shows the SAR computed by the therapy model for the permittivity distribution in Figure Figure 12.31 (a)-(b). The steady state thermal map inside the left breast containing lesion $'|'$ for two different ambient temperatures are shown in Figures Figure 12.32 (a)-(d). Figures Figure 12.33 (a)-(d) show the permittivity map, MR image and tissue SAR inside the left breast for lesion $'||'$ respectively. The corresponding steady state temperature distributions are shown in Figures Figure 12.34 (a)-(d). The thermal profile and tissue SAR inside the coronal sections of the

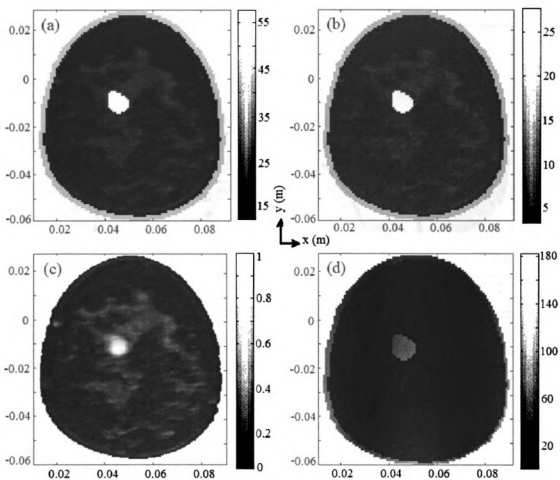

Figure 12.29. Coronal slice of tumor, $'|'$ in MR data IIa used in therapy simulations (a) Relative permittivity, $\epsilon_r(x, y)$ (b) Loss tangent, $\frac{\sigma}{\omega\epsilon_0}$ (c) T2-weighted postcontrast MR image (d) Tissue specific absorption rate (W/kg/m).

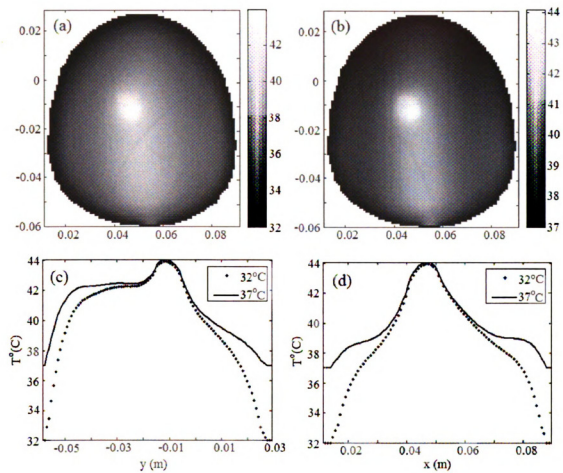

Figure 12.30. Steady state temperature distribution for IIa (a) $T_a = 32°$ C and (b) $T_a = 37°$ C. 1D Thermal profiles along (c) $x = x_c$ and (d) $y = y_c$.

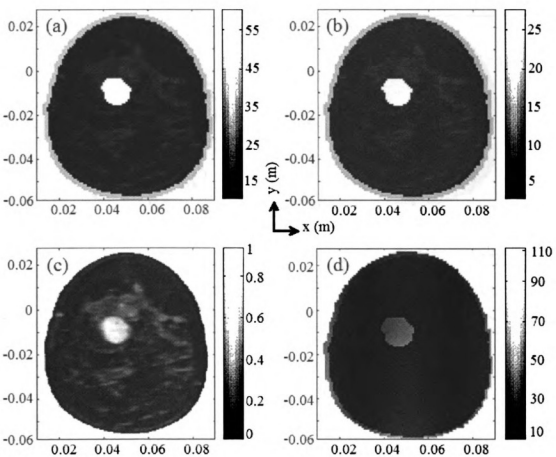

Figure 12.31. Coronal slice of tumor, $'|'$ in MR data IIb used in therapy simulations (a) Relative permittivity, $\epsilon_r(x, y)$ (b) Loss tangent, $\frac{\sigma}{\omega\epsilon_0}$ (c) T2-weighted postcontrast MR image (d) Tissue specific absorption rate (W/kg/m).

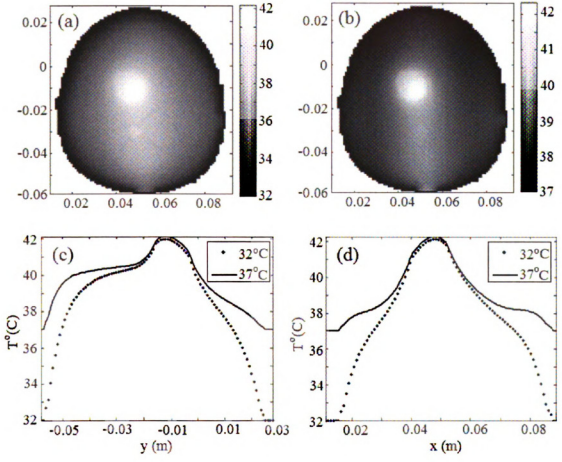

Figure 12.32. Steady state temperature distribution for IIb(a) $T_a = 32°$ C and (b) $T_a = 37°$ C. 1D Thermal profiles along (c) $x = x_c$ and (d) $y = y_c$.

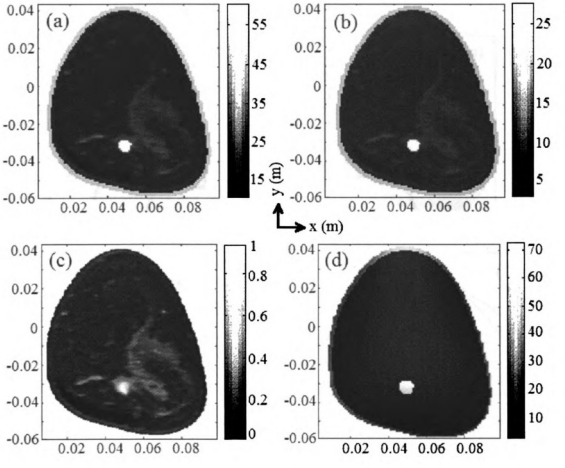

Figure 12.33. Coronal slice of tumor, $'||'$ in MR data IIc used in therapy simulations (a) Relative permittivity, $\epsilon_r(x, y)$ (b) Loss tangent, $\frac{\sigma}{\omega\epsilon_0}$ (c) T2-weighted postcontrast MR image (d) Tissue specific absorption rate (W/kg/m).

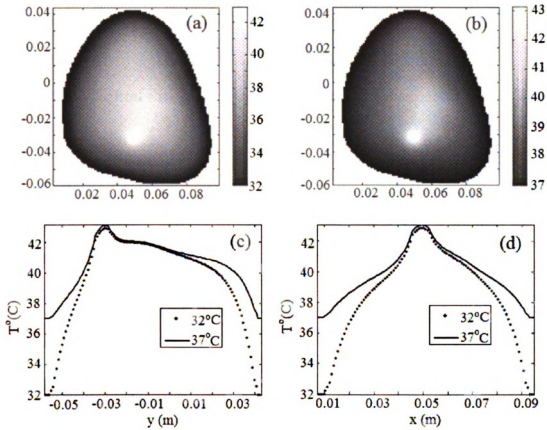

Figure 12.34. Steady state temperature distribution for IIc (a) $T_a = 32°$ C and (b) $T_a = 37°$ C. 1D Thermal profiles along (c) $x = x_c$ and (d) $y = y_c$.

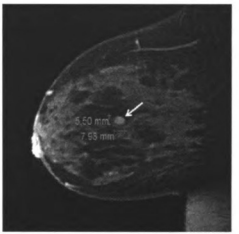

Figure 12.35. Sagittal slice of left breast with abnormal enhancement measuring 8x6 mm.

left breast demonstrate significant tumor temperature elevation and also indicate the ability of the deformable mirror to focus the EM energy at desired location without superficial heating of the skin.

12.8 Patient Case Study III

12.8.1 Clinical History

The patient is a 33-year old woman with previous record of breast cancer diagnosed with biopsy. The subject has a palpable mass in the right breast and a smaller nodule just below the nipple on the right breast that was revealed on the recent X-ray mammogram study. Multi-planar, multi-sequence MR images were acquired before and after gadolinium intake.

12.8.2 MRI findings

The breast tissue is heterogeneously dense. The left breast has a background of punctuate enhancement and several tiny foci that demonstrate rapid washing and washout (centri-petal CM intake) which are difficult to ascertain. An ovoid density

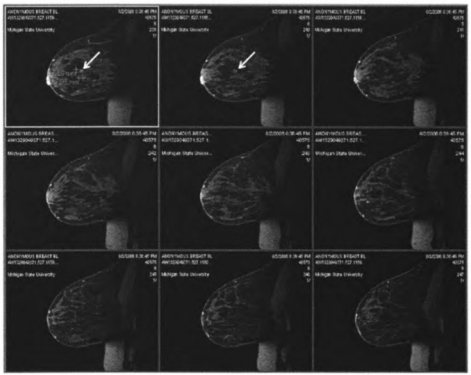

Figure 12.36. Post-contrast T2-weighted sequences of left breast with an abnormal lesion.

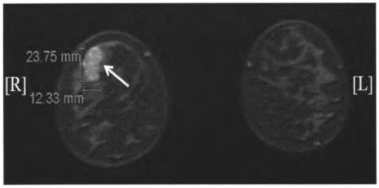

Figure 12.37. Right breast with an abnormal lesion measuring 23x12 mm.

lesion measuring 8x6x6 mm in anterioposterior, superior-inferior and transverse dimensions respectively exists in the left breast. Figure Figure 12.35 shows the lesion with mixed signal enhancement characteristics including regions of rapid wash-in and washout. Figure Figure 12.36 shows the sagittal image sequences of the suspicious lesion found in the left breast. The right breast has a mass in the superior central region with mixed signal characteristics measuring 29 mm in superior-inferior dimension, 12 mm in anterior-posterior dimension and 23 mm in transverse dimension respectively. The coronal slice of this lesion with lobular contour and suspicious enhancement is shown in Figure Figure 12.37. This lesion corresponds to the known palpable malignancy reported by the patient. Coronal views of the T2-weighted post-contrast image sequences of the palpable suspicious lesion found in the right breast are shown in Figure Figure 12.38.

Somewhat nodular enhancement is observed in the sub-aereolar region of the right breast where calcifications were recently removed. Additionally, scattered enhancement is seen in the upper outer quadrant of the left breast with some foci of linearity and additional foci of scattered DCIS that could not be excluded based on the MR images.

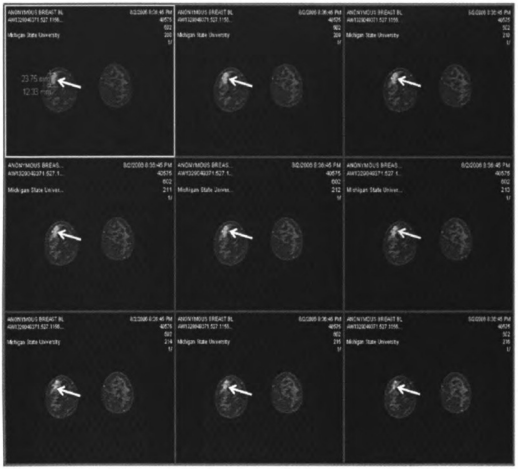

Figure 12.38. Coronal slices of the right breast with a palpable lesion.

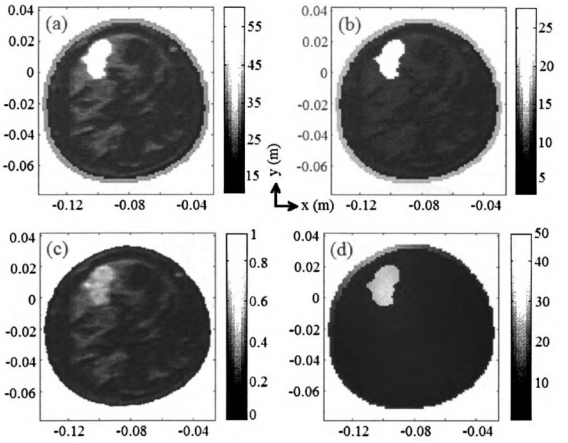

Figure 12.39. Coronal tumor data, III used in therapy simulations (a) Relative permittivity, $\epsilon_r(x, y)$ (b) Loss tangent, $\frac{\sigma}{\omega\epsilon_0}$ (c) T2-weighted postcontrast MR image (d) Tissue specific absorption rate (W/kg/m).

12.8.3 Therapy Simulations

Coronal section of the right breast with a tumor measuring 23x19 mm was used in the dual deformable mirror therapy simulation study. Mirror deformations were estimated to focus the EM energy at the tumor site indicated in Figure Figure 12.37. Figures Figure 12.39(a)-(b) show the spatial distribution of the relative permittivity and loss tangent inside the heterogeneously dense breast. The tissue SAR produced by the estimated mirror deformations is shown in Figure Figure 12.39(c). The steady state temperature distributions maintained by the dual deformable mirrors are shown

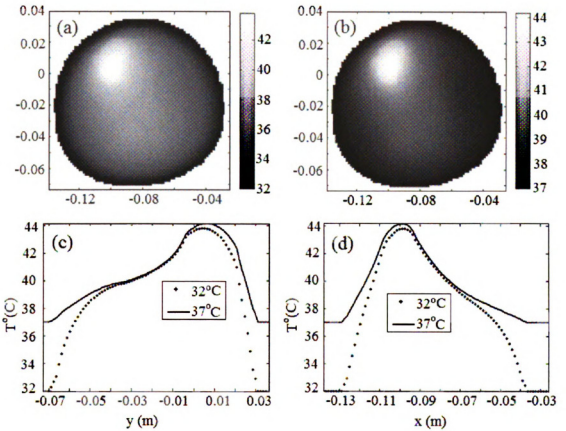

Figure 12.40. Steady state temperature distribution for III (a) $T_a = 32°$ C and (b) $T_a = 37°$ C. 1D Thermal profiles along (c) $x = x_c$ and (d) $y = y_c$.

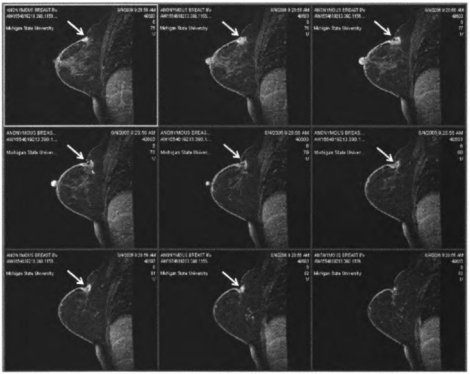

Figure 12.41. Postcontrast T2-weighted sequences of right breast indicating signal enhancement near the post surgical bed.

in Figures Figure 12.40(a)-(d).

12.9 Patient Case Study IV

12.9.1 Clinical History

An abnormal X-ray mammogram was found in this 80-year old patient with prior history of breast carcinoma who underwent surgical resection (lumpectomy). Multi-planar, multi-sequence bilateral breast examination was carried out both pre and post administration of 16 cc of IV contrast.

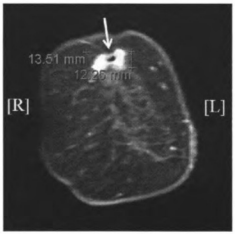

Figure 12.42. Right breast with post-contrast enhancement of the post-surgical bed.

12.9.2 MRI findings

A marked post-contrast enhancement of the post-surgical bed in the right breast is observed. Dynamic contrast enhancement curves for this region revealed several areas of intermediate enhancement profiles as well as few small areas of suspicious enhancement. MR breast diagnosis combined with X-ray mammography findings were reported to indicate disease recurrence. Figure Figure 12.41 shows the sagittal image sequences indicating signal enhancement near the post surgical bed in the right breast.

Within the right breast two small foci of persistent post-contrast enhancement was reported to exist adjacent to the chest wall. Each of these two lesions measuring approximately 1 cm in diameter are shown in Figure Figure 12.42. They appear to be an extension of the breast MR image in Figure Figure 12.43. Coronal views of the T2-weighted postcontrast image sequences adjacent to the chest wall are shown in Figure Figure 12.44.

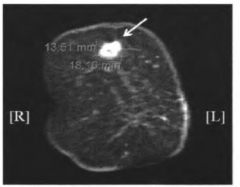

Figure 12.43. Right breast near the post-surgical bed.

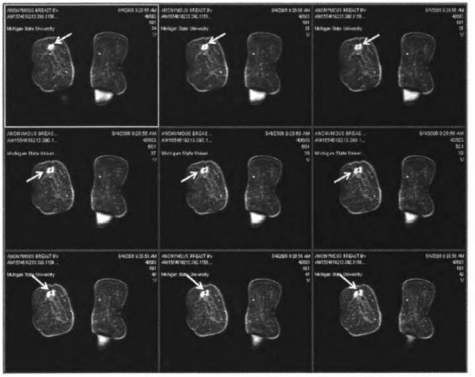

Figure 12.44. Coronal image sequences indicating two small foci of suspicious signal enhancement within the right breast adjacent to the chest wall.

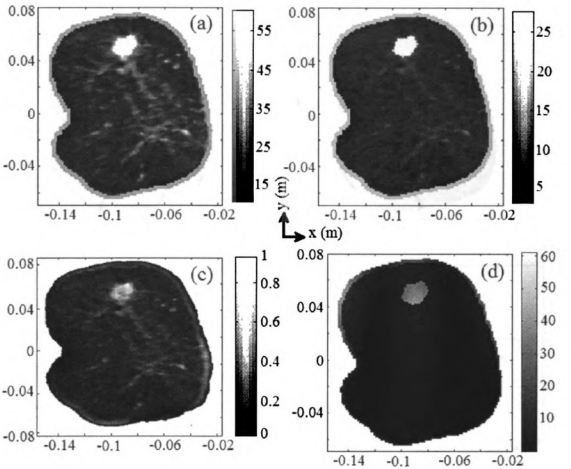

Figure 12.45. Coronal slice of tumor data, IV near the chest wall (a) Relative permittivity, $\epsilon_r(x, y)$ (b) Loss tangent, $\frac{\sigma}{\omega\epsilon_0}$ (c) T2-weighted postcontrast MR image (d) Tissue specific absorption rate at 500 MHz (W/kg/m).

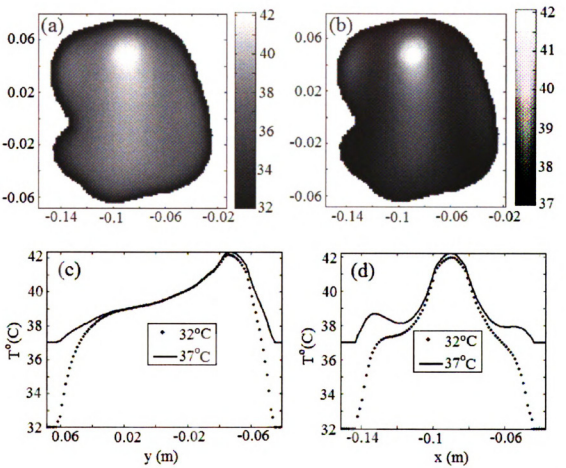

Figure 12.46. Steady state temperature distribution for IV (a) $T_a = 32°$ C and (b) $T_a = 37°$ C. 1D Thermal profiles along (c) $x = x_c$ and (d) $y = y_c$.

12.9.3 Therapy Simulations

Therapy simulations were carried out for the post-contrast enhancement observed near the post surgical bed in the right breast shown in Figures Figure 12.42-Figure 12.43. MR image postprocessing, mirror deformation estimation and tumor temperature elevation procedures were carried out in the dual deformable mirror therapy simulations. Figures Figure 12.45 (a)-(d) show the permittivity map, coronal MR image sequence and EM energy deposited inside the MR breast data with malignancy. Solution to the steady state BHTE are shown in Figures Figure 12.46 (a)-(d) for two different ambient temperatures. Both thermal profiles indicate tumor temperature elevation above 42 ° C with minimal temperature increase in the surrounding benign breast tissue.

12.10 Patient Case Study V

12.10.1 Clinical History

The subject is a 58-year old woman who recently underwent cyst aspiration on the right breast. Multi-echo, multi-planar bilateral breast MR examination was performed and post-gadolinium sequential images were acquired for diagnosis. Tissue around the cyst was diagnosed positive as DCIS and the patient was scheduled for radiation therapy.

12.10.2 MRI findings

MRI of the left breast revealed a large hyperintense fluid collection measuring approximately 85x50 mm which failed to undergo contrast enhancement. The fluid collection shown in Figure Figure 12.47 likely represents proteinaceous or haemorrhagic cysts that demonstrates diffuse surrounding rim enhancement which is relatively thick compared to a typical breast cyst. Additionally, a tiny single foci of enhancement too small for characterization was also observed. A long linear focus of ductal enhance-

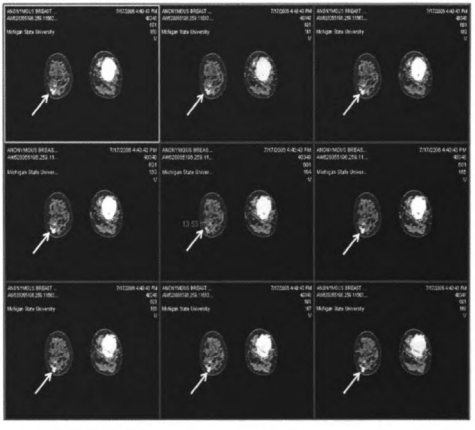

Figure 12.47. Coronal images indicating fluid collection in the left breast and ductal enhancement in the right breast.

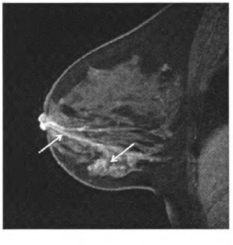

Figure 12.48. Ductal enhancement from nipple to the inferior portion of the right breast.

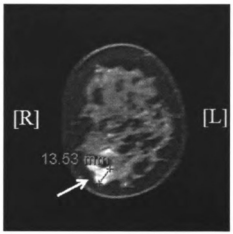

Figure 12.49. Ductal enhancement in the inferior portion of the right breast.

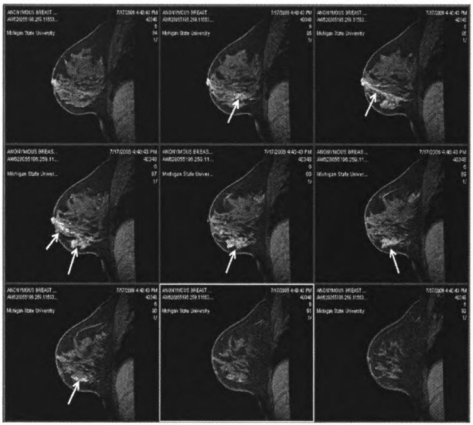

Figure 12.50. T2 weighted postcontrast image sequences indicating ductal enhancement from nipple to the inferior portion of the right breast.

ment extending from the nipple and posterior inferiorly towards the chest wall with an associated irregular area of enhancement in the inferior portion of the breast was observed. Figures Figure 12.48 -Figure 12.49 show the sagittal and coronal views of the suspicious ductal enhancement. Irregular morphology with ductal enhancement was reported as suspicious malignancy. Sagittal image sequence indicating ductal enhancement extending from nipple to the inferior portion of the right breast is shown in Figure Figure 12.50. Figure Figure 12.47 shows the coronal view of the right breast with suspicious ductal enhancement.

12.10.3 Therapy Simulations

Coronal section of the ductal enhancement in the inferior portion of the right breast used in therapy simulations is shown in Figure Figure 12.49. Tissue permittivity distribution for the coronal MR breast image in Figure Figure 12.51(d) is shown in Figures Figure 12.51 (a)-(b). The tissue SAR inside the right breast maintained by the dual deformable mirror therapy model is shown in Figure Figure 12.51 (c). Figures Figure 12.52 (a)-(d) show the steady state thermal map inside the breast tissue reported to have suspicious ductal enhancement. The tissue SAR, 2D temperature distributions and 1D thermal profiles in Figures Figure 12.51-Figure 12.52 calculated using the dual deformable mirror model indicate selective tumor temperature elevation above 42° C; conducive for the thermal therapy of localized breast cancer.

12.11 Noninvasive Ablation - Feasibility Study

Feasibility of extending the dual deformable mirror therapy technique for nonivasive ablation was investigated using coronal sections of MR derived breast images. Prolonged exposure of EM radiation above 42° C combined with radiation or chemotherapy and few minutes above 50° C has been reported to result in tumor tissue necrosis [174]. In the ablation simulations, the tumor temperature elevation procedure was iterated until the tumor temperature was well above 50° C. Coronal breast MR data

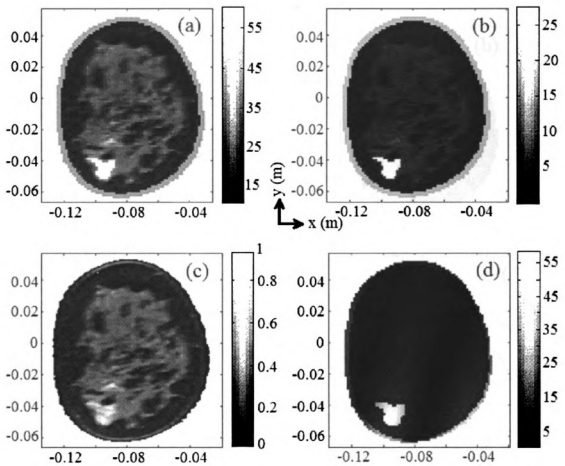

Figure 12.51. Coronal slice of tumor in patient data, V used in therapy simulations (a) Relative permittivity, $\epsilon_r(x, y)$ (b) Loss tangent, $\frac{\sigma}{\omega\epsilon_0}$ (c) T2-weighted postcontrast MR image (d) Tissue specific absorption rate at 500 MHz (W/kg/m).

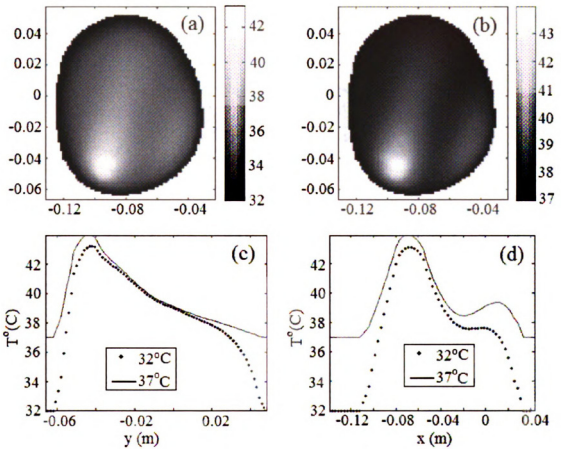

Figure 12.52. Steady state temperature distribution for V (a) $T_a = 32°$ C and (b) $T_a = 37°$ C. 1D Thermal profiles along (c) $x = x_c$ and (d) $y = y_c$.

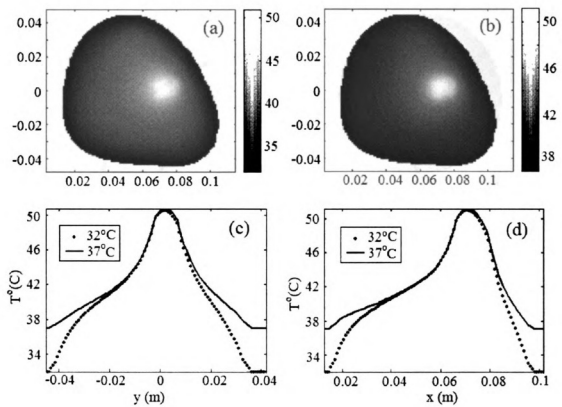

Figure 12.53. Steady state temperature distribution inside patient model, Ia calculated using noninvasive ablation simulations (a) $T_a = 32°$ C and (b) $T_a = 37°$ C. 1D Thermal profiles along (c) $x = x_c$ and (d) $y = y_c$.

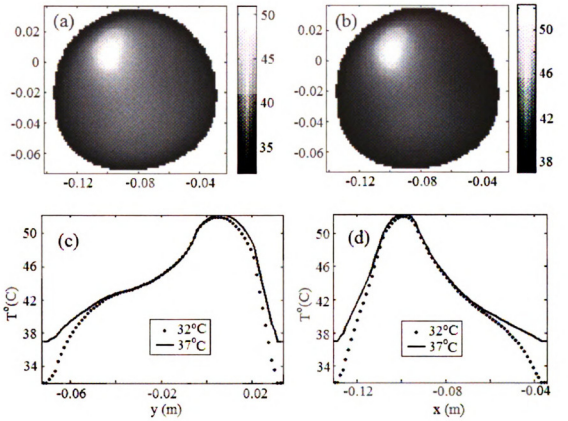

Figure 12.54. Noninvasive ablation using deformable mirror for patient model III (a) $T_a = 32°$ C and (b) $T_a = 37°$ C. 1D Thermal profiles along (c) $x = x_c$ and (d) $y = y_c$.

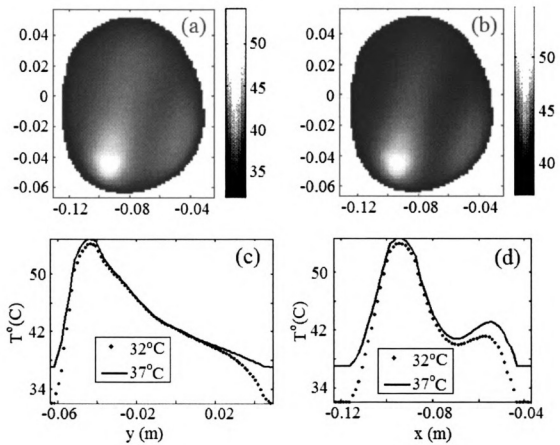

Figure 12.55. Steady state ablation temperature distribution inside patient model V (a) $T_a = 32°$ C and (b) $T_a = 37°$ C. 1D Thermal profiles along (c) $x = x_c$ and (d) $y = y_c$.

Table 12.2. Specific absorption rate inside MR breast tissue models for hyperthermia adjuvant therapy using dual deformable mirrors.

Model ID	Hyperthermia: SAR (W/kg/m)		
	Tumor	Benign	Skin
Ia	56.3410	4.6475	10.8253
Ib	55.6895	6.3772	16.7388
Ic	73.6020	8.8630	22.0754
IIa	64.3034	9.2190	43.5980
IIb	56.2454	8.3706	36.9814
IIc	96.6822	12.5485	30.3879
III	41.9304	3.4282	10.0141
IV	32.3101	2.0345	9.9730
V	52.8896	2.7630	10.8498

belonging to patients I, III and V were used in the ablation computational study. Figures Figure 12.53 - Figure 12.55 show the steady state temperature distributions and 1D thermal profiles inside the coronal postcontrast MR breast data with malignancy.

The computational results for noninvasive tumor ablation indicate selective temperature elevation inside tumor tissue above 50° C that result in irreversible tumor tissue damage over few minutes of exposure. The continuous mirror surface and the adaptive focusing capability of the deformable mirror enables EM radiation to be focused at tumor site without any hot spots or undesired superficial heating. The hyperthermia setup also serves as an noninvasive ablation tool in which the tumor temperature can be selectively increased above 50° C upon exposure for several minutes.

12.12 Conclusions

Computational feasibility study of the deformable mirror therapy technique was evaluated using MRI derived 2D breast data. MR breast data of women belonging to different age groups and breast density reported to have suspicious lesions were stud-

Table 12.3. Steady state thermal statistics for hyperthermia adjuvant therapy for breast cancer using dual deformable mirrors.

Model ID	$T_a = 32°C$			$T_a = 37°C$		
	T_μ^{tumor}	T_μ^{benign}	T_μ^{skin}	T_μ^{tumor}	T_μ^{benign}	T_μ^{skin}
Ia	42.5957	37.0781	32.3425	42.8839	38.5164	37.1089
Ib	42.9738	37.6774	32.3647	43.4726	39.1081	37.1483
Ic	44.3540	38.4518	32.3391	44.8260	39.8087	37.1549
IIa	43.4223	38.1617	32.6177	43.5887	39.7080	37.4138
IIb	43.5474	37.9469	32.6288	43.7440	39.5396	37.4113
IIc	45.2564	39.4288	32.4108	45.4967	40.8554	37.2243
III	42.8612	37.9121	32.4137	43.5185	39.0930	37.1340
IV	41.5710	37.2484	32.4116	41.8426	38.2478	37.1249
V	42.5138	37.4284	32.5733	43.4121	38.6288	37.2780

Table 12.4. Specific absorption rate inside MR breast tissue models for noninvasive ablation using dual deformable mirrors.

Model ID	SAR (W/kg/m)		
	Tumor	Benign	Skin
Ia	126.7672	10.4568	24.3569
III	89.5673	7.3229	21.3910
V	135.3974	7.0732	27.7756

Table 12.5. Steady state thermal statistics for noninvasive ablation of breast cancer using dual deformable mirrors.

Model ID	$T_a = 32°C$			$T_a = 37°C$		
	T_μ^{tumor}	T_μ^{benign}	T_μ^{skin}	T_μ^{tumor}	T_μ^{benign}	T_μ^{skin}
Ia	49.9505	38.9737	32.4785	50.2387	40.4120	37.2449
III	50.2668	40.2899	32.5659	50.9241	41.4709	37.2862
V	52.5167	39.9693	33.0069	53.4149	41.1696	37.7116

ied in the numerical simulations. Consistent performance of the therapy model for breast data with different pathological and physiological conditions indicate the feasibility of an alternate adjuvant therapy technique employing dual deformable mirrors for the treatment of localized breast cancer. Ablation studies on 2D MR breast data belonging to different patients reveal the potential of the deformable mirror as an noninvasive ablation device for cancer therapy. The thermal statistics computed for malignant lesions reported in the MR diagnosis of the five patient models for hyperthermia treatment are summarized in Tables Table 12.2-Table 12.3. Table Table 12.2 lists the tissue SAR (W/kg/m) deposited inside the different soft tissue regions of the MR breast models irradiated by 500 MHz continuous wave excitation. The average steady state temperature inside the different soft tissue regions of the patient models are tabulated in Table Table 12.3. In Tables Table 12.2-Table 12.3, tissue SAR and steady state temperature are the highest inside tumor and are relatively higher within skin than the benign tissue with a composition of fat and fibroglandules. Though higher, the thermal statistics inside skin are well below the toxic level for both $T_a = 32^{\circ}C$ and $T_a = 37^{\circ}C$. In the simulation study, the high intensity lymph nodes were modeled as tissues with permittivity values close to that of the hydrous tumor.

Tissue SAR maintained by the noninvasive ablation numerical model in the coronal sections of MR breast data are summarized in Table Table 12.4. Compared to Table Table 12.2, the SAR values in Table Table 12.4 are consistently higher as ablation requires higher EM energy deposition to elevate the tumor temperature above 50° C. The relatively higher SAR within the tumor tissue compared to the rest of the breast reported in Table Table 12.4 indicates selective energy deposition inside the tumor by the dual deformable mirror therapy model. Temperature inside the different soft tissues of the MR breast data for ablation are listed in Table Table 12.5. In Table Table 12.5, the average steady state temperature maintained by the dual deformable

mirror inside the tumor tissue is approximately 50° C while, the remaining regions of the breast are maintained below 42° C. Both hyperthermia and ablation study indicate selective tumor tissue heating compared to the surrounding benign tissues and skin. Computational study on fibroglandular, heterogeneous and fatty breast data of women belonging to different age groups and clinical history indicate the feasibility of the proposed deformable mirror therapy model as an alternate adjuvant and ablation therapy technique for localized breast cancer treatment. The deformable mirror technique serves as a novel and unique imaging cum therapy device for breast cancer.

CHAPTER 13

MIRROR BASED OPTICAL PROTOTYPE

Introduction

The simplicity of both numerical and experimental techniques in the visible regime of light spectrum led to the construction of a simple optical experimental setup. The optical experimental setup serves as a proof of concept for the deformable mirror microwave tomography technique proposed in this thesis. *Ray tracing*, the most generic modeling technique in geometrical optics is used in the numerical model. The objectives of the experiments are to

1. Evaluate the potential of a perfectly reflecting mirror to steer the light beam to acquire multi-view measurements of a stationary object using fixed source-detector arrangement

2. Investigate the feasibility of material property recovery using multi-view measurements produced in 1

Due to the cost and complexity involved in the microwave regime (100 cm - 1mm), other regimes in the electromagnetic spectrum were considered to establish the proof of concept of the proposed imaging system. Despite the simplicity of ray theory, X-ray regime (10nm - 0.1nm) is not suitable for experimental prototype due to radiation hazards and lack of X-ray mirrors for angle of incidence greater than the grazing angle. The lower end of the electromagnetic spectrum (>10 m) scatters similar to microwaves and requires complex setup and equipments of physically larger dimensions. The visible light spectrum ($\sim 400nm - \sim 700nm$), intermediate between microwaves and X-rays is not radioactive and requires simple and low cost equipments that is relatively easy to model. The advantages of the experimental prototype in optical regime are,

- Light interaction with objects can be studied using geometrical optics
- Ray tracing modeling techniques are simple to implement
- Availability of low cost light source and detectors
- Low system complexity, safe and ease of operability

Refractive index estimation of the object of interest using light measurements for different mirror rotations presented in this chapter sets the stage for potential use of deformable mirror in microwave regime for tomography. The organization of this chapter is as follows. The physics associated with geometrical optics phenomenon implemented in the numerical model is briefly covered in section 13.1. Sections 13.2 and 13.3 explain the mathematical theory and algorithms of the ray tracing model respectively. Details of the experimental setup, calibration procedure and model validation are covered in section 13.4. Iterative inversion results, model comparison with experiments and true solutions are presented in section 13.5. Finally, the outcome and implications of the experiments are discussed in section 13.6.

13.1 Geometrical Optics

Visible light are electromagnetic waves with rapid oscillations of the order of $\sim 10^{-5}$ cm. Geometrical optics is a branch of classical optics that neglects the finiteness of the wavelength and treats light as rays. In this paradigm, energy is transported by rays that obey geometrical laws of optics. The laws of geometrical optics provide rules to propagate the rays in an optical system where a ray defines the normal of an optical wavefront. The approximation, $\lambda \rightarrow 0$ in geometrical optics neglects diffraction and polarization phenomenon.

13.1.1 Equation of Light Rays

Let $\mathcal{W}(x, y, z) = 0$, define the surface of a geometrical wavefront. As per the definition, a light ray is the trajectory perpendicular to the wavefront that determines light propagation. Let $\mathbf{r}$ be a position vector on a ray of length, s from a fixed point in the cartesian coordinate system. The ray obeys [205],

$$\hat{\mathbf{r}} = \frac{d\mathbf{r}}{ds} \tag{13.1a}$$

$$= \frac{\nabla\mathcal{W}}{|\nabla\mathcal{W}|}, \qquad \left[\nabla = \frac{\partial}{\partial x}\hat{x} + \frac{\partial}{\partial y}\hat{y} + \frac{\partial}{\partial z}\hat{z}\right] \tag{13.1b}$$

$$= \frac{\nabla\mathcal{W}}{n}, \qquad [n = \sqrt{\mu_r \epsilon_r}] \tag{13.1c}$$

In (13.1a)-(13.1c), $\hat{\mathbf{r}}$ is the unit vector normal to $\mathcal{W}(x, y, z)$ and n is material refractive index. Differentiating (13.1c) with respect to s yields,

$$\frac{d}{ds}\{n\hat{\mathbf{r}}\} = \frac{d}{ds}\{\nabla\mathcal{W}\} \tag{13.2a}$$

$$= \hat{\mathbf{r}} \cdot \nabla(\nabla\mathcal{W}), \qquad \left[\frac{d}{ds} = \hat{\mathbf{r}} \cdot \nabla\right] \tag{13.2b}$$

$$= \frac{1}{n}\nabla\mathcal{W} \cdot \nabla(\nabla\mathcal{W}), \qquad [From(13.1c)] \tag{13.2c}$$

$$= \frac{1}{2n}\nabla\left[(\nabla\mathcal{W})^2\right] \tag{13.2d}$$

$$= \frac{1}{2n}\nabla n^2 \tag{13.2e}$$

In deriving (13.2e), the *eikonal equation* $(\nabla\mathcal{W})^2 = n^2$ was used [205]. For homogeneous medium, (13.2e) reduces to,

$$\frac{d^2\mathbf{r}}{ds^2} = 0 \tag{13.3}$$

Solution to the homogeneous differential equation (13.3) is the vector equation of a straight line,

$$\mathbf{r} = s\mathbf{a} + \mathbf{b} \tag{13.4}$$

where **a** and **b** are constant vectors. Equation (13.4) implies that light rays in homogeneous medium takes the form of straight lines where the ray direction is given by vector **a**, that passes through **b**.

13.1.2 Laws of Reflection & Refraction

Under Geometrical optics approximations, light waves behave similar to plane waves. Light incident on an object with planar surface undergoes reflection and refraction as shown in Figure Figure 13.1. The incident and reflected rays at the interface of dissimilar objects obeys the *reflection law* [205],

$$\theta_i = \theta_r \tag{13.5}$$

where θ_i and θ_r are the angle subtended by the incident and reflected rays respectively with the surface normal at the point of intersection as illustrated in Figure Figure 13.1. Equation (13.5) implies that the reflected ray lies in the plane of incidence.

At the interface of dissimilar materials, light is partially reflected and partially transmitted. The relationship between the angles of incidence and refraction is given by *Snell's law*,

$$n_1 sin(\theta_i) = n_2 sin(\theta_t) \tag{13.6}$$

Equation (13.6) implies that the refracted ray lies in the plane containing the incident ray and the surface normal at the intersection. In geometrical optics, light propagation in an optical system is defined using the laws of reflection and refraction.

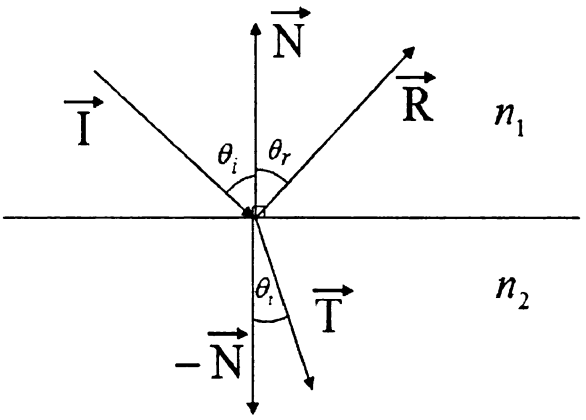

Figure 13.1. Specular reflection and transmission in geometrical optics.

13.2 Ray Tracing - Essentials

Ray tracing is the most general technique used in geometrical physics to model the path taken by light by tracing or following the rays as they interact with objects [154]. It is widely used in 3D computer graphics and in optical systems such as cameras, lenses, telescopes and binoculars. To implement a ray tracer routine it is essential to understand the four fundamental modes of light transport namely,

1. Specular Reflection
2. Diffuse Reflection
3. Specular Transmission
4. Diffuse Transmission

The subsequent sections briefly covers the fundamental modes of light transport and explains the ray tracing algorithm implemented in the numerical model.

13.2.1 Specular Reflection

Specular reflection of light is a phenomenon where light incident on an object bounces off the surface without being absorbed or re-radiated from the surface of the object. This mode of light transport occurs when light is incident on perfectly smooth or specular surfaces. Such perfect, mirror-like reflection obeys the *law of reflection* defined in (13.5). Figure Figure 13.1 shows a light ray bouncing off a flat perfectly reflecting surface. From (13.5), the reflected and surface normal vectors lie in the plane of incidence. Thus, the unit reflected vector, $\mathbf{R}$ can be expressed as a linear combination of the incident and surface normal vectors as,

$$\mathbf{R} = \alpha\mathbf{I} + \beta\mathbf{N} \tag{13.7}$$

In 13.7, the incident and reflected unit vectors $\mathbf{I}$ and $\mathbf{R}$ subtend θ_i and θ_r respectively with the surface normal, $\mathbf{N}$.

From (13.5) and the illustration in Figure Figure 13.1, it is known that $cos(\theta_i) = -\mathbf{I} \cdot \mathbf{N}$ and $cos(\theta_r) = \mathbf{R} \cdot \mathbf{N}$ and (13.5) can be rewritten as,

$$\begin{aligned} cos(\theta_i) &= cos(\theta_r) && \text{(13.8a)} \\ -\mathbf{I} \cdot \mathbf{N} &= \mathbf{N} \cdot \mathbf{R} && \text{(13.8b)} \\ &= \mathbf{N} \cdot (\alpha\mathbf{I} + \beta\mathbf{N}) && \text{(13.8c)} \\ &= \alpha\,(\mathbf{N} \cdot \mathbf{I}) + \beta, \qquad [|\mathbf{N}| = 1, \mathbf{N} \cdot \mathbf{N} = 1] && \text{(13.8d)} \end{aligned}$$

Arbitrarily setting $\alpha = 1$ in (13.8a) yields, $\beta = -2\,(\mathbf{N} \cdot \mathbf{I})$. Substituting for α and β reduces (13.7) to the form,

$$\mathbf{R} = \mathbf{I} - 2\,(\mathbf{N} \cdot \mathbf{I}) \cdot \mathbf{N} \tag{13.9}$$

Equation (13.9) is the vector wave equation for a light ray specularly reflected from

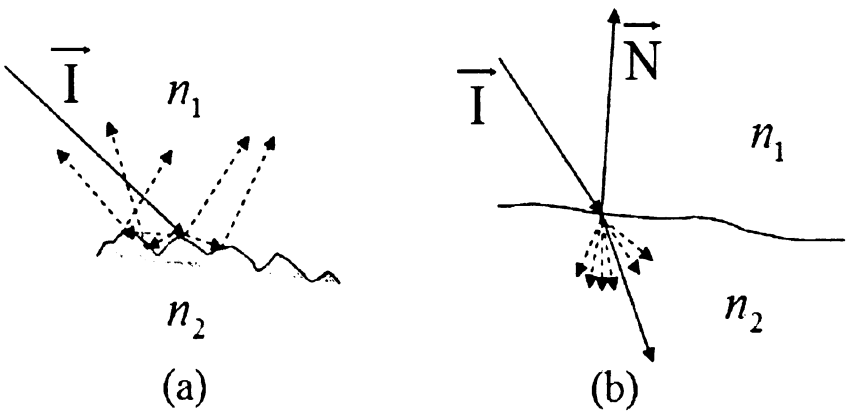

Figure 13.2. Ray optics at non-specular surface (a) Diffuse reflection (b) Diffuse transmission.

an optical interface.

13.2.2 Diffuse Reflection

Light incident on rough or non-specular surfaces undergoes *Diffused reflection* which, causes the incident light to re-radiate along different directions from the point of intersection. On a rough surface, the incident light is either absorbed or re-radiated depending on the optical property of the surface. Such surfaces, diffusely reflect light in all directions as illustrated in Figure Figure 13.2(a).

13.2.3 Specular Transmission

Light impinging a specular transparent object is partly reflected away and partly transmitted inside the transparent object. *Specular Transmission* is the bending of light rays incident on transparent objects with specular surface. The phenomenon also known as *refraction* is illustrated in Figure Figure 13.1. The relationship between the transmitted, incident and reflected rays can be derived using the *Snell's law* in (13.6). Equations (13.5)-(13.6) dictate that the transmitted ray, **T** is coplanar with

the incident ray and surface normal and can be expressed as,

$$\mathbf{T} = \alpha\mathbf{I} + \beta\mathbf{N} \tag{13.10}$$

Taking square of (13.6) and using trigonometric identity yields,

$$\left(1 - cos(\theta_i)^2\right) n_{12}^2 = \left(1 - cos(\theta_t)^2\right) \tag{13.11}$$

where $n_{12} = \frac{n1}{n2}$. Equation (13.11) can be rewritten as,

$$\begin{aligned}
1 + \left(cos(\theta_i)^2 - 1\right) n_{12}^2 &= cos(\theta_t)^2 && \text{(13.12a)}\\
&= [-\mathbf{N} \cdot \mathbf{T}]^2 && \text{(13.12b)}\\
&= [-\mathbf{N} \cdot (\alpha\mathbf{I} + \beta\mathbf{N})]^2 && \text{(13.12c)}\\
&= [\alpha\,(-\mathbf{N} \cdot \mathbf{I}) + \beta\,(\mathbf{N} \cdot \mathbf{N})]^2 && \text{(13.12d)}\\
&= \left[\alpha cos(\theta_i)^2 - \beta\right]^2 && \text{(13.12e)}
\end{aligned}$$

The unknown scalars, α and β can be obtained by imposing the magnitude of the transmitted ray, $\mathbf{T}$ to be equal to unity. The unit magnitude condition yields,

$$\begin{aligned}
1 &= \mathbf{T} \cdot \mathbf{T} && \text{(13.13a)}\\
&= (\alpha\mathbf{I} + \beta\mathbf{N}) \cdot (\alpha\mathbf{I} + \beta\mathbf{N}) && \text{(13.13b)}\\
&= \alpha^2 + 2\alpha\beta\,(\mathbf{I} \cdot \mathbf{N}) + \beta^2 && \text{(13.13c)}\\
&= \alpha^2 - 2\alpha\beta cos(\theta_i) + \beta^2 && \text{(13.13d)}
\end{aligned}$$

Equations (13.12e)-(13.13d) are simultaneously solved for the unknown scalars, α and β. Substituting for α and β in (13.10) yields the final solution for the unit transmitted

ray,

$$\mathbf{T} = n_{12}\mathbf{I} + \left(n_{12}cos(\theta_i) - \sqrt{1 + n_{12}^2 \left(cos(\theta_i)^2 - 1 \right)} \right) \mathbf{N} \tag{13.14}$$

When the term under the radical is negative, (13.14) yields imaginary solution. This optical phenomenon is known as *total internal reflection* where the incident ray is entirely reflected back into the medium containing the incident ray.

13.2.4 Diffuse Transmission

Most of the objects in life support *Diffuse transmission* where light impinging on a rough or imperfectly specular surface is scattered in all directions as it penetrates through a translucent object. Similar to diffuse reflection, diffusely transmitted rays travel in all possible direction as illustrated in Figure Figure 13.2(b).

13.2.5 Reflectance and Transmittance Coefficients

Generic ray tracing algorithm in geometrical optics propagate the light rays inside an optical system using all four fundamental modes of light transportation. The ray tracing routine employed in the numerical model assumes specular objects and neglects diffuse reflection and transmission phenomenon. The intensity of a specularly reflected ray is given by the Fresnel equations [205]. The Fresnel equations give the reflection coefficient of light polarized in parallel and perpendicular to the plane of incidence as,

$$R_p = \frac{n_2 cos(\theta_i) - n_1 cos(\theta_t)}{n_2 cos(\theta_i) + n_1 cos(\theta_t)} \tag{13.15a}$$

$$R_s = \frac{n_1 cos(\theta_i) - n_2 cos(\theta_t)}{n_1 cos(\theta_i) + n_2 cos(\theta_t)} \tag{13.15b}$$

$$\tag{13.15c}$$

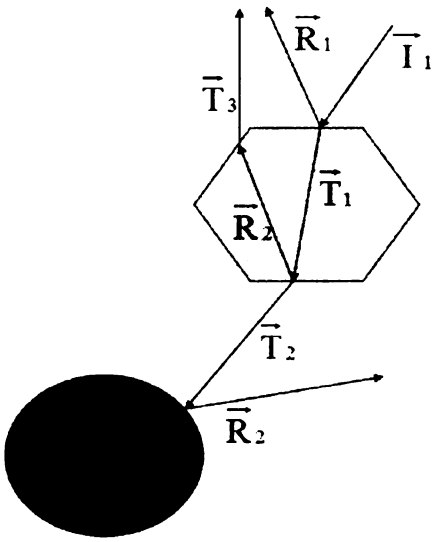

Figure 13.3. Illustration of ray tracing process.

For an unpolarized light, intensity of the reflected and transmitted light rays are given by the expressions,

$$R = \frac{1}{2}\left(R_p^2 + R_s^2\right) \tag{13.16a}$$

$$T = 1 - R \tag{13.16b}$$

13.3 Ray Tracing Model

Ray tracing is a point sampling method where a continuous image is converted into discrete samples or pixels in the image plane. In ray tracing, light rays arriving at the eye or camera are traced backwards to the scene through the image plane. Each ray from the eye is tested for intersection with objects in the scene. If a ray intersects an object, depending on the angle of incidence and optical property of the object, reflected and transmitted rays are spawned. If the ray does not intersect with objects in the scene, the pixel in the image plane is assigned the background

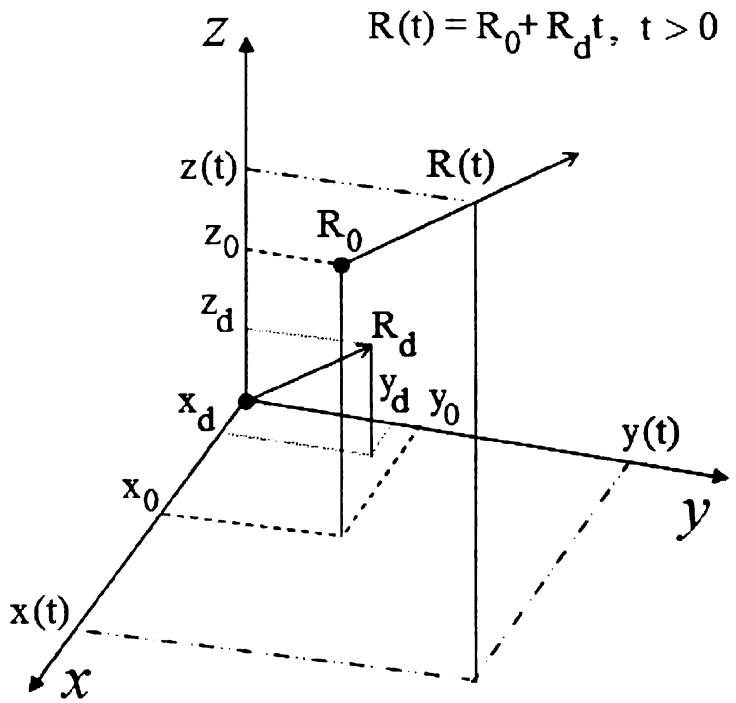

Figure 13.4. Representation of a light ray in ray tracing module.

color. Secondary rays spawned by reflection and refraction are recursively tested for intersection with objects in the scene. Reflected and transmitted rays are continually generated at every ray-object intersections until the energy of an individual ray falls below a predetermined level or if the ray escapes the image scene. Figure Figure 13.3 shows an example of a ray tracing process.

13.3.1 Light Ray

In ray tracing, the fundamental task of backward ray tracing is accomplished by ray-object intersection routines which require a mathematical representation for the light rays. Figure Figure 13.4 illustrates a ray emanating from the origin, $\mathbf{R}_0 = [x_0, y_0, z_0]$ and propagating in the direction of a unit vector, $\mathbf{R}_d = [x_d, y_d, z_d]$. A parametric

representation of a ray is given by the equation,

$$\mathbf{R}(t) = \mathbf{R}_0 + \mathbf{R}_d t, \qquad t > 0. \tag{13.17}$$

In (13.17), t represents the distance of the ray from the origin, $\mathbf{R}_0$. Equation (13.17) can be rewritten in cartesian coordinates as,

$$x(t) = x_0 + x_d t \tag{13.18a}$$

$$y(t) = y_0 + y_d t \tag{13.18b}$$

$$z(t) = z_0 + z_d t \tag{13.18c}$$

13.3.2 Ray-Object Intersection

The key task in ray tracing is to find where a ray intersects an object. In the numerical model, objects in the scene are given a mathematical representation to compute ray-object intersections. Let $\mathcal{L}(x, y, z) = 0$ represent the surface of an object. The ray-object intersection point is computed by substituting (13.18) into $\mathcal{L}(x, y, z) = 0$ and the resulting equation,

$$\mathcal{L}(x_0 + x_d t, y_0 + y_d t, z_0 + z_d t) = 0 \tag{13.19}$$

is solved for t. Substituting t into (13.18) yields the intersection point, $r_i = [x_i, y_i, z_i]$.

13.3.2.1 Ray-Plane Algorithms

Let a plane at a distance D from the origin, $[0, 0, 0]$ be represented as,

$$Ax + By + Cz + D = 0, \qquad A^2 + B^2 + C^2 = 1 \tag{13.20}$$

In (13.20), the sign of D determines location of the plane with respect to the origin in the cartesian coordinate system. The unit vector normal to the surface of the plane

is given by,

$$\mathbf{N}_p = \left[\frac{d\mathcal{L}}{dx}, \frac{d\mathcal{L}}{dy}, \frac{d\mathcal{L}}{dz}\right] \tag{13.21a}$$

$$= [A, B, C] \tag{13.21b}$$

Substituting (13.18) in (13.20) and solving for t yields,

$$t = -\frac{(Ax_0 + By_0 + Cz_0 + D)}{(Ax_d + By_d + Cz_d)} \tag{13.22}$$

If (13.22) yields solution for which $t < 0$, then the ray intersects with the plane behind the ray's origin,$\mathbf{R}_0$. The intersection point on the plane is obtained by substituting (13.22) into (13.18). Ray intersection with polygons is calculated using the ray-plane algorithm for each face of the polygon.

13.3.2.2 Ray-Quadratic Surface Algorithms

Intersection of a ray with quadratic surfaces is calculated following a procedure similar to that explained for a plane. Let a quadratic surface be defined by a polynomial of the form,

$$\mathcal{L}(x, y, z) = 0 \tag{13.23a}$$

$$Ax^2 + 2Bxy + 2Cxz + 2Dx + Ey^2 + 2Fyz + 2Gy + Hz^2 + 2Iz + J = 0 \tag{13.23b}$$

Substituting (13.18) into (13.23) yields a quadratic equation in t of the form,

$$A_Q t^2 + B_Q t + C_Q = 0 \tag{13.24}$$

where A_Q, B_Q, C_Q are scalar coefficients. The roots of the quadratic equation, (13.24) yields,

$$t_0 = \frac{-B_Q - \sqrt{B_Q^2 - 4A_QC_Q}}{2A_Q} \tag{13.25a}$$

$$t_1 = \frac{-B_Q + \sqrt{B_Q^2 - 4A_QC_Q}}{2A_Q} \tag{13.25b}$$

Amongst (13.25a)-(13.25b), the smallest positive root is used to calculate the closest intersection point of the ray with the quadratic surface. Substituting t into (13.18) yields the intersection point, $r_i = [x_i, y_i, z_i]$ on the quadratic surface. The surface normal for the quadratic surface is given by,

$$\mathbf{N}_q = \left[\frac{d\mathcal{L}}{dx}, \frac{d\mathcal{L}}{dy}, \frac{d\mathcal{L}}{dz}\right] \tag{13.26}$$

Depending on the mathematical surface of an object, appropriate ray-object intersection algorithms are used to calculate the closest intersection point. Irrespective of the object surface, the vector normal to the object's surface, $\mathbf{N}$ is calculated such that,

$$-\mathbf{N} \cdot \mathbf{R}_d > 0 \tag{13.27}$$

is true. If the dot product is negative, the direction of the surface normal should be reversed. Substituting $\mathbf{I} = \mathbf{R}_d$ in (13.9) and using (13.16a) yields the specularly reflected ray. The specularly transmitted ray is obtained using (13.14) and (13.16b).

13.3.3 Recursive Ray Tracing

The numerical model implemented for refractive index estimation, employs ray tracing basics covered in the previous sections assuming the mirror and the object of interest have specularly reflecting surfaces. Instead of starting from the eye or camera, the recursive ray tracing routine starts from the light source. For each ray emitted by the light source, ray tracing technique is used to trace the ray from the source to the receiver via the optical system.

The recursive ray tracing routine implemented in the model is summarized below.

1. For each primary ray from light source,

   (a) Find ray intersection with objects in the optical system

      i. Compute incident and surface normal unit vectors, **I** and **N**

      ii. Compute specularly reflected and transmitted rays, **R** and **T** using (13.9) and (13.14)

      iii. Abort ray tracing process if one of the following is true

         A. Reflected ray amplitude is below δ_A, $\delta_A > 0$

         B. Reflected ray escaped the optical system

      iv. Else, go to step (i) to find intersection of **R** with objects

      v. Abort ray tracing process if one of the following is true

         A. Transmitted ray amplitude is below δ_A, $\delta_A > 0$

         B. Transmitted ray intersected the detector array

      vi. Else, go to step (i) to find intersection of **T** with objects

13.4 Optical Experimental Setup

The geometrical optics and ray tracing fundamentals explained in the previous sections are essential in the design and construction of the optical experimental setup. This section explains the design and operation of the experimental setup implemented to determine the refractive index of a specularly reflecting material using mirror. The calibration procedure devised to standardize the ray tracing model prediction for comparison with experimental data is also explained in this section.

13.4.1 Optical System

13.4.1.1 System Design

The schematic diagram of the experimental setup is illustrated in Figure Figure 13.5. The experimental setup consists of a light source, perfectly reflecting mirror and a linear light detector array. The light intensity measured by the light detector is acquired in real time using a personal computer. The material under inspection is placed between the source and

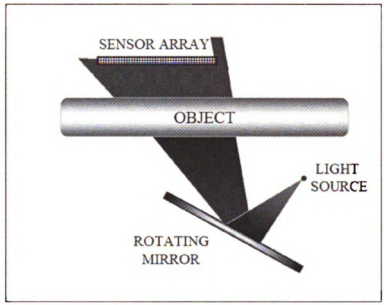

Figure 13.5. Schematic representation of the optical experiment.

the light detector as illustrated in Figure Figure 13.5. The optical system is designed such that the light emitted by the source is primarily incident on the mirror. The incident light reflected by the specularly reflecting mirror propagates through the object under inspection before reaching the linear light detector array. Changing the mirror orientation effectively steers the light incident on the object along different directions and yields multi-view measurements of the stationary object at the detector array.

13.4.1.2 System Implementation

Figure Figure 13.6 shows the optical system. The experimental setup is mounted on an a precision optical bench to ensure stability, repeatability and accuracy. The light source is a light emitting diode (LED) with spectral peak at 640 nm (red color). Figures Figure 13.7(a)-(b) show the spectral and spatial characteristics of the LED used in the experiment [206]. Table Table 13.1 lists the technical specifications of the LED. The LED is connected to a $+5V$ DC power supply using a current limiting resistor as shown in Figure Figure 13.8. In the experiments, the radial spread or beam pattern of the LED is narrowed by creating a

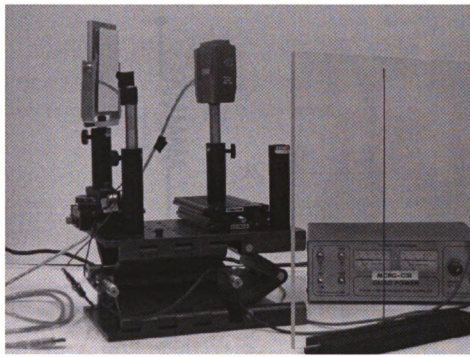

Figure 13.6. Experimental setup.

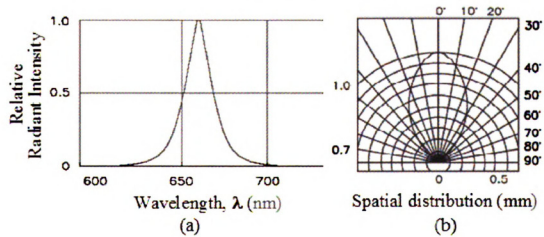

Figure 13.7. Light characteristics of the LED [206] (a) Spectral distribution (b) Spatial distribution.

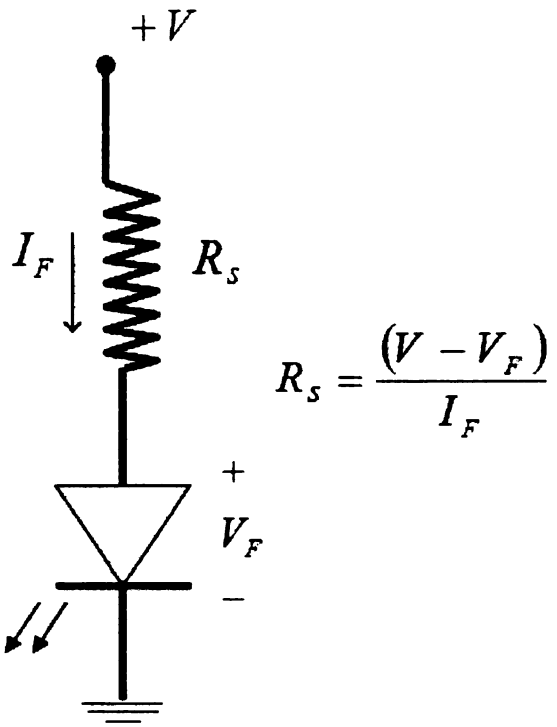

Figure 13.8. Connection diagram for the LED circuit.

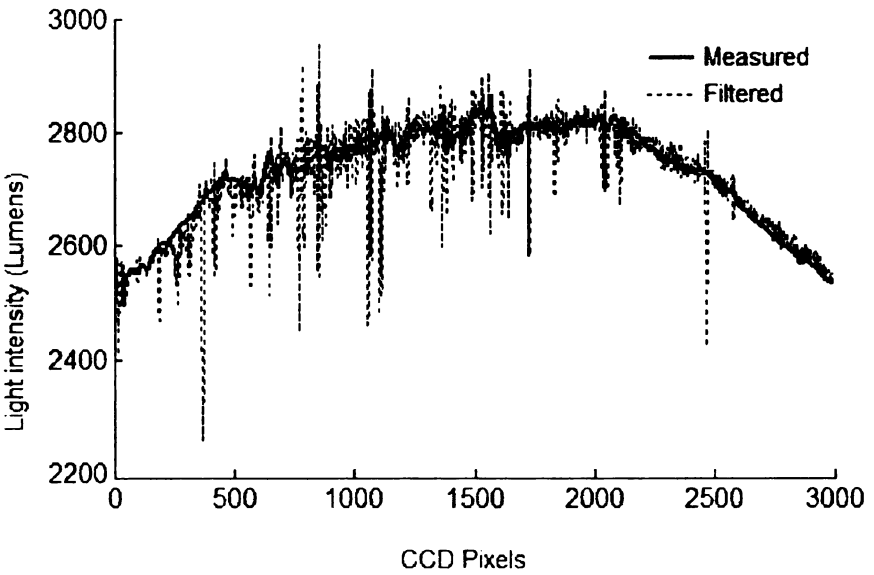

Figure 13.9. Light intensity measured by the 3000 element linear CCD array.

Table 13.1. LED technical specifications [206].

Parameter	Typical Rating	Units
Peak Wavelength, λ_P	660	nm
Dominant Wavelength, λ_D	640	nm
Forward Voltage, V_F	1.85	V
Reverse Current, I_R	10	μA
DC Forward Current, I_F	30	mA

pin hole arrangement for the source. The pinhole arrangement ensures that light from the LED is primarily incident on the mirror and not scattered to the surrounding. The optical setup employs a front surface coated mirror to reflect and steer the light emitted by the source. The mirror is mounted on a precision rotating system to steer the light towards the object at different angles for multi-view measurements. A linear CCD array (ThorLabs USB LC-1) is used to measure the intensity of the light emerging from the object [207]. The CCD array contains 3000 sensors in linear arrangement with each sensor or pixel measuring 7 μm x 200 μ m and a CCD integration time window of 1 μ s - 200 ms in the visible light spectrum.

The object under inspection is a 30.48x30.48 cm clear homogeneous glass slab. The glass slab is mounted on a holder as shown in Figure Figure 13.6. The dotted line in Figure Figure 13.9 shows the light intensity measured by the linear CCD array using the optical setup in Figure Figure 13.6. The CCD data is corrupted due to the presence of measurement noise and bad sensors. The measurement noise and bad pixels in the CCD data are compensated using filtering and interpolation routines. The filtered data is shown in Figure Figure 13.9 in bold line.

13.4.1.3 System Operation

As in Figure Figure 13.6, the source and mirror are positioned opposite to the linear CCD array and the object under inspection is placed in between. The experiments were conducted in a dark room to avoid ambient light from affecting the measurements. During the experiment, light incident on the CCD array was recorded for every mirror rotation

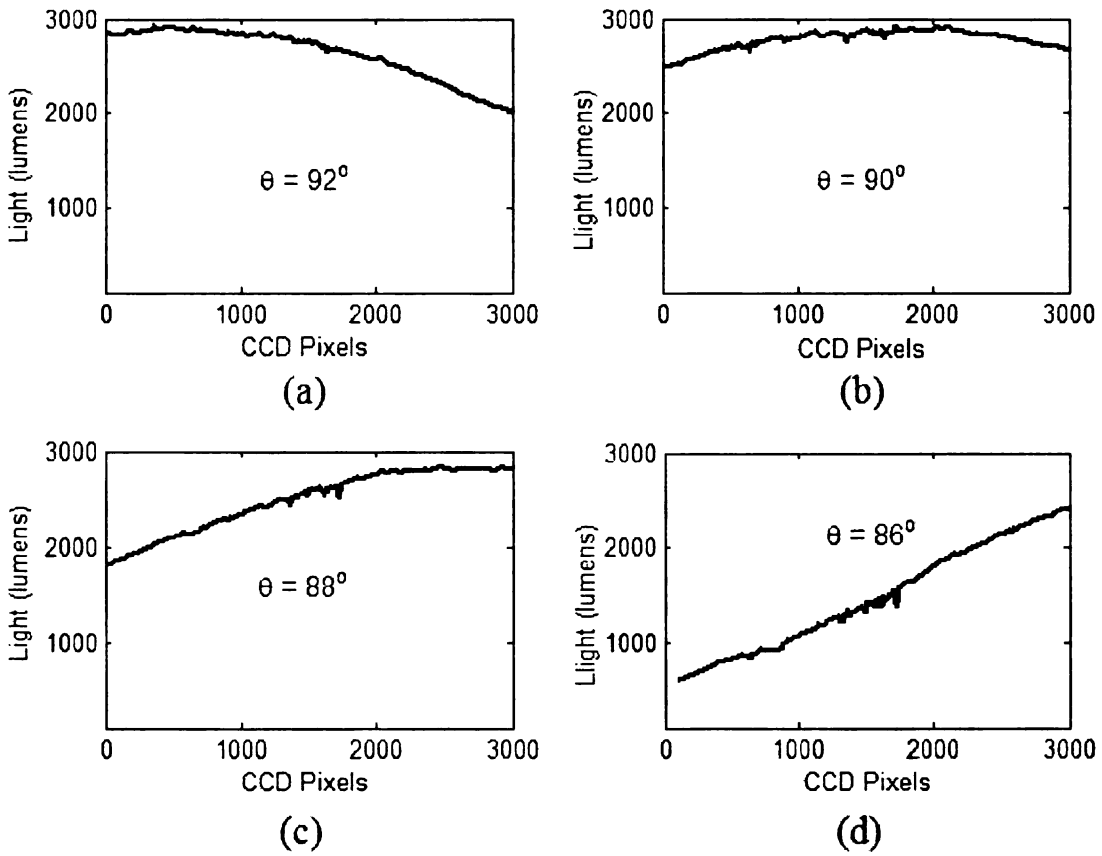

Figure 13.10. CCD measurements for different mirror rotation.

with and without the glass slab. Data collected in the absence of the object same as "Free Space" measurements are used to calibrate the simulation results of ray tracing model. Figure Figure 13.10 shows the Free Space measurements of the linear CCD sensor array for different mirror rotations. In Figure Figure 13.10, it can be observed that rotating the mirror amounts to steering or rotating the light along different directions. This implies that instead of rotating the object or the source-detector pair as it is done in conventional tomography systems, multi-view measurements could be achieved with the use of continuously deformable mirror. This has a revolutionary implication in re-defining the conventional idea of tomography system due to the following reasons:

- Neither the object nor the detector needs to be rotated
- Eliminates the need for closed chamber arrangement for tomography
- Posses the potential to image objects even with a limited field of view

13.4.2 Numerical Model

In ray tracing model, LED was modeled as a point source located at $(x_s, y_s, z = 0)$, radiating equal intensity light rays over [0-180]° in the plane containing the source. The mirror and CCD detector array are modeled as mathematical planes and the glass object is modeled as a planar slab. Infinite plane model for the mirror, object and CCD reduces ray-object intersections to a two-dimensional problem in $z = 0$ plane. Figure Figure 13.11 shows the propagation of a ray emitted by the source traced using the ray tracing module.

13.4.3 Calibration Procedure

Figure Figure 13.10 shows the spatial response of the point light source used in experiments. In ray tracing model, as all rays are equal in intensity, "Free Space" model measurements at the CCD equals unity for all rays. To match model prediction with CCD measurements, the intensity of light rays emitted in the ray tracing module was apodized. A simple and obvious choice for apodization is to calculate cosine of angle between each ray with the surface normal of the source plane. The intensity of the i^{th} light ray in the numerical model

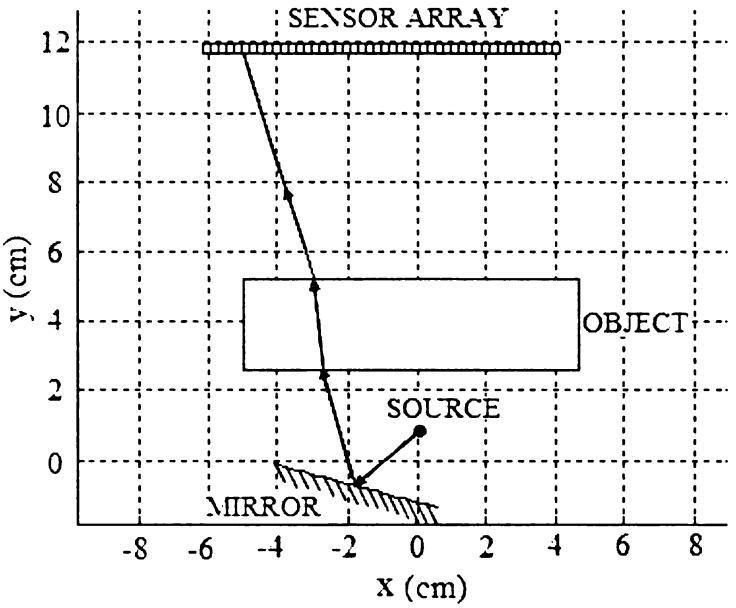

Figure 13.11. Illustration of the ray tracing process implemented in the model.

is given by,

$$I_i = cos(\theta)^m \tag{13.28a}$$

$$= (\mathbf{R}_i \cdot \mathbf{N}_s)^m, \qquad m > 1 \tag{13.28b}$$

The objective of the calibration procedure is to estimate the value of m in (13.28a) such that the model prediction matches CCD measurements for all mirror rotations with and without the glass slab. Free Space measurements obtained for multiple mirror rotations were used to estimate the optimal value, m_{opt} by running the ray tracing simulations for a range of integer values of m. Figure Figure 13.12 shows the apodization function for different values of m. In Figure Figure 13.12 it can be observed that as m increases, the beam pattern rolls off more sharply. Figure Figure 13.13 compares model prediction for $m = 42$ with CCD measurements recorded for two different mirror rotations, θ_A and θ_B. The light source apodization function with $m = 42$ was used for the light source in the

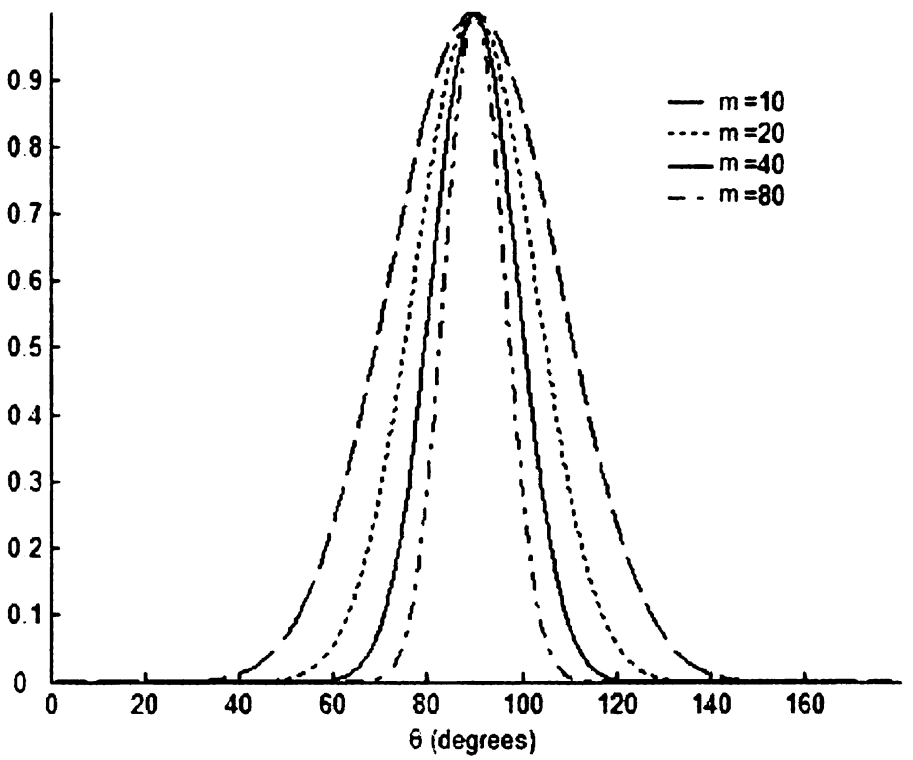

Figure 13.12. Apodization function for varying values of m in (13.28a).

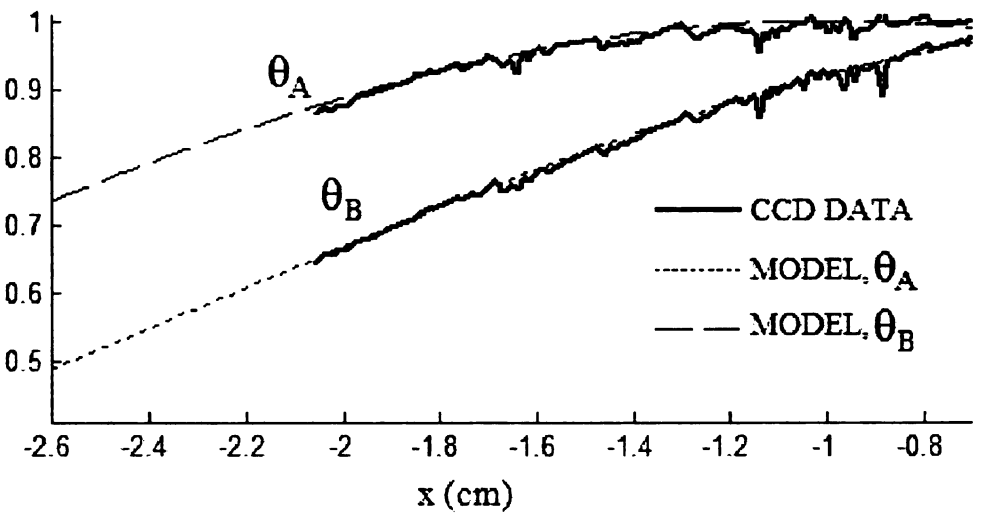

Figure 13.13. Model versus normalized CCD measurements for $m = 42$.

subsequent simulations.

13.5 Inversion Experiments

This section deals with the refractive index estimation for homogeneous plastic and glass slabs using CCD measurements obtained for multiple mirror rotations. Three sets of experiments were carried out. The first one was conducted using the plastic slab alone while the second experiment was conducted for a plastic slab with an obstacle running parallel to the z-axis on the front surface of the glass slab facing the mirror. In the third set of experiments, two glass slabs with an air gap was used. Ray tracing model was used to estimate the refractive index of the glass slab and width of the obstacle. CCD measurements recorded for each mirror rotation were compensated for measurement noise and bad sensors and were normalized to 1.

13.5.1 Experiment I - Refractive Index Estimation

Initial experiments were conducted using a clear plastic slab. The objective of the experiment is to estimate the refractive index of the plastic slab using the multi-view data acquired by rotating the mirror instead of the object. During experiment, the plastic slab was positioned in between the mirror and CCD array parallel to the plane containing the CCD array. The first step is to identify the angle of rotation, $\theta_\perp$ for the mirror that yields measurements identical to normal incidence of a point light source on the CCD array. For $\theta = \theta_\perp$, location of the peak measured in the CCD remains the same for measurements with and without the plastic slab. Mirror rotations for multi-view data used in the experiments were measured with respect to $\theta_\perp^{expt}$, i.e $+2°$ means rotation of the mirror by $2°$ in the anti-clockwise direction with respect to $\theta_\perp^{expt}$. The key task in the ray tracing model is to find the mirror rotation, $\theta_\perp^{model}$. This was achieved by fixing the locations of source and CCD in the model and changing the mirror rotation such that the resulting measurements were equivalent to that for normal incidence. The angle of rotation for which the reflected ray is normally incident on the CCD is denoted by $\theta_\perp^{model}$. The physical location of the source, mirror, object and CCD detector array in the ray tracing model are not identical

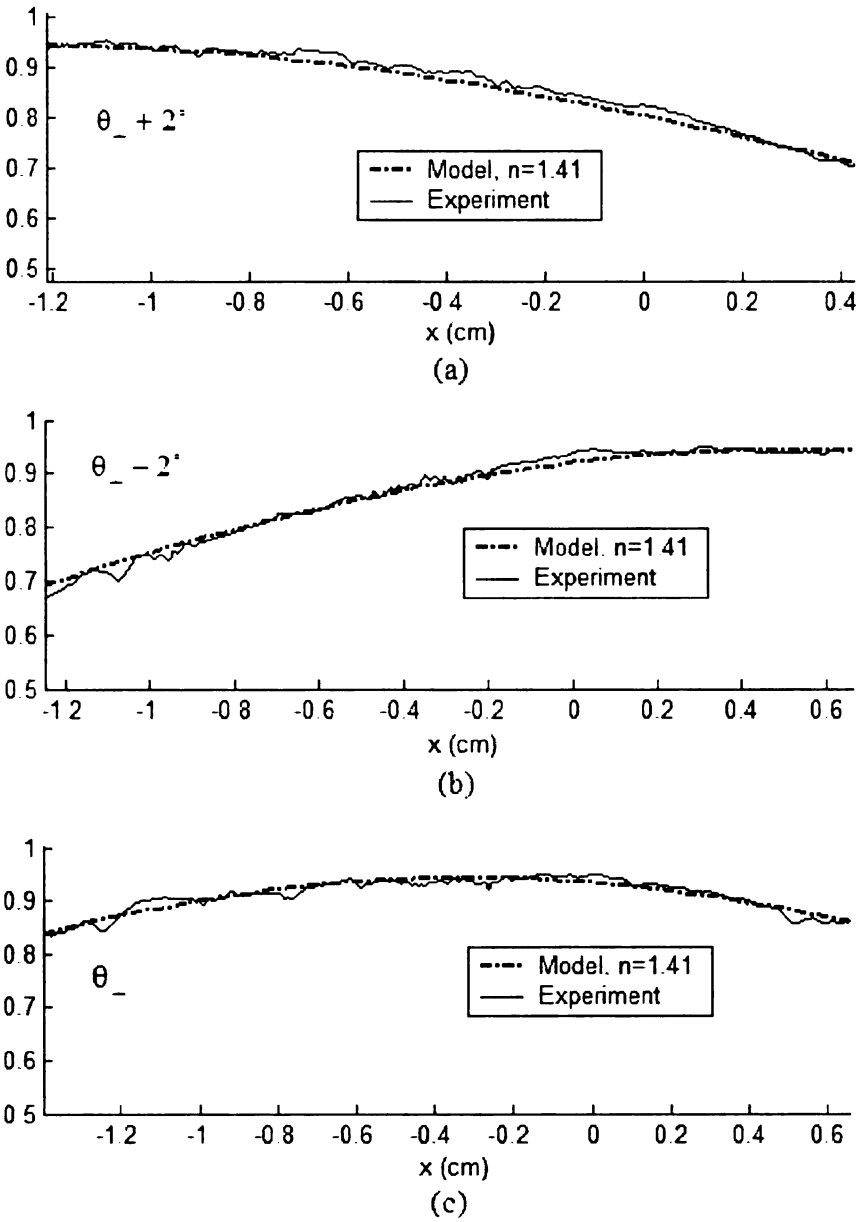

Figure 13.14. Comparison between ray tracing model and CCD measurements for, $n_{est} = 1.41$ (a)$\theta_{\perp} + 2°$ (b)$\theta_{\perp} - 2°$ (c)$\theta_{\perp}$.

Table 13.2. Model estimation error in the object width.

Width (mm)	Model I	Model II	Model III	Model IV
True	0.65	1.3	2.10	1.25
Estimated	0.60	1.2	1.90	1.20
Error	0.05	0.1	0.20	0.05

to their locations in optical setup. But, the offset in the angles between different planes remain constant, i.e. $\theta_{\perp}^{expt} - \theta_{\perp}^{model} = \delta\theta_0$. CCD measurements taken $\pm 4°$ at $2°$ intervals were used to estimate the refractive index of the plastic slab.

Unlike wave propagation problem discussed for microwaves, ray tracing process is cumbersome to compute the Jacobian for inversion. Thus, a simple root finding technique was employed by running the ray tracing module over a range of material refractive index, $n \in [1.0, 5]$. The minimum in the error surface was used to determine the refractive index of the plastic slab. Figure Figure 13.14(a)-(c) show the comparison between CCD measurement and model prediction for $n_{est} = 1.41$ which minimized the measurement error for all mirror rotations.

13.5.2 Experiment II - Refractive Index & Block Width Estimation

In the second set of experiments, a thin opaque cylindrical obstacle was used to generate the CCD measurements. The objective is then to estimate the width of the obstacle in addition to the refractive index of the glass slab. An opaque object in the path of light prevents transmission through the object. Figures Figure 13.15(a)-(d) show the normalized CCD data of the plastic slab with obstacles of different dimensions positioned normal to the imaging plane and in contact with the plastic slab facing the mirror. The minima in the CCD data corresponds to the sensor noise floor in the absence of light and is due to light obstruction by the opaque object. In Figures Figure 13.15(a)-(d), width of the minima in the measurement increases with increase in the physical width of the opaque object. Light intensity measured by the 3000-element linear array recorded for five mirror rotations at $2°$ interval were used to estimate the unknowns; refractive index and obstacle width.

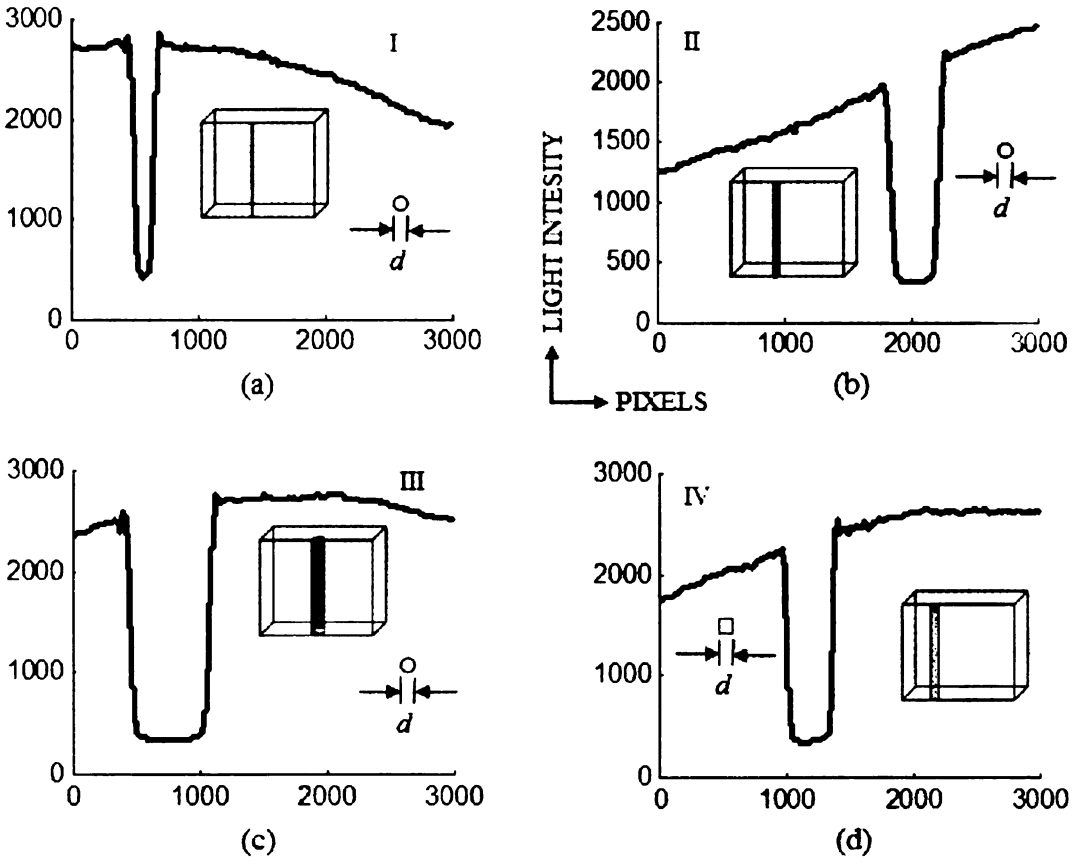

Figure 13.15. Normalized CCD measurement for the plastic slab with opaque object (a) Object I, $d = 0.65mm$ (b) Object II, $d = 1.3mm$ (c) Object III, $d = 2.10mm$ (e) Object V, $d = 1.25mm$.

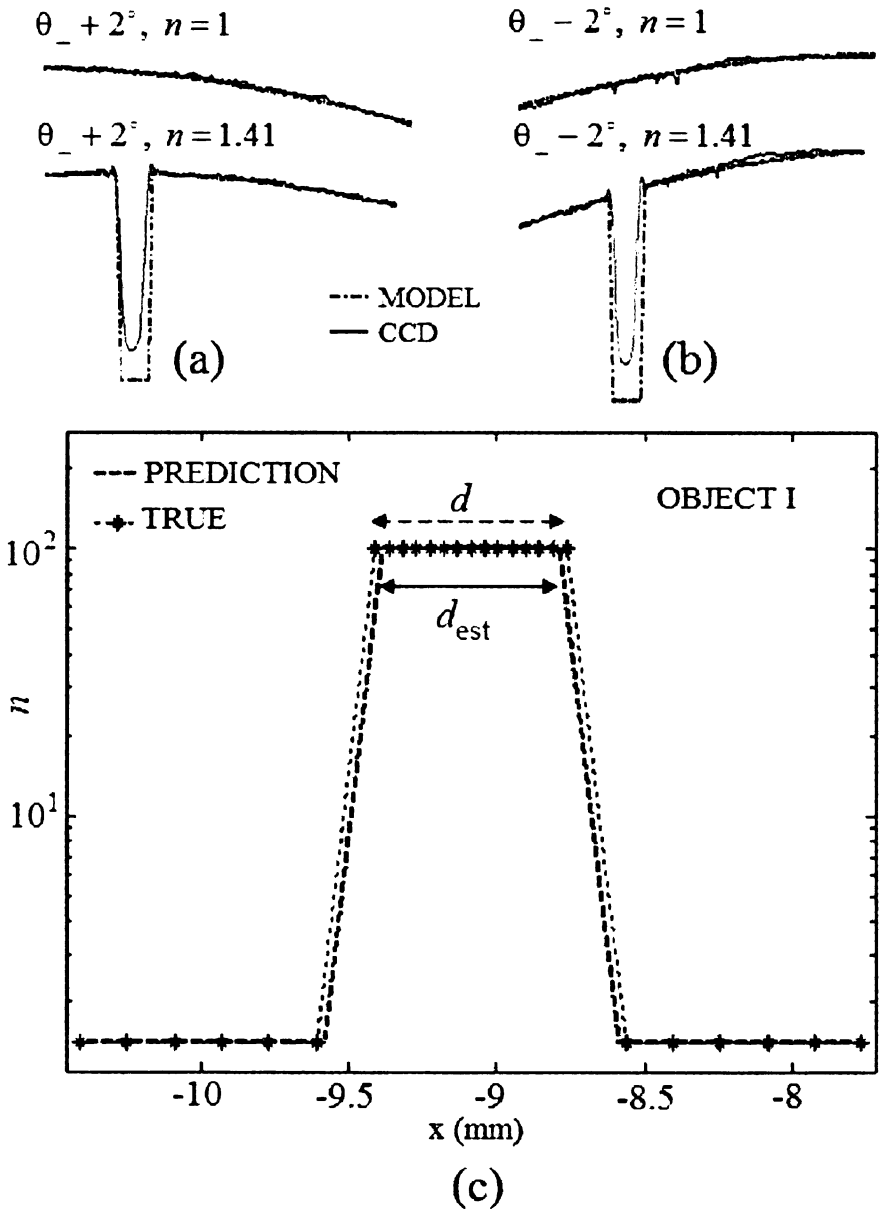

Figure 13.16. Comparison between ray tracing model and normalized CCD measurements of the plastic slab with Object I for $n_{est} = 1.41, d_{est} = 0.60mm$ (a) $\theta_\perp + 2°$ (b) $\theta_\perp - 2°$ (c) Estimated width profile for Object I.

A technique similar to refractive index estimation explained above was implemented to estimate the refractive index and width of the opaque object using the CCD measurements. The ray tracing module was executed for a wide range of refractive index and widths of the opaque object. The error between model and measurements was calculated for each mirror rotations for (n_i, d_i). The parameter vector, (n^i_{est}, d^i_{est}) that correspond to the minimum in the error surface yields the best estimate for the refractive index and the physical width of the opaque object. Figures Figure 13.16-Figure 13.19 show the comparison between model and experiment for the estimated 1D refractive index profile. Estimation error between the model and true solution for the obstacles studied in this investigation are summarized in Table Table 13.2. The good agreement between model and true solution indicate the feasibility of using mirror to obtain multi-view data for reliable tomographic reconstruction. In contemporary tomography systems this is accomplished either by rotating the object or the source-detector pair. Though simple, the proof of concept experiments demonstrate the robustness of the approach to measurement noise and yields a very good estimate for the 1D inverse problem.

13.5.3 Experiment III - 1D Refractive Index Profile

Experiment was carried out to reconstruct the 1D profile of material refractive index. Figure Figure 13.20 shows the experimental setup used in the experiment. In Figure Figure 13.20, light measurements were recorded for a multi-layered problem consisting on glass-air-glass. The physical dimensions of the individual layers are mentioned in FigureFigure 13.20. Figures Figure 13.21(a)-(c) show the measurements for $\theta_\perp - 2°$, $\theta_\perp$ and $\theta_\perp + 2°$ rotations of mirror respectively. The polynomial data fit of CCD measurements for all mirror rotations were used to reconstruct the permittivity profile of the homogeneous layered medium. This was accomplished by minimizing the cost function,

$$C(\vec{n}, \vec{\theta}) = \|L^{ccd} - L^{model}\| \tag{13.29}$$

where $\vec{n}$ is the unknown refractive index vector; $\vec{\theta}$ is a vector containing all mirror rotations; L^{ccd} and L^{model} are smoothed CCD measurements and model prediction respectively

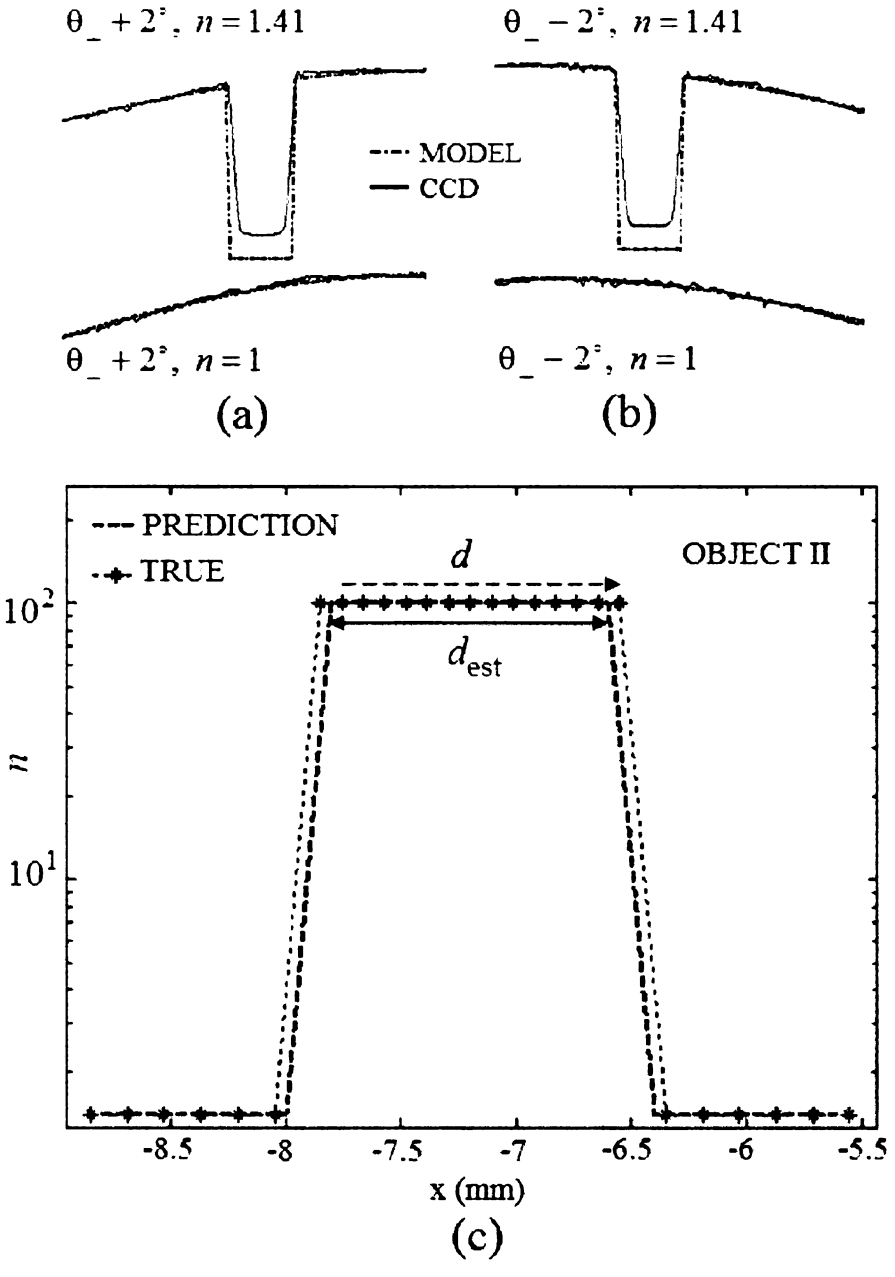

Figure 13.17. Comparison between ray tracing model and normalized CCD measurements of the plastic slab with Object II for $n_{est} = 1.41, d_{est} = 1.2mm$ (a) $\theta_\perp + 2°$ (b) $\theta_\perp - 2°$ (c) Estimated width profile for Object II.

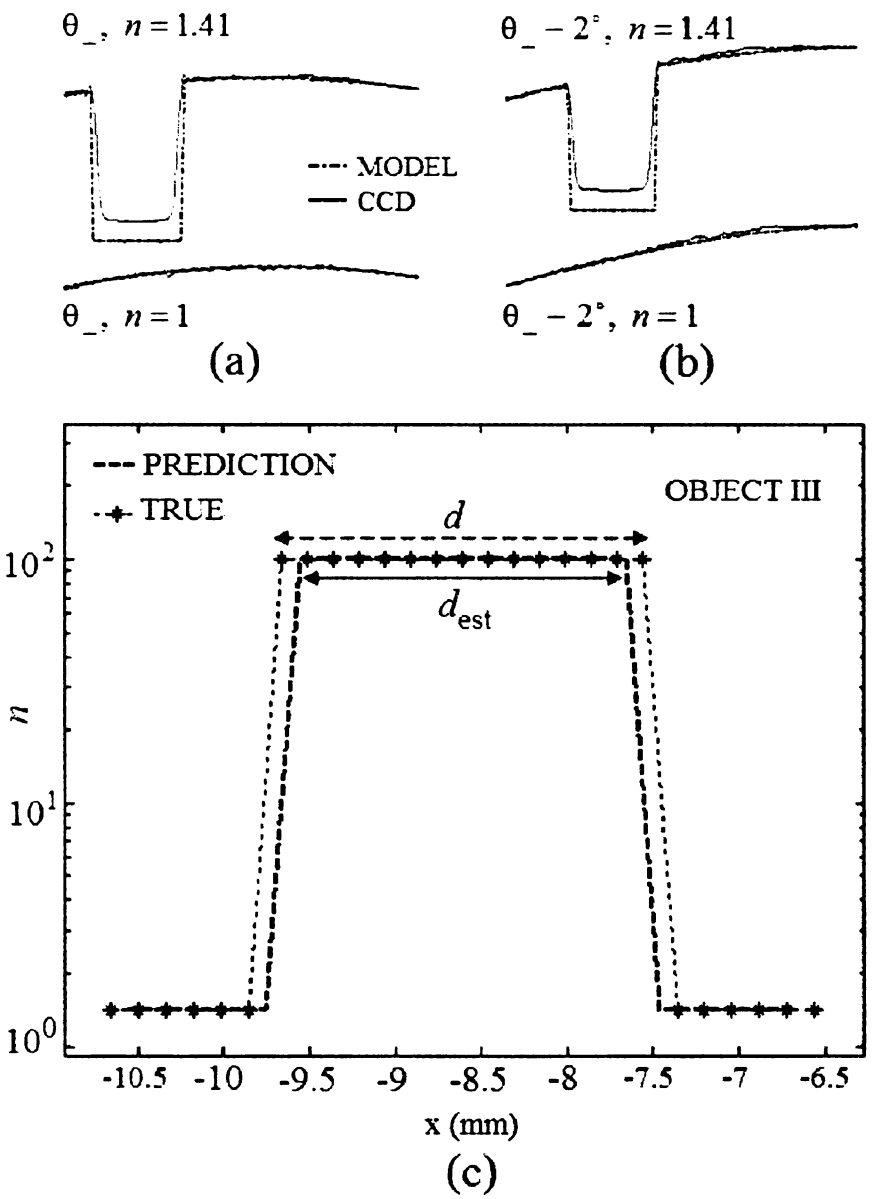

Figure 13.18. Comparison between ray tracing model and normalized CCD measurements of the plastic slab with Object III for $n_{est} = 1.41, d_{est} = 1.9mm$ (a) $\theta_{\perp}$ (b) $\theta_{\perp} - 2^{\circ}$ (c) Estimated width profile for Object III.

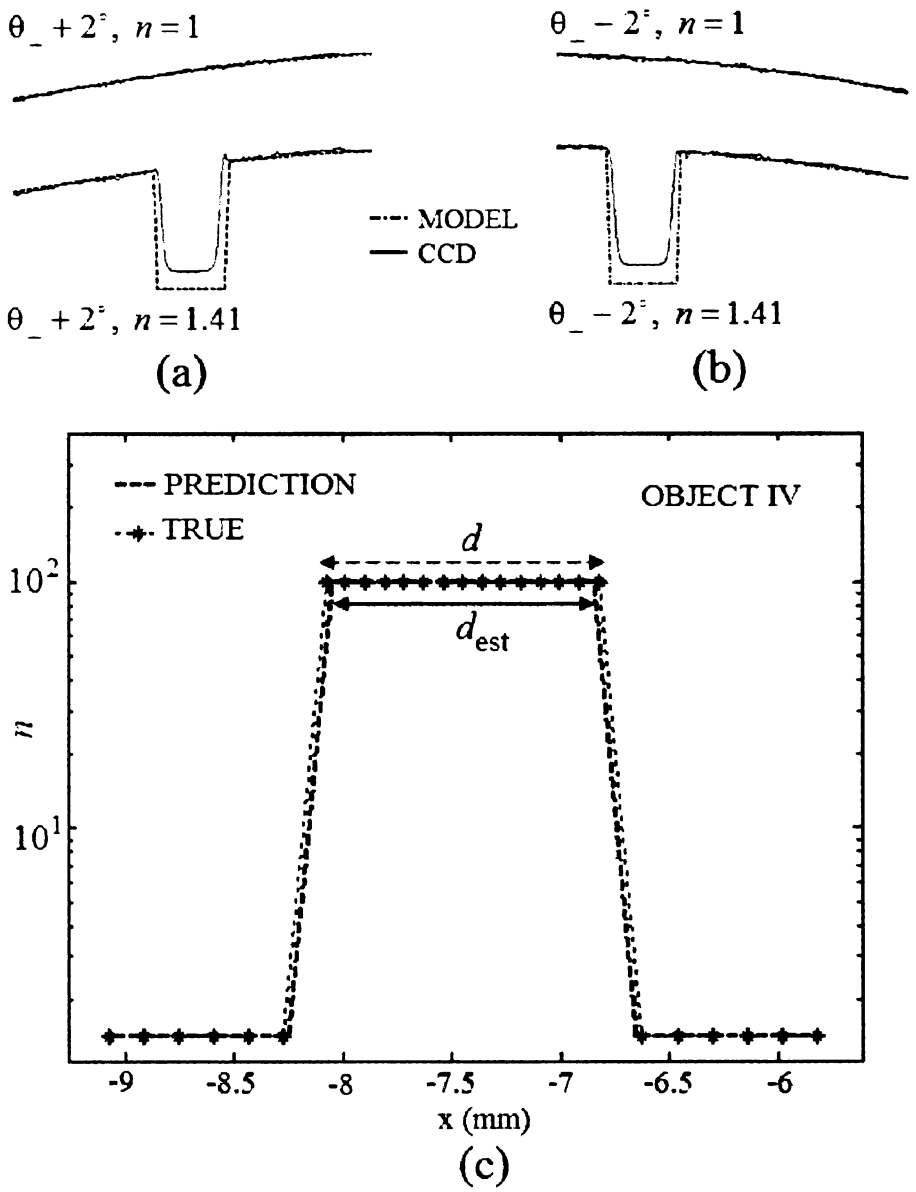

Figure 13.19. Comparison between ray tracing model and normalized CCD measurements of the plastic slab with Object IV for $n_{est} = 1.41, d_{est} = 1.2mm$ (a) $\theta_\perp + 2°$ (b) $\theta_\perp - 2°$ (c) Estimated width profile for Object IV.

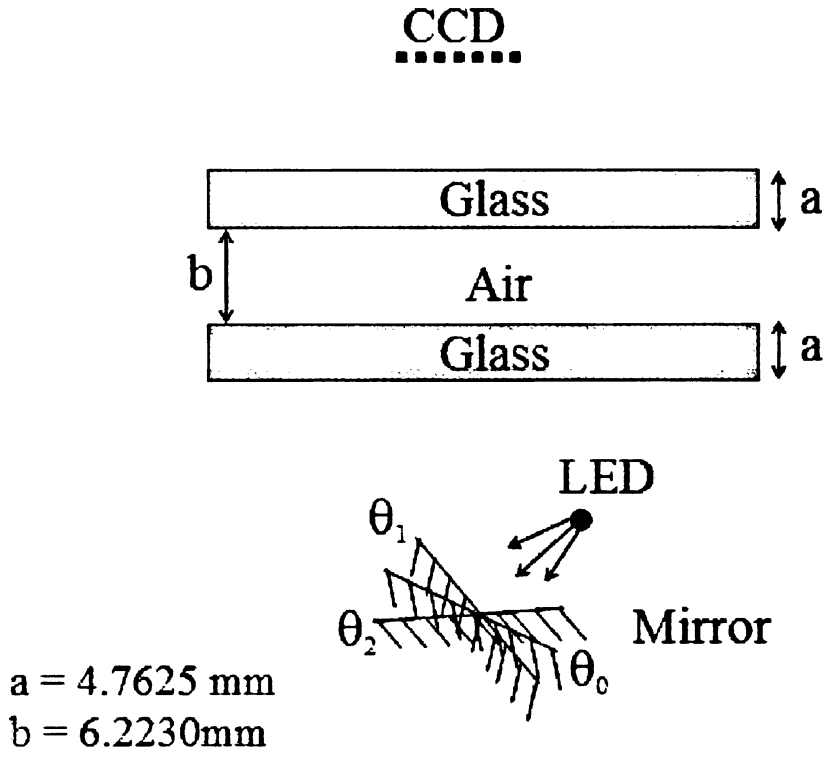

Figure 13.20. Illustration of experimental setup for layered medium.

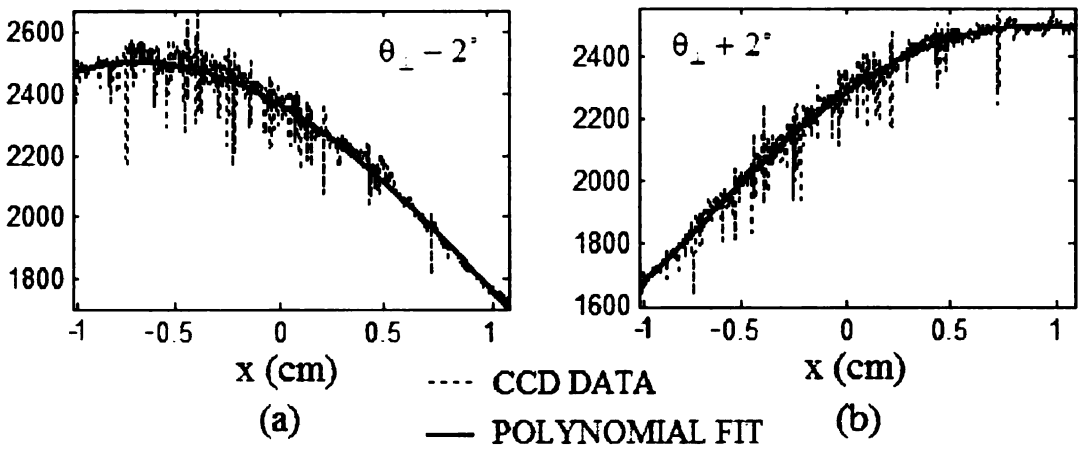

Figure 13.21. CCD measurements of layered medium for (a) $\theta_\perp - 2°$ (b) $\theta_\perp + 2°$ mirror rotations.

for $\vec{\theta}$. The multivariate unconstrained optimization in (13.29) is solved iteratively using gradient search technique. The refractive index vector that minimizes (13.29) is iteratively obtained using the update equation,

$$\vec{n}_t^{est} = \vec{n}_{t-1}^{est} - \lambda \Delta \vec{n}_{t-1}^{est} \tag{13.30}$$

In (13.30), $\Delta \vec{n}_{t-1}^{est} = \{\frac{dC}{d\vec{n}}\}$ is the gradient and $\lambda \in (0, 1]$ is the step length of gradient. The optimal gradient step length in (13.30) is obtained by solving,

$$\lambda_{opt} = arg\ min \lambda_i C(\vec{n}_{t-1}^{est} - \lambda_i \Delta \vec{n}_{t-1}^{est}, \vec{\theta}) \tag{13.31}$$

In ray tracing model, the gradient in (13.30) is constructed numerically using the central finite difference method,

$$\nabla C_{n_k} = \frac{1}{2\Delta n} \left[C(\vec{n} + \Delta \hat{e}_k, \vec{\theta}) - C(\vec{n} - \Delta \hat{e}_k, \vec{\theta}) \right], \quad k = 1, 2, ..., K \tag{13.32}$$

where $\hat{e}_k$ is the unit vector along k^{th} dimension. The iterative process was initiated with $n_k = 1.01, \forall k$ and equations (13.29)-(13.32) were solved until (13.29) is less than a

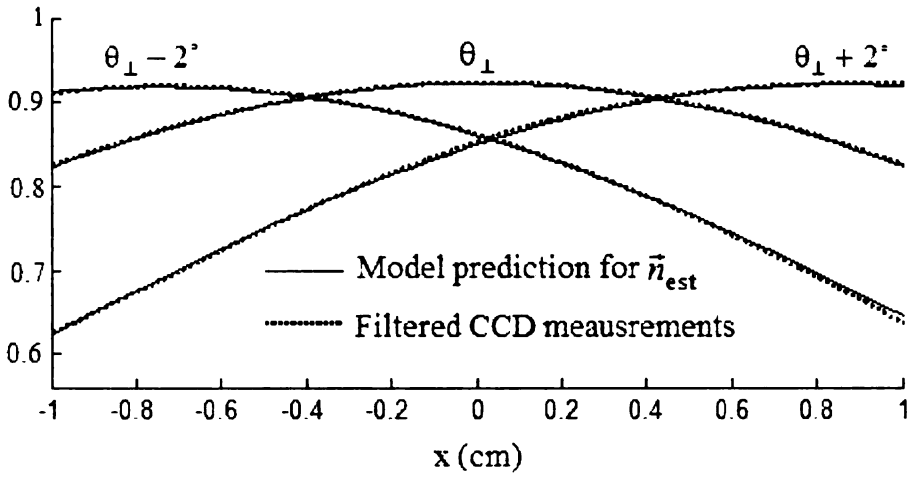

Figure 13.22. Comparison between filtered CCD measurements and ray tracing model for $\{n_1, n_2, n_3\}^{est}$.

predetermined threshold, δ_c. Figure Figure 13.22 shows the comparison between model and filtered CCD measurements for $\vec{n}^{est}$ that minimizes (13.29). Figures Figure 13.23 (a)-(b) shows the reconstructed 1D refractive index profile and reconstruction error respectively for the best estimate. The 1D profile of the layered medium is in good agreement with the true solution. In the iterative inversion process, the thickness of individual layer was used as a prior information and the estimates were constrained within [1, 1.9].

13.6 Discussions

The fundamental physics and mathematical principles of geometrical optics necessary to understand the experiments were covered in this chapter. The basics of ray tracing model and implementation of a recursive ray tracer module were also explained in brevity. The design and operation of the experimental setup and development of a calibration routine for source apodization gives insight into the complexities involved in the experimental setup. Comparison between the CCD measurements and ray tracing model for multiple mirror rotations validates the model and calibration procedure. The simple experimental results indicate the potential use of mirror in re-directing the incident electromagnetic radiations

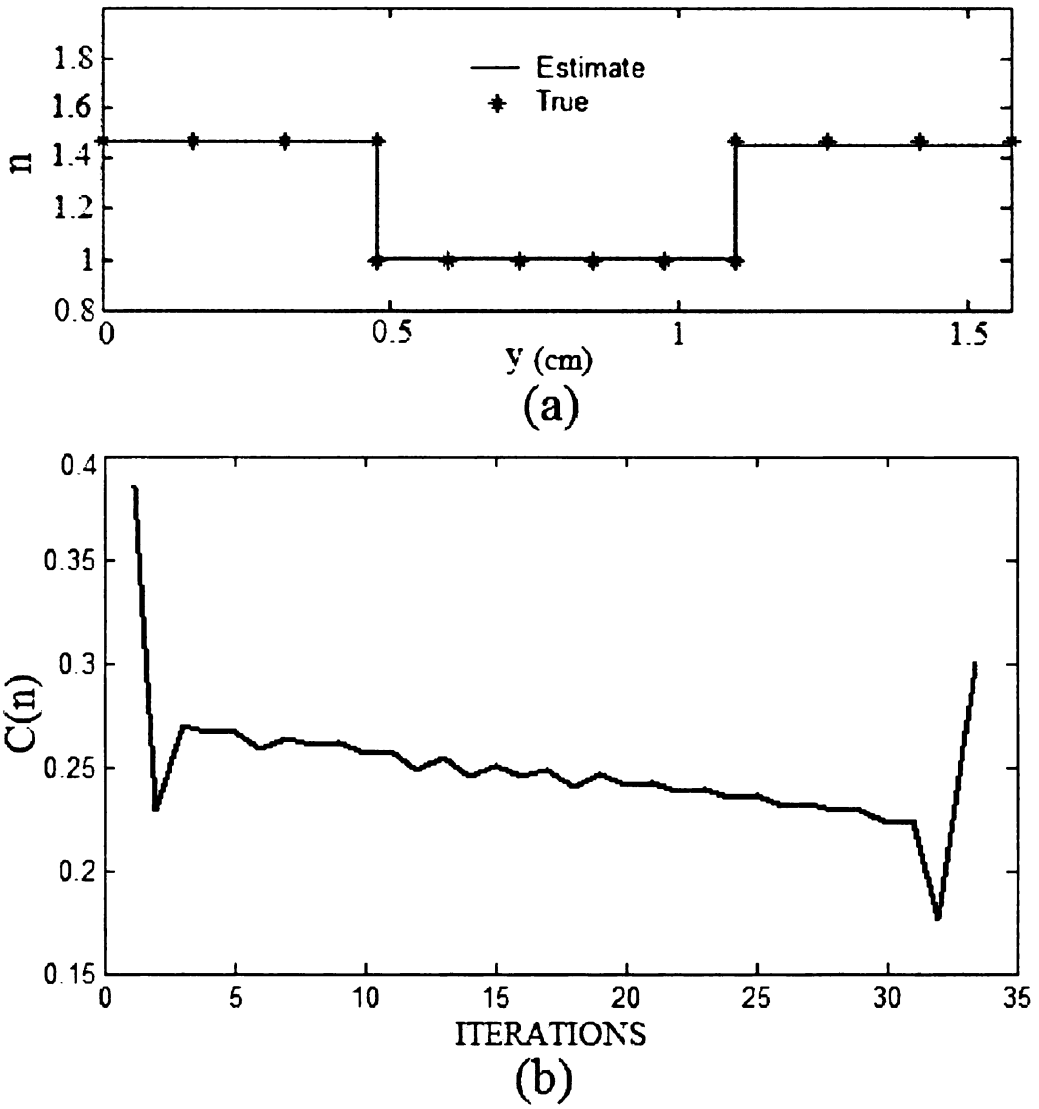

Figure 13.23. Inversion results (a) Reconstructed 1D refractive index profile (b) Reconstruction error.

for multi-view measurements of the object under inspection. Refractive index estimation of an object with unknown optical property using a single flat surface perfectly reflecting mirror and fixed source and detector demonstrate the feasibility of using mirror for material property inversion. The agreement between model and true solution for the 1D inverse problem indicate the robustness of the mirror based inversion technique to measurement and numerical errors. The proof of concept experimental and numerical simulations in the visible spectrum appear encouraging. The results also indicate the feasibility of extending the idea to develop alternate microwave tomography technique employing deformable mirror.

CHAPTER 14

SUMMARY

14.1 Concluding Remarks

A novel microwave technique employing adaptive optics for macro level biomedical imaging is presented in this thesis with an application for imaging and treating localized breast tumors in women. The imaging cum therapy technique employing active mirror is proposed as an alternate to the widely used mammography and radiation therapy that employs ionizing X-rays.

14.1.1 Microwave Breast Imaging

Mathematical theory, equations and fundamental principles governing the physics of the problem associated with microwave mirror based tomography are explained in chapters 4-7. Systematic procedures followed in the selection of optimal mirror shapes for multi-view data with minimal measurement redundancy are discussed in chapter 9 via 2D computer simulations. Mirror shapes that yield diversity in field measurements inside the imaging region are used for tomographic reconstruction of the dielectric breast tissue. The efficiency of mirror based tomography in improving the solution stability without the need to increase the number of receiver antennas was demonstrated using inhomogeneous two-dimensional breast models. Simulation results for heterogeneous breast models presented in chapter 10 appear promising and demonstrate the robustness of mirror based tomography technique to yield stable solution in the presence of additive random measurement noise.

Proof of concept simulations presented in chapter 13 using simple optical prototype indicate the ability of the mirror to acquire multi-view measurements to recover the material property. Preliminary results on refractive index estimation using optical experiments and numerical inversion based on ray tracing model for homogeneous clear plastic and Pyrex glass slabs demonstrate feasibility of the proposed deformable mirror tomography technique to provide multi-view measurements for reliable reconstruction without the need to rotate the object or source/detector arrangement.

14.1.2 Microwave Thermal Therapy

A microwave hyperthermia technique employing dual membrane mirrors is proposed in chapter 11 to treat localized breast tumors. The proposed deformable mirror hyperthermia assembly with fixed microwave sources is a potential alternative to contemporary methods employing phase-focused, phase-modulated arrays and multiple discrete antennas which require phase and amplitude optimization techniques for field focusing. System functionality, theory, field equations and bio-heat transfer model are presented in chapter 11 and the computational feasibility study using mathematical breast models indicate the ability of dual mirror therapy technique to achieve selective tumor temperature elevation. The continuously deformable mirror can be viewed as a flexible conformable antenna array that can scan the breast tissue more effectively and preferentially deposit EM energy at the tumor site. Unlike phased array and phased focus hyperthermia applicators, the proposed dual mirror technique does not require multiple antennas for tumor temperature elevation. Extended simulation studies on dual mirror model for noninvasive tumor ablation in chapter 11 indicate the prospects of deformable mirror setup as a potential cancer ablation tool.

Computer simulations of the dual mirror therapy technique evaluated using MRI derived 2D breast data of women reported in chapter 12 are encouraging. Computational studies on MRI data include fibroglandular, heterogeneous and fatty breast data of women belonging to different age groups with different clinical history. Ablation studies on MR breast data reveal the potential of deformable mirror for use in noninvasive ablation of breast tumors.

14.2 Thesis Contribution

The contribution of this thesis is in the development and numerical evaluation of an alternate imaging and treatment technique for breast cancer that has

- low health risk
- is sensitive to malignant tumors
- detects breast cancer at early stage

- is noninvasive and simple to perform
- minimal discomfort to women
- provides consistent and easy to interpret results

The deformable mirror tomography cum therapy technique proposed in this thesis aims to comply to the above listed capabilities of an ideal breast imaging system in that it employs microwave radiation which

- is nonradioactive and hence safe to use
- possess significant dielectric contrast between malignant and benign breast tissues in low giga hertz frequencies
- easily penetrates the breast comprising predominantly of fat
- does not require painful breast compression
- capable of yielding consistent quantitative results

Unlike contemporary microwave imaging and hyperthermia techniques, the proposed deformable mirror technique aims to meet the requirements of an efficient breast imaging cum therapy system. The novelty of the proposed technique lies in the use of adaptive optics to accomplish the task of imaging and treating localized breast tumors. The salient features of the deformable mirror microwave tomography technique for breast imaging model include

- capability of adaptive mirror to deform its shape to steer the EM field at different angles
- ability to provide information rich multi-view measurements for reliable tomographic reconstruction using multiple mirror deformations without the need for
    - source-detector or object rotation and
    - multiple transceivers surrounding the object

- reduced microwave system complexity due to the use of single transmitter and multiple receivers leading to
    - reduced computational complexities as there is no need for antenna compensation routines to account for secondary field induced on neighboring inactive transceivers and cross talk minimization, and
    - lack of antenna switching routines as in conventional tomography
- potential to yield a multitude of measurements for imaging without the need for an increase in the number of receivers which is achieved by adaptively changing the mirror deformation

The potential advantages of the dual mirror therapy technique proposed for hyperthermia and ablation include

- ability of deformable mirror to focus EM radiation at desired spatial location
- the large mirror surface ensures efficient field focusing for selective tumor temperature elevation
- accomplishes efficient field focusing using single transmitter unlike multiple antennas used in conventional hyperthermia techniques
- offers minimal collateral damage to the surrounding benign tissue
- ability to deliver higher thermal dosage for tumor ablation

Although the thesis describes the application of deformable mirror technique for analyzing breast tissue,

- The imaging technique can be employed for evaluating other non- and poorly conducting structures.
- For instance, the therapy technique could be employed in neutering of pets in veterinary medicine and in the treatment of prostate cancer.

- Besides microwaves, the deformable mirror tomography system can be extended for other penetrating radiations such as Terahertz and optics.
- One key and immediate application of this tomography technique is in Terahertz imaging. Terahertz radiations are non-ionizing radiations with very high resolution as compared to microwaves and ultrasound and are reflected by metallic objects.
- There is a greater potential in using deformable mirror tomography for Terahertz radiations as an alternate for the ionizing X-rays widely used in material and medical diagnosis and homeland security applications.

14.3 Future Work

A systematic computational study is presented in this thesis to evaluate the feasibility of a novel tomography cum therapy technique with emphasis on breast cancer. The theory and experimental setup modeled in the feasibility study and the outcome of computer simulations play a key role in the implementation of a microwave prototype system. Several challenges lies ahead in realizing the proposed mirror based imaging and therapy technique.

The first and foremost task in future would be to test, understand and evaluate the limitations of continuously deformable mirrors available in market. The challenges associated with the deformable mirror include

- choice of actuator circuit that yield maximum amount of deflection
- limitations of feedback control for actuator potential distribution
- real time correction for deviation in deformation
- fabrication of larger dimension mirrors
- with thin metal coating to reflect microwaves

Continuously deformable mirrors are widely used in real time applications for wavefront and defocus correction and in optical communications, projection displays, retinal and intravenous imaging applications where the mirror deflection is controlled adaptively in feedback

mode. Thus, issues related to real-time control of mirror deformation are well studied and documented. With advance in semiconductor fabrication larger mirrors can be custom manufactured. Deformable mirror with thin aluminum coating used in optics to reflect/direct light implies the availability of metal coated deformable mirror for microwaves.

Besides understanding the functionality and characteristics of deformable mirror, other challenges include developing antenna/system calibration and synchronization routines for data acquisition, data compensation and numerical inversion. Prior to experimentation inside therapy tank, free space measurements of the field pattern maintained by deformable mirror should be acquired to characterize the deformable mirror assembly. Experiments inside therapy tank requires water tight container with a window for mirror-transmitter assembly. Microwaves reflected by the mirror can penetrate through the low-dielectric constant window and propagate into the therapy tank containing the imaging object. The choice of low-dielectric constant material and field emitted by mirror-transmitter assembly inside the therapy tank require thorough experimental analysis. Robust and computationally fast numerical inversion routines need to be developed.

Lessons learnt in controlling and deploying the deformable mirror inside therapy tank are directly applicable in the design and implementation of the therapy setup. For therapy, field focusing capability of the mirror-transmitter assembly should be evaluated via experiments. To begin with thermal elevation due to field focusing can be evaluated using thermocouples. System optimization for efficient performance will require iterative use of both computational model and experiments on phantom objects.

BIBLIOGRAPHY

BIBLIOGRAPHY

[1] American Cancer Society, "Cancer Facts & Figures 2005," Atlanta, GA.

[2] American Cancer Society, "Cancer Facts & Figures 2004," Atlanta, GA.

[3] American Cancer Society, "Cancer Facts & Figures - 1997," Atlanta, GA.

[4] American Cancer Society, "Cancer Facts & Figures - 1998," Atlanta, GA.

[5] American Cancer Society, "Cancer Facts & Figures - 1999," Atlanta, GA.

[6] American Cancer Society, "Cancer Facts & Figures 2000," Atlanta, GA.

[7] American Cancer Society, "Cancer Facts & Figures 2001," Atlanta, GA.

[8] American Cancer Society, "Cancer Facts & Figures 2002," Atlanta, GA.

[9] American Cancer Society, "Cancer Facts & Figures 2003," Atlanta, GA.

[10] American Cancer Society, "Breast Cancer Facts & Figures 2005-2006," Atlanta, GA.

[11] Manfreid Sabel and H. Aichinger, "Recent developments in breast imaging," Phys. Med. Biol., vol. 41, pp. 315-368, 1996.

[12] http://www.hologic.com/lc/bhnbc.htm

[13] Ismail Jatoi, Lippincott Williams and Wilkins, editors, "Manual of Breast Diseases," Philadelphia, 2001.

[14] G. Svane, E. J. Potchen, A. Sierra and E. Azavedo, "Screening Mammography Breast Cancer Diagnosis in Asymptomatic Women," Mosby - Year Book, Inc., Missouri, 1993.

[15] S. E. Singletary and G. L. Robb, "Advanced Therapy of Breast Disease," B. C. Decker Inc., 2000.

[16] Michel Gautherie, Ernest Albert, and Louis Keith, editors, "Thermal Assessment of Breast health," MTP Press Limited, Boston, 1984.

[17] P. T. Huynh, A. M. Jarolimek, and S. Daye, "The false-negative mammogram," Radiographics, vol. 18, pp. 11371154, 1998.

[18] Valerie P. Jackson, "The current role of ultrasonography in breast imaging," Radiologic Clinics of North Amer., Vol. 33, no. 6, pp. 1161-1170, Nov 1995.

[19] Dirk Grosenick, Heidrun Wabnitz, Herbert H. Rinneberg, K. Thomas Moesta, and Peter M. Schlag, "Development of a time-domain optical mammograph and first in vivo applications," Applied Optics, vol. 38, no. 13, pp. 2927-2943, May 1999.

[20] Troy O. McBride, Brian W. Pogue, Ellen D. Gerety, Steven B. Poplack, Ulf L. Osterberg, and Keith D. Paulsen, "Spectroscopic diffuse optical tomography for the quantitative assessment of hemoglobin concentration and oxygen saturation in breast tissue," vol. 38, no. 25, pp. 5480-5490, September 1999.

[21] V. Cherepenin, A. Karpov, A. Korjenevsky, V. Kornienko, Y. Kultiasov, M. Ochapkin, O. Trochanova and D. Meister, "Three-dimensional EIT imaging of breast tissues: system design and clinical testing," IEEE Trans. Medical Imaging, vol. 21, no. 6, pp. 662-667, 2002.

[22] Zou Y, Guo Z, "A review of electrical impedance techniques for breast cancer detection," Med Eng Phys., vol. 25, no.2, pp. 79-90, March 2003.

[23] Donald B Plewes, Jonathan Bishop, Abbas Samani and Justin Sciarretta, "Visualization and quantification of breast cancer biomechanical properties with magnetic resonance elastography," Phys. Med. Biol., vol. 45, pp. 15911610, 2000.

[24] McKnight A L, Kugel J L, Rossman P J, Manduca A, Hartmann L C, Ehman R L, "MR elastography of breast cancer: preliminary results," American J. Roentgenology, vol. 178, no. 6, pp. 1411-7, June 2002.

[25] E.C. Fear, S. C. Hagness, P. M. Meaney, M. Okoniewski, M. A. Stuchly, "Enhancing Breast Tumor Detection with Near-Field Imaging," IEEE Microwave Magazine, March 2002, pp. 48-56.

[26] Aruthur W. Guy, "History of Biological Effects and Medical Applications of Microwave Energy," IEEE Trans. MTT, Vol. 32, No. 9, September 1984, pp. 1182-1200.

[27] Constantine A. B., "Advanced engineering electromagnetics," Wiley Publcations, New York, 1989.

[28] Edward J. Rothwell and Michael J. Cloud, "Electromagnetics," CRC Press, Boca Raton, 2001.

[29] Herman P. Schwan, "Interaction of Microwave and Radio Frequency radiation with Biological Systems," IEEE Trans. MTT, vol. 19, no.2, pp. 146-152, February 1971.

[30] K. R. Foster and H. P. Schwan, "Dielectric properties of tissues and biological materials: A critical review," CRC Critical Reviews in Biomed. Eng., vol. 17, no. 1, pp. 25-104, 1989.

[31] H. N. Kirtikos, K. R. Foster and H. P. Schwan, "Effect of Surface Cooling and Blood Flow on the Electromagnetic heating of Tissue," IEEE Microwave Symposium, San Diego, CA, June 1977.

[32] Hiee Hinrikus, Jaanus Lass and Jevgeni and Riipulk, "The sensitivity of living tissue to microwave field," Proc. 20th Annual Int. Conf. IEEE Eng. in Med. Biol. Soc., vol. 20, no. 6, pp. 3249-3252, 1998.

[33] Maria A. Stuchly, "Electromagnetic fields and health protecting against harm while harnessing the benefits," IEEE Potentials, pp. 34-39, April 1993.

[34] Itsuo Yamaura, "Measurement of 1.8-2.7 GHz Microwave Attenuation in the Human Torso," IEEE Trans. MTT, vol. 25, no. 8, pp. 707-710, August 1977.

[35] Wissler, Eugene H. "Pennes 1948 paper revisited," J. Appl. Physiol., vol. 85, no. 1, pp. 3541, 1998.

[36] Alavaro Augusto A. de Salles, "Biological Effects of Microwave and RF," SBMO/IEEE MTT-S IMOCC Proc., pp. 51-56, 1999.

[37] Michal Okoniewski, Maria A. Stuchly, "A study of the Handset Antenna and Human Body Interaction," IEEE Trans. MTT, vol. 44, no. 10, pp. 1855-1864, October 1996.

[38] Ronald J. Spiegel, "A Review of Numerical Models for Predicting the Energy Deposition and Resultant Thermal Resposnce of Humans Exposed to Electromagnetic Fields," IEEE Trans. MTT, vol. 32, no. 8, pp. 730-746, August 1984.

[39] I. Chatterjee, O. P. Gandhi and M. J. Hagmann, "Numerical and Experimental Results for Near Field Electromagnetic Absorption in Man," IEEE Trans. MTT, vol. 30, no. 11, pp. 2000-2005, November 1982.

[40] C Gabriel, S Gabriely and E Corthout, "The dielectric properties of biological tissues: I. Literature survey," Phys. Med. Biol. 41, pp. 22312249, 1996.

[41] S Gabriely, R W Lau and C Gabriel, "The dielectric properties of biological tissues: II. Measurements in the frequency range 10 Hz to 20 GHz," Phys. Med. Biol. 41, pp. 22512269, 1996.

[42] S Gabriely, R W Lau and C Gabriel, "The dielectric properties of biological tissues: III. Parametric models for the dielectric spectrum of tissues," Phys. Med. Biol. 41, pp. 22712293, 1996.

[43] Fred Sterzer, "Microwave Medical Devices," IEEE Microwave Magazine, pp. 65-70, March 2002.

[44] Arye Rosen, Maria A. Stuchly and Andre Vander Vorst, "Applications of RF Microwaves in Medicine," IEEE Trans. MTT, vol. 50, no. 3, pp. 963-974, March 2002.

[45] S. S. Chaudhary, R. K Mishra, arvind Swarup and Joy Thomas, "Dielectric Properties of Normal and Malignant Human Breast Tissues at Radiowave & Microwave Frequencies," Indian J. Biochem. BioPhys., Vol. 21, pp. 76-79, February 1984.

[46] A.J. Surowiec, S.S. Stuchly, J.R. Barr, and A. Swarup, "Dielectric properties of breast carcinoma and the surrounding tissues," IEEE Trans. Biomed. Eng., vol. 35, pp. 257-263, Apr. 1988.

[47] William T. Joines, Yang Zhang, Chenxing Li and Randy L. Jirtle, "The measured electrical properties of normal and malignant human tissues from 50 to 900 MHz," Med. Phys., Vol. 21, pp. 547-550, April 1994.

[48] John G. Proakis and Dimitris G. Manolakis, "Digital signal processing: principles, algorithms, and applications," 3rd edition, Prentice-Hall, NJ, USA 1996.

[49] Roger F. Harrington, "Time-Harmonic Electromagnetic Fields," Wiley-IEEE Press, 2001.

[50] Jianming Jin, "The Finite Element Methods in Electromagnetics," 2nd edition, John Wiley & Sons, Inc., New York 2001.

[51] Peterson, Andrew; Ray, Scott; Mitra, Raj, "Computational Methods For Electromagnetics," Oxford University Press, 1998.

[52] Korada Umashankar and Allen Taflove, "Computational Electromagnetics," Artech House, March 1993.

[53] K. L. Carr, "Microwave radiometry: its importance to the detection of cancer," IEEE Trans. Microwave Theory Tech., vol. 37, pp. 1862-1869, Dec. 1989.

[54] B. Bocquet, J. C. Van de Velde, A. Mamouni, Y. Leroy, G. Giaux, J. Delannoy, and D. Del Valee, "Microwave radiometric imaging at 3 GHz for the exploration of breast tumors," IEEE Trans. Microwave Theory Tech., vol. 38, pp. 791-793, June 1990.

[55] R. A. Kruger, K. K. Kopecky, A. M Aisen, D. R. Reinecke, G. A. Kruger, and W.L. Kiser, "Thermoacoustic CT with radio waves: A medical imaging paradigm," Radiology, vol. 211, pp. 275-278, 1999.

[56] A. C. Kak and M. Slaney, "Principles of Computerized Tomographic Imaging," IEEE Press, 1988.

[57] J. Radon, "Uber due bestimmung von funktionen durch ihre intergralwette langs gewisser mannigfaltigkeiten," Ber. Verb. Saechs. Akad. Wiss., Leipzig. Math. Phys. Kl., 69, pp. 262-277, 1917.

[58] G. N. Hounsfield, "A method of and apparatus for examination of a body by radiation such as x-ray or gamma radiation," Patent Specification 1283915, The Patent Office, London, England, 1972.

[59] G. N. Hounsfield, "Computerized transverse axial scanning tomography: Part 1, description of the system," British J. radiol., 46, pp. 1015-1022, 1973.

[60] A. M. Cormack, "Representation of a function by its line integrals, with some radiologicl applications," J. Appl. Phys., 34, pp.2722-2727, 1963.

[61] G. J. Vanderplaats, "Medical X-ray Techniques in Diagnostic Radiology," Fourth edition, Martinus Nijhoff Publishers, The Netherlands, 1980.

[62] Andrew R. Webb, "Introduction to biomedical imaging," Wiley, Hoboken, New Jersey, 2003.

[63] R. Gordon, R. Bender, and G. T. Herman, "Algebraic reconstruction techniques (ART) for three dimensional electron microscopy and X-ray photography," J.Theor. Biol. 29, pp. 471-481, 1970.

[64] G. T. Herman and A. Lent, "Iterative reconstruction algorithms," Comput. Biol. Med. 6, pp. 273-294, 1976.

[65] G. N. Ramachandran and A. V. Lakshminarayanan, "Three dimensional reconstructions from radiographs and electron micrographs: Application of convolution instead of Fourier transforms," Proc. Nat. Acad. Sci., 68, pp. 2236-2240, 1971.

[66] L. A. Shepp and B. F. Logan, "The Fourier reconstruction of a head section," IEEE Trans. Nucl. Sci., NS-21, pp. 21-43, 1974.

[67] X-ray book on CT generations.

[68] G. T. Herman, "Algebraic Reconstruction Techniques Can Be Made Computaionally Efficient," IEEE Trans. Med. Img., vol. 12, n0. 3, pp. 600-609, September, 1993.

[69] Huaiqun Guan and Richard Gordon, "Computed tomography using algebraic reconstruction techniques (ART) with different projection access schemes: a comparison study under practical situations," Phys. Med. Biol., vol. 41, pp. 1727-1743, 1996.

[70] L. Wang, "Cross-section reconstruction with a fan-beam scanning geometry," IEEE Trans. Comput., vol. C-26, pp. 264-268, March 1977.

[71] R. M. Lewitt, "Ultra-fast convolution approximation for computerized tomography," IEEE Trans. Nucl. Sci., vol. NS-26, pp. 2678-2681, 1979.

[72] H. Stark, J. W. Woods, I. Paul, and R. Hingorani, "Direct Fourier reconstruction in computer tomography," IEEE Trans. Acoust. Speech Signal Processing, vol. ASSP-29, pp. 237-244, 1981.

[73] W. C. Chew, Waves and Fields in Inhomogeneous Media, Van Nostrand Reinhold, New York, 1990.

[74] A. J. Devaney and George C. Sherman, "Nonuniqueness in Inverse Source and Scattering Problems," IEEE Trans. Ant. Propag., Vol. 30, pp. 1034-1037, September 1982.

[75] Norman Bleistein and Jack K. Cohen, "Nonuniqueness in the inverse source problems in acoustics and electromagnetics," J. Math. Phys. Vol. 18, pp. 194-201, February 1997.

[76] Mario Bertero, Patrizia Boccaci, "Introduction to Inverse Problems in Imaging," Institute of Physics Publishing, 1998.

[77] R. K. Mueller, M. Kaveh, and G. Wade, "Reconstructive tomography and applications to ultrasonics," Proc. IEEE, vol. 67, pp. 567-587, 1979.

[78] L. A. Chemov, "Wave Propagation in a Random Medium," New York, McGraw-Hill, 1960.

[79] E. Wolf, "Three-dimensional structure determination of semitransparent objects from holographic data," Opt. Commun., vol. 1, pp. 153-156, 1969.

[80] Tah-Hsiung Chu and Ken-Yu Lee, "Wide-Band Microwave Diffraction Tomography Under Born Approximation," IEEE Trans. Ant. Prop., vol. 37, no. 4, pp. 515-519, April 1989.

[81] G. A. Tsihrintzis and and A. J. Devaney, "Higher-order(Nonlinear) Diffraction Tomography," IEEE ICASSP, SanDiego, CA. USA, 2000.

[82] Y. M. Wang and W. C. Chew, "An Iterative Solution of the Two-Dimensional Electromagnetic Inverse Scattering Problem," Int. J. Ing. Sci., col. 1, pp. 100-108, 1989.

[83] W. C. Chew, W. H. Weedon, J. H. Lin, Y. M. Wang and M. Moghaddam, "Nonlinear Diffraction Tomography - The use of Inverse Scattering for Imaging," IEEE 27th Asilomar Conference on Signals, Systems and Computers, pp. 120-129, 1993.

[84] W. C. Chew and Y. M. Wang, "Reconstruction of Two-Dimensional Permittivity Distribution Using the Distorted Born Iterative Method," IEEE Trans. Med. Imag., vol. 9, no. 2, pp. 218-225, June 1990.

[85] A. Ishimaru, "Wave Propagation and Scattering in Random Media," New York, Academic Press, 1978.

[86] A. J. Devaney, "A computer simulation study of diffraction tomography," IEEE Trans. Biomed. Eng., vol. BME-30, pp. 377-386, July 1983.

[87] Hsueh-Jyh Li, Nabil Farhat, Yuhsyen and Charles L. Werner, "Image Understanding and Interpretation in Microwave Diversity Imaging," IEEE Trans. Ant. Prop., vol. 37, no. 8, pp. 1048-1057, August 1989.

[88] M. Azimi and A. C. Kak, "Distortion in diffraction imaging caused by multiple scattering," IEEE Trans. Med. Imaging, vol. MI-Z, pp. 176-195, Dec. 1983.

[89] M. Kaveh and M. Soumekh, "Computer-assisted diffraction tomography in Image Recovery, Theory and Applications," H. Stark, Ed. New York, Academic Press, 1986.

[90] M. Slaney and A. C. Kak, "Diffraction tomography," Proc. SPIE, vol. 413, pp. 2-19, Apr. 1983.

[91] Tah-Hsiung and Nabil H. Farhat, "Frequency-Swept Microwave Imaging of Dielectric Object," IEEE Trans. MTT, vol. 36, no. 3, pp. 489-493, March 1988.

[92] M. Slaney, A. C. Kak, and L. E. Larsen, "Limitations of imaging with first order diffraction tomography," IEEE Trans. Microwave Theory Tech., vol. MTT-32, pp. 860-873, Aug. 1984.

[93] A. E. Bulyshev, A. E. Souvorov, S. Y. Semenov, R. H. Svenson and G. P. Tatsis, "A Computer Simulation of Three-Dimensional Microwave Tomography," Proc. IEEE/EMBS, Oct. 30-Nov. 2, Chicago, IL. USA, 1997.

[94] A. E. Souvorov, A. E. Bulyshev, S. Y. Semenov, R. H. Svenson, A. G. Nazarov, Y. E. Sizov and G. P. Tatsis, "Microwave Tomography : A two-dimensional Newton Iterative Scheme," IEEE Trans. MTT, vol. 46, pp. 1654-1659, November 1998.

[95] Lawrence Carin, Jeffrey Sichina and James F. Harvey, "Microwave Underground Propagation and Detection," IEEE Trans. MTT, vol. 50, no. 3, pp. 945-952, March 2002.

[96] Keiichi Ueno, Noriyoshi Osumi and Takunori Mashikko, "An Underground Object Imaging System with Computerized Reconstruction," IEEE ICASSP, Tokyo, 1986.

[97] Daniels D. J., Gunton D. J. and Scott H. F., "Introduction to subsurface radar," IEE Proc., Part F, vol. 135, no. 4, pp. 278-284, 1988.

[98] Mast J. E, Lee H., Murtha J. P., "Application of microwave pulse-echo radar imaging to the nondestructive evaluation of buildings," Int J. Imag. Syst. Tech., vol. 4, pp. 164169, 1992.

[99] Michael Chang, Peter Chou and Hua Lee, "Tomographic Microwave Imaging for Nondestructive Evaluation and Object Recognition of Civil Structures and Materials," IEEE Proc. ASILOMAR-29, pp. 1061-1065, 1996.

[100] Pieraccini M, Luzi G, Mecatti D, Noferini L, Atzeni C., "A microwave radar technique for dynamic testing of large structures," IEEE Trans. Microwave Theory Tech, vol.51, pp.16031609, 2003.

[101] Kim Y. J., Jofre L., Flaviis D. F., Feng Q. M., "Microwave reflection tomographic array for damage detection of civil structures," IEEE Trans. Antennas Propag., vol. 51, pp. 3022-3032, 2003.

[102] E. C. Fear, Xu Li, Susan C. Hagness and Maria Stuchly, "Confocal Microwave Imaging for Breast Cancer Detection: Localization of Tumors in Three Dimensions," IEEE Trans. Biomed. Imag., vol. 49, no. 8, pp. 812-821, August 2002.

[103] T. C. Guo and W. W. Guo, "Computation of electromagnetic wave scattering from an arbitrary three-dimensional inhomogeneous dielectric object," IEEE Trans. Magn., vol. 25, pp. 2872-2874, 1989.

[104] Nadine Joachimowicz, Christian Pichot and Jean-Paul Hugonin, "Inverse Scattering: An Iterative Numerical Method for Electromagnetic Imaging," IEEE Trans. Ant. Prop., Vol. 39, No. 12, pp. 1742-1752, December 1991.

[105] Salvatore Caorsi, Gian Luigi Gragnani, Mattea Pastorino, "A Multiview Microwave Imaging Syste, for Two-Dimensional Penetrable Objects," IEEE Trans. Micro. Theo. Techn. Vol. 39, pp. 845-851, May 1991.

[106] Salvatore Caorsi, Gian Luigi Gragnani, Mattea Pastorino, "Reconstruction of Dielectric Permittivity Distributions in Arbitrary 2-D Inhomogeneous Biological Bodies by a Multiview Microwave Numerical Method," IEEE Trans. Med. Imag., vol. 12, no. 2, pp. 232-239, June 1993.

[107] Meaney P. M, Paulsen K. D, Hartov A., Crane R. K., "An active microwave imaging system for reconstruction of 2-D electrical property distributions," IEEE Trans. Biomed. Eng., vol. 42, pp. 1017-1026, 1995.

[108] Paulsen K. D, Meaney P. M., Moskowitz M. J. and Sullivan, Jr. J. M., "A dual mesh scheme for finite element based reconstruction algorithms," IEEE Trans. on Med. Imag., vol. 14, pp. 504-514, 1995.

[109] Meaney P. M, Paulsen K. D and Ryan T. P., "Two-dimensional hybrid element image reconstruction for TM illumination," IEEE Trans. Ant. and Prop., vol. 43, pp. 239-247, 1995.

[110] Meaney P. M, Paulsen K. D and Chang J. T., "Near-field microwave imaging of biologically based materials using a monopole transceiver system," IEEE Trans. on Microwave Theor. and Tech., vol. 46, pp.31-45, 1998.

[111] S. Y. Semenov, R. H. Svenson, A. E. Bulyshev, A. E. Souvorov, V. Y. Borisov, Y. Sizov, A. N. Starostin, K. R. Dezern, G. P. Tatsis and V. Y. Baranov, "Microwave Tomography: Two-Dimensional System for Biological Imaging," IEEE Trans. Biomed. Imag., vol. 43, no. 9, pp. 869-877, September 1996.

[112] Ann Franchois and Christian Pichot, "Microwave Imaging - Complex Permittivity Reconstruction with a Levenberg-Marquardt Method," IEEE trans. Ant. Propag., vol. 45, no. 2, pp. 203-215, February 1997.

[113] I. T. Rekanos and T. D. Tsiboukis, "A combined finite elementConjugate gradient spatial method for the reconstruction of unknown scatterer profiles," IEEE Trans. Magn., vol. 34, pp. 28292832, Sept. 1998.

[114] A.Joisel, J.Mallorqui, A.Broquetas, J.-M.Geffrin, N.Joachimowicz, M.Vall-Lossera, L.Jofre, J-Ch.Bolomey, "Microwave Imaging Techniques for Biomedical Applications," Proc. IMTC/99, Special Session on Microwave Imaging, Venice, Italy, May 1999.

[115] Dun Li, Paul M. Meaney and Keith D. Paulsen, "Conformal Microwave Imaging for Breast Cancer Detection," IEEE Trans. Micro. Wave. Theo. Techn., Vol. 51, no. 4, pp. 1179-1186, April 2003.

[116] J. W. Hardy, "Active Optics: A New Technology for the Control of Light," Proc. IEEE, vol. 66, pp. 651, 1978.

[117] J. W. Hardy, "Adaptive Optics - a progress review," Proc. SPIE, vol. 1542, pp. 2-17, 1991.

[118] R.K. Tyson, "Handbook on adaptive optics," New York, Marcel Dekker, 2000.

[119] A.C. Claus, "On Amrchimedes' burning glass," Appl. Opt., vol. 12, p. A14, 1973.

[120] B. Hulburd and D. Sandler, "Segmented mirrors for atmospheric compensation," Opt. Eng., vol. 29, no. 10, pp. 11861190, 1990.

[121] J. P. Chevillard, P. Connes, M. Cuisenier, J. Friteau and C. Mailot, "Near infrared astronomical light collector," Appl. Opt., vol. 16, pp. 1817-1833, 1977.

[122] S. Timoshenko and S. Woinowsky-Krieger, "Theory of plates and shells," McGraw-hill, 1959.

[123] J.M. Younse, "Mirrors on a chip," IEEE spectrum, vol. 30, 11, pp.27-31, Nov 1993.

[124] L.J. Hornbeck, "Digital light processing and MEMS: timely converegence for a bright future," Proc. SPIE, 2783, pp. 2-13, 1996.

[125] L.J. Hornbeck, "Digital Light Processing ^{TM} for high-brightness, high-resolution applications," Proc. SPIE, vol. 3013, Projection Displays III, pp. 27-40, 1997.

[126] Dana Dudley, Walter M. Duncan, and John Slaughter, "Emerging digital micromirror device (DMD) applications," Proc. SPIE, vol. 4985, MOEMS Display and Imaging Systems, pp. 14-25, January 2003.

[127] E.P. Wagner II, B. W. Smith, S. Madden, J.D. Winefordner, M. Mignardi, "Construction and Evaluation of a Visible Spectrometer Using Digital Micromirror Spatial Light Modulation," Applied Spectroscopy, vol. 49, no.11, pp. 1715-1719, November 1995.

[128] H.J. Robertson, "Development of an active optics concept using a thin deformable mirror," NASA CR-1593, 1970.

[129] J. E. Pearson and S. Hansen, "Experimental studies of a deformable mirror adaptive optical system," J. Opt. Soc., Am., vol. 67, pp. 325-333, 1977.

[130] J. W. Hardy, J. E. Lefebvre and C. L. Koliopoulos, "Real time atmospheric compensation," J. Opt. Soc. Am., vol. 67, pp. 360-369, 1977.

[131] Ronald P. Grosso and Martin Yellin, "The membrane mirror as an adaptive optical element," J. Opt. Soc. Am., vol. 67, no. 3, pp. 399-, March 1977.

[132] R. H. Freeman and J. E. Pearson, "Deformable mirrors for all seasons and reasons," Applied Optics, vol. 21, No. 4, pp.580-588, February 1982.

[133] G. Vdovint and L. Sarro , "Flexible reflecting membranes micromachined," Silicon Semicond. Sci. and Technol. 9, 1570-1572, 1994.

[134] G. Vdovin and P. M. Sarro, "Flexible mirror micromachined in silicon," Appl. Opt., 34, pp. 29682972, 1995.

[135] T. G. Bifano, R. Krishnamoorthy, J. K. Dorton, J. Perreault, N.Vandelli, M. N. Horenstein, and D. A. Castanon, "Continuous membrane surface-micromachined silicon deformable mirror," Opt. Eng., 36, 13541360, May 1997.

[136] G. Vdovin. P.M. Sarro, S. Middelhoek, "Technology and applications of Micromachined Silicon Adaptive Mirrors," Optical Engineering, 36, pp. 5509-5513, 1997.

[137] H. Toshiyoshi and H. Fujita, "An electrostatically operated torsion mirror for optical switching devices," Proc. Transducers, pp.297-300, 1995.

[138] R. Krishnamoorthy, T. G. Bifano and N.Vandelli, "Development of microelectromechancial deformable mirrors for phase modulation of light," Optical Engineering, vol.36(2), pp.542-548, February 1997.

[139] M. Ikeda, H. Goto, M. Sakata, K.I. Wakabayashi, M. Takeuchi and T. Yada, "Two dimensional silicon micromachined optical scanner integrated with photo detector," Proc. SPIE, 2328, pp.118-123, 1995.

[140] R. A. Miller, Yu-Chong Tai, "Micromachined electromagnetic scanning mirrors," Optical Engineering, vol. 36, no.5, pp.1399-1407, May 1997.

[141] Junzhong Liang, David R. Williams, and Donald T. Miller, "Supernormal vision and high-resolution retinal imaging through adaptive optics," J. Opt. Soc. of Amer. A, vol.14, No.11, pp.2884-2892, Nov 1997.

[142] Y. Pan, H. Xie, and G. K. Fedder, "Endoscopic optical coherence tomography based on a microelectromechanical mirro," Opt. Lett., 26, 19661968, 2001.

[143] O. Albert, L. Sherman, G. Mourou, and T. B. Norris, "Smart microscope: an adaptive optics learning system for aberration correction in multiphoton confocal microscopy," Opt. Lett., vol.25, No.1, pp.52-54, January 2000.

[144] Micro-Opto-Electro-Mechanical Systems section in Optical Engineering, Vol. 36, No.5, May 1997.

[145] R. N. Bracewell, "Strip integration in radio astronomy," Aust. J. Phys., vol. 9, pp. 198-217, 1956.

[146] G.T. Herman, "Image reconstruction from projections: the fundamentals of computerized tomography," San Francisco, Academic Press, 1980.

[147] R. Gordon and G. T. Herman, "Reconstruction of pictures from their projections," Commun. Assoc. Comput. Mach., vol. 14, pp. 759-768, 1971.

[148] S. Kaczmarz, "Angenaherte auflosung von systemen linearer gleichungen," Bull. Acad. Pol. Sci. Lett. A, vol. 6-8A, pp. 355-357, 1937.

[149] A. H, Delaney and Y. Bresler, "A fast iterative tomographic reconstruction algorithm," pp. 2295-2298, IEEE 1995.

[150] K. Mueller, R. Yagel, and J.J. Wheller, "Fast implementations of algebraic methods for the 3D reconstruction from cone-beam data," IEEE Transactions on Medical Imaging, vol. 18, no. 6, pp. 538-547, 1999.

[151] http://www.ctlab.geo.utexas.edu/overview/index.php

[152] http://www.asnt.org/publications/Materialseval/basics/may00basics/may00basics.htm

[153] W. H. Bragg and W. L. Bragg, "X-rays and crystal structure," G. Bell, London 1925.

[154] A. S. Glassner, "An introduction to Ray Tracing," San Diego, Academic Press, 1989.

[155] D. L. Windt, E. M. Gullikson, and C. C. Walton, "Normal incidence reflectance of optimized W/B4C X-ray multilayers in the range 1.4 nm - 2.4 nm," Opt. Lett. 27, pp. 22122214, 2002.

[156] K. Tanabe, "Projection method of solving a system of singular system of linear equations and its applications," Numer. Math., 17, pp.203-214, 1971.

[157] J. Du Mond, and J. P. Youtz, "Selective X-Ray Diffraction from Artificially Stratified Metal Films Deposited by Evaporation," Phys. Rev., 48, pp. 703-704, 1935.

[158] E. Spiller, "Low-Loss Reflection Coatings Using Absorbing Materials," Appl. Phys. Lett., 20, pp. 365-367, 1972.

[159] John F. Seely, G. Gutman, J. Wood, G. S. Herman, M. P. Kowalski, J. C. Rife, W. R. Hunter, "Normal-incidence reflectance of W/B4C multilayer mirrors in the 34-50-wavelength region," Applied Optics, 32, pp. 3541-3543, 1993.

[160] P. Hoghoj, K. D. Joensen, F. E. Christensen, J. Susini, E. Ziegler, A. K. Freund, E. Lueken, C. Riekel, "Measurement of multilayer reflectivities from 8 keV to 130 keV," SPIE, 2001, pp. 354-359, 1994.

[161] Oberto Citterio and Stephen L. ODell, "Optics for EUV, X-Ray, and Gamma-Ray Astronomy," Proceedings of SPIE, 5168, January 2004.

[162] Curtis R. Vogel "Computational Methods for Inverse Problems," Society for Industrial and Applied Mathematics, 2002.

[163] Xu Li and Susan C. Hagness, "A Confocal Microwave Imaging Algorithm for Breast Cancer Detection," IEEE Microwave and Wireless Components Letters, Vol. 11, no. 3, pp. 130-132, March 2001.

[164] Gary D. Knott, "Interpolating Cubic Splines (Progress in Computer Science & Applied Logic)," Birkhauser Verlag AG , 1999.

[165] Bartels R. H., Beatty J. C. and Barsky B. A., "An Introduction to Splines for Use in Computer Graphics and Geometric Modelling," San Francisco, CA: Morgan Kaufmann, 1998.

[166] K. Arunachalam, S. S. Udpa and L. Udpa, "Active Microwave Breast Cancer Imaging Using Deformable Mirror," The 2006 IEEE AP-S International Symposium on Antennas and Propagation and USNC/URSI National Radio Science Meeting, July 9 - 15, Albuquerque (USA), 2006.

[167] K. Arunachalam, L. Udpa and S. S. Udpa, "Active Microwave Imaging using a Deformable Mirror," The 12th Biennial IEEE Conference on Electromagnetic Field Computation, April 30th to May 3rd, Miami (USA), 2006.

[168] Arunachalam Kavitha, Udpa Lalita and Udpa Satish S, "Imaging using Deformable Mirror for Inverse Scattering Applications," 9th Workshop on Optimization and Inverse Problems in Electromagnetics, September 13th-15th, Sorrento (Italy), 2006.

[169] R. O. Duda, P. E. Hart and D. G. Stork, "Pattern Classification," 2nd ed., John Wiley and Sons, 2001.

[170] O. C. Zienkiewicz and R. L. Taylor, "The Finite Element Method," McGraw Hill, NewYork, 1989.

[171] P.P Silvester and R. L. Ferrari, "Finite Elements for Electrical Engineers," Cambridge University Press, 1990.

[172] Churchill R. Vance, "Complex variables and applications," New York : McGraw-Hill, 1984.

[173] Kavitha Arunachalam, Satish S. Udpa and Lalita Udpa, "Deformable Mirror Tomography An Alternative Imaging Technique for Inverse Scattering Applications," submitted to Ineternational Journal of Applied Electromagnetics and Mechanics (IJAEM).

[174] Paul R. Stauffer and S. N. Goldberg, "Introduction: Thermal ablation therapy," Int. J. Hyperthermia, vol. 20, no. 7, pp. 671677, Nov 2004.

[175] M. W. Dewhirst, B. L. Vglianti, M. Lora-Michiels, M. Hanson, and P. J. Hoopes, "Basic principles of thermal dosimetry and thermal thresholds for tissue damage from hyperthermia," Int. J. Hyperthermia, vol. 19, no. 3, pp. 267294, 2003.

[176] D. F. Kacher, and F A. Jolesz, "MR imagingguided breast ablative therapy," Radiol Clin N Am, vo.l. 42, pp. 947 962, 2004.

[177] K. Hynynen, O. Pomeroy, D. N. Smith, P. E. Huber, N. J. McDannold, J. Kettenbach, J. Baum, S. Singer, and F. A. Jolesz, "MR Imagingguided Focused Ultrasound Surgery of Fibroadenomas in the Breast: A Feasibility Study," Radiology, vol. 219, pp. 176185, 2001.

[178] J. E. Kennedy, G. R. Ter Haar, and D. Cranston, "Review article High intensity focused ultrasound: surgery of the future?,"The British Journal of Radiology, vol. 76, pp. 590599, 2003.

[179] H. Mumtaz, M. A. Hall-Craggs, A. Wotherspoon, M. Paley, G. Buonaccorsi, Z. Amin, I. Wilkinson, M. W. Kissin, T. I. Davidson, I. Taylor, and S. G. Bown, "Laser Therapy for Breast Cancer : MR Imaging and Histopathologic Correlation," Radiology vol. 200, pp. 651-658, 1996.

[180] S. Fujimoto, K. Kobayashi, M. Takahashi, K. Nemoto, I. Yamamoto, T. Mutou, T. Toyasawa, T. Ashida, S. Hayashi, N. Igarashi and H. Ohkubo, "Clinical pilot studies on pre-operative hyperthermic tumour ablation for advanced breast carcinoma using an 8MHz radiofrequency heating device," Int. J. Hyperthermia, vol. 19, pp. 13-22, 2003.

[181] E. S. Ebbini, S. I. Umemura, S.I., M. Ibbini, C. A. Cain, "A cylindrical-section ultrasound phased-array applicator for hyperthermia cancer therapy," IEEE Trans. Ultrason. Ferroelect. Freq. Contr., vol. 35, pp. 561 - 572, 1988.

[182] A. J. Fenn , G. L. Wolf and R. M. Fogle, "An adaptive microwave phased array for targeted heating of deep tumors in intact breast: animal study results," Int. J. Hyperthermia, vol. 15, pp. 45-61, 1999.

[183] V. N. Mazokhin, D. N. Kolmakov, N. A. Lucheyov, E. A. Gelvich and I. I. Troshin, "A HFEM installation allowing simultaneous whole body and deep local EM hyperthermia," Int. J. Hyperthermia, vol. 15, no. 4, pp. 309- 329, 1999.

[184] J. C. Camart, D. Despretz, B. Prevost, J. P. Sozanski, M. Chive and J. pribetich, "New 434MHz interstitial hyperthermia system monitored by microwave radiometry: theoretical and experimental results," Int. J. Hyperthermia, vol. 16, no. 2, pp. 95-111, 2000.

[185] L. Wu, R. J. McGough, O. A. Arabe, and T. V. Samulski, "An RF phased array applicator designed for hyperthermia breast cancer treatments," Phys. Med. Biol., vol. 51, pp. 120, 2006.

[186] M. Hiraoka, M. Mitsumori, N. Hiroi, Sh. Ohno, Y. Tanaka, Y. Kotsuka, and K. Sugimachi, "Development of RF and Microwave Heating Equipment and Clinical Applications to Cancer Treatment in Japan," IEEE Trans. MTT, vol. 48, no. 11, November 2000.

[187] S. K. Das, S. T. Clegg and T. V. Samulski, "Electromagnetic thermal therapy power optimization for multiple source applicators," Int. J. Hyperthermia, vol. 15, No. 4, pp. 291-308, 1999.

[188] M. Seebass, R. Beck, J. Gellermann, J. Nadobny and P. Wust, "Electromagnetic phased arrays for regional hyperthermia: optimal frequency and antenna arrangement," Int. J. Hyperthermia, vol. 17, pp. 321-336, 2001.

[189] J. Wiersma, R. A. M. Van Maarseveen, and J. D. P. Van Dijk, "A flexible optimization tool for hyperthermia treatments with RF phased array systems," Int. J. Hyperthermia, vol. 18, No. 2, pp. 73-85, 2002.

[190] H. Kroeze, J. B. Van de Kamer, A. C. De Leeuw and J. J. W. Lagendijk, "Regional hyperthermia applicator design using FDTD modelling," Phys. Med. Biol., vol. 46, pp. 19191935, 2001.

[191] K. D. Paulsen, S. Geimer, J. Tang, and W. Boyse, "Optimization of pelvic heating rate distributions with electromagnetic phased arrays," Int. J. Hyperthermia, vol. 15, no. 3, pp. 157-186, 1999.

[192] C. Baroni, M. G. Giri, G. Meliadoa, S. Maluta, and G. Chierego, "A method for the quantitative evaluation of SAR distribution in deep regional hyperthermia," Int. J. Hyperthermia, vol. 17, no. 5, pp. 369-381, 2001.

[193] M. Converse, E. J. Bond, S. C. Hagness, and B. D. Van Veen, "Ultrawide-Band Microwave SpaceTime Beamforming for Hyperthermia Treatment of Breast Cancer: A Computational Feasibility Study," IEEE Trans MTT, vol. 52, no. 8, August 2004.

[194] K. Arunachalam, S. S. Udpa and L. Udpa, "Microwave Breast Cancer Hyperthermia Using Deformable Mirror," The 2006 IEEE AP-S International Symposium on Antennas and Propagation and USNC/URSI National Radio Science Meeting, July 9 - 15, Albuquerque (USA), 2006.

[195] Kavitha Arunachalam, Satish S. Udpa and Lalita Udpa, "An RF Therapy System for Breast Cancer Treatment Using Deformable Mirror," The 33rd Annual Review of Progress in Quantitative Nondestructive Evaluation (QNDE), July 30-August 4, Portland (USA), 2006.

[196] P. Bernardi, M. Cavagnaro, S. Pisa and E. Piuzzi, Specific Absorption Rate and Temperature Elevation in a Subject Exposed in the Far-Field of Radio-Frequency Sources Operating in the 10900-MHz Range, IEEE Trans. Biomed. Eng., vol. 50, no. 3, March 2003.

[197] J. B. Van De Kamer, N. Van Wieringen, A. A. C. De Leeuw and J. J. W. Lagendijk, "The significance of accurate dielectric tissue data for hyperthermia treatment planning," Int. J. Hyperthermia, vol. 17, no. 2, pp. 123-142, 2001.

[198] Albert Macovski, "Medical imaging systems," Prentice-Hall, Englewood Cliffs, NJ, 1983.

[199] *http : //yhspatriot.yorktown.arlington.k12.va.us/ ckaldahl/Links/MRI_links_adv.html*

[200] *http : //www.partnershipforbreastcare.org/PBC/problems/ways/mri.aspx*

[201] Uwe Fischer, "Practical MR Mammography," George Thieme Verlag, New York, 2004.

[202] S. H. Heywang-Kobrunner and R. Beck, "Contrast-enhanced MRI of the Breast," Springer Verlag, 1995.

[203] http://training.seer.cancer.gov/

[204] Anil K. Jain, "Fundamentals of Digital Image Processing," Prentice Hall, Englewood Cliffs, NJ, 1989.

[205] M. Born and E. Wolf, "Principles of Optics," sixth edition (with corrections), Pergamon Press, 1989.

[206] "WP813SRD/D 10mm GaAlAs red LED," April 19 2005, Rev. 2, Kingbright Coroporation, CA, USA.

[207] "LC1-USB 2.0 CCD Line Camera," October 16 2004, 10695-D02 Rev. A, Thorlabs Inc., NJ, USA.